The role of shear zones in the exhumation of the ultrahigh-pressure Western Gneiss Region

A Dissertation
SUBMITTED TO THE FACULTY OF
UNIVERSITY OF MINNESOTA
BY

Roxanne Nikole Renedo

IN PARTIAL FULFILLMENT OF THE REQUIREMENTS
FOR THE DEGREE OF
DOCTOR OF PHILOSOPHY

Donna Whitney, Christian Teyssier

September 2016

Acknowledgements

Many thanks to Donna Whitney, Christian Teyssier, Peter Hudleston, David Kohlstedt, Haakon Fossen (University of Bergen), Sandra Piazolo (Macquarie University), Stacia Gordon (University of Nevada, Reno) and the past and present members of the Structure, Tectonics, and Metamorphic Petrology research group.

Abstract

The study of ultrahigh-pressure terranes informs our understanding of continental collision, subduction, and exhumation in both ancient and modern orogens. However, these studies rarely focus on the metamorphosed continental crust that forms the bulk of ultrahigh-pressure terranes. Here, we document a combined petrologic and structural investigation of mylonite zones in metamorphosed continental crust of the ultrahigh-pressure Western Gneiss Region of Norway that sheds light on the exhumation of ultrahigh-pressure terranes through the study of the continental crust. One of these shear zones, the Salt Mylonite Zone, is a prime example of the importance of the quartzofeldspathic gneiss that is associated with ultrahigh-pressure (coesite-bearing) eclogite. Eclogite in the Salt mylonite zone preserves quartz fabrics formed near UHP conditions (prism <c> fabric) and omphacite fabrics that are consistent with constrictional deformation near UHP conditions. Ti-in-quartz thermobarometry indicates equilibration of eclogite at temperatures > 750 °C and for quartzofeldspathic gneiss indicates quartz deformation/recrystallization took place over a range of temperatures from near UHP conditions to amphibolite facies conditions. Gneiss in the Salt Mylonite Zone preserves two dominant microstructures: phase-separated gneiss and phase-mixed gneiss. Despite preserving the same assemblage and being in close proximity (shared pressure and temperature conditions), fabrics between the two gneiss types differ due to habit. In both gneiss types, reverse zoning in plagioclase (Na-rich cores, Ca-rich rims) is ubiquitous. The compositional zoning records grain growth by grain boundary migration

during exhumation-induced decompression. The study of the Salt Mylonite Zone is proof that shear zones in continental crust preserve a vital record of exhumation of ultrahigh-pressure terranes.

Preliminary studies were conducted on two additional shear zones, The Finnøya Mylonite Zone and the Svartberget Mylonite Zone. Like the Salt Mylonite Zone, both contain evidence of deformation over a wide range of conditions. The Finnøya Mylonite Zone contains clinopyroxene-garnet gneiss with a composition similar to associated deformed eclogite pods. This shear zone, in particular, suggests that eclogite may have experienced extensive melting and mylonitization during exhumation from peak conditions. The Svartberget Mylonite Zone is composed of paragneiss and was deformed at sillimanite-stable conditions. The associated mafic material was synkinematically deformed as evidenced by elongate, foliation-parallel amphibolite and retrogressed eclogite pods. The abundant shear zones in the Western Gneiss Region of Norway record local exhumation from UHP to amphibolite-facies conditions. Understanding the deformational history of these individual shear zones can contribute to the overall understanding of the exhumation of the WGR.

Table of Contents

List of Tables

List of Figures

1. Introduction

Ultrahigh-pressure (UHP) metamorphism describes coesite-stable rocks formed due to regional metamorphism. Coesite, the high pressure polymorph of silica, is stable at temperatures > 700 °C and pressures > 2.8 GPa (equivalent to 90 km depth). Coesite was first discovered in metamorphic rocks simultaneously by Chopin (1984) in the Western Alps and Smith (1984) in the Western Gneiss Region of Norway (WGR). The discovery of coesite was the first evidence that continental crust could subduct to depths far greater than previously thought, and thus opened up a new field of study. Subsequent studies of UHP metamorphism led to the identification of entire UHP terranes: regions that display evidence of UHP metamorphism. Now, more than 20 UHP terranes have been identified worldwide (e.g. Gilotti, 2013) and our understanding of the kinematics of continental collision, subduction, and exhumation continues to grow.

Decades of study has led to a detailed understanding of certain aspects of UHP metamorphism which include: general tectonic setting, regional geology, timing (including age of metamorphism and duration of metamorphism), and peak pressure and temperature conditions. However, fundamental questions still remain regarding the mechanics of subduction and exhumation of UHP terranes. The following study focuses on better understanding the exhumation path of one UHP terrane to gain insight into the exhumation processes of UHP terranes.

1.1. Proposed UHP exhumation mechanisms

Two broad types of UHP terranes have been identified that may have different exhumation mechanisms: (1) small UHP terranes (<10,000 km^2), and (2) large UHP terranes (>10,000 km^2) (Kylander-Clark et al., 2012). Small UHP terranes are 1 to 5 km thick and composed of tectonically emplaced slices of UHP rocks surrounded by lower pressure rocks (Henry et al., 1993). These terranes are generally exhumed within 10 Myr of the onset of collision (Rubatto and Hermann, 2001, Monteleone et al., 2007) and are young, no older than 50 Myr old (Kylander-Clark et al., 2012 and references therein). Large UHP terranes, on the other hand, are a minimum of 10 km thick. The duration of UHP metamorphism is 15-25 Myr (Hacker et al., 2006; Mattinson et al., 2006; Kylander-Clark et al., 2008), exhumation takes place over 10-30 Myr (Kylander-Clark et al., 2009), and all large UHP terranes are older, at least 200 Myr old (e.g. Hacker et al., 2006).

Many models have been proposed to explain the exhumation of UHP terranes. Two broad types of exhumation models exist: syn-convergence exhumation models and syn-extensional exhumation models. Eduction, buoyancy-driven exhumation, and channel flow are the three models that are most often called upon for the exhumation of large UHP terranes, like the WGR. All three models are syn-convergent. Eduction (Andersen et al., 1991) is a process by which the rigid, subducted continental crust isostatically rebounds following detachment from the denser, oceanic lithosphere on the leading edge of the subducting plate. Buoyancy-driven exhumation (Chemenda et al., 1995) is accomplished when the relatively weak upper layer of subducted material detaches from the slab below and then is exhumed along the subduction channel, largely driven by buoyancy. Exhumation by channel flow (Gerya et al., 2008) is accomplished by

circulation within the subduction channel; incoming material pushes old, metamorphosed material out of the channel. These syn-convergence models are able to generate and explain some, but not all, of the features observed in large UHP terranes.

Syn-extensional exhumation (e.g. Butler et al., 2015) is another possible mechanism for the exhumation of large UHP terranes, however it is less commonly discussed in the literature. Extensional features are common in UHP terranes (e.g. Krabbendam and Dewey, 1998, Suo et al., 2001), which suggests that syn-extensional exhumation is a possible mechanism for UHP exhumation. Syn-extensional exhumation remains rarely discussed as it is difficult to identify a mechanism responsible for the transition from convergence to divergence.

1.2. The Western Gneiss Region of Norway

The WGR (Fig. 1) is the largest and best exposed UHP terrane in the world. It is situated in western Norway and covers over 50,000 km^2 of which at least 5,000 km^2 are UHP (e.g. Hacker et al., 2010). The WGR is a polymetamorphic terrane that underwent a Proterozoic granulite facies deformation event at ~950 Ma (peak conditions ~900°C and 1.0 GPa) prior to the WGR-forming Caledonian Orogeny (~480 Ma – 380 Ma) (Brueckner and van Roermund, 2004; Hacker et al., 2010). The Caledonian Orogeny occurred in stages including: (1) the closure of the Iapetus ocean and unconformable emplacement of allochthonous nappes onto Baltica (from ~430 to ~410 Ma) (Gee, 1975; Torsvik et al., 1996; Tucker et al., 2004), (2) the continent-continent collision of Baltica and Laurentia, (3) the subsequent westward subduction of Baltica beneath Laurentia to

UHP conditions (~425 Ma - ~400 Ma) (Andersen et al., 1991, Andersen et al., 1998; Carswell et al., 2003; Root et al., 2004; Tucker et al., 2004; Hacker and Gans, 2005; Kylander Clark et al., 2007), and (4) exhumation of the UHP terrane to mid-crustal levels (by ~390 to ~380 Ma) (Andersen et al., 1998; Root et al., 2005; Hacker, 2007; Kylander-Clark et al., 2008; Young et al., 2011).

The WGR is divided broadly into two parts: (1) the (U)HP terrane, the focus of this study, exposed in the west and (2) the allochthonous nappe complex that overlies the (U)HP terrane, exposed in the east (Gee, 1975; Cuthbert et al., 2000; Hacker et al., 2010) (Fig. 1). The (U)HP terrane is comprised of Proterozoic orthogneiss (c. 1650 Ma and 950 Ma) (~90%) with minor (~5%) eclogite, peridotite and other mafic material, and minor (~5%) pegmatite dikes and migmatites. The orthogneiss, which makes up the bulk of the terrane, is tonalitic to granodioritic in composition (Smith, 1984; Krabbendam and Wain, 1997), is highly deformed, and preserves primarily amphibolite facies assemblages due to the post-UHP, lower-grade metamorphic overprint (Griffin and Brueckner, 1985; Terry and Robinson, 2003; Labrousse et al., 2004). The eclogite, while a relatively minor component of the UHP terrane, is the lithology that most commonly preserves evidence of UHP metamorphism. Coesite and microdiamond, minerals only stable at UHP conditions, are often found as inclusions in stronger phases (garnet and clinopyroxene) in eclogite. Coesite has been identified in all three UHP domains (Smith, 1984; Wain, 1997; Wain et al., 2000; Carswell et al., 2003; Butler et al., 2012) and microdiamond has been identified in the southern and northern UHP domains (Dobrzhinetskaya et al., 1995; Vrijmoed et al., 2006; Smith and Godard, 2013).

Structurally, three distinct UHP terranes are defined in the WGR (Fig. 1). These domains, the cores of eroded antiforms, expose the deepest subducted material (Root et al., 2005; Hacker, 2007), and only HP rocks occur in the intervening regions. Boundaries between the UHP domains and the surrounding HP material have a constant gradient in peak pressure-temperature (P and T, respectively) conditions indicating that there is no tectonic boundary between the UHP and HP domains (Wain et al., 2000; Young et al., 2007). The peak metamorphic conditions recorded by eclogites in the WGR increases to the northwest. From south to north, the peak conditions are: 700-800 °C and ~3.0 GPa in the southern UHP domain (Wain, 1997; Johnston et al., 2007); 750-800 °C and ~3.0 GPa in the central UHP domain (Butler et al., 2012); and >800 °C and 3.5-4.0 GPa (Terry et al., 2000) in the northern UHP domain. This gradient in peak conditions is consistent with the deepest subduction occurring in the northwestern most part of the WGR (Griffin and Brueckner, 1985; Labrousse et al., 2002; Tucker et al., 2004).

2. Fabric development during exhumation from ultrahigh-pressure in an eclogite-bearing shear zone, Western Gneiss Region

Published in Journal of Structural Geology, Volume 71, February 2015, 58-70

Abstract

Petrofabrics and trace-element thermobarometry of deformed quartzofeldspathic gneiss and associated coesite-bearing eclogite in the Salt Mylonite Zone (Western Gneiss Region, Norway) document a pressure-temperature-deformation path from ultrahigh-pressure to amphibolite-facies conditions. The Salt Mylonite Zone is dominated by quartzofeldspathic gneiss with a strong foliation and lineation. Coesite-bearing eclogite within the shear zone contains a foliation and lineation (defined by elongate omphacite) consistent with that of the host gneiss suggesting that gneiss and eclogite were deformed in the same kinematic framework. In eclogite, omphacite preserves LS- to L-type CPO, and quartz preserves prism <c> fabrics that developed in quartz near coesite-quartz transition conditions. The quartzofeldspathic gneiss in the mylonite zone records prism and rhomb <a> slip in quartz and reverse zoning in plagioclase (higher Ca rims) consistent with re-equilibration during decompression. The Ti concentration in quartz in gneiss is higher than that of quartz in eclogite, suggesting quartz recrystallized at a lower pressure in the gneiss. Ti-in-quartz thermobarometry of rutile-bearing eclogite and titanite-bearing gneiss indicates equilibration at $T > 750$ °C and $T < 650$ °C, respectively. This mylonite zone preserves a discontinuous record of fabric development from incipient stages of exhumation of ultrahigh-pressure rocks to crustal conditions.

2.1. Introduction

Numerous (>20) ultrahigh-pressure (UHP) terranes have been identified globally (Zheng, 2012); the abundance of these terranes shows that the exhumation of deeply-subducted continental crust is a common consequence of continental collision. UHP terranes record chemical and physical processes that occur during continental collision, subduction, and exhumation. An unresolved question concerns the exhumation mechanism(s) of UHP terranes, a query that may be approached, in part, by documenting the conditions and mechanisms of deformation in shear zones that were active from mantle depths (high pressure, HP, and possibly UHP conditions) to lower- to mid-crustal depths.

The Western Gneiss Region (WGR) is one of the largest and best-exposed UHP terranes. Here, evidence of HP and UHP metamorphism is typically preserved in lenses (pods) of eclogite dispersed in highly deformed quartzofeldspathic gneiss (e.g., Smith, 1984; Wain, 1997; Carswell et al., 2003a; Carswell et al., 2003b; Hacker et al., 2010). Discrete shear zones in the quartzofeldspathic gneiss are documented throughout the WGR. In some of these shear zones, both gneiss and eclogite underwent extreme deformation and now record a range of pressure-temperature-deformation (*P-T-d*) conditions from before exhumation to emplacement at crustal levels.

We have investigated in detail a ductile shear zone that consists of quartzofeldspathic gneiss that hosts a strongly deformed UHP (coesite-bearing) eclogite layer: the Salt mylonite zone (SMZ; Figs. 1, 2a). In this paper, we document and discuss the conditions under which mesoscopic structures and microfabrics developed in eclogite

and gneiss in the SMZ. Ti-in-quartz thermobarometry and microfabric analysis are used to explore deformation conditions and mechanisms as a function of pressure (*P*). We show that eclogite fabrics likely formed under HP conditions (*P* > 2 GPa) following decompression from UHP conditions, and that fabrics in the quartzofeldspathic gneiss developed over a wide range of *P* and temperature (*T*) conditions during decompression to crustal levels (*P* < 1 GPa).

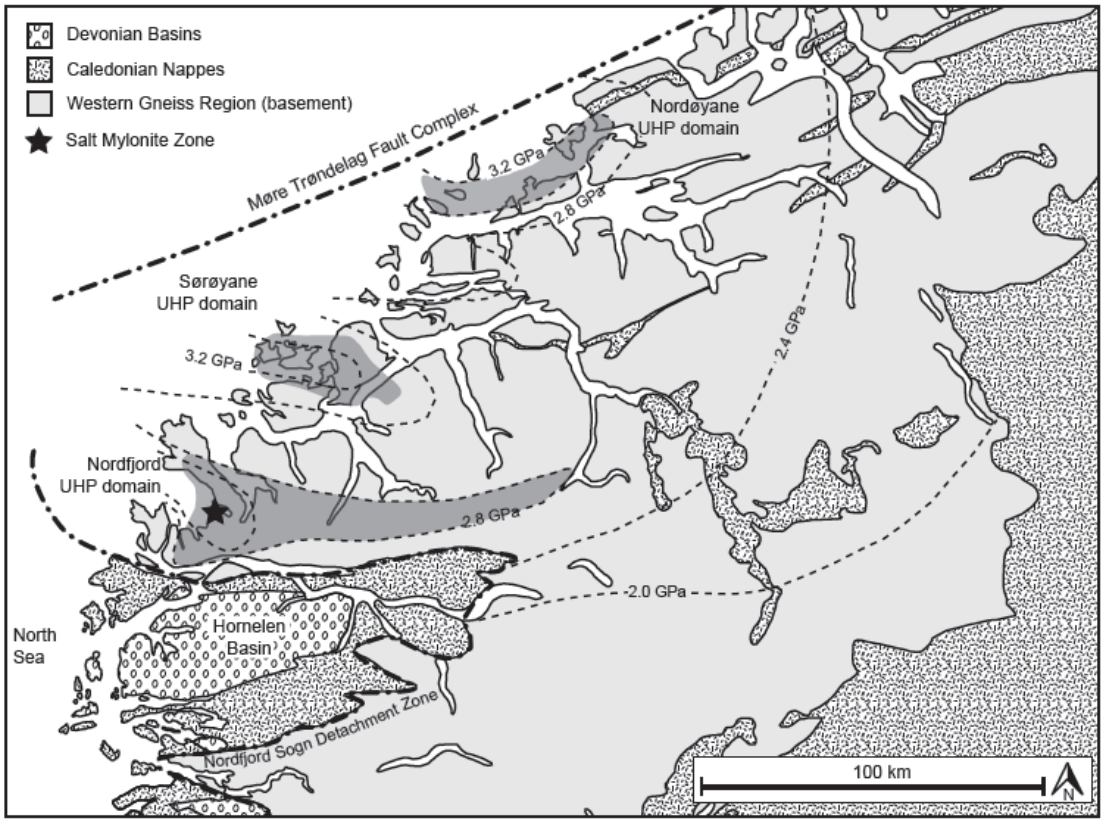

Figure 1. Map of the WGR, Norway. The HP (light gray) and UHP (dark gray) WGR is bound by the Nordfjord Sogn detachment zone to the south and west and by the Møre-Trondelag fault complex to the north. The Nordfjord Sogn detachment zone separates the basement from the overlying allochthonous nappes and Devonian basins (i.e., the Hornelen basin). The three UHP domains are exposed along the western coast, from south to north they are: the Nordfjord, the Sørøyane, and the Nordøyane UHP domains. Isobars (from Hacker et al., 2010 and references therein) are shown on the map; these data suggest a general *P* (and *T*) increase to the NW. The SMZ is located in the Nordfjord UHP domain (black star).

2.2. Overview of the Western Gneiss Region

The WGR of Norway (Fig. 1) is a large UHP terrane that covers 50,000 km^2; at least 5% of the WGR preserves UHP conditions, primarily in eclogite lenses hosted in gneiss (e.g., Hacker et al., 2010). The WGR formed during the Caledonian orogeny as a result of the subduction of Baltica beneath Laurentia (ca. 425-400 Ma) during which UHP conditions were attained (Andersen et al., 1991; Andersen et al., 1998; Carswell et al., 2003a; Root et al., 2004). Exhumation of the terrane to amphibolite-facies conditions was largely achieved by ca. 390-380 Ma (Andersen et al., 1998; Hacker, 2007; Young et al., 2011).

The WGR is dominated by strongly deformed, tonalitic to granodioritic, migmatitic gneiss (e.g., Hacker et al., 2010). The gneiss preserves primarily amphibolite-facies assemblages that may represent re-equilibration during exhumation and overprinting of (U)HP assemblages and textures (Griffin and Brueckner, 1985; Wain, 1997; Terry and Robinson, 2003; Labrousse et al., 2004). Moreover, the gneiss contains metamorphosed mafic (eclogite, amphibolite) and ultramafic rocks (peridotites) that form centimeter to kilometer layers and lenses.

UHP metamorphism in the WGR is identified by the presence of index minerals including coesite and microdiamond (e.g., Smith, 1984; Griffin and Brueckner, 1985; Wain 1997; Wain et al., 2000; Cuthbert et al., 2000; Butler et al., 2012; Smith and Godard, 2013). Coesite and polycrystalline quartz (Pcq, interpreted as a pseudomorph after coesite; Smyth, 1977) are commonly found as inclusions in garnet and clinopyroxene in eclogite (e.g., Smith, 1984) and less commonly as inclusions in garnet

and clinozoisite in gneiss (Wain, 1997). Microdiamond has also been reported from garnet-kyanite gneiss (Dobrzhinetskaya et al., 1995) and metamorphosed ultramafic rocks (Vrijmoed et al., 2006).

The occurrence of UHP minerals in the WGR defines three UHP domains. From south to north these are the Nordfjord, Sørøyane, and Nordøyane UHP domains (Fig. 1). Rocks in the intervening regions record HP (but not UHP) conditions (Wain, 1997; Root et al., 2005; Hacker, 2007). Previous research suggests a general increase of *P* and *T* to the northwest in the WGR (e.g., Hacker et al., 2010), with the lowest peak conditions preserved in the Nordfjord UHP domain (700-800 °C and ~2.8-3.0 GPa; Wain, 1997; Johnston et al., 2007) and the highest peak conditions preserved in the Nordøyane UHP domain (>800 °C and 3.5-4.0 GPa; Terry et al., 2000). This interpretation is complicated, however, by the recent discovery of microdiamond of unknown age in eclogite from the Nordfjord UHP domain (Smith and Godard, 2013), indicating minimum pressures of ~3.5 GPa for at least part of this domain. If this diamond-forming metamorphism is Caledonian, then this, along with the coexistence of HP and UHP eclogite (Wain, 1997; Wain et al., 2000), is further evidence of heterogeneity in WGR *P-T* conditions and/or in the preservation of peak metamorphic assemblages.

The structures of the WGR, from the scale of the orogen to mesoscopic fabrics, suggest that exhumation was accommodated by oblique extension. At the largest scale, this is indicated by the interplay of the Nordfjord-Sogn detachment zone and the Møre-Trondelag fault complex, the normal and strike slip fault zones, respectively, that bound the WGR (Norton, 1986; 1987, Braathen et al., 2000). The interplay of these fault zones

has led to the development of corrugated detachments (Krabbendam and Dewey, 1998). In this regard, the UHP domains have been interpreted as possible transtensional antiforms (Krabbendam and Dewey, 1998; Fossen et al., 2013). Mineral and stretching lineations are oblique to the trend of the orogen (Fossen, 2010), and constrictional fabrics have been documented in rocks throughout the WGR (e.g., Barth et al., 2010). These features are consistent with oblique extension, at least at amphibolite-facies conditions (Krabbendam and Dewey, 1998).

2.3. The Salt Mylonite Zone

The SMZ (Fig. 2a) is a 60 m wide zone of localized ductile deformation in deformed, quartzofeldspathic gneiss (referred to as the 'country-rock gneiss'). The country-rock gneiss is medium grained, contains layer-parallel leucosomes, preserves a well-developed foliation with variable orientation, a pervasive east plunging mineral lineation, and contains variably retrogressed eclogite pods and amphibolite (± garnet) layers and lenses (m-scale). In comparison, within the SMZ, the quartzofeldspathic gneiss is characterized by 'stripes' of fine-scale compositional layering. The striped gneiss is finer-grained, displays a strong, planar east-west trending foliation, with a consistent steep to moderate dip to the north (Fig. 3a), and a well-defined mineral lineation, with a shallow to moderate plunge to the east. Although overall fine-grained, some gneiss layers within the SMZ contain large (up to 1 cm) potassium feldspar porphyroclasts with recrystallized tails that display σ and δ morphologies (Passchier and Simpson, 1986) that indicate consistent top-to-the-west (left-lateral) sense of shear (Fig. 3b). A meter-scale

fold that appears to have initiated around a large mafic pod also displays a westward vergence (Fig. 3c).

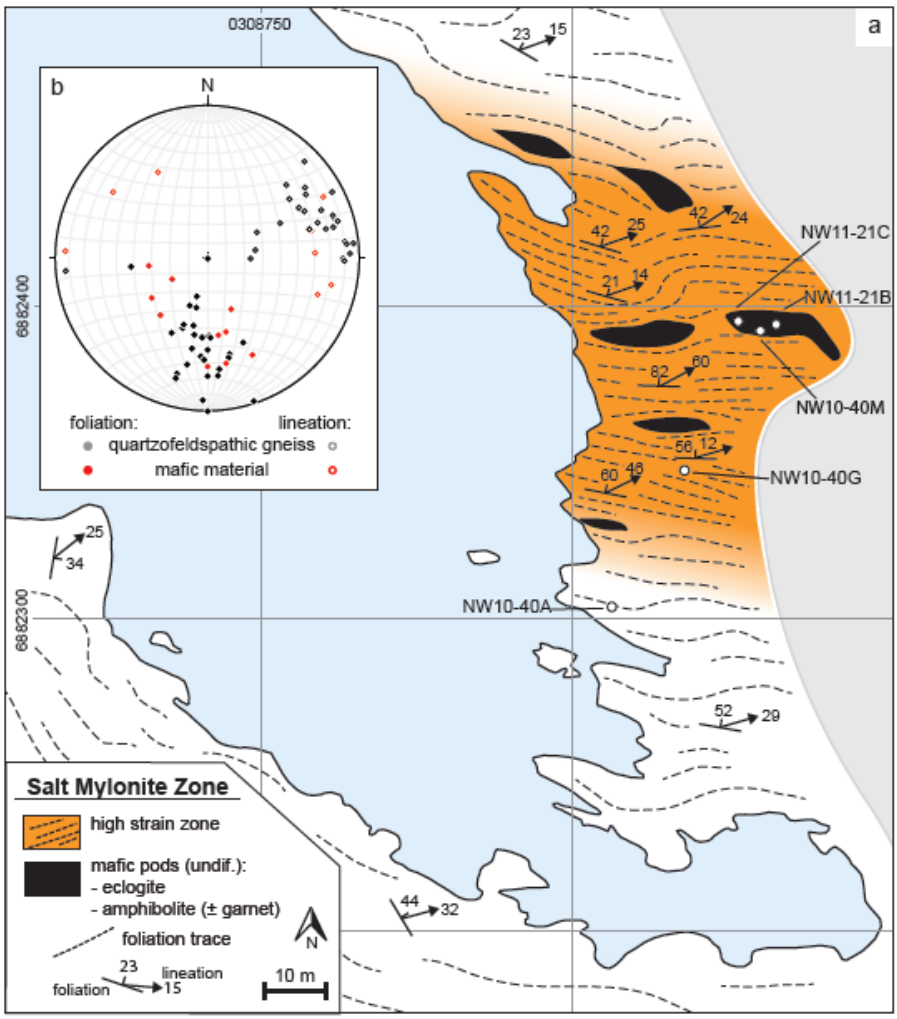

Figure 2. (a) Map of the SMZ (highlighted in orange) with quartzofeldspathic gneiss structural measurements and sample locations. Mafic material (eclogite and amphibolite, black) is contained within the quartzofeldspathic host gneiss. (b) Stereonet of structural measurements from the SMZ. The foliation of the quartzofeldspathic host gneiss (poles to planes represented by black, filled circles) and mafic material (eclogite and amphibolite, poles to planes represented by red filled circles) are similarly oriented, whereas gneiss and mafic material lineations (hollow circles of the same color) are slightly more variable.

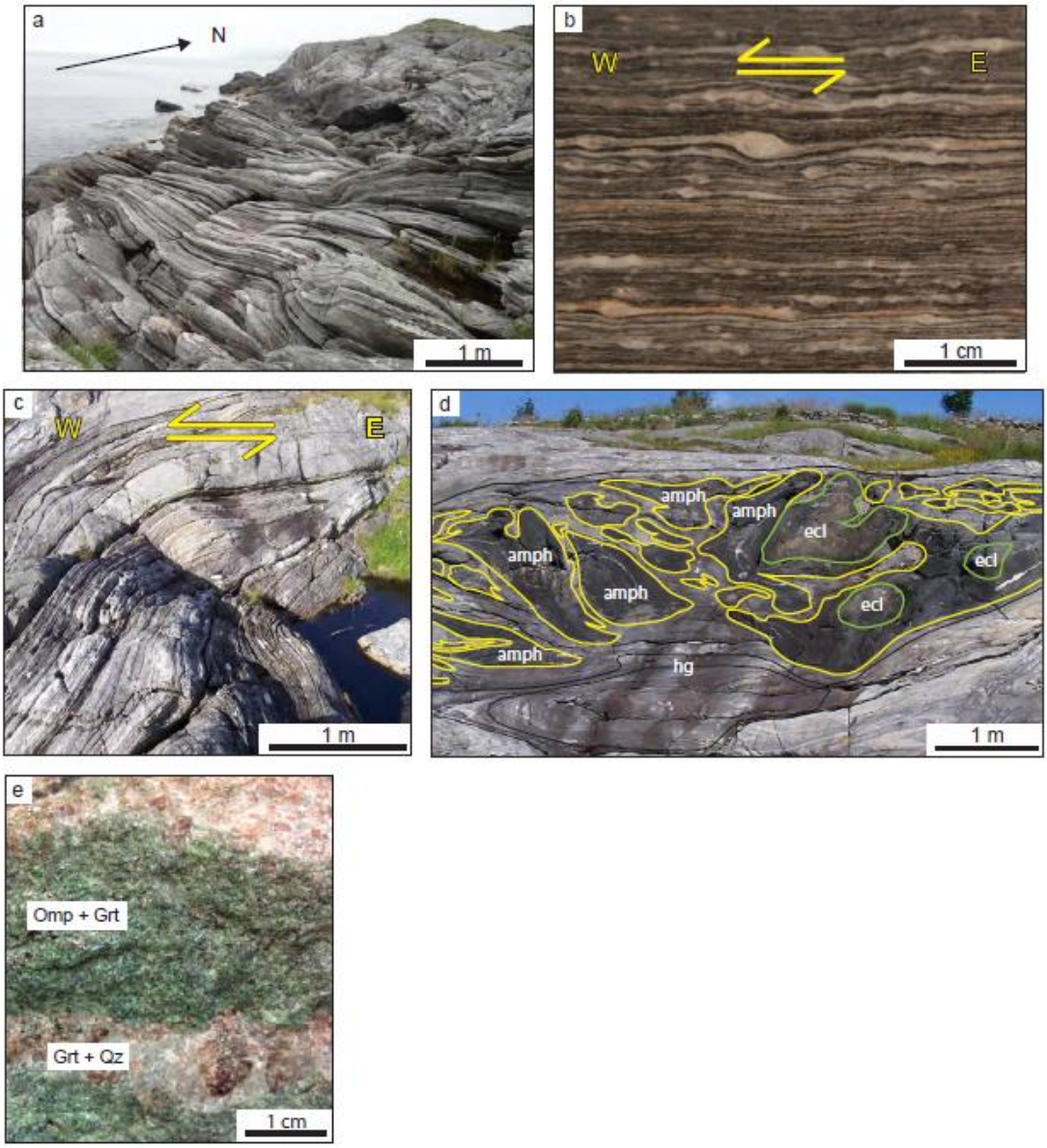

Figure 3. Field photos of the SMZ. (a) Striped gneiss (e.g., sample NW10-40G) with consistent planar foliation and moderate N-dip. (b) K-feldspar porphyroclasts in striped gneiss showing top-to-the-west sense of shear. (c) Meter-scale fold in the striped gneiss of the SMZ that shows a westward vergence. (d) Retrogressed mafic pod at the northern end of the SMZ. Eclogite (ecl) cores what was likely an entire eclogite pod that has since retrogressed to amphibolite ± garnet (amph). It is surrounded by hornblende-bearing quartzofeldspathic gneiss (hg). The outlines are to delineate between rock types but the contacts are gradational in nature. (d) Fresh, layered eclogite (e.g., samples NW10-40M, and NW11-21B and C) showing the relationship between foliation-parallel, quartz-rich layers and more abundant omphacite-rich layers. Mineral abbreviations after Whitney and Evans (2010).

Metamorphosed mafic rocks (eclogite and amphibolite ± garnet) comprise ~10% of the SMZ and occur as layers and pods within the striped gneiss. Some amphibolite layers are thin (mm- to cm-scale) and show no clear relationship to eclogite; other amphibolites form the retrogressed rims of eclogite pods (Fig. 3d). The orientation of foliation in eclogite and amphibolite in the SMZ is consistent with the fabric in the host, striped quartzofeldspathic gneiss. However, the eclogite and amphibolite lineations display more variation than the gneiss (Fig. 2b).

2.4. Mineral compositions and textures of eclogite and gneiss

Major element compositions of clinopyroxene in eclogite and plagioclase in gneiss were determined by electron-microprobe analysis (JEOL JXA-8900, Department of Earth Sciences, University of Minnesota Twin Cities). Qualitative (energy-dispersive spectroscopy) element maps were acquired using a 15 kV accelerating voltage, 100 nA current, a focused beam, and stage-rastering step sizes ranging from 1 to 3 μm depending on grain size. Quantitative (wavelength-dispersive spectroscopy) clinopyroxene analyses (to determine jadeite content) were acquired using a 15 kV accelerating voltage, 25 nA current, and a focused beam. Quantitative plagioclase analyses were acquired using a 15 kV accelerating voltage, 20 nA current, and a 5 μm beam. ZAF correction was applied to all analyses. Natural mineral standards were used for calibration. Representative compositions are in Table 1.

	Clinopyroxene					Plagioclase							
sample	NW11-31A		NW11-21B		**sample**	NW10-40A		NW10-40A		NW10-40G		NW10-40G	
location	in SMZ		in SMZ		**location**	out of SMZ		out of SMZ		in SMZ		in SMZ	
lithology	Ecl		Ecl		**lithology**	Gn, Pl core		Gn, Pl rim		Gn, Pl core		Gn, Pl rim	
SiO_2	55.62		55.28		**SiO_2**	61.81		60.24		60.89		59.59	
TiO_2	0.07		0.07		**Al_2O_3**	24.47		25.62		25.41		26.21	
Al_2O_3	14.62		10.08		**FeO**	0.04		0.16		0.13		0.16	
FeO	3.55		2.59		**CaO**	5.24		6.64		6.20		7.35	
MnO	0.02		0.05		**Na_2O**	9.07		7.79		7.98		7.35	
MgO	7.30		10.89		**K_2O**	0.30		0.23		0.33		0.27	
CaO	11.43		15.40										
Na_2O	7.69		5.34		**Total**	100.93		100.68		100.94		100.90	
Total	100.31		99.91										
Si	1.95	2.00	1.96	2.00	**Si**	2.74	3.00	2.68	3.00	2.69	3.00	2.64	3.00
Al^{IV}	0.05		0.04		**Al^{IV}**	0.26		0.32		0.31		0.36	
Al^{VI}	0.56	1.03	0.39	1.04	**Al^{VI}**	1.00		1.00		1.01		1.01	
Ti	0.00		0.00		**Fe**	0.00		0.01		0.01		0.01	
Mg	0.38		0.57		**Ca**	0.24	1.00	0.31	1.00	0.29	1.00	0.35	1.00
Fe^{2+}	0.10		0.08		**Na**	0.77		0.68		0.68		0.63	
Mn	0.00		0.00		**K**	0.01		0.01		0.02		0.02	
Ca	0.43	0.98	0.59	0.97									
Na	0.52		0.38		**Ab**	76		68		69		63	
					An	23		31		29		35	
Jd	0.53		0.37		**Or**	1		1		2		2	

Table 1. Representative mineral compositions for omphacite in eclogite and plagioclase in gneiss.

2.4.1. Eclogite

The primary, and best-preserved, occurrence of eclogite in the SMZ is a large, tabular eclogite outcrop that is 3-5 m thick and approximately 20 m long (samples NW10-40M, NW11-21B, C; Fig. 2a). This eclogite body contains a well-developed, shallowly to moderately N-NE dipping foliation and a subhorizontal E-W lineation. The foliation is defined by compositional layering between omphacite-rich layers and less

abundant quartz-rich layers (mm- to cm-scale in thickness) (Figs. 3e, 4a). Elongate omphacite grains define the lineation. The edges of the eclogite body are retrogressed to amphibolite ± garnet. In the omphacite-rich layers the primary assemblage is omphacitic clinopyroxene (70-80 modal %; X_{Jd} = 0.34-0.57) + garnet (10-20%) + quartz (<10 %) + rutile (<5 %) with accessory zircon. The quartz-rich layers are composed of quartz (>65 modal %) + garnet (30 %) + rutile (<5%) with accessory zircon.

Omphacite is coarse-grained (up to 6 mm long), elongate with an average aspect ratio of 3:1 (lineation-parallel plane), and typically does not display major-element zoning. Omphacite grain boundaries are ubiquitously replaced by symplectitic intergrowths of clinopyroxene + plagioclase or hornblende + plagioclase (Fig. 4b). Garnet is anhedral to subhedral in the omphacite-rich layers and subhedral in the quartz-rich layers. Garnet grains range in size from 0.5-6 mm and are typically larger in quartz-rich layers (>1 mm) than in omphacite-rich layers (<1 mm).

Quartz in eclogite occurs in three distinct habits: (1) as interstitial grains in the omphacite-rich regions, (2) in quartz-rich layers (Fig. 4a), and (3) as inclusions in garnet in quartz-rich layers (Fig. 4b). Quartz in omphacite-rich layers occurs as isolated grains or in clusters of up to four grains. The interstitial quartz is medium-grained (up to 1.5 mm), anhedral, and displays weak undulatory extinction. Quartz grains in quartz-rich layers are large (up to 3 mm diameter), irregular in shape, display strong undulatory extinction, and highly sutured grain boundaries (Fig. 4c). Subgrains and recrystallized grains suggest recrystallization dominated by grain boundary migration (GBM) mechanisms (Hirth and Tullis, 1992; Stipp et al., 2002). Quartz-rich layers contain

abundant garnets with quartz and Pcq inclusions. Quartz inclusions in garnet are typically single grains that show weak to no undulatory extinction. Pcq inclusions are observed only in garnets in quartz-rich layers, these inclusions range in size from 100 to 200 μm and are composed of numerous elongate quartz grains that radiate from the center of the inclusion (Fig. 4d).

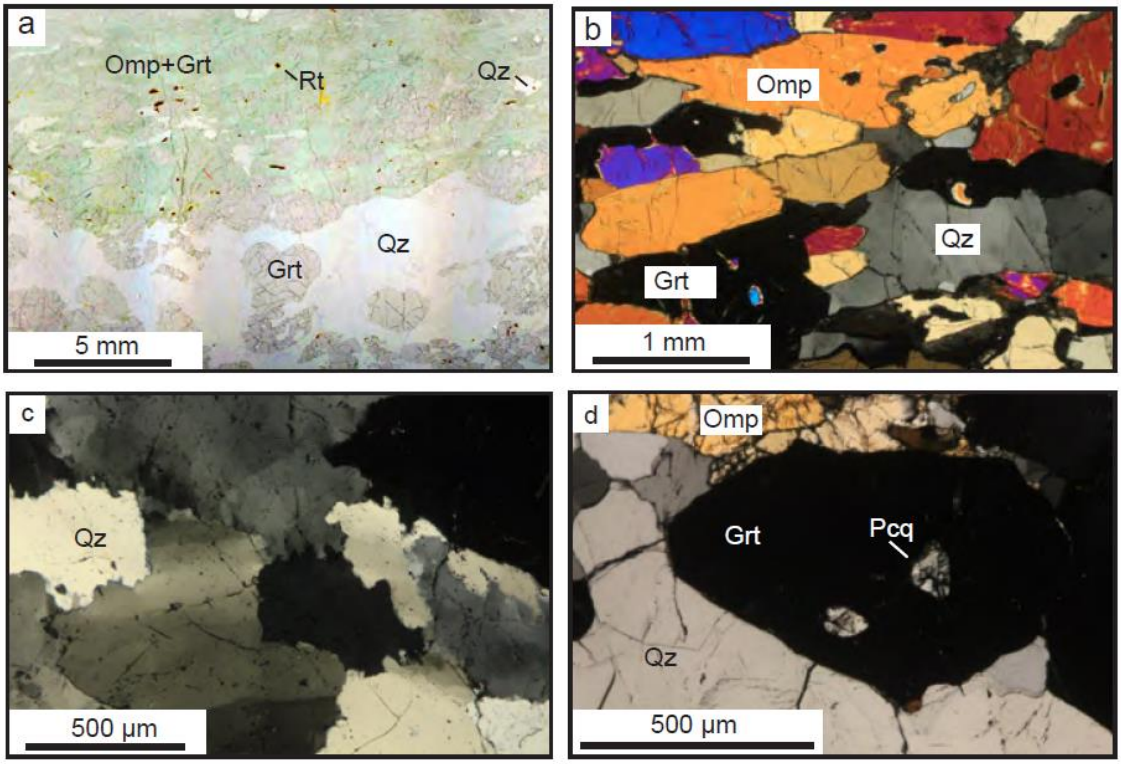

Figure 4. Eclogite photomicrographs. (a) Thin section scan of coesite-eclogite (sample NW11-40M, lineation-parallel) showing a garnet-rich quartz layer within omphacite-rich regions. Garnets in the quartz-rich layer are larger and more euhedral than those in the omphacite-rich regions. (b) Omphacite-rich region of coesite-eclogite (sample NW11-21B, lineation-parallel) showing elongate habit of omphacite crystals. (c) Quartz in quartz-rich layer (sample NW10-40M, lineation-parallel) showing irregular grain boundaries and strong undulatory extinction. (d) Garnet porphyroblast in a quartz-rich layer (sample NW10-40M, lineation-parallel) that contains two polycrystalline quartz inclusions that show characteristic palisade texture.

2.4.2. Quartzofeldspathic gneiss

Quartzofeldspathic gneiss is the dominant rock type in the SMZ, as it is in the rest of the WGR. The striped gneiss within the SMZ (e.g., sample NW10-40G) and the coarser-grained, country-rock gneiss outside of the SMZ (e.g., sample NW10-40A) have similar mineral assemblages and modal abundances. The gneiss is comprised of plagioclase (40-65 modal %) + quartz (15-40%) + biotite (>10%) ± hornblende ± epidote/allanite ± garnet with accessory oscillatory-zoned zircon, titanite, magnetite and rare ilmenite and apatite. Though both gneiss types preserve the same assemblage, they display fabric and textural differences.

In the striped gneiss, quartz occurs in monomineralic, foliation-parallel ribbons that contain high aspect ratio quartz grains (~100 x 350 μm) (Fig. 5a). The ribbons are one grain thick, and quartz grain boundaries are straight and perpendicular to the ribbon boundaries. Some quartz grains show undulatory extinction. Quartz ribbons are longer in lineation-parallel planes (>5 cm) than in lineation-perpendicular planes (<1 cm).

The regions between quartz ribbons are dominated by plagioclase but also contain biotite, epidote, titanite, and hornblende in varying amounts, and rare, highly disaggregated garnet. Plagioclase in the striped gneiss occurs as small, equant grains (~100 μm diameter) with straight edges, triple junctions with 120° interfacial angles, and rare twins (granoblastic texture). Plagioclase displays optically visible zoning (Fig. 5b). Electron-microprobe analysis reveals that the plagioclase is reverse zoned (Fig. 5c). Plagioclase preserves more sodic cores (~An_{30}) and more calcic rims (~An_{40}); the average ΔAn from core to rim is 10 mol%. Zoning is observed in nearly all grains in the striped gneiss.

Some small grains do not display zoning, most likely because of a sectioning effect (the center of the grain is not on the plane of the thin section) or a size effect (the grain is sufficiently small such that during recrystallization the whole grain was replaced with a new, lower Na grain). Potassium feldspar porphyroclasts are partially to fully replaced by subgrains (~150 μm diameter) that lack internal distortion (Fig. 5d).

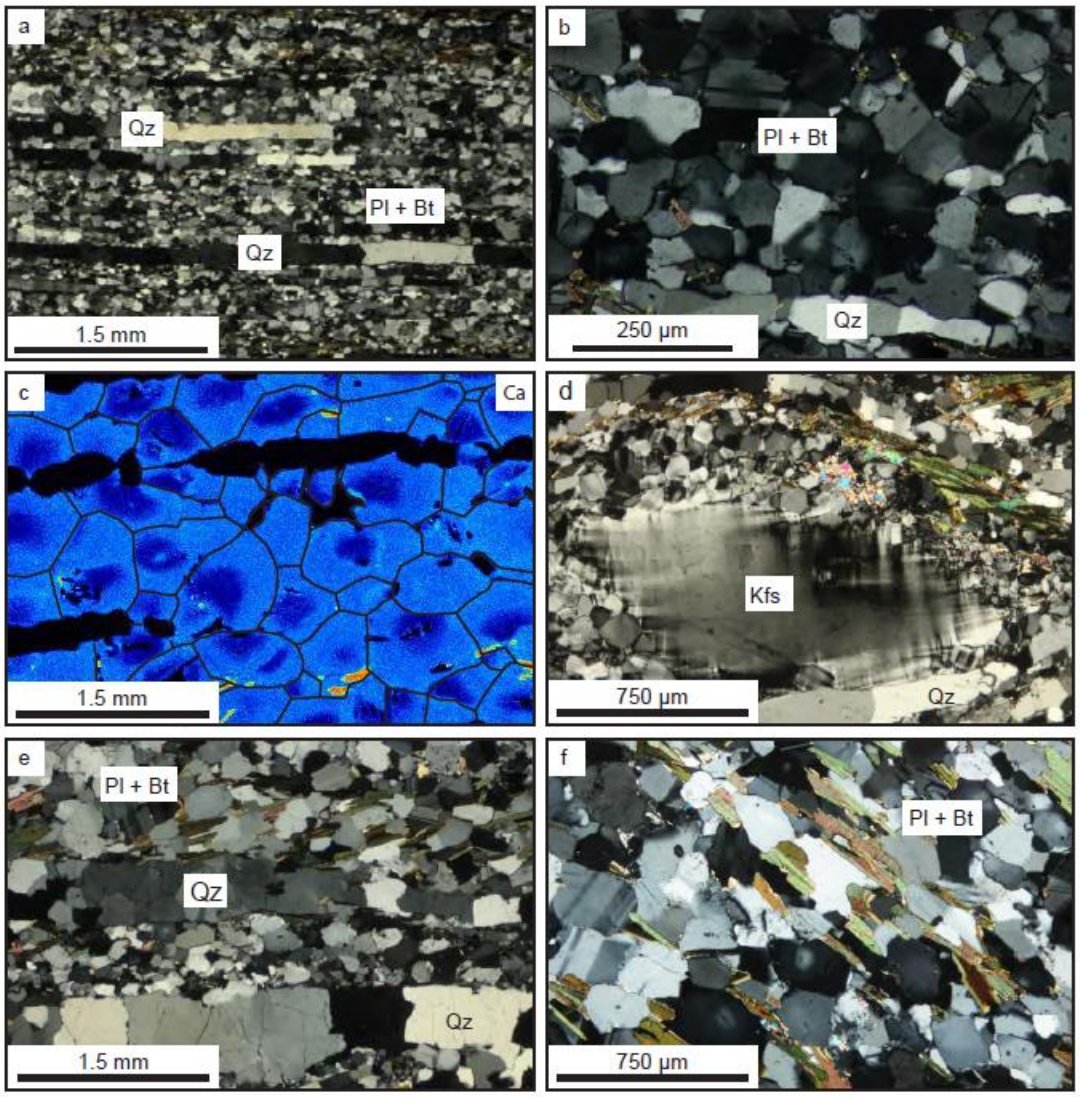

Figure 5. Quartzofeldspathic gneiss photomicrographs within and outside of the SMZ. (a) Striped gneiss (sample NW10-40G, lineation-parallel) showing characteristic foliation-parallel quartz ribbons. Recrystallized plagioclase and biotite comprise the regions between quartz ribbons. (b) Recrystallized plagioclase in striped gneiss (sample NW10-40G, lineation-parallel). The plagioclase displays optically visible reverse zoning, lacks twinning, and commonly displays straight grain boundaries and triple junctions. (c) Ca element map of plagioclase in striped gneiss (sample NW10-40G, lineation-parallel). This element map shows the reverse compositional zoning preserved in plagioclase with lower An cores and higher An rims. Grain boundaries were superimposed on the image. (d) Partially recrystallized K-feldspar porphyroclast in striped gneiss (sample NW10-40F, lineation-parallel). Quartz ribbons wrap the asymmetric porphyroclast. (e) Country-rock gneiss (sample NW10-40A, lineation-parallel) showing characteristic foliation-parallel quartz ribbons. Quartz-quartz grain boundaries are serrated and grains commonly display undulatory extinction. Plagioclase and biotite comprise the regions between quartz ribbons. Grain size in the country-rock gneiss is significantly larger than in the striped gneiss. (f) Country-rock gneiss (sample NW10-40A, lineation-parallel) showing optically visible reverse zoning in plagioclase. The plagioclase displays frequent twinning and serrated grain boundaries.

Differences between the striped gneiss of the SMZ and the country-rock gneiss are primarily related to grain size and grain-boundary geometry. Quartz occurs in foliation-parallel ribbons in both gneisses, but in the country-rock gneiss, grain size is larger (0.5 x 1.5 mm), grains more commonly display undulatory extinction, and grain boundaries are curved (Fig. 5e). Plagioclase grains in the country-rock gneiss are coarser (typically 250-300 μm diameter), display more abundant twinning, and exhibit serrated grain boundaries. Plagioclase grains in the country-rock gneiss also display core-to-rim reverse zoning (Fig. 5f), but the compositional variation from core (~An_{25}) to rim (~An_{31}) is less distinct than in the striped gneiss with an average ΔAn from core to rim of 6 mol%. Biotite crystals (~250 μm x 1 mm long) are aligned parallel to the principal foliation and occur as isolated grains. Potassium feldspar porphyroclasts are largely made of equant, strain-free subgrains and new grains (~250 μm diameter).

2.5. Ti-in-quartz thermobarometry

Ti-in-quartz thermobarometry was applied to eclogite and gneiss from the SMZ. This trace-element thermobarometer is used to build on previous major-element thermobarometry (Wain, 1997) to reconstruct *P*-*T* conditions for eclogite and gneiss in the SMZ. Ti-in-quartz thermobarometry is based on the *P*- and *T*-dependent substitution of Ti into silica tetrahedra in the quartz structure; Ti solubility increases as *P* decreases and as *T* increases. Two widely-used calibrations of this thermobarometer have been proposed, first by Wark and Watson (2006) and Thomas et al. (2010) (includes a dependence on a_{TiO2}), and second by Huang and Audétat (2012) (independent of a_{TiO2}). Over the range of pressures of interest for this study (1.0 GPa < *P* < 2.8 GPa), Thomas et al. (2010) is significantly more pressure sensitive than Huang and Audétat (2012). The calibrations cross over at 2 GPa. As it is unclear which calibration is more appropriate for this study we report results using both.

Titanium concentration ([Ti]) in quartz was measured using secondary ion mass spectrometry (SIMS) at the Northeast National Ion Microprobe Facility (NENIMF) at Woods Hole Oceanographic Institution following the analytical process of Nachlas et al. (2014). Raw data is given in Appendix 1. Analytical error for SIMS [Ti] measurements reported in this study is ±0.1 ppm; this error corresponds to < 1° C difference in *T* estimate after either calibration. The effect of the analytical error is significantly smaller than the error associated with the thermodynamic parameters used to derive the calibrations; therefore error is not provided in the thermobarometry results. Qualitative trace-element variation in quartz was assessed using cathodoluminescence (CL). This

was completed using a JEOL 6500 FEG-SEM (Characterization Facility, University of Minnesota Twin Cities) equipped with a Gatan MonoCL 2 System. Previous studies (e.g. Müller et al., 2003) have documented a correlation between CL and Ti content, here we use CL as a qualitative proxy for Ti content in quartz.

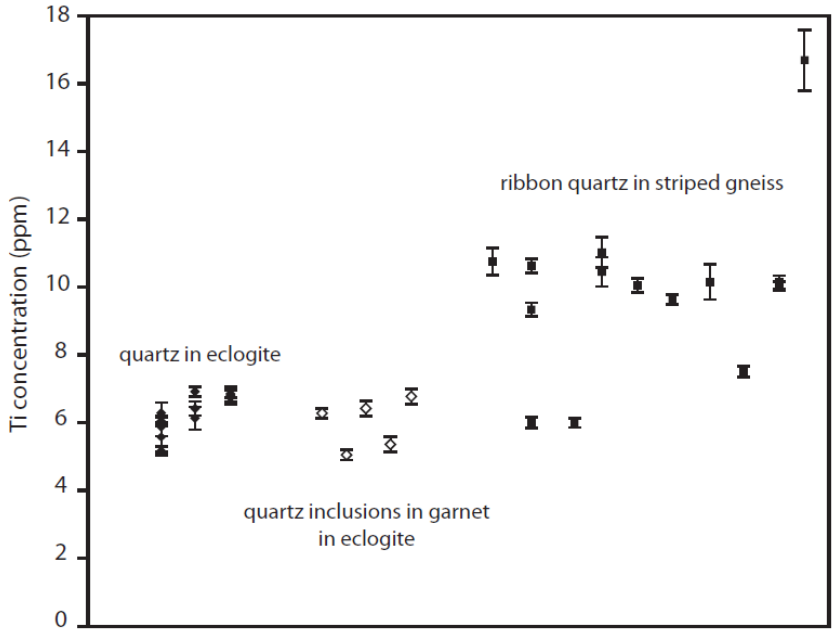

Figure 6. Graph of [Ti] in quartz by lithology and habit. Quartz in eclogite, both in the quartz-rich layers and as inclusions in garnet, preserves similar [Ti]. [Ti] in quartz in quartzofeldspathic gneiss displays considerable variation within grains (each column of data corresponds to one grain) and among grains. Error bars are 1 standard deviation.

In rutile-bearing eclogite from the SMZ (sample NW11-21B), [Ti] was analyzed in quartz in quartz-rich layers (Fig. 4c) and in quartz inclusions in garnet (Fig. 4d). Quartz in these textural locations preserves similar [Ti]: 5.2-6.9 ppm (n=16), with a mean [Ti] of 6.2 ± 0.6 ppm (Fig. 6, Table 2). The small range in [Ti] in eclogite allows us to use the mean [Ti] for the thermobarometry (Fig. 7). CL images of quartz in eclogite suggest that quartz grains in both settings are largely homogeneous with respect to Ti

content, but reveal the presence of numerous darker, healed fractures or veins that are not observable with visible light spectroscopy.

	Point	[Ti] (ppm)		Site
		Mean	Standard Deviation	
Quartzofeldspathic gneiss (NW-1040G)	50	10.8	0.4	Qz ribbon
	51	10.7	0.2	Qz ribbon
	52	9.4	0.2	Qz ribbon
	53	6.0	0.2	Qz ribbon
	54	6.0	0.1	Qz ribbon
	55	11.0	0.5	Qz ribbon
	56	10.5	0.4	Qz ribbon
	57	2.0	-0.1	Qz ribbon
	58	2.0	0.2	Qz ribbon
	59	10.1	0.2	Qz ribbon
	60	9.6	0.2	Qz ribbon
	61	10.2	0.5	Qz ribbon
	62	7.5	0.1	Qz ribbon
	63	10.0	0.1	Qz ribbon
	64	10.2	0.2	Qz ribbon
	65	16.7	0.9	Qz ribbon
Eclogite (NW11-21B)	86	5.2	0.2	Qz layer
	87	5.9	0.3	Qz layer
	88	6.3	0.3	Qz layer
	89	5.6	0.4	Qz layer
	90	6.1	0.1	Qz layer
	91	6.1	0.3	Qz layer
	92	6.4	0.2	Qz layer
	93	6.9	0.2	Qz layer
	94	6.8	0.2	Qz layer
	95	6.9	0.1	Qz layer
	96	6.8	0.2	Qz layer
	97	6.9	0.1	Inclusion
	98	70.6	2.6	Inclusion
	99	5.1	0.1	Inclusion
	100	91.0	7.3	Inclusion
	101	6.4	0.2	Inclusion
	102	5.4	0.2	Inclusion
	103	6.8	0.2	Inclusion

Table 2. Ti concentration (measured by SIMS) of quartz in eclogite and quartzofeldspathic gneiss.

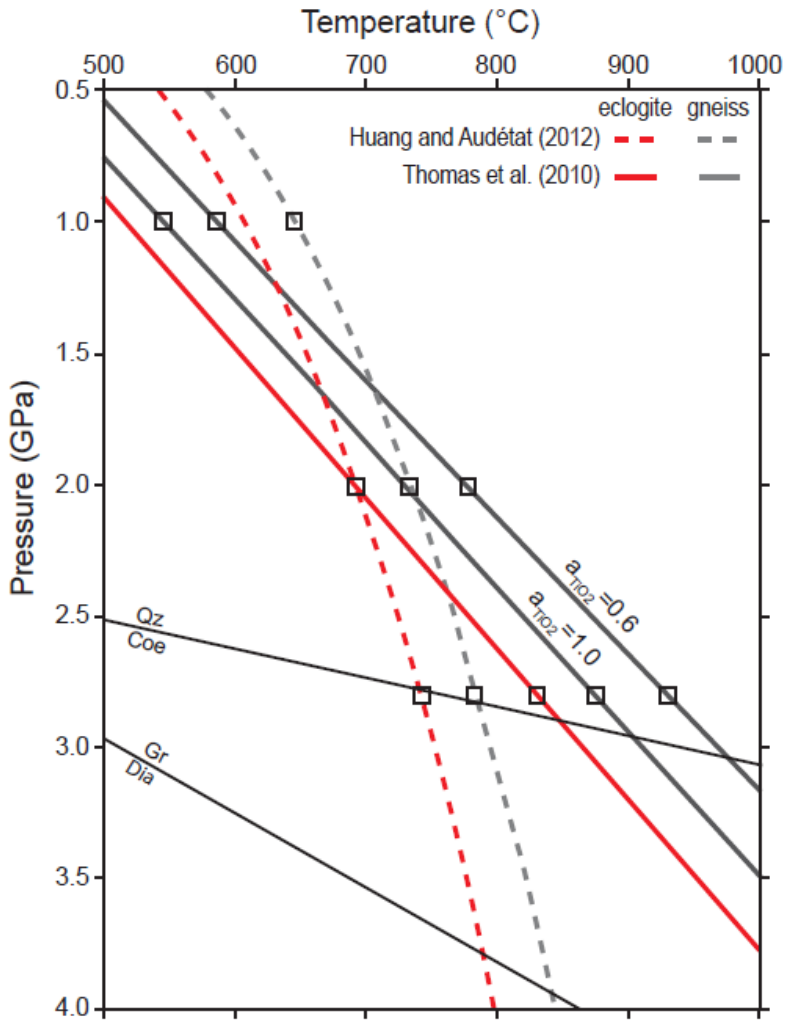

Figure 7. P-T diagram summarizing results of eclogite and gneiss Ti-in-quartz thermobarometry. This graph shows *P*-*T* curves of the two calibrations for both lithologies over the *P* and *T* range of interest for this study plotted using the mean [Ti] for each lithology (6.2 ppm for eclogite and 9.9 ppm for gneiss). The Thomas et al. (2010) calibration includes two calculations for gneiss (solid gray lines) due to the presence of titanite, one using a_{TiO2} = 0.6 and one using a_{TiO2} = 1.0, and one calculation for eclogite (a_{TiO2} = 1, solid red line). Calculations resulting from Huang and Audétat (2012) are shown in dashed lines (gneiss – gray, eclogite – red). Pressures of interest (*P* = 2.8, 2.0, and 1.0 GPa, see text) are highlighted on each calibration by a small box in order to show the range of temperature estimates for each scenario.

The minimum peak *P* for this eclogite body is 2.8 GPa (Wain, 1997). If this corresponds to the *P* at which [Ti] equilibrated in the quartz, then the calculated temperature (a_{TiO2} = 1, rutile present) is 831 °C after Thomas et al. (2010) and 739 °C

after Huang and Audétat (2012) (Fig. 7, Table 3). If [Ti] equilibrated at P = 2.0 GPa (quartz stable, eclogite-facies conditions), then the calculated temperature using both calibrations coincide at 690 °C (a_{TiO2} = 1, rutile present). Results of Ti-in-quartz thermobarometry for this eclogite broadly agree with previous major-element thermobarometry results for UHP eclogite in this region (~740-840 °C, Wain, 1997).

In the striped gneiss, [Ti] in quartz was measured in multiple (n=5) quartz ribbons, and as transects within individual grains (up to 3 points per grain). [Ti] in quartz varies from 6.0 to 16.7 ppm (n=14), with a mean [Ti] of 9.9 ± 2.6 ppm. The maximum observed intergranular variation in [Ti] is 10.7 ppm, and the maximum intragranular variation is 4.6 ppm (Fig. 6, Table 2). CL images reveal two main patterns: (1) quartz grains with a bright core and a darker rim and (2) quartz grains with a mottled pattern. These variations do not directly correspond with differences in measured [Ti].

			Quartzofeldspathic Gneiss			**Eclogite**
Calibration	Pressure (GPa)	a_{TiO2}	Minimum [Ti] (5.99 ppm)	Mean [Ti] (9.90 ppm)	Maximum [Ti] (16.73 ppm)	Mean [Ti] (6.30 ppm)
Thomas et al. (2010)	2.8	1	828 °C	876 °C	931 °C	831 °C
		0.6	877 °C	930 °C	990 °C	n/a
	2.0	1	688 °C	730 °C	778 °C	691 °C
		0.6	731 °C	777 °C	830 °C	n/a
	1.0	1	514 °C	548 °C	587 °C	n/a
		0.6	549 °C	586 °C	629 °C	n/a
Huang and Audétat (2012)	2.8		736 °C	784 °C	838 °C	739 °C
	2.0		688 °C	733 °C	785 °C	691 °C
	1.0		605 °C	646 °C	693 °C	n/a

Table 3. Temperature estimates resulting from Ti-in-quartz thermobarometry.

Application of Ti-in-quartz thermobarometry to the striped gneiss is complicated due to the absence of rutile and presence of titanite in the system, which introduces uncertainty in a_{TiO2}. For titanite-bearing systems, a_{TiO2} can range from 0.6 to 1.0 (Ghent and Stout, 1984; Behr and Platt, 2011). Therefore, T estimates using the Thomas et al.

(2010) calibration were calculated with a_{TiO2} = 0.6 and 1.0, then compared to assess the spread in *T* estimate as a function of changing a_{TiO2}. Huang and Audétat (2012) assume a_{TiO2}=1 and do not allow for a_{TiO2} variation; therefore, *T* estimates at a given *P* are considered a minimum. For this range of [Ti], *T* estimates resulting from an input of a_{TiO2} = 0.6 yield estimates up to 50 °C lower than those calculated with a_{TiO2}=1 at a given *P*.

Since pressure at the time of equilibration of Ti in quartz within the gneiss is uncertain, we calculated temperatures for three scenarios that represent the possible range of *P* of Ti equilibration in quartz: (1) *P* in the gneiss was at UHP conditions, the same as recorded by the eclogite (>2.8 GPa); (2) *P* in the gneiss was high, but lower than recorded by the eclogite (2.0 GPa) and (3) *P* was substantially lower than that of the eclogite and consistent with amphibolite-facies equilibration (1.0 GPa). Because [Ti] in quartz is variable, with no systematic zoning, we considered the minimum, average, and maximum values of [Ti] for each scenario.

Temperature estimates for the striped gneiss (Fig. 7, Table 3) range from 514 °C to 990 °C depending on input parameters. Temperature estimates based on maximum [Ti] are 75-115 °C higher than those based on minimum [Ti] (Table 3). Temperature estimates based on mean [Ti] fall in between those estimates based on maximum and minimum [Ti] (presented herein and displayed in Fig. 7). At *P* = 2.8 GPa (scenario 1), *T* estimates are 876 °C (a_{TiO2} = 1) and 930 °C (a_{TiO2} = 0.6) using the calibration of Thomas et al. (2010) and 784 °C using the calibration of Huang and Audétat (2012). At *P* = 2.0 GPa (scenario 2), *T* estimates using the calibration of Thomas et al. (2010) and Huang and Audétat

(2012) coincide at 730 °C (a_{TiO2} = 1), with a higher *T* estimate of 777 °C corresponding to a_{TiO2} = 0.6 using the calibration of Thomas et al. (2010). At *P* = 1.0 GPa (scenario 3), *T* estimates are 548 °C (a_{TiO2} = 1) and 586 °C (a_{TiO2} = 0.6) using the calibration of Thomas et al. (2010) and 646 °C using the calibration of Huang and Audétat (2012).

Additional uncertainties related to our application of this thermobarometer are: the rocks most likely equilibrated at much higher pressures (*P* > 2 GPa for the eclogite) than the calibration conditions, and it is not known how the transformation of coesite to quartz (and vice versa) affects the solubility of Ti in quartz (Thomas et al., 2012). Despite uncertainty in the details of the Ti-in-quartz thermobarometry there is a significant difference in the [Ti] between eclogite and gneiss. The difference in [Ti] reflects the conditions of Ti equilibration conditions, higher *T* for the eclogite (near the quartz-coesite transition), and lower *T* for the gneiss (amphibolite-facies).

2.6. Microstructural analysis: EBSD

The crystallographic orientation of minerals in gneiss and eclogite in the SMZ is used to evaluate grain-scale deformation mechanisms during ductile shear zone evolution. Crystallographic fabrics were measured by electron backscatter diffraction (EBSD) analysis. Thin-section preparation included polishing with diamond paste to 1 μm grit size followed by SYTON polishing (1.5-2 hours) in order to maximize indexing. Samples were coated with a thin carbon coat prior to analysis. EBSD data for omphacite and quartz in eclogite were acquired at the University of Minnesota - Duluth's Research Instrumentation Laboratory with a JEOL 6500 FEG scanning electron microscope (SEM)

equipped with an Oxford Instruments NordlysS detector and HKL Channel 5 software. SEM conditions were 20 kV accelerating voltage, 4 nA beam current, working distance of 23 mm, and dynamic focus for 70° sample tilt. These data were collected as a series of maps with a 50 or 100 μm step size and covered areas approximately 1 x 2 cm. EBSD data for quartz in gneiss were acquired at Macquarie University with a Zeiss EVO SEM equipped with an Oxford Instruments NordlysMax detector and the Aztec Software package. SEM conditions were 20 kV accelerating voltage, 8 nA beam current, working distance of 12-14 mm, and dynamic focus for 70° sample tilt. Step sizes ranged from 3 to 6 μm and covered areas of approximately 3 x 3 mm.

EBSD data analysis was completed using HKL Channel5 post-processing software. The reference coordinates (XYZ) were defined according to the macroscopic foliation and lineation: X is parallel to the lineation, Y is orthogonal to the lineation, and Z is perpendicular to the foliation. All data are plotted as one point per grain on lower hemisphere, equal area projections. In the case of quartz we also present upper hemisphere projections. Pole figures are shown as both point plots and contoured plots (contoured at multiples of 1 multiples of uniform distribution, m.u.d.). The number of grains (n) and the maximum m.u.d. are given for each sample.

2.6.1. Eclogite fabrics

Two eclogite samples from the fresh, layered eclogite body in the SMZ were selected for EBSD analysis. Sample NW11-21B consists of omphacite-rich eclogite with

garnet and interstitial quartz. Sample NW11-21C includes omphacite-rich eclogite as well as a garnet-bearing quartz layer.

Omphacite in NW11-21B (Fig. 8, top) shows a strong crystallographic preferred orientation (CPO) with [001]-axes forming a point maximum parallel to the lineation and [010]-axes forming a point maximum normal to the lineation. The (100)-poles are less organized but form a weak girdle sub-perpendicular to the lineation. Omphacite in NW11-21C (Fig. 8, middle) shows a similar pattern; the [001]-axes form a girdle in the plane of the foliation with the largest concentration of axes nearly lineation-parallel, and the [010]-axes and (100)-poles both form weak, partial girdles at a high angle to the lineation. The macroscopic mineral fabric of omphacite is consistent with the observed crystallographic fabrics (the long axis of omphacite grains is parallel to the c-axis).

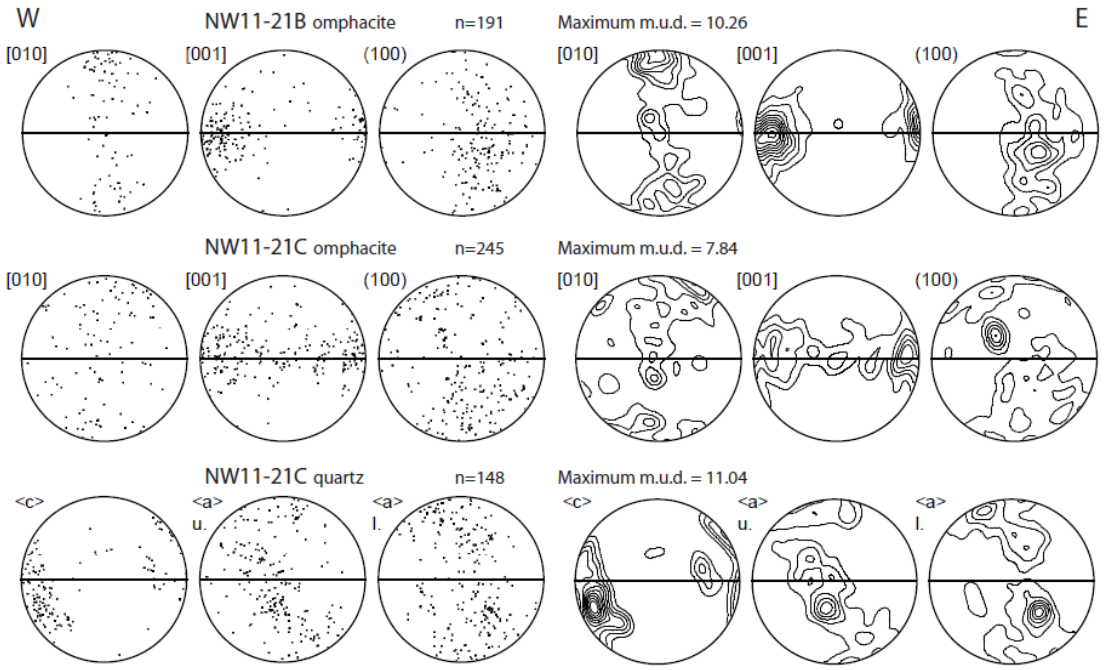

Figure 8. Omphacite and quartz fabrics from eclogite (samples NW11-21B and C). Data is displayed as point data on the left and as contoured plots (contoured in multiples of 1 m.u.d.) on the right. Upper (u.) and lower (l.) hemisphere data plotted for quartz.

Though quartz occurs in multiple habits in the eclogite, we measured the crystallographic fabrics of quartz from the quartz-rich layers because it shows clear evidence of dynamic recrystallization during fabric development (Fig. 4c). Quartz preserves a strong CPO with the c-axes forming a point maximum oblique (~20°) to the lineation and a-axes forming a partial, inclined girdle nearly normal to the c-axis concentration (Fig. 8, bottom).

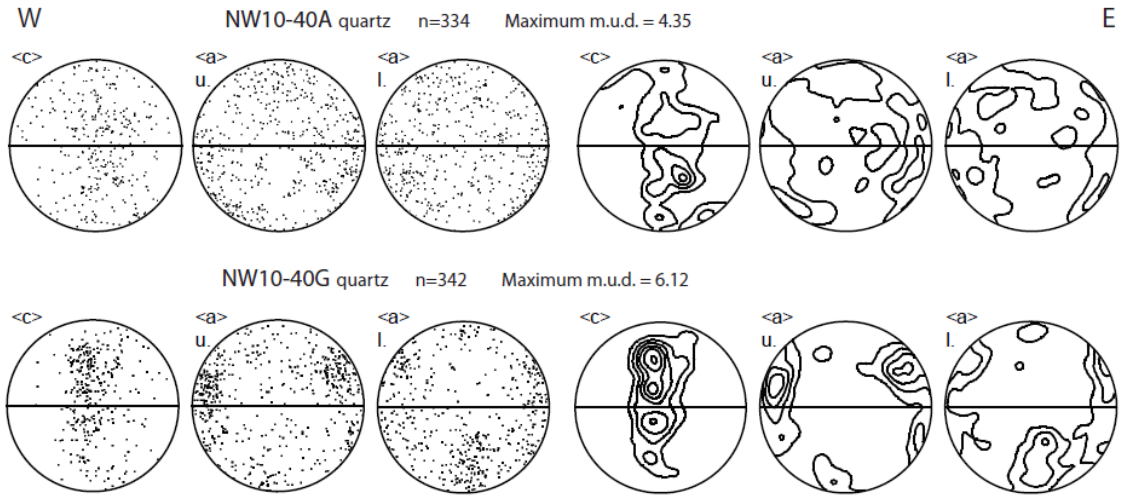

Figure 9. Quartz fabrics from striped (top, sample NW10-40G) and country-rock (bottom, sample NW10-40A) gneiss. Data is displayed as point data on the left and as contoured plots (contoured in multiples of 1 m.u.d.) on the right. Upper (u.) and lower (l.) hemispheres displayed.

2.6.2. Quartzofeldspathic gneiss fabrics

Quartz fabrics from ribbons in quartzofeldspathic gneiss were analyzed in two samples from the Salt region, one country-rock gneiss from outside of the SMZ (sample NW10-40A) and one striped gneiss within the SMZ (sample NW10-40G). Quartz from the gneiss outside of the SMZ displays a fabric of moderate strength. The c-axes form a girdle perpendicular to lineation, and the a-axes are fairly evenly distributed on the

primitive circle (Fig. 9, top). Quartz from the gneiss within the SMZ shows a similar, though stronger, CPO with a partial girdle of c-axes perpendicular to the lineation and a-axes distributed around the primitive circle with point maxima concentrations (Fig. 9, bottom). The striped gneiss shows a stronger concentration of a-axes on the great circle than the country-rock gneiss.

2.7. Discussion

2.7.1. Fabric development from high- to medium-pressure conditions

Omphacite in UHP eclogite in the SMZ is elongate and defines the foliation. One sample (NW11-21B) shows an omphacite fabric (Fig. 8) with a point maximum of [001]-axes parallel to the lineation and a diffuse girdle of [010]-axes normal to the lineation. A second eclogite sample (NW11-21C) has a weak girdle of [001]-axes in the plane of the foliation and an asymmetric partial girdle of [010]-axes near-normal to the lineation. These fabrics are best characterized as L- to LS-type patterns and are thought to develop during constrictional deformation and plane strain (Helmstaedt et al., 1972; Boundy et al., 1992; Godard and Van Roermund, 1995). L-type CPO have been generated experimentally in simple shear (Zhang et al., 2006; Zhang and Green, 2007), in models of pure shear and simple shear (Bascou et al., 2001), as well as in models of transtension (Bascou et al., 2002). Omphacite fabrics developed in models of transtension show a CPO with a girdle of [010]-axes perpendicular to lineation, as opposed to point maxima (Bascou et al., 2002). LS-type fabrics are intermediate fabrics between L- and S- type

end-members, and this fabric pattern likely represents a combination of conditions that generate L- and S- type fabrics (Ábalos, 1997).

Similar omphacite fabrics to the ones presented in this study (L- and LS-type patterns) have been reported from other eclogites in the WGR from the Nordfjord UHP domain as well as in the Sulu UHP terrane of China (Bascou et al., 2001; Zhang and Green, 2007). Asymmetric omphacite fabrics have been documented in naturally-deformed eclogite samples (Ábalos, 1997, Mauler et al., 2000, Bascou et al., 2001) and have been interpreted as a consequence of non-coaxial deformation.

Quartz in the SMZ eclogite records a strong, asymmetric CPO generated by activation of the prism <c> slip system. Activation of this slip system is accomplished by high-*T* deformation, as well as likely water-present conditions (Tullis, 1977; Blumenfeld et al., 1986; Mainprice et al., 1986). The asymmetry in the c-axis orientation presented here is consistent with a sinistral sense of shear (Blumenfeld et al., 1986; Garbutt and Teyssier, 1991), which is consistent with kinematic indicators in the ductile deformation zone and, more broadly, with motion on the Møre-Trondelag fault zone.

Similar quartz fabrics to the one presented in this study have been recently documented in HP/UHP eclogites from the Sulu terrane (Zhang et al., 2013). This study also shows that coesite preserves a weak fabric in naturally deformed eclogite. Though the SMZ eclogite reached UHP conditions, as evidenced by the presence of Pcq, the prism <c> fabric preserved in the quartz-rich layers developed during deformation under HP, quartz-stable conditions near the quartz-coesite transition. The similarity of [Ti] in quartz inclusions in garnet with quartz in the quartz-rich layers supports that the quartz

deformation occurred at high *T* and suggests that the quartz, and possibly omphacite as well, was not altered by subsequent deformation and/or recrystallization (i.e., the quartz did not continue to deform or equilibrate as the rocks were exhumed).

Quartz in the striped and country-rock gneiss preserves fabrics generated by consistently lower *T* deformation than those in the eclogite. The country-rock gneiss displays a diffuse quartz CPO (Fig. 9, top) that includes evidence of activation of the basal, prism, and rhomb <a> slip. Quartz fabrics in the striped gneiss (Fig. 9, bottom) suggest that quartz deformed in the dislocation creep regime with activation of the prism <a> and rhomb <a> slip systems. The lack of evidence for basal <a> slip in the striped gneiss suggests that this fabric developed at higher *T* than the country-rock gneiss (Stipp et al., 2002). No significant asymmetry in CPO patterns of quartz in gneiss is observed.

2.7.2. Proposed model of ductile shear zone evolution

The SMZ comprises UHP eclogite and now amphibolite-facies quartzofeldspathic gneiss. The eclogite in the SMZ experienced UHP conditions (Fig. 10, phase 1) as indicated by Pcq inclusions (e.g., Fig. 4d) and rare coesite inclusions (e.g., Carswell et al., 2003a) in garnet. Concordance of foliation and lineation orientations in gneiss and eclogite and rare petrographic evidence (e.g. Pcq inclusions in gneiss, Wain, 1997) suggest that the quartzofeldspathic gneiss also experienced UHP conditions, at least locally. Therefore, despite the fact that the gneisses in this study do not preserve obvious evidence for UHP conditions, it is likely that the gneiss and associated mafic inclusions

were deformed in a similar kinematic framework over a shared P-T path during exhumation from mantle depths.

During the initial stages of exhumation (Fig. 10, phase 2, passing into the quartz stability field) eclogite fabrics developed, including a quartz CPO generated by prism <c> slip and LS- to L-type omphacite CPO patterns. Ti-in-quartz thermobarometry in eclogite suggests high-*T* deformation (~750-830 °C). This *T* estimate is consistent with the dominant activation of the prism <c> slip system in quartz. The omphacite fabrics in this study are consistent with deformation during constriction and/or plane strain, with no evidence of flattening. Amphibolite-facies constrictional fabrics are well documented in the WGR and have been interpreted as indicative of transtension (Krabbendam and Dewey, 1998; Terry and Robinson, 2003; Barth et al., 2010). The omphacite fabrics reported in this study might also be interpreted as a result of transtension at HP to nearly UHP conditions.

It is not clear when strain localization occurred during the exhumation/ decompression history and when the SMZ initiated. However, structures and fabrics consistent with deformation and metamorphism at amphibolite-facies conditions are now widespread (Fig. 10, phase 3). Amphibolite-facies retrogression in the eclogite is indicated by the presence of hornblende + plagioclase symplectite that variably replaces omphacite grain boundaries. Plagioclase reverse zoning (Figs. 5c, 10, phase 3) suggests plagioclase recrystallization and growth during continued decompression. *T* estimates from Ti-in-quartz thermobarometry at crustal depths (*P* = 1.0 GPa) range from 550 to 650 °C, consistent with the observed amphibolite-facies assemblages and fabrics.

In summary, the SMZ preserves a suite of fabrics in eclogite and quartzofeldspathic gneiss that record decompression from UHP conditions to mid-crustal levels. Eclogite contained within the gneiss preserves prism <c> quartz fabrics and LS- to L-type omphacite fabrics, and Ti-in-quartz thermobarometry suggests deformation at *P* and *T* near the quartz-coesite transition. The host gneiss preserves quartz fabrics consistent with activation of the prism and rhomb <a> slip systems in quartz and reverse zoning in plagioclase owing to continued recrystallization during decompression to amphibolite-facies conditions (< 650 °C according to Ti-in-quartz thermobarometry).

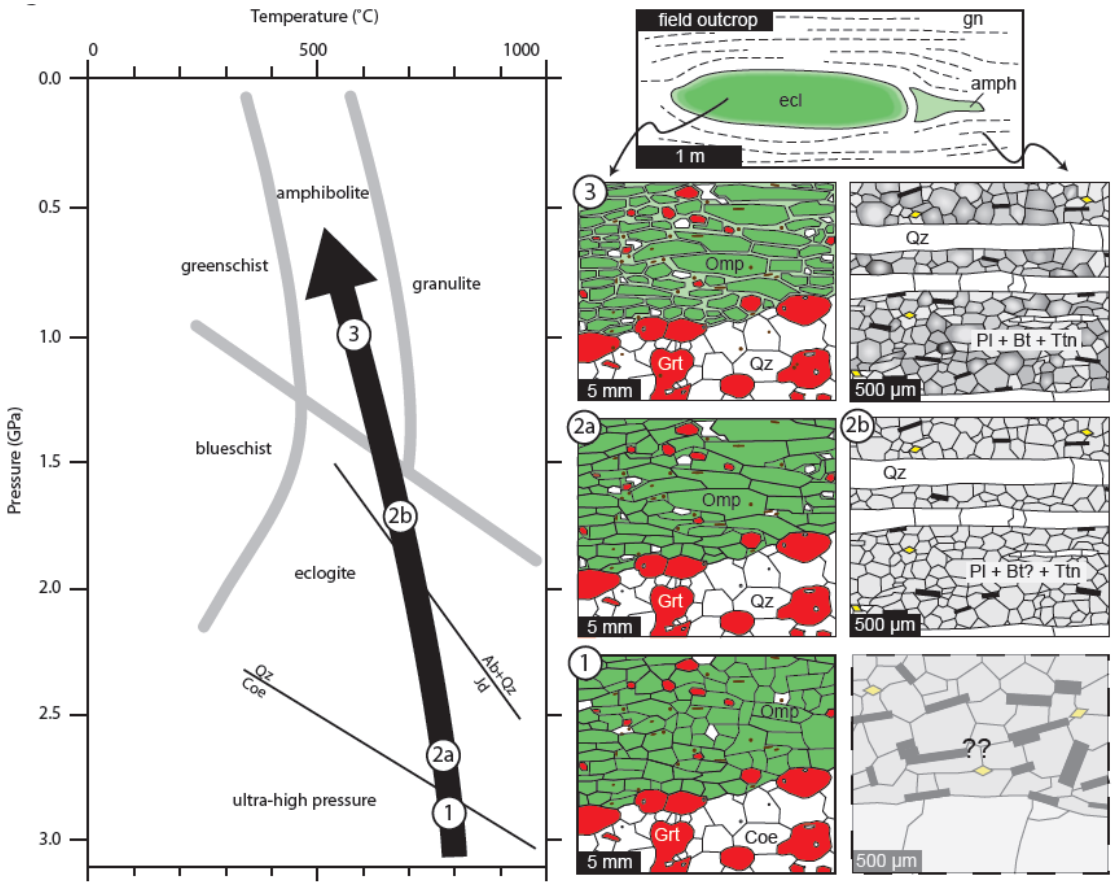

Figure 10. Schematic figure showing the fabric development during exhumation and decompression of the SMZ. Phase 1: Eclogite (and likely gneiss, at least locally) experienced ultrahigh-pressure (coesite-stable) conditions prior to fabric development. Phase 2a: At HP conditions (quartz stable), omphacite and quartz fabrics in eclogite developed. The Ti-in-quartz thermobarometry suggests temperatures from 750-830 °C for this phase. Phase 2b: Quartz fabrics in quartzofeldspathic gneiss began to develop. Plagioclase is Na-rich (lighter gray). Phase 3: By amphibolite-facies (mid-crustal) conditions, the eclogite developed a Hbl + Pl symplectite that variably replaces Omp-Omp grain boundaries. Dynamic recrystallization of plagioclase at continually decreasing pressures led to the development of reverse zoning (represented by darker gray rims). Quartz in quartzofeldspathic gneiss may have continued to develop fabrics down to *P* of ~ 1 GPa where Ti-in-quartz thermbarometry *T* estimates range from ~515-700 °C.

3. Syn-exhumation deformation mechanisms of plagioclase and quartz, Western Gneiss Region, Norway

To be submitted to Tectonophysics

Abstract

We present microstructural and compositional data for plagioclase and quartz from gneiss in and near an amphibolite-facies shear zone, the Salt Mylonite Zone, in the Western Gneiss Region of Norway. The gneiss composition is similar in and adjacent to the shear zone and is dominated by plagioclase and quartz. Microstructurally, the gneiss can be phase-separated (ribbon gneiss) or phase-mixed. Quartz in mylonitic and non-mylonitic phase-separated gneiss deformed by dislocation creep as evidenced by internal grain deformation features and a strong crystallographic preferred orientation. Plagioclase in non-mylonitic, phase-separated gneiss preserves a fabric formed during dislocation creep evidenced by a weak crystallographic preferred orientation and a dominant, foliation-parallel misorientation axes orientation. In contrast, plagioclase in mylonitic, phase-separated gneiss deformed by diffusion creep. The plagioclase layers display crystallographic preferred orientations; however, the fabrics vary from layer to layer and are interpreted to result from host-controlled recrystallization of original plagioclase grains. In the mylonitic, phase-mixed gneiss, quartz deformed by diffusion creep during mylonitization as evidenced by a lack of internal deformation features and near-random crystallographic orientations. Plagioclase in the mylonitic, phase-mixed gneiss preserves a weak fabric; deformation occurred by diffusion creep as evidenced by random

misorientation angle distribution and misorientation axis orientation. Plagioclase in all samples exhibits reverse zoning (Na-rich cores, Ca-rich rims) recording grain growth by grain boundary migration during exhumation-induced decompression. In the case of the phase-mixed mylonitic gneiss, oriented grain growth (thicker foliation-parallel rims than foliation-perpendicular rims) resulted in a shape preferred orientation and a weak plagioclase fabric. Amphibolite-facies orthogneiss in the Western Gneiss Region is a source of abundant information regarding the path that both (ultra)high-pressure eclogite bodies and associated gneiss host experienced during decompression from mantle depths.

3.1. Introduction

Localization of strain in the form of ductile shear zones is a common mechanism of stress accommodation in the middle to lower continental crust. These shear zones are a natural laboratory to study the effect of localized deformation on feldspar and quartz, the main-rock forming minerals in the continental crust. Quartz is thought to be the main mineral phase controlling the rheology of the middle and upper continental crust (e.g. Kirby, 1983). However, in the generally more mafic lower crust quartz is not as abundant (< 20%) and the pressure-temperature (P-T) conditions favor plagioclase as the dominant rheological mineral (Carter and Tsenn, 1987; Ord and Hobbs, 1989). Careful investigation of high-grade ductile shear zones in continental crust offers insight into the deformation mechanisms of these minerals during strain localization.

This study focuses on the Salt mylonite zone (SMZ), a ductile shear zone in the Western Gneiss Region (WGR) of Norway that developed during the exhumation of this

ultrahigh-pressure (UHP) terrane (Renedo et al., 2015). We characterize and compare quartzofeldspathic gneiss within and adjacent to the SMZ in terms of (1) microstructural features, (2) plagioclase composition and zoning, and (3) quartz and plagioclase crystallographic fabrics, substructures, and misorientation relationships. Using these data, we infer mechanisms and conditions of gneiss deformation within and beyond the SMZ. We evaluate the effect of phase-mixed versus phase-separated structures and decompression on fabric development.

3.2. Analysis of deformation mechanisms in quartzofeldspathic rocks

In the high-temperature ductile regime, localized deformation is influenced by various processes; the most important deformation mechanisms are dislocation creep and diffusion creep. Dislocation creep is accomplished by the movement of dislocations throughout a material. The movement and organization of dislocations, by subgrain rotation and/or grain boundary migration, result in the formation of subgrains and recrystallized grains (e.g. Guillope and Poirier, 1979; Tullis and Yund, 1985). Diffusion creep is accomplished through the physical movement of atoms in a material and can be driven by a chemical or stress gradient (e.g. McClay, 1977; Wheeler, 1992). A necessary feature of diffusion creep is the movement of grains past one another, known as grain boundary sliding (Raj and Ashby, 1971). Diffusion creep can be greatly enhanced by the presence of fluids; if diffusion and transportation of material is fluid-mediated the process is referred to as dissolution-precipitation creep (DPC) (e.g. Tullis and Yund, 1980).

Determining the various deformation mechanisms that operate during natural rock deformation relies on microstructural characteristics and crystallographic and shape preferred orientations (CPO and SPO, respectively). Optically visible indications of dislocation creep include deformation twins, subgrain boundaries, and rotation recrystallization features (e.g. Hirth and Tullis, 1992; Piazolo et al., 2002). Deformation by dominant diffusion creep does not result in the formation these internal deformation features. The presence of a CPO is commonly attributed to dominant deformation by dislocation creep (e.g. Ji and Mainprice, 1990) and a lack of or weak CPO is commonly attributed to dominant deformation by diffusion creep (e.g. Jiang et al., 2000; Czaplinska et al., 2015). However, CPO can be generated by diffusion creep (Miyazaki et al., 2013) and DPC (e.g., Bons and den Brok, 2000), and a pre-existing CPO can be preserved during deformation by diffusion creep (e.g. Jiang et al., 2000; Wheeler, 2009). A well-developed SPO is commonly associated with deformation by dislocation creep (e.g. Lister and Snoke, 1984) or DPC (e.g. Imon et al., 2004; Menegon et al., 2008) and a weak SPO is more consistent with deformation by diffusion creep (Wheeler, 2009).

Crystallographic and shape preferred orientations offer useful insight into deformation mechanisms; however, interpretations based solely on these characteristics are generally ambiguous and incomplete. Other measures of grain-scale relations, for example the misorientation between grains, can be used to enhance interpretation of deformation mechanisms. Misorientation is the angle-axis pair that brings grain pairs, adjacent (neighboring) or non-adjacent, into coincidence (e.g. Lloyd et al., 1997). Misorientation patterns emerge depending on the active deformation mechanism(s). In

dislocation creep, misorientation axes show a preferred orientation controlled by the active slip systems. Subgrain rotation will result in a higher frequency of low angle misorientations between adjacent grains. Grain boundary migration will not affect the distribution of misorientation angles between adjacent grains (Trimby et al., 1998; Wheeler et al., 2001; Halfpenny et al., 2012). Deformation by diffusion creep should not result in specific preferred misorientation axes, or specific patterns misorientation angles between adjacent grains. However, diffusion creep accommodated grain boundary sliding should result in a misorientation axes orientation that is perpendicular to lineation and in the foliation plane (Prior and Hirth, 2007). Accordingly, detailed investigation of the crystallographic orientation of grains, their misorientation pattern to each other, and the orientation of misorientation axes are needed to determine the deformation mechanisms for each phase of interest.

Quartz deformation has been well-characterized (e.g. Hirth and Tullis, 1992; Stipp et al., 2002), but plagioclase deformation remains less well-understood owing to its low-symmetry structure and compositional solid solution. Earlier studies of plagioclase deformation were limited by technology: many techniques could not be applied to the triclinic mineral and the ones that could were time consuming or expensive. However, the electron backscatter diffraction method (EBSD, Prior and Wheeler, 1999) can efficiently and accurately determine the complete orientation of feldspar grains. This method has allowed for more thorough investigations of plagioclase deformation.

Studies of (nearly) monomineralic experimentally- and naturally-deformed plagioclase have documented deformation by dominant dislocation creep on numerous

slip systems (e.g. Marshall and McLaren, 1977; Olsen and Kohlstedt, 1984, 1985; Ji and Mainprice, 1990; Kruse and Stünitz, 1999; Svahnberg and Piazolo, 2010, 2012). Other studies, of both naturally- and experimentally-deformed rocks, have documented plagioclase deformation by dominant diffusion creep with and without fluids present (Tullis and Yund, 1991; Dimanov et al., 1999; Jiang et al., 2000; Rybacki and Dresen, 2000). These studies of (nearly) monomineralic plagioclase rocks are important for characterizing how plagioclase responds to deformation over a range of conditions. However, few rocks are monomineralic and secondary phases typically complicate the behavior of rocks during deformation (Handy, 1990; Bruegmann & Dresen 2008; Czaplinska et al., 2015). For example, Mehl and Hirth (2008) documented a switch in plagioclase deformation mechanisms in a metagabbro between monomineralic layers (dislocation creep) and polymineralic layers (diffusion creep). There remains a great need for continued investigation into polymineralic systems, both natural and experimental.

Plagioclase deformation can also be associated with a change in composition owing to the compositional solid solution. Differences in composition are commonly observed between original parent grains and associated recrystallized grains (e.g., Brown et al., 1980; Sodre Borges and White, 1980; Olsen and Kohlstedt, 1985; Molli, 1994; Kruse and Stünitz, 1999). Plagioclase composition changes can also be observed through the zoning of recrystallizing grains (e.g., Svahnberg and Piazolo, 2010; Pearce and Wheeler, 2014). These compositional changes recorded in plagioclase can be used to understand how pressure and temperature conditions changed during recrystallization.

3.3. The Salt Mylonite Zone (SMZ)

The SMZ is a discrete, ductile shear zone hosted in quartzofeldspathic gneiss in the southern UHP domain of the WGR (Figs. 1a, 1b). It is distinguished from the surrounding non-mylonitic gneiss by an overall decrease in grain size and consistent foliation and lineation orientation (Fig. 1c). The boundary of the SMZ is gradational over approximately 1m. Both the non-mylonitic and mylonitic gneiss have the same mineral assemblage: plagioclase (40-65 modal %) + quartz (15-40%) + biotite (> 10%) ± hornblende ± muscovite ± epidote/allanite ± garnet with accessory zircon, titanite, magnetite and rare ilmenite and apatite. The non-mylonitic gneiss preserves a well-developed foliation and lineation with variable orientation and plunge, respectively. The mylonitic gneiss displays a strong, planar east-west striking foliation with a consistent steep to moderate northward dip, and a well-defined mineral lineation with a shallow to moderate eastward plunge (Fig. 1c). Banding (cm- to dm- scale) caused by both compositional and grain size variation is observed throughout the mylonite zone.

Mafic rocks are present within and beyond the SMZ (Fig. 1c). The mafic rocks range in mineral composition from amphibolite to eclogite, and in shape from layers to pods (cm- to m-scale). The SMZ is of particular interest for investigating the significance of ductile shear zones in the WGR because it contains a deformed coesite-eclogite body (Wain et al., 1997; Carswell et al., 2003). Trace-element thermobarometry and quartz fabrics in eclogite suggest fabric development at P > 2.0 GPa (Renedo et al., 2015). The close association between gneiss and coesite-eclogite suggests that mylonite zones may be an important facilitator for exhumation of UHP material.

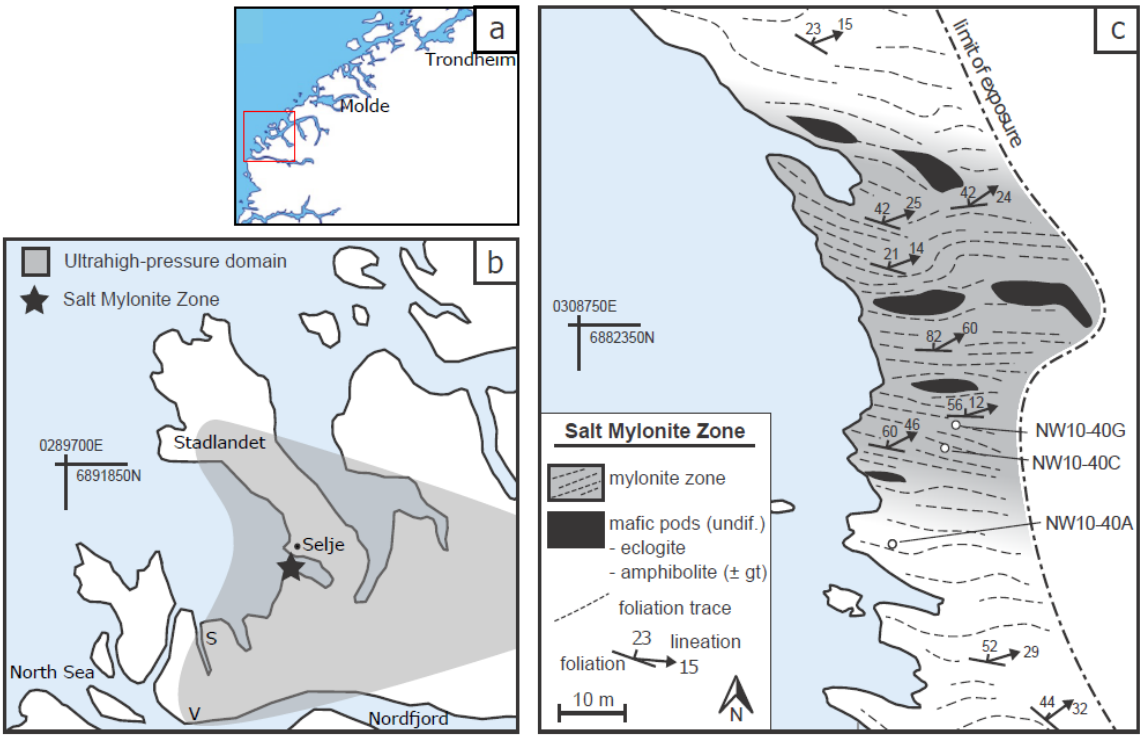

Figure 11. (a) Map of the western coast of Norway. The extent of Fig. 1b is outlined in red. (b) Map of the western extent of the southern UHP domain (highlighted in gray) in the Western Gneiss Region of Norway showing the location of the SMZ (black star). Other notable eclogite locations in the southern UHP domain Verpeneset (V) and Straumen (S) are located on the map. (c) Map of the SMZ (highlighted in gray) and adjacent area showing sample locations and structural measurements. Mafic material (eclogite and amphibolite, black) is contained within the quartzofeldspathic host gneiss both within and outside of the mylonite zone.

3.4. Methods

Three representative quartzofeldspathic gneiss samples from the Salt area were selected for detailed analysis. These samples represent the observed microstructural and grain size variation in and adjacent to the shear zone: one from outside of the SMZ (sample NW10-40A), and two from within the SMZ (samples NW10-40C and NW10-40G) (Fig. 1c). Samples were characterized using electron microprobe analysis (EMPA)

to determine plagioclase composition, and EBSD to determine crystallographic characteristics of quartz and plagioclase.

	non-mylonitic, phase-separated gneiss (NW10-40A)		mylonitic, phase-mixed gneiss (NW10-40C)		mylonitic, phase-separated gneiss (NW10-40G)	
	core	rim	core	rim	core	rim
SiO_2	63.64	60.21	61.61	59.63	62.69	58.23
Al_2O_3	23.09	25.72	24.16	25.43	23.94	26.52
FeO	0.12	0.05	0.08	0.10	0.09	0.18
CaO	3.46	6.35	4.70	6.07	4.33	7.50
Na_2O	9.46	7.90	8.73	7.85	8.95	7.23
K_2O	0.22	0.16	0.19	0.28	0.36	0.23
Total	99.99	100.39	99.47	99.36	100.36	99.89
Si	2.81	2.67	2.74	2.67	2.77	2.61
Al^{IV}	1.20	1.34	1.33	1.34	1.24	1.40
Fe^{2+}	0.00	0.00	0.00	0.00	0.00	0.01
Ca	0.16	0.30	0.22	0.29	0.20	0.36
Na	0.81	0.68	0.75	0.68	0.77	0.63
K	0.01	0.01	0.01	0.02	0.02	0.01
Ab	82	69	76	69	77	63
An	17	30	23	29	21	36
Or	1	1	1	2	2	1

Table 4. Representative plagioclase EMPA analyses.

Quantitative (wavelength-dispersive spectroscopy) and qualitative (energy-dispersive spectroscopy) plagioclase analyses were acquired by EMPA at the University

of Minnesota - Twin Cities in the Department of Earth Sciences on a JEOL JXA-8900. Qualitative element maps were acquired using a 15 kV accelerating voltage, 100 nA current, a focused beam, and stage-rastering step sizes ranging from 1-3 μm. Quantitative plagioclase analyses were acquired using a 15 kV accelerating voltage and a 20 nA current with a 1 μm beam. Natural mineral standards were used for calibration. Representative compositions are shown in Table 1. Plagioclase and quartz fabrics were characterized by EBSD. These data were acquired at Macquarie University with a Zeiss EVO scanning electron microscope equipped with an Oxford Instruments NordlysMax detector and the Aztec software package. Conditions were 20 kV accelerating voltage, 8 nA beam current, working distance of 12-14 mm, and dynamic focus for 70° sample tilt. In order to maximize plagioclase indexing, HKL software was configured to index bytownite, low albite, and anorthite. All plagioclase feldspar phases recorded indistinguishable orientation data and were therefore combined during processing and are reported here as bulk plagioclase.

Data analysis was completed using HKL Channel5 post-processing software. Reference coordinates (XYZ) were defined according to the macroscopic foliation and lineation: X is lineation-parallel in the plane of the foliation, Y is lineation-perpendicular in the plane of the foliation, and Z is foliation-perpendicular. All EBSD analyses were collected on XZ sections. Data were noise-reduced whereby grains smaller than 3x3 pixels, incompletely indexed grains, and border grains were removed from the dataset. The resulting grain boundary maps were compared with data quality maps and thin sections to ensure accurate data refinement.

Refined EBSD data were used to quantitatively characterize microstructural (modal abundance, grain size, aspect ratio, clustering) and crystallographic (orientation, misorientation) data for each map. Grain sizes (defined as the diameter of a circle of equivalent area) should be considered a minimum owing to incomplete indexing. Clustering analysis, to quantify the connectivity of quartz grains, was conducted using phase maps following the procedure of Hippertt et al. (2001). Orientation data are plotted as one point per grain on lower hemisphere, equal area projections; upper hemisphere projections are also presented for quartz. Pole figures are shown as both point plots and contoured plots. Contour intervals are integers in multiples of uniform distribution (m.u.d.), with the maximum m.u.d. given for each contoured plot. Contours are based on a 15° half width. Fabrics are presented for the total map area unless otherwise specified. Misorientation is shown with two plots following the procedure of Fliervoet et al. (1999). The misorientation angle distribution (MAD) histogram displays the frequency of a given range of misorientation angles for adjacent and non-adjacent grain pairs. The histogram also includes the theoretical line depicting a perfectly random distribution. Inverse pole figures are used to plot the misorientation axes for adjacent grains within a specified range of angles in both crystal and sample coordinate systems.

3.5. Petrographic and microstructural sample descriptions

3.5.1. Non-mylonitic, phase-separated gneiss: sample NW10-40A

This quartzofeldspathic country-rock gneiss was collected 10 m south of the SMZ (Figs. 1c, 2a). Quartz occurs dominantly in continuous and discontinuous foliation-

parallel ribbons, the remainder occurs as isolated grains or clusters of grains in the plagioclase-rich regions (Fig. 3a). Quartz ribbons are composed of a single layer of brick-shaped quartz grains (up to 1 x 2.5 mm). Ribbons are longer in the lineation-parallel direction (> 5 cm) than in the lineation-perpendicular direction (< 1 cm). Ribbon grains commonly display undulatory extinction and quartz-quartz grain boundaries are lobate (Fig. 3a). Isolated quartz grains are smaller than ribbon grains and show less evidence of internal deformation. Plagioclase dominates the regions between the ribbons. Plagioclase grain size is variable, though coarse overall (up to 3 mm). Plagioclase has serrated grain boundaries, is commonly twinned, and is zoned (Fig. 3b). Lesser amounts of biotite, potassium feldspar, and other secondary phases occur in the plagioclase-rich regions.

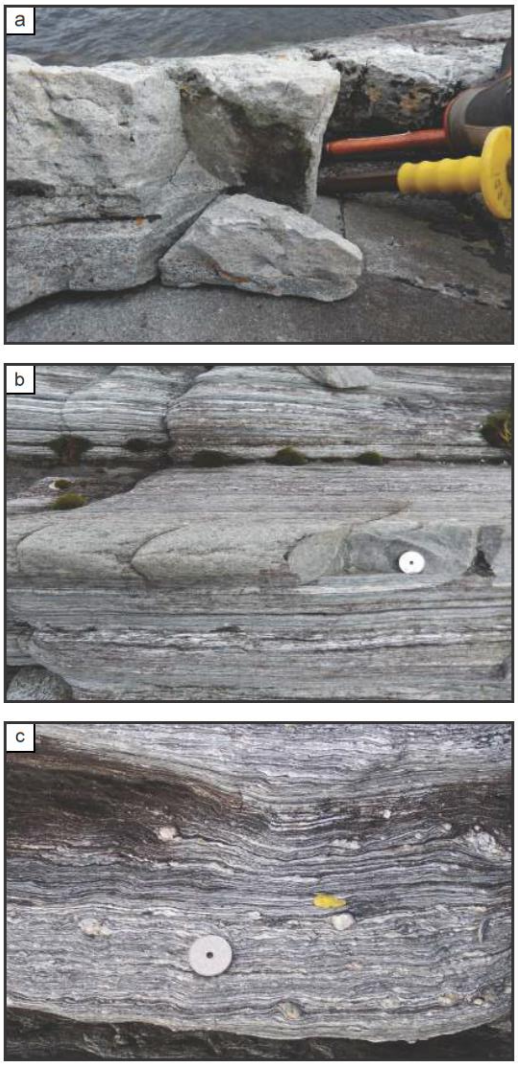

Figure 12. Field photos of representative rock types in the SMZ. (a) Non-mylonitic, phase-separated gneiss (NW10-40A). (b) Mylonitic, phase-mixed gneiss (NW10-40C). (c) Mylonitic, phase-separated gneiss (NW10-40G).

3.5.2. Mylonitic, phase-mixed gneiss: sample NW10-40C

This mylonitic gneiss sample (Fig. 2b) was collected from a granular layer within the SMZ. Granular layers are coarser, more resistant, and less common than fine-grained, compositionally-layered mylonitic gneiss (e.g. sample NW10-40G). Granular gneiss is characterized by nearly homogeneously distributed quartz, plagioclase, and biotite.

Quartz occurs as individual grains or elongate clusters of < 20 grains (Fig. 3c). Grains in clusters are larger (150 μm - 1 mm) than isolated grains (25 - 200 μm) and display evidence of internal deformation (undulatory extinction) that is not observed in isolated grains. Plagioclase ranges in size from 25 μm to 2 mm. Grains are inequant, and plagioclase-quartz grain boundaries are dictated by the quartz grain shape. Plagioclase locally displays twinning and is zoned (Fig. 3d). Biotite exhibits a SPO that defines the foliation. Potassium feldspar and other secondary phases are present throughout.

3.5.3. Mylonitic, phase-separated gneiss: sample NW10-40G

This compositionally-layered, mylonitic, phase-separated gneiss (Figs. 1c, 2c) is the dominant gneiss in the mylonite zone. Layers alternate on a cm-scale between biotite + hornblende poor (5-15%) and biotite + hornblende-rich (up to 50%) quartzofeldspathic gneiss. Quartz occurs exclusively in foliation-parallel ribbons. Ribbons are one grain thick, are made up of high aspect ratio quartz grains (up to 0.2 x 1 mm) (Fig. 3e), and are oblate (> 5 cm parallel to lineation, < 1 cm perpendicular to lineation). Quartz-quartz grain boundaries are normal to ribbon boundaries. Quartz grains show undulatory extinction and evidence of bulging recrystallization. Quartz ribbons separate regions dominated by plagioclase and secondary phases including biotite, hornblende, and potassium feldspar. Plagioclase is fine-grained (20 - 200 μm) and occurs as equant grains with straight edges and rare twins (granoblastic texture). Plagioclase is zoned (Fig. 3f).

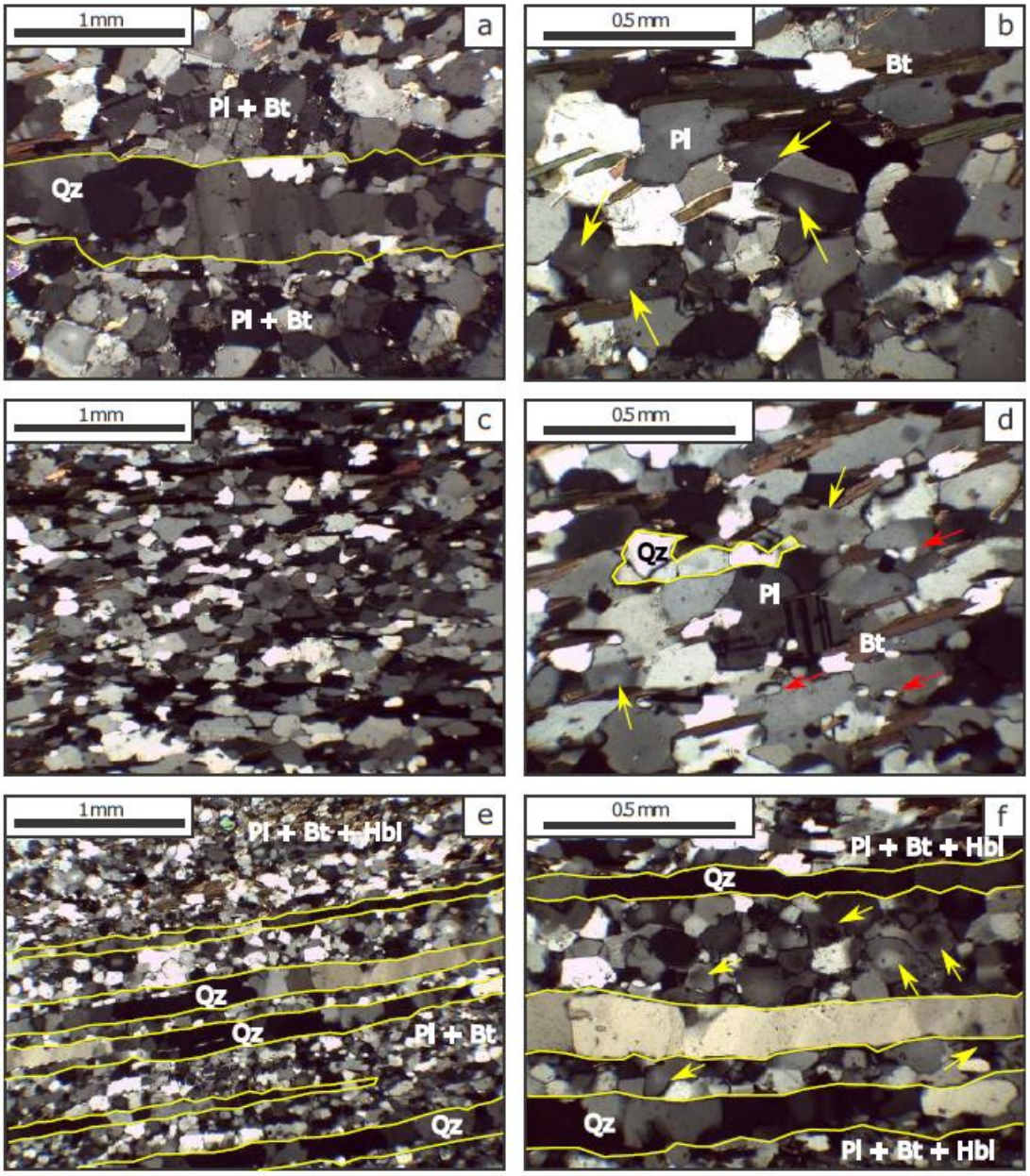
1mm
a
Pl + Bt
Qz
Pl + Bt
0.5mm
b
Bt
Pl
1mm
c
0.5mm
d
Qz
Pl
Bt
1mm
e
Pl + Bt + Hbl
Qz
Qz
Pl + Bt
Qz
0.5mm
f
Pl + Bt + Hbl
Qz
Qz
Pl + Bt + Hbl

.

Figure 13. Photomicrographs in cross-polarized light. NW10-40A: (a) A foliation-parallel Qz ribbon separates plagioclase rich regions, Qz ribbon boundary outlined in yellow. Qz grains display undulatory extinction and lobate boundaries. (b) Pl-rich region showing twinning and zoning, yellow arrows identify zoned grains. NW10-40C: (c) Homogeneously distributed Qz, Pl, and Bt. (d) Pl in phase-mixed mylonite is elongate parallel to foliation and displays twinning and zoning, yellow arrows identify zoned grains. One Qz cluster is outlined in yellow. Isolated Qz grains can be observed between Pl grain boundaries, identified by red arrows. NW10-40G: (e) Qz ribbons, outlined in yellow, separate Pl ± Bt ± Hbl-rich regions. Elongate Qz grains display undulatory extinction and straight grain boundaries. (f) Pl grains are equant, have straight grain boundaries, meet at triple-junctions, and are largely devoid of twinning. Pl zoning is ubiquitous, zoned grains identified by yellow arrows. Abbreviations after Whitney and Evans, 2010.

3.6. Patterns of plagioclase composition and zoning

Plagioclase in all samples displays optically-visible zoning (Figs. 3b, 3d, and 3f). EMPA investigation shows that plagioclase preserves reverse zoning with relatively anorthite-poor (An) cores and An-rich rims (Tables 1 and 2, Figs. 4 and 5). The zoning is characterized by a core of similar composition (intra- and inter-granular) with asymmetric rims of varying thickness. Cores are defined by the region of lowest An content. The location of the core does not necessarily correspond to the center of the grain; in some cases the zoning asymmetry is such that cores are located on the edge of the grain adjacent to grain boundaries or phase boundaries. Cores are equant or slightly elongate parallel to foliation. Rim thickness varies from grain to grain (Fig. 4).

	NW10-40A	NW10-40C	NW10-40G
Core (min An)	17	13	16
Rim (max An)	32	32	37
Max ΔAn*	15 mol%	17 mol%	19 mol%

*The maximum intragranular compositional change

Table 5. Reverse zoning in plagioclase by sample.

Based on these patterns, plagioclase can be divided into four grain types with respect to zoning: (1) grains with a central core and symmetric or asymmetric rims, (2) grains with a core on the grain edge and symmetric or asymmetric rims, (3) grains that lack zoning and preserve a core composition, and (4) grains that lack zoning and preserve a rim composition. Grain types (3) and (4) are smaller than types (1) and (2). All grain types occur in all samples and occur throughout the sample regardless of proximity to phase boundaries. Intergranular rim compositions are more consistent than intergranular core compositions in each sample (Fig. 5); this is likely owing to a sectioning effect (the grain center is not in the thin section plane). Therefore, the most reliable core compositions are the least anorthitic ones.

The least intense reverse zoning is displayed in the non-mylonitic gneiss (NW10-40A). Grains preserve a minimum core composition of An17, a maximum rim composition of An32, and a maximum intragranular difference of An15. A similar, though slightly more pronounced, zoning is displayed in the mylonitic, phase-mixed gneiss (NW10-40C). Grains preserve a minimum core composition of An13, a maximum rim composition of An32, and a maximum intragranular difference of An17. Reverse zoning of the greatest magnitude is displayed in the mylonitic, phase-mixed gneiss (NW10-40G). Grains preserve a minimum core composition of An16, a maximum rim composition of An37, and a maximum intragranular difference of An19 (Table 3, Fig. 5).

In the phase-separated samples (NW10-40A, G) no systematic zoning patterns (e.g. core location, rim thickness) are discernible. However, plagioclase zoning in the mylonitic, phase-mixed gneiss (NW10-40C) is such that foliation-parallel rims are

thicker (25-200 μm) than foliation-perpendicular rims (10-100 μm). The average ratio (parallel: perpendicular) is 2.2:1 (n = 30). Cores are 50-75 μm in diameter in the non-mylonitic gneiss, and 30-50 μm in diameter in both mylonitic gneisses.

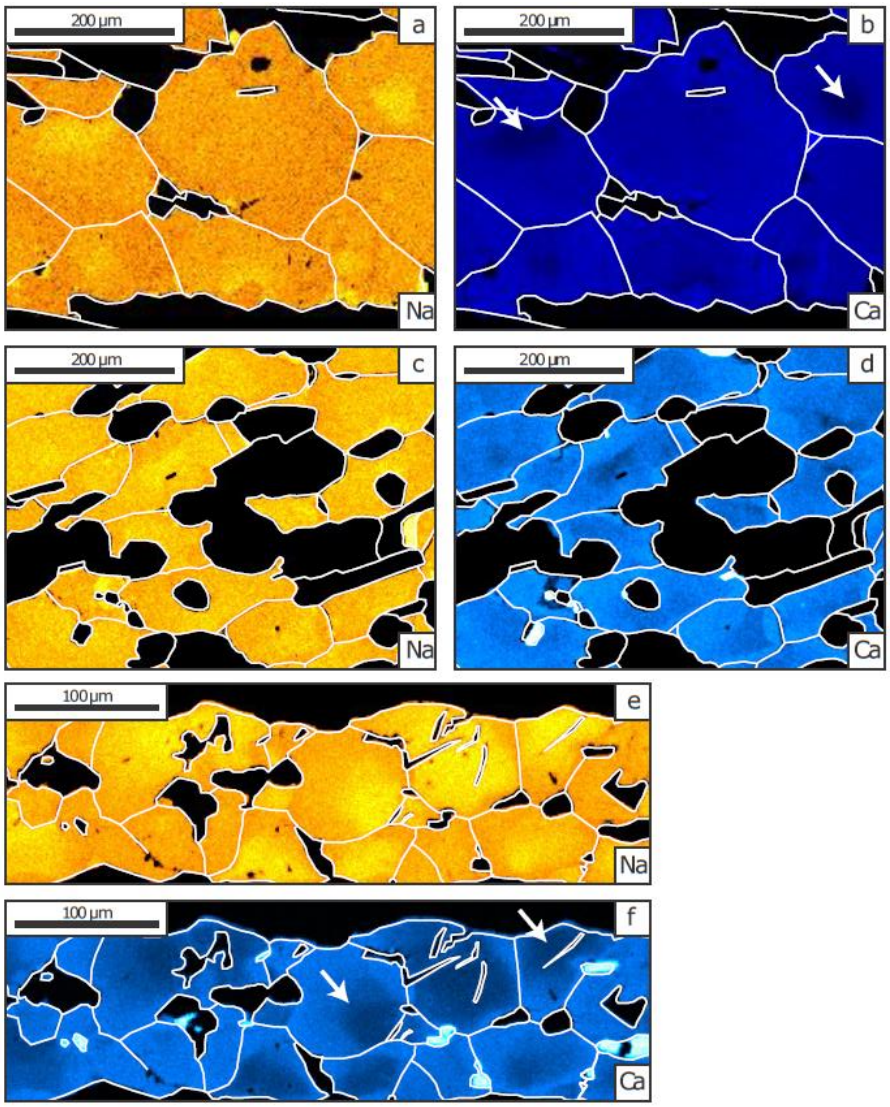

Figure 14. Qualitative EMPA maps of plagioclase zoning. NW10-40A: Na (a) and Ca (b) maps show ubiquitous, asymmetric reverse zoning. In (b), one arrow points to a Pl-Pl grain boundary with an edge-located core (left) and one arrow points to a Pl-Pl grain boundary with a centrally located core (right). NW10-40C: Na (c) and Ca (d) maps show reverse zoning, Pl SPO, and variable plagioclase grain shape. NW10-40G: Na (e) and Ca (f) maps show equant Pl grains with strain grain boundaries and ubiquitous asymmetric reverse zoning. In (f), one arrow points to a Pl-Qz phase boundary with a core far from the phase boundary (left) and one arrow points to a Pl-Qz phase boundary where the Pl core is adjacent to the phase boundary.

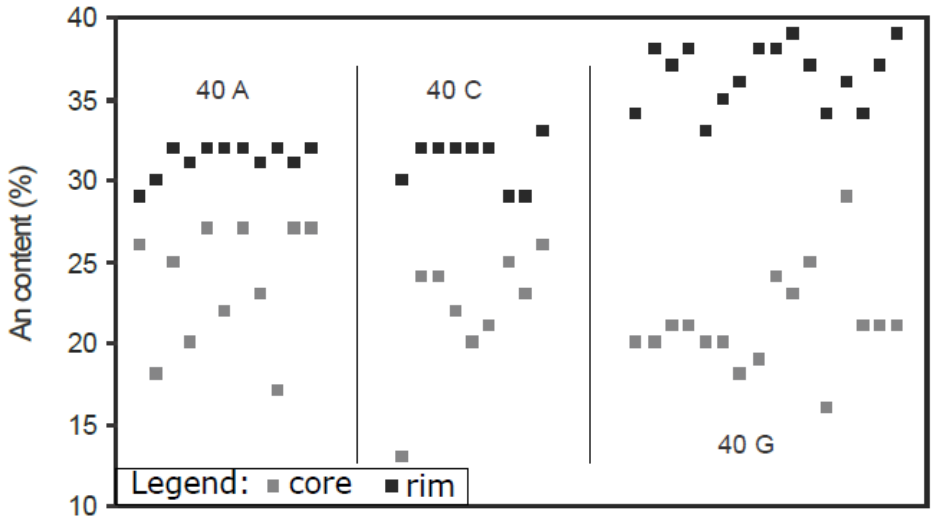

Figure 15. Plot of Pl core (gray, highest Na content) and rim (black) compositions by sample. Each column corresponds to the core and rim of one grain.

3.7. Quantitative microstructural analysis

3.7.1. Non-mylonitic, phase-separated gneiss: sample NW10-40A

Foliation-parallel quartz ribbons separate plagioclase-dominated domains in this sample (Fig. 6a). Clustering analysis results (1.98, n = 114) are consistent with quartz occurring dominantly as ribbons. Ribbon grains are larger (median = 75 μm; range 20 to 485 μm) than isolated quartz grains (median = 30 μm; range 20 to 110 μm) and more commonly preserve evidence of internal deformation (undulatory extinction, Dauphiné twins, subgrain boundaries). Aspect ratio does not vary significantly by habit (Table 4). Quartz grains preserve a fabric characterized by a girdle of <c>-axes normal to the lineation and <a>-axes clustered around the great circle (Fig. 6b). Ribbon grains preserve this fabric most strongly; a similar but weaker fabric is observed in discontinuous ribbon grains and isolated grains. Adjacent quartz grain pairs preserve a greater-than-random abundance of low-angle misorientations (from 10-60°) (Fig. 6c).

	Quartz			Plagioclase
NW10-40A	**Isolated**	**Discontinuous ribbon**	**Continuous ribbon**	**All**
Modal abundance	32%			44%
n**	77	79	122	433
Grain size (μm): median (min †, max)	30 (20,110)	60 (20, 145)	85 (20, 485)	75 (20, 320)
Aspect ratio: median (min, max)	1.6 (1.1, 4.5)	1.6 (1.1, 3.9)	1.6 (1.0, 4.7)	1.7 (1.0, 5.7)
NW10-40C	**Isolated**	**Clusters**		**All**
Modal abundance	29%			54%
n	127	794		937
Grain size: median (min, max) (μm)	40 (20, 90)	60 (20, 200)		70 (20, 270)
Aspect ratio: median (min, max)	1.7 (1.0, 4.6)	1.6 (1.0, 4.7)		2.0 (1.0, 6.0)
NW10-40G			**Ribbon**	**All**
Modal abundance	27%			40%
n			223	644
Grain size: median (min, max) (μm)			40 (20, 260)	40 (20, 120)
Aspect ratio: median (min, max)			1.9 (1.0, 9.0)	1.8 (1.0, 4.4)

* Modes do not sum to 100%, remainder is secondary phases and not indexed points
** Number of grains does not include any grains that intersect the edge of the map
…† Minimum grain size is limited by data refinement

Table 6. Microstructural and crystallographic summary of EBSD map analyses.

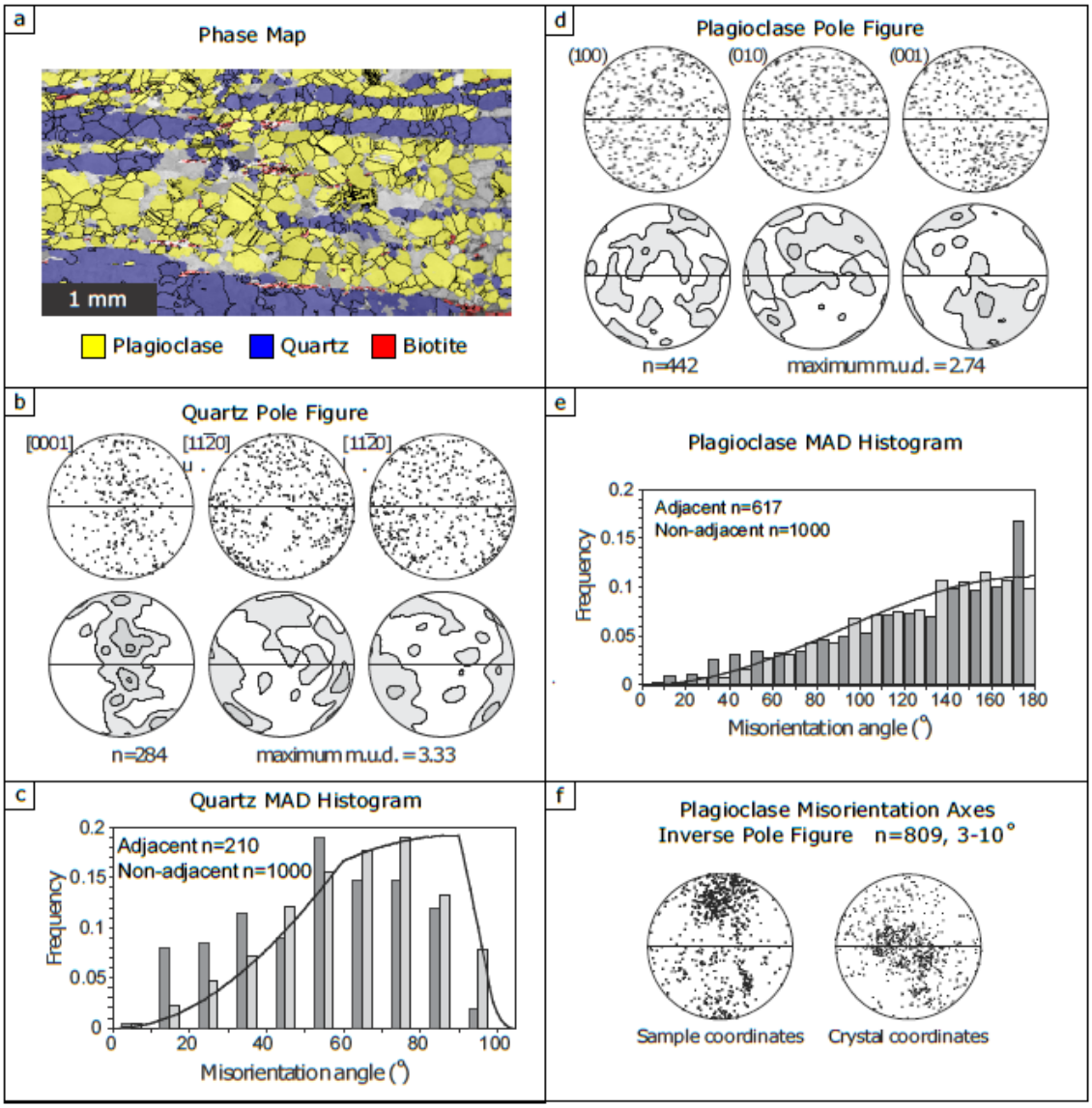

Figure 16. NW10-40A crystallographic fabrics: (a) Phase map showing distribution of Qz (blue), Pl (yellow), and Bt (red). The remainder is not indexed (gray). (b) Qz pole figures in points (above) and contoured (below). (c) Misorientation angle distribution for Qz grain pairs, both correlated (dark gray) and uncorrelated (light gray). (d) Pl pole figures in points (above) and contoured (below). (e) Misorientation angle distribution of Pl grain pairs, both correlated (dark gray) and uncorrelated (light gray). (f) Misorientation axis inverse pole figures for Pl plotted in sample coordinates (left) and crystal coordinates (right).

Plagioclase comprises the bulk of the matrix. Plagioclase grains are similar in size to quartz ribbon grains (median = 75 μm; range 20 to 320 μm). Plagioclase preserves

a weak to very weak CPO characterized by a partial girdle of (001)-poles oriented near-normal to lineation. For (100)- and (010)- poles the distribution is close to random (Fig. 6d). Overall MAD is near-random with a greater than random abundance of low angle boundaries (from 10-60°) and twin boundaries (180°) for adjacent grain pairs (Fig. 6e). Adjacent grain pairs with low angle misorientation (from 3-10°) have misorientation axes that are near-normal to lineation and perpendicular to foliation (Fig. 6f, sample coordinates).

3.7.2. Mylonitic, phase-mixed gneiss: sample NW10-40C

Plagioclase and quartz are homogeneously distributed in this sample (Fig. 7a). Quartz occurs as clusters or isolated grains. The lowest quartz clustering analysis, therefore the lowest quartz interconnectivity, is associated with this sample (1.45, n = 150). Isolated quartz grains are smaller (median = 40 μm; range 20 to 90 μm) than quartz grains in clusters (median 60 μm; range from 20 – 200 μm). The aspect ratio is low (median = 1.6; range 1.0 to 4.7) and does not vary significantly between habits (Table 4). Quartz fabric in this sample is indistinct (Fig. 7b). The overall MAD is random with little preference for low-angle grain boundaries for adjacent grain pairs (Fig. 7c).

Plagioclase is coarser than quartz (median = 70 μm; range 20 to 270 μm). Plagioclase grains are elongate parallel to the foliation (median = 2.0; range 1.0 to 6.0) (Fig. 7a, Table 4). Plagioclase preserves a fabric in which the (001)-poles form a girdle near normal to lineation (Fig. 7d). This fabric intensifies when higher AR grains are plotted independently (Fig. 7e). The MAD is near-random (Fig. 7f). Misorientation axes

for adjacent grain pairs with low angle misorientations (from 3 - 10°) are randomly oriented relative to crystallographic axes but if plotted in sample coordinates show a preference of being close to the y-direction (i.e. normal to lineation and in the foliation plane) (Fig. 7g).

Figure 17. NW10-40C crystallographic fabrics: (a) Phase map showing distribution of Qz (blue), Pl (yellow), and Bt (red). The remainder is not indexed (gray). (b) Qz pole figures in points (above) and contoured (below). (c) Misorientation angle distribution for Qz grain pairs, both correlated (dark gray) and uncorrelated (light gray). (d) Pl pole figures in points (above) and contoured (below). (e) Misorientation angle distribution of Pl grain pairs, both correlated (dark gray) and uncorrelated (light gray). (f) Misorientation axis inverse pole figures for Pl plotted in sample coordinates (left) and crystal coordinates (right).

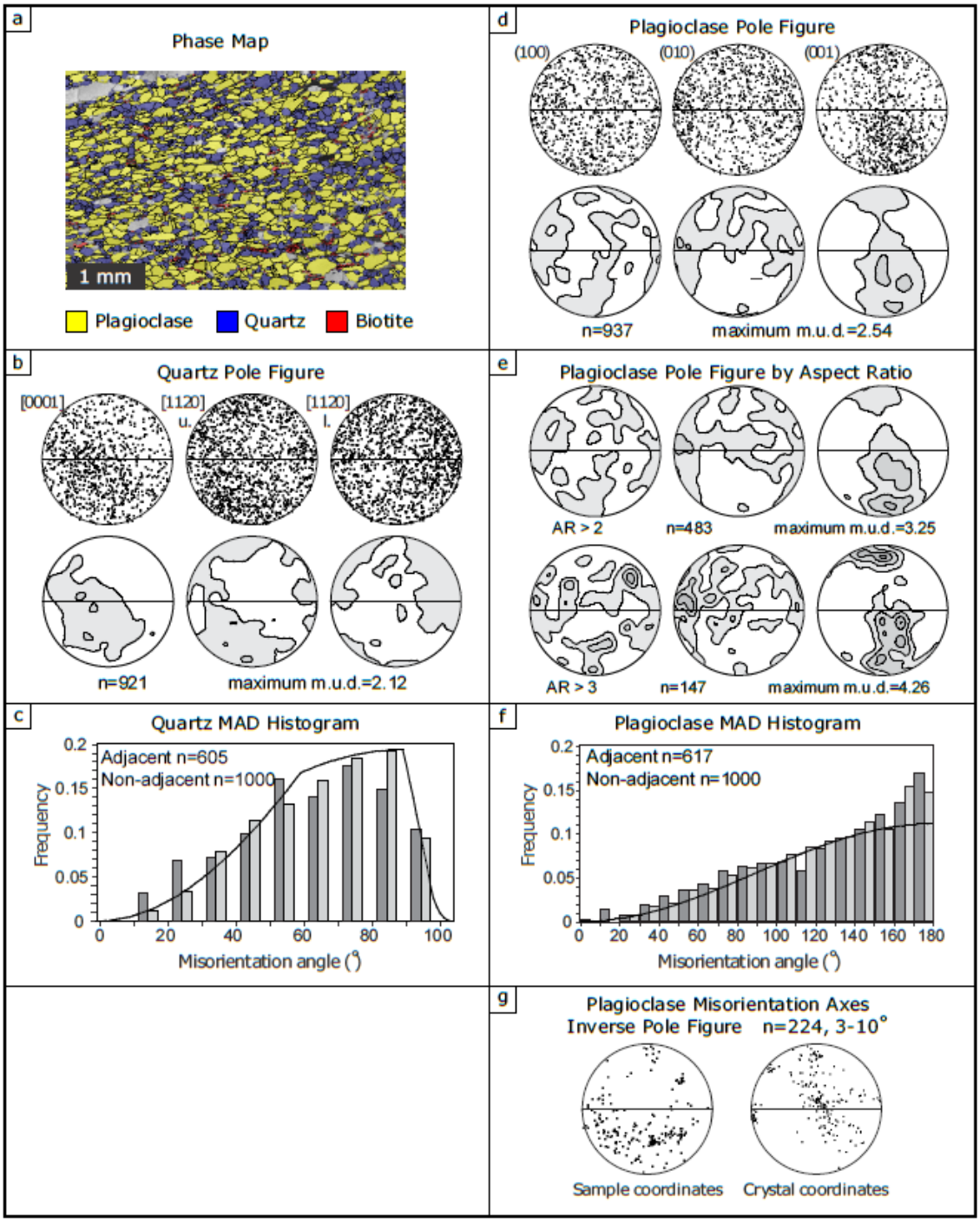
a
Phase Map
1 mm
Plagioclase
Quartz
Biotite
b
Quartz Pole Figure
[0001]
[1120] u.
[1120] l.
n=921
maximum m.u.d.=2.12
c
Quartz MAD Histogram
Adjacent n=605
Non-adjacent n=1000
Frequency
Misorientation angle (°)
d
Plagioclase Pole Figure
(100)
(010)
(001)
n=937
maximum m.u.d.=2.54
e
Plagioclase Pole Figure by Aspect Ratio
AR > 2
n=483
maximum m.u.d.=3.25
AR > 3
n=147
maximum m.u.d.=4.26
f
Plagioclase MAD Histogram
Adjacent n=617
Non-adjacent n=1000
Frequency
Misorientation angle (°)
g
Plagioclase Misorientation Axes
Inverse Pole Figure n=224, 3-10°
Sample coordinates
Crystal coordinates

3.7.3. Mylonitic phase-separated gneiss: sample NW10-40G

Quartz in this sample occurs almost exclusively in ribbons (> 90%), the ribbons separate plagioclase-dominated regions (Fig. 8a). The highest quartz clustering analysis is associated with this sample (2.52, n = 110). Quartz is comparatively fine-grained (median = 40 μm; range 20 to 260 μm). Quartz displays a fabric characterized by a partial girdle of <c>-axes perpendicular to the lineation and <a>-axes distributed around the great circle (Fig. 8b). Misorientation angles between adjacent and non-adjacent grains are non-random with a greater-than-random abundance of low angle grain boundaries (from 10-60°) (Fig. 8c).

Plagioclase in this mylonitic gneiss preserves a consistent grain size (median = 40 μm; range 20 to 120 μm). The plagioclase fabric is random when the complete map area is plotted. However, individual plagioclase layers each preserve a distinct CPO which differs from layer to layer (Fig. 8d). Overall MAD is near-random; however, adjacent grain pairs show a greater than random abundance of low angle boundaries (from 10-60°) and twin boundaries (180°) (Fig. 8e). Adjacent grain pairs with low angle misorientation (from 3-10°) are uncommon, but show a diffuse point maximum near-normal to lineation (Fig. 8f, sample coordinates).

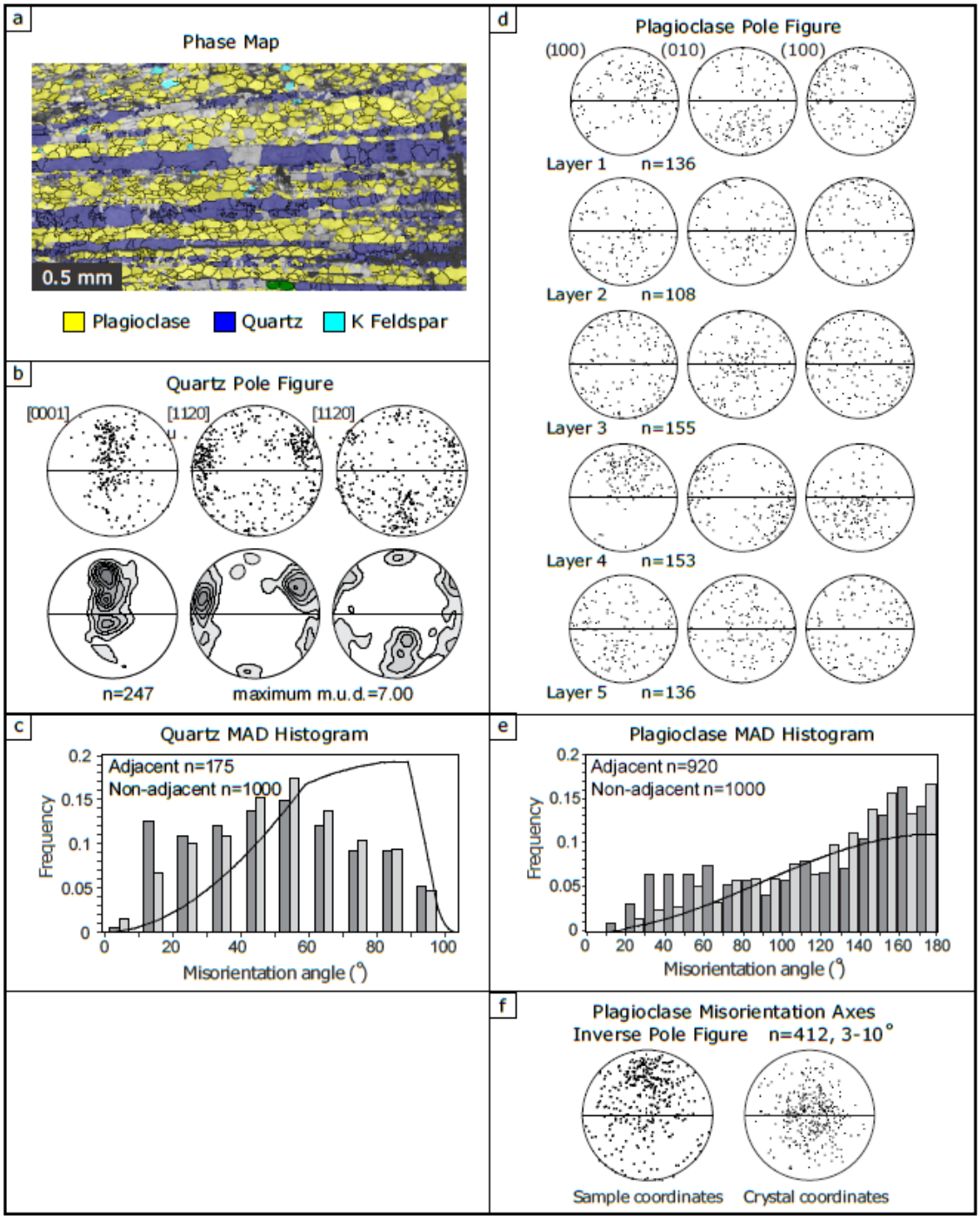
a
Phase Map
0.5 mm
Plagioclase
Quartz
K Feldspar
b
Quartz Pole Figure
[0001]
[1120]
[1120]
n=247
maximum m.u.d.=7.00
c
Quartz MAD Histogram
Adjacent n=175
Non-adjacent n=1000
Frequency
Misorientation angle (°)
d
Plagioclase Pole Figure
(100)
(010)
(100)
Layer 1 n=136
Layer 2 n=108
Layer 3 n=155
Layer 4 n=153
Layer 5 n=136
e
Plagioclase MAD Histogram
Adjacent n=920
Non-adjacent n=1000
Frequency
Misorientation angle (°)
f
Plagioclase Misorientation Axes
Inverse Pole Figure n=412, 3-10°
Sample coordinates
Crystal coordinates

Figure 18. NW10-40G crystallographic fabrics: (a) Phase map showing distribution of Qz (blue) and Pl (yellow). The remainder is not indexed (gray). (b) Qz pole figures in points (above) and contoured (below). (c) Misorientation angle distribution for Qz grain pairs, both correlated (dark gray) and uncorrelated (light gray). (d) Pl pole figures in points for each layer visible in the phase map. (e) Misorientation angle distribution of Pl grain pairs, both correlated (dark gray) and uncorrelated (light gray). (f) Misorientation axis inverse pole figures for Pl plotted in sample coordinates (left) and crystal coordinates (right).

3.8. Discussion

3.8.1. Deformation mechanisms of quartzofeldspathic gneiss in and near the SMZ

Phase-separated microstructure

Phase-separated gneiss is characterized by elongate quartz ribbons separating plagioclase-rich domains. The non-mylonitic gneiss (NW10-40A) and one mylonitic gneiss sample (NW10-40G) presented here preserve this microstructure. We infer that in this microstructure, quartz, the weaker of the two dominant phases, accommodates the bulk of the strain and feldspar, the stronger of the two phases, is largely protected from strain (Handy, 1990; Hippertt et al., 2001).

The non-mylonitic, phase-separated gneiss sample (NW10-40A) is the dominant rock type in the region outside of the SMZ. Quartz deformed by dominant dislocation creep through the activation of the prism <a>, rhomb <a>, and basal <a> slip systems. This is evidenced by the pronounced CPO (Fig. 6b) and a greater-than-random abundance of low angle grain boundaries (Fig. 6c). According to the CPO, deformation occurred at temperatures > 600 ºC (Passchier and Trouw, 2005; Law, 2014). Plagioclase deformation was partially accomplished by dislocation creep. Plagioclase exhibits a weak CPO (Fig. 6d) and adjacent grains have a greater-than-random distribution of low angle

grain boundaries (Fig. 6e). Misorientation axes show a preferred orientation (Fig. 6f), the pattern of which can be explained by slip on the [001](010) slip system (Fig. 9).

The mylonitic, phase-separated gneiss (NW10-40G) is the dominant rock type in the SMZ and is a higher strain version of the former sample. Phase distribution is the same in both samples, but the mylonitic gneiss has a significantly smaller grain size. Quartz deformation occurred by dominant dislocation creep through the activation of the prism <a> slip system. This is evidenced by a strong CPO characterized by a partial <c>-axis girdle normal to lineation (Fig. 8b), and a greater-than-random abundance of low-angle grain boundaries (Fig. 8c). The overall CPO pattern is similar to the lower strain equivalent and quartz deformation occurred at temperatures > 600 ºC (Passchier and Trouw, 2005; Law, 2014). Plagioclase layers each display a distinct CPO that varies by layer (Fig. 8d). Misorientation angles deviate from random over the 10-60° range (Fig. 8e) and misorientation axes from 3-10° have a preferred orientation (Fig. 8f). The presence of a CPO is commonly associated with deformation by dislocation creep; however, in this case it is unlikely that dislocation creep is the dominant plagioclase deformation mechanism. If dislocation creep were dominant, the preferred orientation of adjacent layers would be similar and related to the kinematic framework (Paterson and Weiss, 1961).

Alternatively, the presence of a different CPO in adjacent plagioclase layers without additional dislocation creep indicators (i.e. greater-than-random abundance of low-angle grain boundaries, twinning) can be explained by deformation of first dislocation creep modified subsequently via diffusion creep. Mylonitization of the gneiss

was initially accompanied by dynamic recrystallization in the dislocation creep regime. The fine-grained, equant plagioclase that makes up the plagioclase-rich layers are recrystallized grains that were derived from larger host grains. The orientation of these recrystallized grains was controlled by the host grain (e.g. Ji and Mainprice, 1990) resulting in a CPO in each layer that mimicked the orientation of the original host grain. Once the grain size was sufficiently small, subsequent deformation was dominated by diffusion creep, resulting in the weakening of the then pre-existing preferred orientation. An abundance of low-angle grain boundaries (Fig. 8c) is consistent with host-controlled recrystallization. A similar pattern, varying yet distinct CPO in a small area, was observed by Jiang et al. (2000); they favor a similar explanation for the formation of distinct, but varying, CPO in albite domains.

A direct comparison of these two samples allows us to investigate the effects of increased strain on quartz and plagioclase deformation mechanisms. Quartz in a phase-separated microstructure accommodates the bulk of the strain and does so by deforming in dislocation creep. The weak plagioclase fabric in the non-mylonitic, phase-separated gneiss suggests that deformation in plagioclase was accomplished, at least in part, by dislocation creep. The fabric is explained by activation of the [001](010) slip system which is dominant for plagioclase over a range of conditions including amphibolite-facies (e.g. Marshall and McLaren, 1977; Olsen and Kohlstedt, 1985). The fabric formed prior to or in the early stages of the SMZ-forming deformation and only to low strain as deformation was partitioned into the mylonitic rocks. Plagioclase deformation mechanisms in the phase-separated mylonite do not show pronounced microstructures

indicative of deformation by dislocation creep. Instead, plagioclase in near monomineralic layers may have, subsequent to initial recrystallization, deformed by diffusion creep.

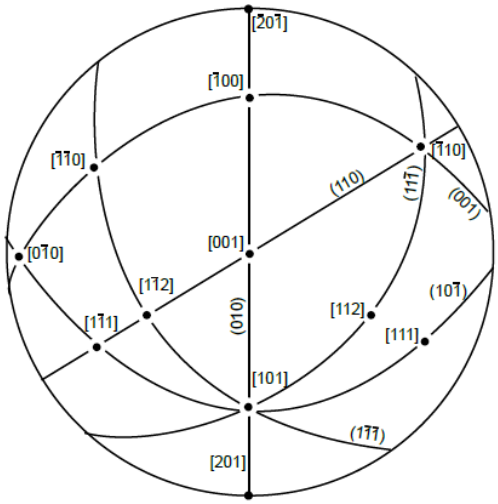

Figure 19. Pl inverse pole figure with observed slip systems plotted on an upper hemisphere Wulff net (after Kruse et al., 2001).

Phase-mixed microstructure

In the phase-mixed microstructure, quartz and plagioclase are homogeneously distributed throughout the sample. The homogeneous distribution of phases creates a framework microstructure (Hippertt et al., 2001) where plagioclase, the stronger phase, is the load bearing phase and accommodates the bulk of the strain. Quartz is randomly oriented (Fig. 7b) and preserves a pronounced SPO (Table 4). Quartz deformation by diffusion creep explains the absence of a CPO and the presence of a SPO. However, post-deformational grain growth is necessary as the current grain size (60 μm average) is too large for diffusion creep to be favorable at amphibolite facies conditions (e.g. Rybacki and Dresen, 2000). Plagioclase exhibits a weak CPO characterized by a girdle of (010)

poles normal to lineation and [001] parallel to lineation (Fig. 7d). Despite the presence of a CPO, the other crystallographic features do not support the conclusion that plagioclase deformation was exclusively by dislocation creep. Microstructural evidence of dislocation creep is largely lacking (e.g. deformation twins, undulose extinction, common subgrain boundaries), misorientation angle distribution follows a random pattern (Fig. 7f), and the low-angle misorientation axes are randomly oriented with respect to the crystal lattice (Fig. 7g). The plagioclase fabric observed in this sample is best explained not by effects due to high strain deformation, but by dominance of grain growth following deformation instead. This is recorded in the plagioclase compositional zoning.

3.8.2. Origin of plagioclase zonation

Plagioclase in the gneiss of the SMZ preserves ubiquitous reverse zoning (more sodic cores, more anorthitic rims). This zoning preserves a vital record of changes in pressure and temperature conditions during shear zone formation and evolution. This record is especially important as these quartzofeldspathic gneisses do not preserve phases suitable for traditional thermobarometry. Increasing An content from core to rim in plagioclase has been associated with (re)crystallization during an increase in temperature (e.g. Rambaldi, 1973) or a decrease in pressure (e.g. Pearce and Wheeler, 2014). We interpret the plagioclase zoning documented here to be consistent with recrystallization during decompression. Petrologic evidence including the development of epidote rims on allanite and the retrogressive breakdown of rare garnet in the gneiss, as well as previous

Ti-in-quartz thermobarometry of quartz in the gneiss (Renedo et al., 2015) support this interpretation.

Similar zoning patterns to those preserved in the SMZ plagioclase have been observed in naturally-deformed rocks and modelled. Cathodoluminescence imaging of quartz in the contact metamorphosed Appin quartzite reveals grains with bright rims and dark cores (Holness and Watt, 2001; Bergmann & Piazolo, 2010). EMPA of plagioclase in gneiss from the Lewisian Gneiss Complex reveals reverse zoned plagioclase (Pearce and Wheeler, 2014). Zoning features of particular importance documents in both cases include: (1) variable rim thickness, both inter- and intra-granular, (2) the presence of only one core per grain, and (3) variable core location. In both cases, zoning was formed as grain boundaries migrated during changing pressure and temperature conditions. In the Appin quartzite, fluid influx during grain boundary migration led to the growth of new quartz with high luminescence (Holness and Watt, 2001; Bergmann & Piazolo, 2010). In the Lewisian gneiss, new material was incorporated into the growing plagioclase grains as grain boundaries migrated. New material equilibrated to the current conditions during recrystallization thus recording the changing conditions with its changing composition (Pearce and Wheeler, 2014).

Simulations of grain growth by Jessell et al. (2003) and Pearce and Wheeler (2010) result in aggregates that display core to rim zoning that mimic the naturally-formed zoning documented here. Zoning features from models include: re-equilibration of material at the grain boundary, non-concentric zoning, asymmetry, and truncation of zoning against phase boundaries (Pearce and Wheeler, 2010). Models also show that

grain cores can be used to infer aggregate details prior to grain growth including grain composition, size, and aspect ratio (Jessell et al., 2003).

With this framework, we interpret the plagioclase zoning in the following way. At peak mylonitization, plagioclase grains were the size and composition of the cores: cores range from 30-50 μm and 50-75 μm in diameter in the mylonitic and non-mylonitic gneiss, respectively, and core compositions range from An13-17 (Fig. 4). Plagioclase grains grew over decreasing pressure and temperature conditions as the shear zone was exhumed. As new material was incorporated into growing grains the material re-equilibrated with boundary conditions resulting in the observed compositional zoning. In the phase-separated gneiss samples (NW10-40A, G) there is no systematic grain growth pattern. However, the zoning asymmetry in the phase-mixed mylonite (NW10-40C) is such that rims are consistently thicker parallel to foliation than perpendicular to foliation in the XZ section. This systematic grain growth is such that grains with the thickest foliation-parallel rims (grains of the highest AR) have a preferred orientation where [001] is parallel to lineation. It is well documented that: (1) [001] is the direction of easy slip in plagioclase (Marshall and McLaren, 1977; Olsen and Kohlstedt, 1985), (2) favorably oriented grains grow more easily post-deformation (e.g. Culshaw and Fyson, 1984; Neumann, 2000), and (3) systematic grain growth can result in a CPO (Bons & den Brok, 2000; Imon et al. 2004). Therefore, we interpret the weak plagioclase fabric in the mylonitic, phase-mixed gneiss as forming by oriented grain growth during exhumation in a low-stress dissolution-precipitation creep regime. Fluid presence is likely as re-

equilibration to changing PT conditions was very effective as documented by the compositional core-to-rim zoning.

3.8.3. Model of shear zone formation and evolution

Eclogite in the SMZ preserves unequivocal evidence for burial to UHP conditions during the Caledonian orogeny (Carswell et al., 2003) and there is strong evidence that the gneiss of the SMZ was also subducted to UHP conditions with the eclogite (Wain et al., 1997; Renedo et al, 2015). Two microstructurally distinct rock types were deformed in the SMZ: phase-separated gneiss and phase-mixed gneiss. Because the WGR is a polymetamorphic terrane (e.g. Hacker et al., 2010) we cannot determine the origin of the microstructural variation; however, we discuss how microstructural variation affects response to deformation in the context of shear zone formation and evolution.

At peak mylonitization of the SMZ, grain size in the mylonitized quartzofeldspathic gneiss was small (30-50 μm) and the composition was uniform and relatively An-poor (An13-17) (determined by cores of plagioclase grains). In the phase-separated gneiss, quartz, in the form of ribbons accommodated the bulk of the deformation and did so by dislocation creep. Plagioclase in nearly monomineralic layers deformed by diffusion creep. In the phase-mixed gneiss, deformation of both quartz and plagioclase was accomplished by diffusion creep. Phase-mixed gneiss is less abundant and more rheologically rigid than the phase-separated gneiss; it is likely that strain was partitioned into the phase-separated gneiss more effectively during mylonitization.

Quartz and plagioclase grains grew via grain boundary migration as the shear zone was exhumed from high pressure. The post-deformational grain growth of plagioclase is particularly visible where grain growth is tracked by compositional zoning. Reverse zoning in plagioclase in phase-separated gneiss reveals grain growth without any systematic pattern. Grain growth in the phase-mixed gneiss, however, is systematic: rims are thicker parallel to syn-deformational foliation than perpendicular. This oriented grain growth led to the development of a weak CPO in plagioclase during shear zone exhumation.

During continued exhumation, pressure and temperature conditions continued to decrease to, and ultimately through, the lower boundary conditions for grain boundary migration in plagioclase. Plagioclase grain growth ceases first in the non-mylonitic gneiss and phase-mixed gneiss (rim composition An32) and last in the phase-separated mylonitic gneiss (rim composition An37).

3.9. Conclusions

The quartzofeldspathic gneiss records the exhumation and decompression path of the SMZ through the preservation of fabrics and zoning in plagioclase. The crystallographic fabrics reveal that during mylonitization:

- Quartz accommodated strain and deformed by dislocation creep in phase-separated gneiss through a combination of prism <a>, rhomb <a>, and basal <a> slip systems.

- Plagioclase in phase-separated gneiss deformed at relatively low strains, due to strain localization into quartz, and shows evidence of deformation by dislocation creep on the [001](010) slip system.
- Plagioclase in mylonitic, phase-separated gneiss switched from dislocation creep to diffusion creep once grain sizes and stresses were favorable.
- Quartz in the mylonitic, phase-mixed gneiss deformed dominantly by diffusion creep.
- Plagioclase in the mylonitic, phase-mixed gneiss deformed originally by dislocation creep, then switched to diffusion creep when grain sizes were favorable.

Reverse zoning (low An cores, high An rims) in plagioclase reveals that during exhumation of the SMZ (post-mylonitization):

- New material was incorporated into growing plagioclase grains during changing conditions, through grain boundary migration at low stresses. This new material continuously re-equilibrated chemically to reflect the changing pressure and temperature conditions.
- Grain growth in the phase-mixed, mylonitic gneiss was systematic: grains grew preferentially in the direction of easy slip, [001]. The result of this oriented grain growth was to accentuate a pre-existing fabric.

4. The distribution, characteristics, and significance of shear zones in basement gneiss in the ultrahigh-pressure Western Gneiss Region of Norway

4.1. Introduction

Ultrahigh-pressure (UHP) terranes are the deep roots of ancient orogenic belts now exposed at the surface of the Earth. These sites provide an important opportunity to study ancient orogenic processes, which informs our understanding of modern continental collision, subduction, and eventual exhumation. UHP terranes have been the focus of much research over the past three decades (e.g. Hacker et al., 2010 and references therein). We have developed a detailed understanding on certain aspects of UHP terranes and metamorphism (e.g. timing and duration of UHP metamorphism, peak conditions of UHP metamorphism); however fundamental questions about broad scale exhumation mechanisms remain unanswered.

Here, we try to address the ongoing questions on exhumation mechanisms of UHP terranes, specifically within the Western Gneiss Region (WGR) of Norway. We do so by studying structurally significant sites that display discrete mylonite zones in the basement gneiss of the WGR. Petrologic and macro- and micro-structural features were studied and compared to determine the deformation mechanisms and pressure-temperature (P-T) conditions of each mylonite zone. We integrate P-T conditions, rock textures, and compositional information of the metamorphosed continental crust with the existing body of work on the WGR. In doing so, we work towards understanding the

evolution of these shear zones and ultimately determining their significance in the exhumation of the WGR.

4.1.1. The Western Gneiss Region of Norway

The WGR is the largest and best-exposed UHP terrane in the world. It covers over 50,000 km^2, and at least 5,000 km^2 preserves UHP conditions (e.g. Hacker et al., 2010). Within the WGR, UHP rocks define three distinct domains in the otherwise high-pressure (HP) terrane (Fig. 20a). These UHP domains are defined by the occurrence of coesite (e.g. Smith, 1984; Wain, 1997; Wain et al., 2000; Carswell et al., 2003; Butler et al., 2012) and microdiamond (Dobrzhinetskaya et al., 1995; Vrijmoed et al., 2006). Based on their form, the UHP domains have been interpreted as the cores of antiforms which expose the deepest-subducted material (Root et al., 2005; Hacker, 2007). The boundaries between the UHP and surrounding HP domains show a constant pressure-temperature (P-T) gradient indicating that there is no tectonic boundary juxtaposing the domains (Wain et al., 2000; Young et al., 2007).

Extensive studies on the WGR, focused primarily on mafic rocks, have yielded an understanding of the timing and duration of metamorphism (e.g. Carswell et al., 2003; Kylander-Clark et al., 2007; Young et al., 2011; DesOrmeau et al., 2015) and the peak conditions of metamorphism (e.g. Wain, 1997; Terry et al., 2000; Butler et al., 2012). UHP conditions in the WGR lasted approximately 25 Myr (~425 Ma - ~ 400 Ma) (Andersen et al., 1991, Andersen et al., 1998; Carswell et al., 2003; Root et al., 2004; Tucker et al., 2004; Hacker and Gans, 2005; Kylander Clark et al., 2007). Exhumation to

amphibolite facies (mid-crustal levels) occurred by ~390 - ~380 Ma (Andersen et al., 1998; Root et al., 2005; Hacker, 2007; Kylander-Clark et al., 2008; Young et al., 2011).

The WGR displays an increase in peak P and T conditions to the NW. The southern and central UHP domains display lower peak conditions: 700-800 °C and ~3.0 GPa (Wain, 1997; Johnston et al., 2007), and 750-800 °C and ~3.0 GPa (Butler et al., 2012), respectively. The northern UHP domain shows the highest peak conditions at >800 °C and 3.5-4.0 GPa (Terry et al., 2000). The degree of migmatization follows the same pattern: the southern UHP domain preserves minor (up to 10%) amounts of migmatite while the northern UHP domain displays abundant (up to 50%) migmatite (Griffin and Brueckner, 1985; Labrousse et al., 2002; Tucker et al., 2004).

The WGR is a structurally-bounded terrane; it is limited to the north by the Møre-Trondelag fault complex (MTFC) and to the south and west by the Nordfjord Sogn detachment zone (NSDZ). The MTFC is a sinistral, strike-slip fault complex (Gabrielsen and Ramberg, 1979). The NSDZ is a low-angle normal fault zone that juxtaposed the (U)HP terrane of the WGR with overlying low-grade metasediments (Norton, 1986). These fault complexes were both active during the exhumation of the WGR; a combination of extension and strike-slip motion (transtension) affected the rocks of the WGR and was the primary exhumation mechanism at crustal depth (Andersen et al., 1991; Fossen, 1992; Krabbendam and Dewey, 1998; Fossen, 2010). Features of amphibolite facies transtension are well-documented throughout the WGR, including constrictional fabrics in the gneiss and large-scale E-W trending folds (Krabbendam and Dewey, 1998; Fossen, 1992). Little is understood about near-peak, mantle depth

exhumation; however, constrictional fabrics defined by omphacite crystallographic preferred orientation within eclogite (Renedo et al., 2015) are consistent with transtensional deformation at near-UHP conditions.

Despite a detailed understanding of many aspects of the WGR, fundamental questions about the mantle depth exhumation mechanisms of the WGR remain. Eduction (Andersen et al., 1991), buoyancy-driven exhumation (Chemenda et al., 1995), and exhumation by channel flow (Gerya et al., 2008) are three syn-convergence models that have been proposed for the exhumation of UHP terranes. Additionally, syn-extensional exhumation is another possible mechanism that is less commonly suggested (Butler et al., 2015). No consensus on mantle depth exhumation mechanism of the WGR has been reached. Documenting large scale structural features and petrologic trends throughout the UHP terranes will help to discern between possible models.

In an attempt to address these questions, we look to the metamorphosed continental crust that makes up the bulk (> 90%) of the WGR. Rarely do researchers focus on the gneiss as it ubiquitously preserves a generic amphibolite-facies assemblage and very rarely displays explicit evidence for UHP metamorphism. Recent research that has focused on the gneiss (e.g. Peterman et al., 2009; Young et al., 2015) show a wide range of results and conflicting interpretations. More research on the gneiss is needed to reach consensus on the results and significance of the findings.

Previous researchers have noted the existence of discrete mylonite zones in the gneiss of the WGR (Smith, 1984; Vrijmoed et al., 2006; Hacker et al., 2010), but these structurally significant sites have rarely been studied. Renedo et al. (2015) documented a

shear zone in the southern UHP domain, the Salt Mylonite Zone, which preserves UHP eclogite and amphibolite-facies gneiss that record a shared pressure-temperature-deformation path from (U)HP to amphibolite-facies conditions (see Chapter 2). The SMZ is one of many shear zones in the metamorphosed continental crust of the WGR closely associated with (U)HP material; each of these shear zones preserves a record of the local (U)HP evolution. A detailed analysis of these shear zones and of the metamorphic evolution they preserve will contribute to understanding the exhumation of the WGR.

4.2. Methods

More than 10 discrete, ductile shear zones were identified and sampled in the WGR (Fig. 20a). Three mylonitic shear zones were selected for detailed field mapping and sampling. Shear zones were selected based on distribution throughout the WGR and association with (U)HP mafic material. Structurally oriented samples of gneiss and eclogite/amphibolite were collected. A detailed table of sample location and assemblage is provided in Appendix 2. Foliation and lineation of the gneiss was measured within and adjacent to the mylonite zones. Mafic layers and pods were carefully mapped and measured (e.g. long and short axis of pods, thickness of layers, foliation and lineation where possible) within and adjacent to the mylonite zones.

Mineral assemblages and microstructures of samples were documented using polarized light microscopy. Electron microprobe analysis (EMPA) was conducted on select samples to characterize chemical variation (qualitative analyses) and to determine major element compositions (quantitative analyses). EMPA analysis was conducted at the

Department of Earth Sciences, University of Minnesota Twin Cities on a JEOL JXA-8900 microprobe. Qualitative (energy-dispersive spectroscopy) element maps were acquired using a 15 kV accelerating voltage, 100 nA current, a focused beam, and stage-rastering step sizes ranging from 1 to 3 μm depending on grain size. Quantitative (wavelength-dispersive spectroscopy) mineral analyses were acquired using a 15 kV accelerating voltage, 25 nA current, and a focused beam. For plagioclase, the current was reduced to 20 nA, and the beam was widened to 5 μm. ZAF correction was applied to all analyses. Natural mineral standards were used for calibration. Representative compositions are given in Table 7, 8, and 9 and a complete set of EMPA analyses is given in Appendix 3. Quantitative EMPA analyses were used to conduct garnet-clinopyroxene thermobarometry for all three mylonite zones. The thermobarometer uses the clinopyroxene activity model of Holland (1990) and the garnet activity model of Ganguly et al. (1996).

4.3. Shear zones in the Western Gneiss Region

In this study, 11 discrete ductile shear zones in the metamorphosed continental crust were observed and documented (Fig. 20a). All shear zones documented here share the following characteristics: (1) shear zones are discrete, shear zone boundaries are commonly visible, and the contact between the mylonite zone and surrounding gneiss is gradual but distinct (Figs. 21a, b), (2) all of the documented shear zones are associated with high- to ultrahigh-pressure mafic material, including amphibolite (± garnet) and eclogite (Figs. 21c, d and e), and (3) the structural orientation (foliation and lineation) of

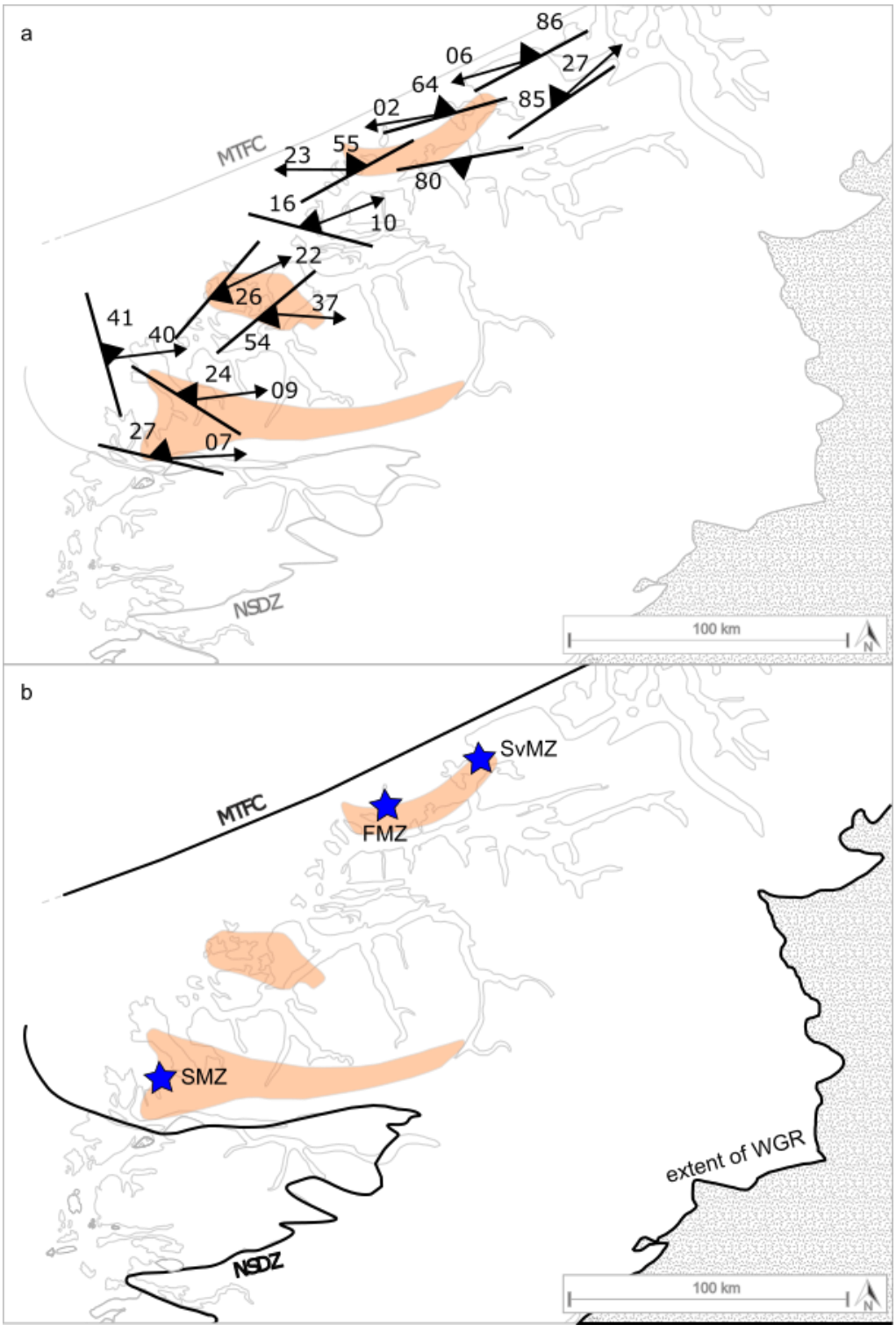
a
86
06
27
64
85
02
MTFC
23
55
80
16
10
22
26
37
41
40
54
24
09
27
07
NSDZ
100 km
N
b
SvMZ
MTFC
FMZ
SMZ
extent of WGR
NSDZ
100 km
N

Figure 20. (a) WGR map locating discrete shear zones. UHP domains are highlighted in orange. Each shear zone is indicated by a strike and dip symbol with the average foliation and lineation of the shear zone. (b) WGR map with the three focus shear zones (blue stars). The limits of the WGR are indicated: the NSDZ and MTFC to the north and south, respectively, and the limit of the WGR to the east.

the shear zones conform to the detachment fault to which they are closest (Fig. 20a). Shear zones vary in other respects; in particular, rock type (Fig. 21a: orthogneiss, Fig. 21b: paragneiss) and degree of migmatization (Fig. 21d).

Three mylonitic shear zones were selected for detailed study: the Salt mylonite zone (SMZ) in the southern UHP domain, and the Finnøya mylonite zone (FMZ) and the Svartberget mylonite zone (SvMZ), both in the northern UHP domain (Fig. 20b). The SMZ displays a well-documented coesite-eclogite body in a discrete, quartzofeldspathic mylonite zone (Smith, 1984; Wain et al., 2000; Renedo et al., 2015). The FMZ is a lithologically-diverse mylonite zone located near the Harøya coesite-eclogite locality (Butler et al., 2012). The SvMZ is a complex mylonite zone directly adjacent to a microdiamond-bearing peridotite body (Vrijmoed et al., 2000, 2006).

Garnet

sample	NW10-40J		NW10-40E
location	in SMZ		in SMZ
lithology	mafic gneiss		amph
SiO_2	37.26		38.94
Al_2O_3	21.63		22.55
FeO	26.97		21.00
MnO	3.57		0.48
MgO	1.37		6.51
CaO	9.26		10.99
Total	99.98		100.48
Si	2.97		2.97
Al	2.04		2.03
Fe	1.80	2.99	1.34
Mn	0.24		0.03
Mg	0.16		0.74
Ca	0.79		0.90
Alm	60		45
Pyp	5		25
Sps	8		1
Grs	26		30

Plagioclase

sample	NW10-40J		NW10-40J		NW10-40D		NW10-40I	
location	in SMZ		in SMZ		in SMZ		in SMZ	
lithology	mafic gneiss		mafic gneiss		amph		amph	
SiO_2	60.85		58.63		48.84		50.88	
Al_2O_3	25.12		26.56		32.96		32.11	
FeO	0.13		0.09		0.21		0.17	
CaO	5.74		7.82		15.57		12.64	
Na_2O	8.24		7.00		2.44		4.17	
K_2O	0.29		0.24		0.02		0.06	
Total	100.37		100.33		100.07		100.03	
Si	2.70	3.00	2.61	3.00	2.23	3.00	2.31	3.00
Al^{IV}	0.30		0.39		0.77		0.69	
Al^{VI}	1.01		1.00		1.00		1.02	
Fe	0.00		0.00		0.01		0.00	
Ca	0.27	1.00	0.37	0.99	0.76	0.99	0.61	0.99
Na	0.71		0.61		0.23		0.37	
K	0.02		0.02		0.01		0.01	
Ab	71		61		23		62	
An	27		38		76		37	
Or	2		1		1		1	

Clinopyroxene

sample	NW11-21B	
location	in SMZ	
lithology	ecl	
SiO_2	55.28	
TiO_2	0.07	
Al_2O_3	10.08	
FeO	2.59	
MnO	0.05	
MgO	10.89	
CaO	15.40	
Na_2O	5.34	
Total	99.9	
Si	1.96	2.00
Al^{IV}	0.04	
Al^{VI}	0.4	1.03
Ti	0.00	
Mg	0.58	
Fe^{2+}	0.07	
Mn	0.00	
Ca	0.59	1.05
Na	0.36	

Garnet

sample	NW11-21B
location	in SMZ
lithology	ecl
SiO_2	41.00
Al_2O_3	22.92
FeO	17.19
MnO	0.41
MgO	15.30
CaO	3.47
Total	100.29
Si	3.00
Al	1.98
Fe	1.08
Mn	0.03
Mg	1.67
Ca	0.27
Alm	35
Pyp	55
Sps	1
Grs	9

Table 7. Representative SMZ EMPA analyses.

	Garnet			
sample	NW10-54C		NW10-53A	
location	in FMZ		in FMZ	
lithology	myl		ecl	
SiO_2	38.57		38.78	
Al_2O_3	20.89		21.21	
FeO	22.46		22.80	
MnO	3.18		2.03	
MgO	3.58		4.94	
CaO	11.44		10.89	
Total			100.69	
Si	3.02		3.00	
Al	1.93		1.94	
Fe	1.47	3.04	1.48	2.99
Mn	0.20		0.13	
Mg	0.42		0.57	
Ca	0.96		0.90	
Alm	48		38	
Pyp	14		15	
Sps	7		4	
Grs	31		23	

	Plagioclase					
sample	NW10-54C		NW10-54H		NW10-53A	
location	in FMZ		in FMZ		in FMZ	
lithology	myl		myl		Ecl	
SiO_2	59.98		62.70		59.67	
Al_2O_3	24.94		23.36		25.63	
FeO	0.13		0.11		0.20	
CaO	7.04		5.32		7.01	
Na_2O	7.25		8.12		7.38	
K_2O	0.20		0.27		0.26	
Total	99.56				100.15	
Si	2.68	3.00	2.78	3.00	2.66	3.00
Al^{IV}	0.32		0.22		0.34	
Al^{VI}	0.99		1.00		1.00	
Fe	0.01		0.00		0.01	
Ca	0.34	0.99	0.25	0.98	0.33	0.99
Na	0.63		0.71		0.64	
K	0.01		0.02		0.01	
Ab	64		72		65	
An	35		26		34	
Or	1		2		1	

	Clinopyroxene			
sample			NW10-53A	
location	in FMZ		in FMZ	
lithology	myl		ecl	
SiO_2	51.41		50.35	
TiO_2	0.17		0.18	
Al_2O_3	4.83		5.29	
FeO	10.18		10.52	
MnO	0.40		0.38	
MgO	10.78		10.86	
CaO	20.66		21.21	
Na_2O	1.67		1.25	
Total	100.14		100.04	
Si	1.92	2.00	1.88	2.00
Al^{IV}	0.08		0.12	
Al^{VI}	0.14	1.05	0.11	1.01
Ti	0.00		0.01	
Mg	0.60		0.60	
Fe^{2+}	0.32		0.29	
Mn	0.01		0.01	
Ca	0.83	0.95	0.85	0.94
Na	0.12		0.09	

Table 8. Representative FMZ EMPA analyses.

Garnet

sample	NW11-10AA		NW11-10B	
location	in SvMZ		in SvMZ	
lithology	myl. gneiss		myl.gneiss	
SiO_2	37.44		37.35	
Al_2O_3	20.87		21.05	
FeO	22.79		24.75	
MnO	14.86		11.41	
MgO	2.74		3.56	
CaO	1.48		1.76	
Total	100.19		99.9	
Si	3.01		3.00	
Al	1.98		1.99	
Fe	1.53	3.00	1.66	3.01
Mn	1.01		0.78	
Mg	0.33		0.43	
Ca	0.13		0.15	
Alm	51		55	
Pyp	11		14	
Sps	34		26	
Grs	4		5	

Plagioclase

sample	NW11-10A		NW11-10F		NW11-10N		NW11-10N	
location	in SvMZ		in SvMZ		in SvMZ		in SvMZ	
lithology	myl. gneiss		myl. gneiss		ecl		ecl	
SiO_2	59.46		60.18		62.64		57.02	
Al_2O_3	25.75		25.63		24.01		28.05	
FeO	0.02		0.08		0.13		0.29	
CaO	6.86		6.71		5.15		9.42	
Na_2O	7.50		7.38		8.5		6.13	
K_2O	0.24		0.20		0.18		0.09	
Total	99.85		100.22		100.61		100.99	
Si	2.65	3.00	2.67	3.00	2.76	3.00	2.53	3.00
Al^{IV}	0.35		0.33		0.25		0.47	
Al^{VI}	1.00		1.01		1.01		1.00	
Fe	0.00		0.00		0.01		0.01	
Ca	0.33	1.00	0.33	0.99	0.24	0.99	0.45	0.99
Na	0.65		0.63		0.73		0.53	
K	0.01		0.01		0.01		0.01	
Ab	66		66		74		54	
An	33		33		25		46	
Or	1		1		1		1	

Clinopyroxene

sample	NW11-10N		
location	In SvMZ		
lithology	ecl		
SiO_2	52.34		
TiO_2	0.31		
Al_2O_3	2.62		
FeO	9.61		
MnO	0.15		
MgO	12.66		
CaO	21.77		
Na_2O	0.84		
Total	100.30		
Si	1.95	2.00	
Al^{IV}	0.05		
Al^{VI}	0.07	1.07	
Ti	0.01		
Mg	0.70		
Fe^{2+}	0.30		
Mn	0.00		
Ca	0.87	0.93	
Na	0.06		

Garnet

sample	NW11-10N	
location	In SvMZ	
lithology	ecl	
SiO_2	39.29	
Al_2O_3	21.54	
FeO	24.56	
MnO	0.83	
MgO	5.98	
CaO	8.58	
Total	100.79	
Si	3.02	
Al	1.95	
Fe	1.58	2.02
Mn	0.05	
Mg	0.69	
Ca	0.71	
Alm	52	
Pyp	23	
Sps	2	
Grs	23	

Table 9. Representative SvMZ EMPA analyses.

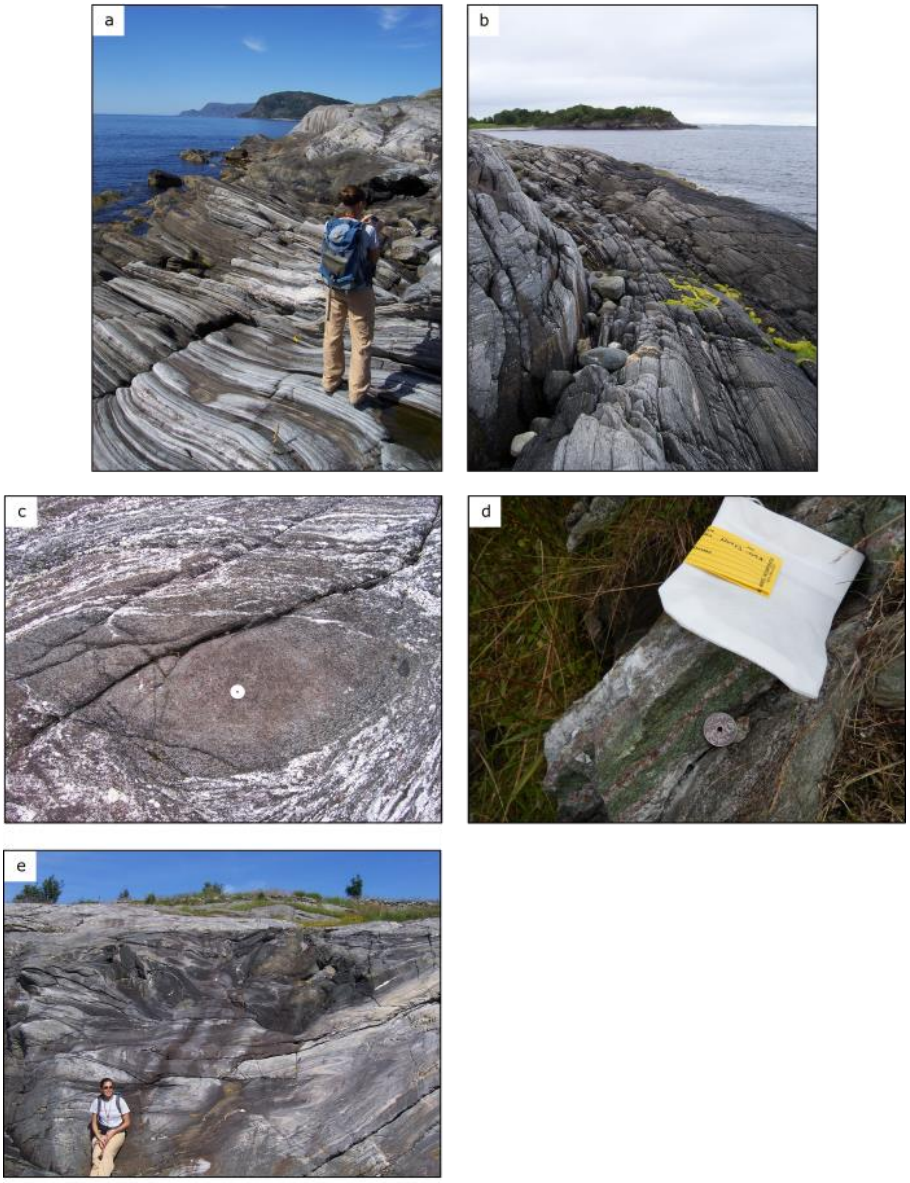

Figure 21. Photos of shear zones throughout the WGR. (a) Mylonitic orthogneiss (foreground) has a gradual contact with non-mylonitic orthogneiss (background). (b) Contact between mylonitized mafic gneiss (right) and adjacent non-mylonitic mafic gneiss. (c) Migmatite-rich gneiss surrounding a retrogressed eclogite pod. The core of the pod has the assemblage Omp + Grt while the edges have the assemblage Hbl + Pl + Grt. (d) UHP eclogite pod with foliation-parallel, coesite-bearing Qz + Grt vein. (e) Mafic pod that preserves stages of eclogite retrogression including Grt-amphibolite, amphibolite, and mafic gneiss. Mineral abbreviations after Whitney and Evans, 2010.

4.4. Salt Mylonite Zone

4.4.1. Field description

The SMZ is located in the southernmost UHP domain (Figs. 20b and 22). The mylonite zone is 60 m wide across strike and has a gradual contact with the adjacent non-mylonitic gneiss that is the dominant rock type of the region. The gneiss outside of the SMZ is deformed, preserves a visible foliation and lineation, and is folded. Mafic pods and layers are preserved in gneiss throughout the Salt region.

Gneiss within the SMZ preserves a strong, planar foliation that dips moderately north, and a shallowly east-plunging lineation (Renedo et al., 2015). Contained within the gneiss of the SMZ are mafic (metabasaltic) pods and layers that range in size and shape from cm-scale layers to pods that are 3 m thick and >10 m long. The metabasaltic material ranges in composition from coesite-bearing eclogite to amphibolite ± garnet. In some cases, eclogite pods are retrogressed to amphibolite and hornblende-rich gneiss (Renedo et al., 2015). The metabasaltic pods and layers are foliation-parallel and the gneiss foliation wraps around the edges of the pods. The foliation and lineation of the UHP eclogite body, defined by elongate omphacite, is consistent with the foliation and lineation of the surrounding gneiss. These field relationships suggest that gneiss and mafic material, including eclogite, were deformed under the same kinematic conditions.

4.4.2. Petrography

Gneiss within and outside of the SMZ preserves the same amphibolite-facies assemblage: quartz + plagioclase + K-feldspar + biotite ± hornblende ± garnet ± white mica. Accessory minerals include zircon, epidote, allanite, apatite, ilmenite, rutile, and titanite. Though the mineral assemblage is the same, important microstructural variations are observed between gneiss within and outside of the SMZ.

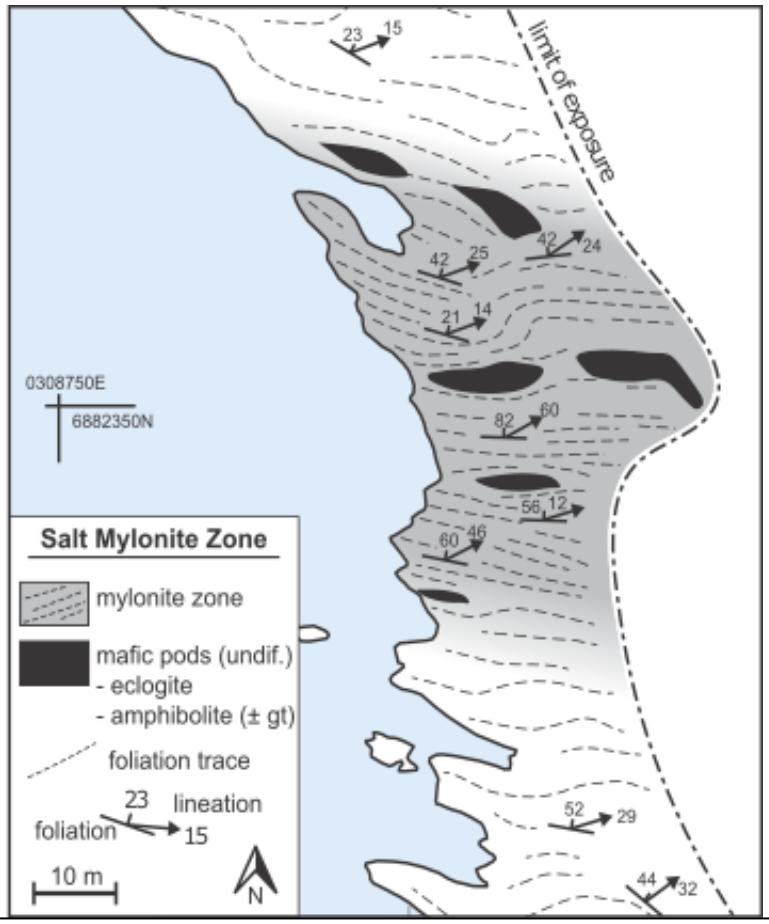

Figure 22. Map of the SMZ showing the mylonite zone (highlighted in gray) and the distribution of mafic material (black) throughout the shear zone.

Outside of the SMZ, the gneiss is coarse-grained. Porphyroclasts of K-feldspar are up to 1 cm; quartz, plagioclase, and biotite are up to 5 mm. Microstructurally, gneiss outside of the SMZ is characterized by foliation-parallel quartz ribbons which separate

regions dominated by plagioclase and biotite (Fig. 23a). Quartz ribbons are thick (up to 2 mm) and made up of elongate grains (up to 5 mm long). Quartz-quartz grain boundaries are lobate and preserve evidence of bulging recrystallization. Grains commonly display undulatory extinction. Plagioclase grains are coarse (up to 5 mm), nearly equant, have irregular grain boundaries, and are zoned (Fig. 23b). Biotite defines the foliation, which varies in orientation locally. K-feldspar porphyroclasts can be extensively recrystallized and display top-to-the-west kinematic indicators.

Within the SMZ, the quartzofeldspathic gneiss is overall finer-grained, although grain size varies throughout the shear zone. Two dominant microstructural gneiss types are observed in the SMZ: phase-separated gneiss and phase-mixed gneiss. Phase-separated gneiss, characterized by foliation-parallel quartz ribbons, is the dominant gneiss type in the SMZ (~75%). In the mylonitic gneiss, quartz ribbons are thin (no more than 1 mm). Quartz-quartz grain boundaries are dominantly normal to the ribbon boundaries. Grains preserve undulatory extinction and microstructures consistent with sub-grain rotation and bulging recrystallization (Fig. 23c). Plagioclase and biotite dominate the regions between quartz ribbons. Plagioclase grain boundaries are straight and commonly meet at triple junctions. Plagioclase is zoned. Biotite defines the foliation (Fig. 23d).

Phase-mixed gneiss (~25%) is characterized by homogeneously distributed quartz, plagioclase, and biotite (Fig. 23e). Quartz occurs as isolated grains or clusters of near-equant grains (< 15 grains) that are foliation-parallel. Plagioclase grain boundaries are irregular; plagioclase phase boundaries are determined by the shape of adjacent quartz grains (Fig. 23f).

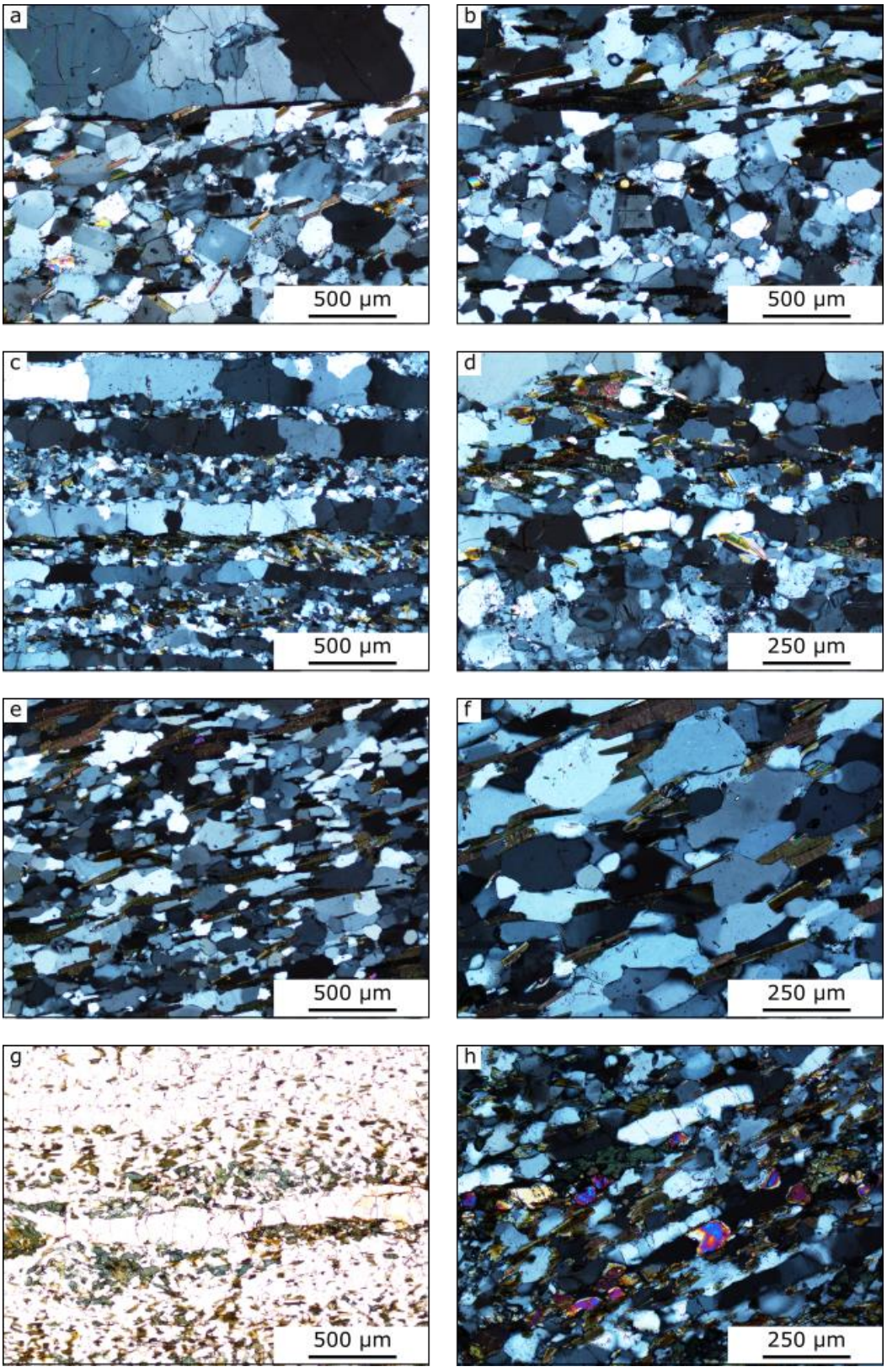
a
500 µm
b
500 µm
c
500 µm
d
250 µm
e
500 µm
f
250 µm
g
500 µm
h
250 µm

Figure 23. Photomicrographs (cross-polarized: a-f, h; plane-polarized: g) of quartzofeldspathic gneiss in and near the SMZ. Non-mylonitic, phase-separated gneiss: (a) Qz ribbon (top) adjacent to a Pl + Bt region. (b) Pl + Bt-rich region. Plagioclase twinning and zoning is visible. Irregular Pl grain shape is visible. Biotite defines the foliation. Mylonitic, phase-separated gneiss: (c) Foliation-parallel Qz ribbons, made up of high aspect ratio grains, separate regions dominated by Pl and Bt. (d) Pl grains are near equant, often meet at triple junctions, and are ubiquitously zoned. Mylonitic, phase-mixed gneiss: (e) Qz, Pl, and Bt are homogenously distributed. (f) Pl grains are inequant and display irregular grain boundaries. Pl zoning is visible. Bt defines the foliation. Mylonitic, mafic gneiss: (g) Foliation-parallel Qz ribbons separate regions dominated by Pl, Bt, and Hbl. (h) Mafic gneisses contain abundant epidote. Faint Pl zoning is visible.

Layers of mafic gneiss, hornblende and biotite-rich (up to 50 modal % mafic minerals) occur throughout the SMZ (Fig. 23g). The mafic gneiss also contains a significant amount of epidote (up to 10%) (Fig. 23h). Mafic gneiss layers are up to 10 cm thick and can occur as isolated layers in the quartzofeldspathic gneiss or as part of an interbedded sequence of mafic and felsic gneiss.

Metabasalts in the SMZ range in composition from amphibolite to UHP eclogite and in shape from cm-scale pods to m-scale layers. The most abundant metabasalt in the SMZ region are garnet amphibolites. Garnets are highly retrogressed with irregular, embayed grain boundaries, and are surrounded by plagioclase (Fig. 24a) or hornblende + ilmenite coronas (Fig. 24b). The remainder of the rock is composed primarily of plagioclase + hornblende + biotite; quartz is present in minor amounts. Grain sizes in garnet amphibolites are highly variable: garnets range in size from 3 mm to 1 cm in diameter and hornblende is up to 8 mm long.

The primary, well-preserved eclogite body in the SMZ is a foliated and lineated coesite-eclogite (Fig. 21d). The eclogite is composed of omphacite + garnet and preserves

foliation-parallel quartz + garnet veins (Fig. 24c). The eclogite is coarse-grained: omphacite is up to 1 cm long, and garnet is up to 8 mm in diameter. The vein garnets

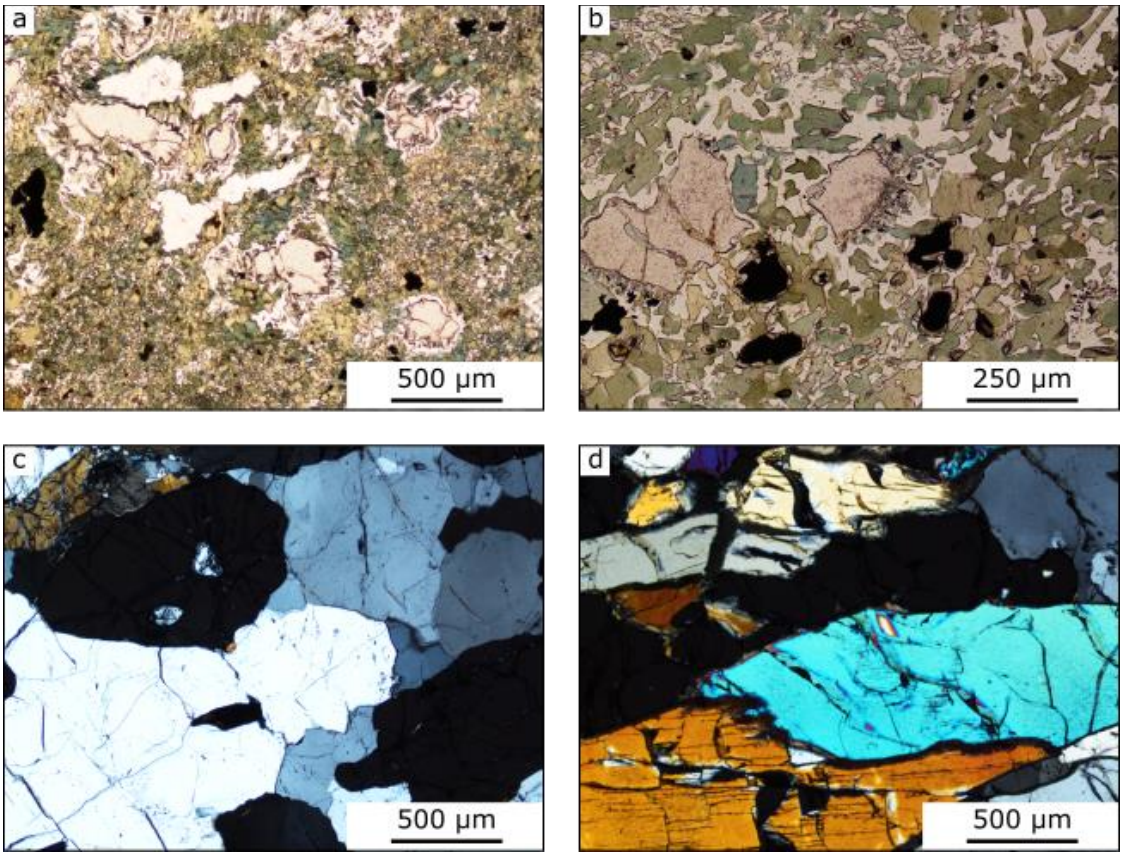

Figure 24. Photomicrographs (cross-polarized: a-b; plane-polarized: c-d) of metabasalts in the SMZ. Garnet amphibolite: (a) Hbl and Pl matrix with Qz clusters and retrogressed Grt. Garnets are embayed and surrounded by Pl coronas. (b) Garnet amphibolite retrogression textures, Grt with Hbl + Ilm coronas and Ilm with Ttn coronas in a Hbl + Pl matrix. Eclogite: (c) Qz + Grt vein in eclogite, pcq inclusions are preserved in Grt. (d) Cpx in eclogite. Cpx preserves an SPO. Cpx grain boundaries have been replaced with a symplectitic intergrowth of Hbl + Pl.

contain coesite (Carswell et al., 2003) and polycrystalline quartz inclusions (Wain et al., 1997; Renedo et al., 2015) (Fig. 24d). The edges of this well-preserved eclogite body are retrogressed wherein clinopyroxene is replaced by a symplectitic intergrowth of hornblende and plagioclase.

Most metabasaltic bodies in and near the SMZ have a distinct boundary with the surrounding host gneiss; however, one metabasaltic pod in the SMZ preserves a gradual contact with the surrounding gneiss and gives insight into the metamorphic evolution of the SMZ. A large (3 x 6 m) metabasaltic body preserves a transition from retrogressed eclogite at the core to mafic gneiss at the edges (Fig. 21e). The retrogressed eclogite preserves minor amounts of omphacite; however most of the omphacite has been replaced with a symplectitic intergrowth of hornblende + plagioclase. Polycrystalline quartz inclusions are also observed. A progressive transition to garnet amphibolite and to mafic gneiss is preserved outward from the retrogressed eclogite.

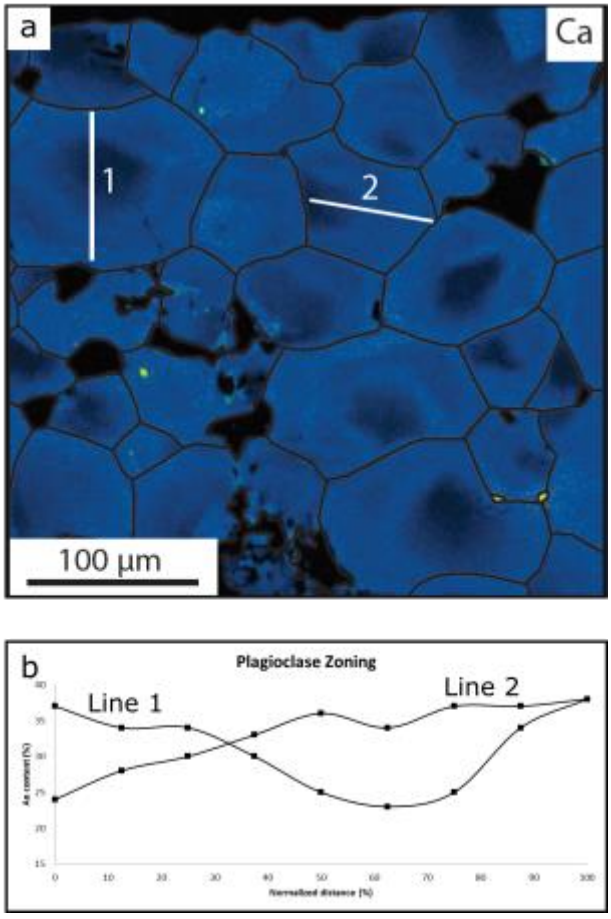

Figure 25. (a) Qualitative EBSD map of Pl with ubiquitous reverse zoning. (b) Quantitative Pl analyses across two grains (identified in a). Zoning can be concentric or asymmetric.

4.4.3. Mineral composition

Plagioclase in gneiss within and outside of the shear zone preserves reverse zoning: cores are more sodic than rims. Plagioclase from non-mylonitic gneiss outside of the SMZ preserves a rim composition near An32 and a core composition near An17; the maximum intragranular core to rim difference is An15. Plagioclase from mylonitic gneiss within the SMZ preserves a rim composition near An37 and a core composition near

An17; the maximum intragranular core to rim difference is An19. Zoning is not necessarily concentric or equidimensional (Fig. 25). See Chapter 3 for a detailed description of plagioclase zoning in and near the SMZ.

In mafic gneiss, plagioclase preserves less evidence of zoning. Rim compositions are near An32 and core compositions near An24; the maximum intragranular core to rim difference is An8 (Fig. 26, left). Rare garnets in the mafic gneiss layers (NW10-40G, 40J) are primarily almandine-grossular-spessartine solid solutions: Alm45-67Pyp3-7Sps1-17Grs21-37 (Fig. 26, right). The garnets preserve a range of compositions, however no systematic zoning is observed.

Amphibolites in the SMZ are dominantly composed of hornblende and plagioclase that replaced clinopyroxene during eclogite retrogression. The composition of plagioclase in amphibolites is highly variable, ranging from An19 to An89 (Fig. 26, left). Individual samples preserve plagioclase that varies up to An30. No systematic variation in plagioclase composition was observed. Garnets in amphibolite are primarily almandine-pyrope-grossular solid solutions: Alm42-56Pyp18-28Sps1-2Grs23-33 (Fig. 26, right).

Eclogites in the SMZ region preserve an original assemblage of omphacite and garnet with variable levels of retrogression. Garnet composition in eclogite is primarily an almandine-pyrope-grossular solid solution: Alm35-47Pyp24-54Sps1Grs10-31 (Fig. 26, right). Clinopyroxene is not zoned and is dominantly a diopside-hedenbergite-jadeite solid solution (Fig. 26, bottom): sodium content varies among eclogite bodies (Fig. 21e).

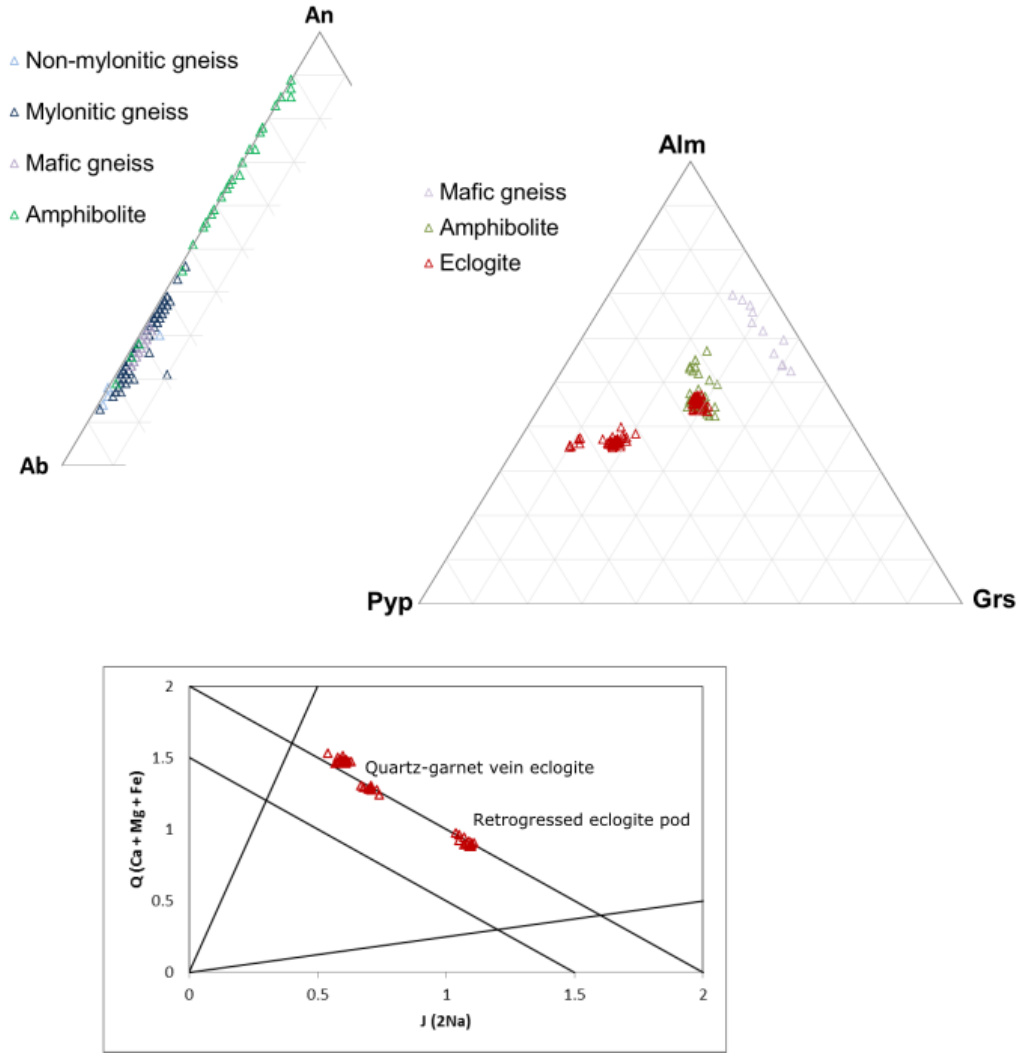

Figure 26. EMPA results in the SMZ. Left: Ternary Pl diagram with compositions plotted by rock type. Right: Grt ternary diagram with compositions plotted by rock type. Bottom: Cpx quad diagram.

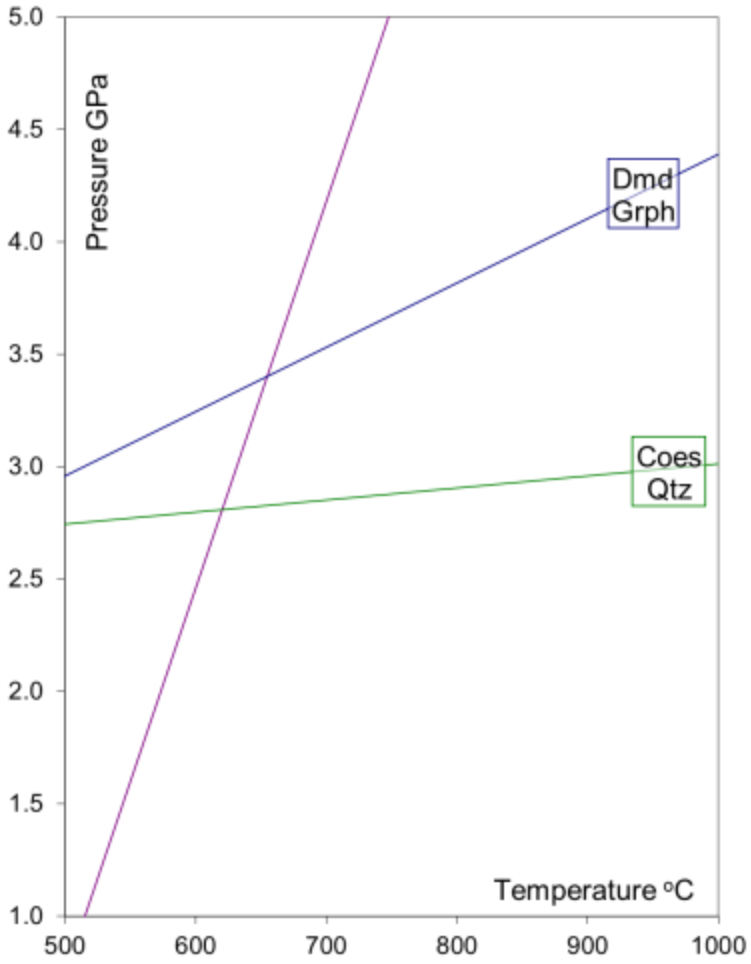

Figure 27. Grt-Cpx thermobarometry results for the SMZ. One Grt-Cpx pair is plotted in P-T space. Coe-Qz and Gr-Dia transition are indicated. The range of likely equilibration pressure is indicated (gray box).

4.4.4. Thermobarometry

Garnet-clinopyroxene thermobarometry was conducted on one grain pair from the coesite-eclogite. Pressure of eclogite deformation ranges from 2 GPa, inferred from quartz fabrics in quartz veins in eclogite (Renedo et al., 2015), to 2.8 GPa, inferred from polycrystalline quartz inclusions after coesite in garnet. Using this range of pressures (2.0 – 2.8 GPa), the resulting temperature estimate of garnet-clinopyroxene equilibration is 600 - 650º C (Fig. 27).

4.5. Finnøya Mylonite Zone (FMZ)

4.5.1. Field description

The FMZ is located in the northernmost UHP domain (Figs. 21 and 28). This mylonite zone is exposed on the southwestern end of the island of Finnøya and spans approximately 30 m across strike. Regional gneiss on the island is coarse and lithologically variable; it includes garnet-biotite schist, quartzofeldspathic gneiss ± garnet, and amphibolite.

The gneiss of the FMZ is lithologically variable which is consistent with the heterogeneity of the region. Hornblende-gneiss, pyroxene-gneiss, and migmatitic orthogneiss are all present and mylonitized. The rocks of the FMZ preserve a consistent WSW-striking foliation with a moderate to steep dip to the north and lineation with a moderate plunge to the NW or NE (Fig. 28). Porphyroclasts throughout the shear zone gneiss suggest top-to-the-west deformation (Fig. 29a).

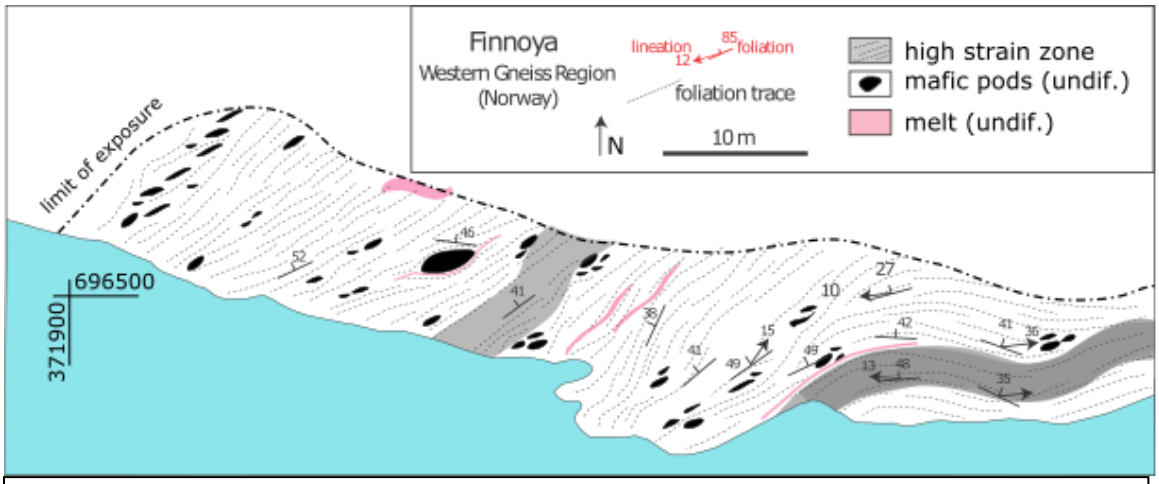

Figure 28. FMZ map. High strain shear zones, mafic pods, and melt are located. Strike and dip shown throughout exposure. Approximate UTM location indicated.

Contained within the gneiss of the FMZ are metabasaltic pods, leucosomes, and pegmatite dikes. Metabasaltic pods range in size from 10 cm to >1 m thick and in composition from amphibolite to retrogressed eclogite. Amphibolite pods, the most common metabasalt in the FMZ, occur in swarms, are commonly deformed, and suggest top-to-the-west deformation (Fig. 29c). One large retrogressed eclogite body is present in the FMZ (Fig. 29d); it is compositionally layered; the strike and dip of the layering is consistent with that of the surrounding gneiss. Multiple generations and types of melt are present in the FMZ. Layer-parallel (stromatic) leucosomes are observed throughout the mylonite zone and have been deformed along with the mylonitic gneiss (Fig. 29e). Leucosomes are also present on the margins of metabasaltic material, and less commonly in between boudins (Fig. 29c). One large, scapolite-bearing pegmatite dike crosscuts the mylonitic foliation (Fig. 29f).

4.5.2. Petrography

One suite of samples from the FMZ was selected for detailed study. The samples are from a traverse (~10 m) across the strongly mylonitized clinopyroxene-gneiss (Fig. 29b). The garnet-clinopyroxene gneiss in the FMZ has the assemblage quartz + plagioclase + K-feldspar + garnet + hornblende + biotite + clinopyroxene with accessory zircon, allanite, apatite, ilmenite, titanite and scapolite. Plagioclase is the most abundant phase, grains are fine (up to 0.5 mm), inequant, and have lobate grain and phase boundaries. Occasional triple junction boundaries are observed. Plagioclase twinning is common (Figs. 30a, b). Quartz is homogeneously distributed throughout the gneiss.

Quartz is smaller than plagioclase (up to 0.3 mm). Grain boundaries are lobate and undulatory extinction is observed but not ubiquitous (Fig. 30b). Garnets in the gneiss are coarse (up to 4 mm), but significantly retrogressed with heavily embayed edges and abundant fractures (Figs. 30c, d). Clinopyroxene is coarse (up to 4 mm) and commonly associated with hornblende that is progressively replacing clinopyroxene (Figs. 30e, f). K-feldspar porphyroclasts are partially recrystallized, myrmekite is commonly observed adjacent to recrystallizing K-feldspar porphyroclasts (Fig. 30g).

Layer-parallel leucosomes of varying thickness (mm- to cm-scale) are interlayered in the garnet-clinopyroxene gneiss (Fig. 30h). The leucosomes preserve the composition quartz + K-feldspar ± plagioclase ± garnet ± biotite with accessory zircon, allanite, apatite, and scapolite. Grain sizes are coarser than in the mylonite (up to 0.75 mm). The mylonitic gneiss and the leucosomes preserve similar microstructures; this is consistent with field observations that suggest that the leucosomes and mylonitic gneiss were deformed together.

Retrogressed eclogite pods are preserved throughout the clinopyroxene-gneiss suite and the FMZ. The original clinopyroxene + garnet assemblage has been retrogressed to clinopyroxene + hornblende + plagioclase + garnet. Accessory minerals include zircon, apatite, and allanite. The minerals are coarse grained (up to 6 mm). Garnets are inequant, heavily embayed, and are commonly surrounded by plagioclase coronas (Fig. 31a). Pyroxene is well-preserved, though evidence of replacement by hornblende is observed (Fig. 31b).

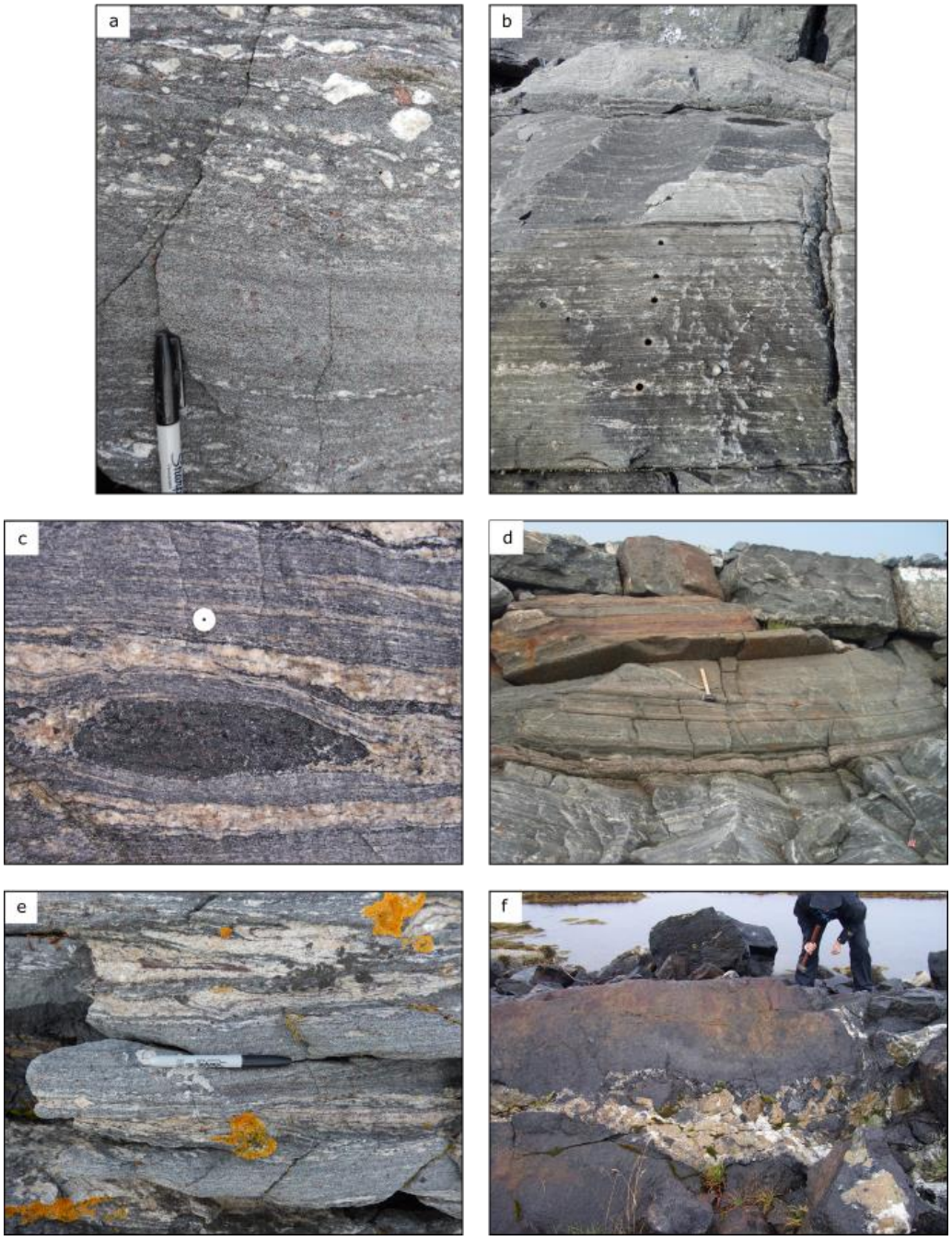

Figure 29. Photos of the FMZ. (a) Augen-rich and augen poor gneiss are both present throughout the FMZ. (b) Image of the Cpx-gneiss that is studied in detail. Drill cores from sampling are visible. (c) Amphibolite pod with tails of melt and layer-parallel migmatites visible above and below. (d) Layered mafic pod, a thick (10 cm) layer of melt is on the margin. (e) Mylonitic, augen-free gneiss with abundant deformed layer-parallel leucosomes. (f) Foliation-perpendicular view of the mylonitic gneiss which shows a large scapolite pegmatite dike cross-cutting foliation.

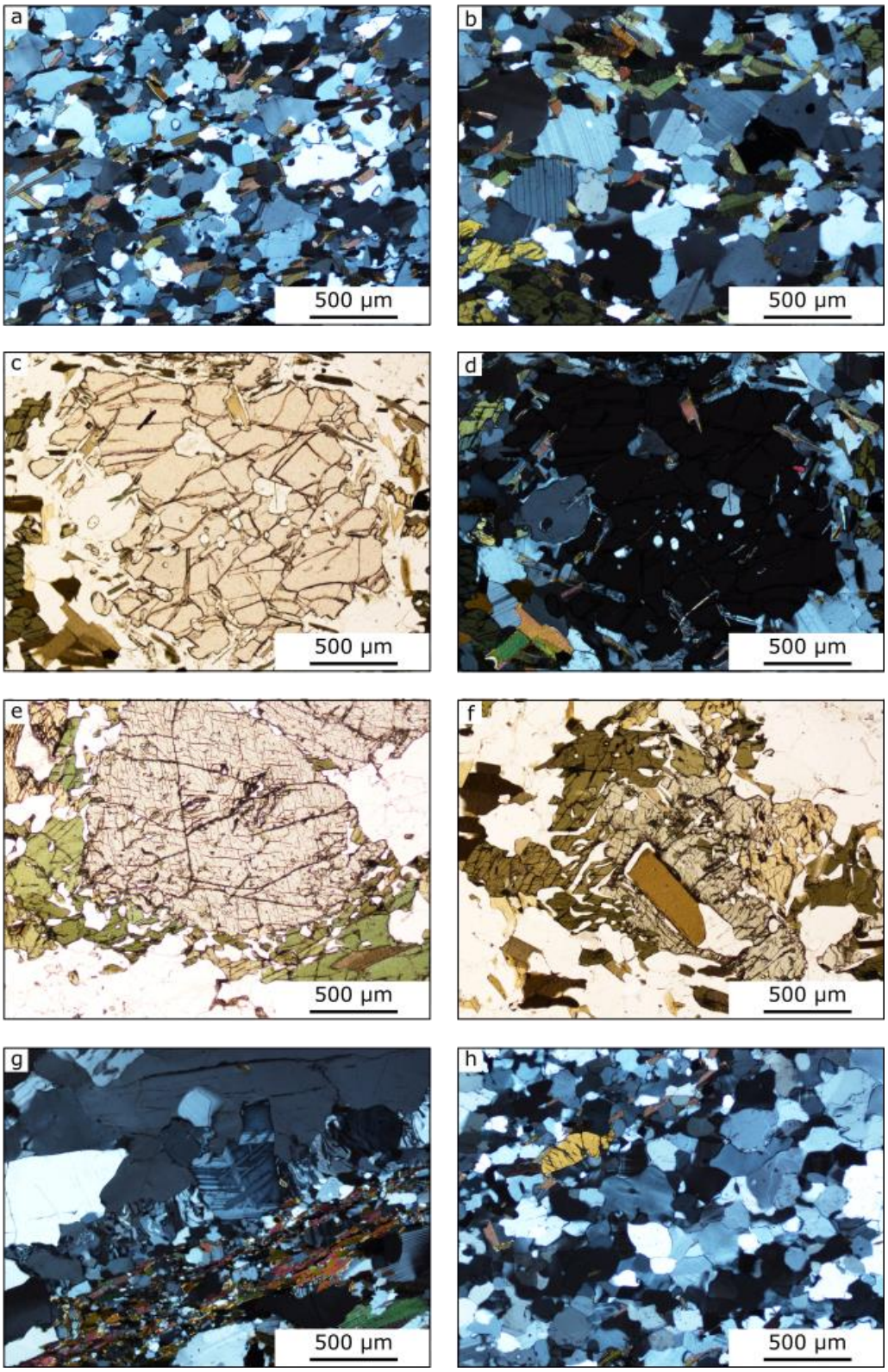
a
500 µm
b
500 µm
c
500 µm
d
500 µm
e
500 µm
f
500 µm
g
500 µm
h
500 µm

Figure 30. Photomicrographs (cross-polarized: a-b, d, g-h; plane-polarized:c, e-f) of Cpx-gneiss in the FMZ. (a) Mylonite. Pl, Qz, Bt, and Hbl are distributed homogeneously throughout the gneiss. Pl twinning is visible. (b) Mylonite. A coarser mylonite sample, irregular Pl and Qz boundaries are visible. As are coarser Hbl and Bt throughout. (c) Grt in gneiss. Grt preserves heavily embayed edges is surrounded by a corona. (d) In cross-polarized light the twinning of Pl grains is seen in the corona. (e) Cpx in gneiss, Hbl is present on the edges of the Cpx. (f) Cpx actively being replaced by Hbl and closely associated with Bt. (g) Tail of a K-feldspar porphyroclasts with well-developed myrmekite. (h) Cpx-gneiss (top) and foliation-parallel leucosomes (bottom). The leucosomes are distinguished from the gneiss by a lack of Bt and Hbl and a larger grain size.

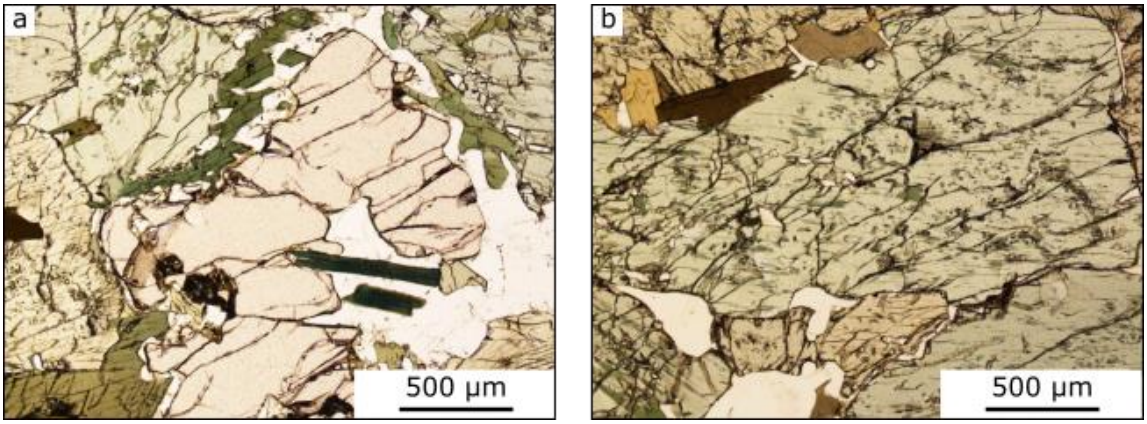

Figure 31. Eclogite photomicrographs (plane-polarized light). (a) Grt + Cpx, Grt is extensively retrogressed and surrounded by a plagioclase corona and Hbl is visible on Cpx grain boundaries. (b) Cpx in eclogite, Hbl is visible in Cpx.

4.5.3. Mineral composition

Plagioclase in the mylonitic clinopyroxene-gneiss preserves a composition of An60-76Ab23-39Or1-2. There is no systematic variation in plagioclase composition by habit (Fig. 32, left). Garnet in the gneiss has a variable composition but shows no systematic zoning. Garnet is primarily an almandine-pyrope-grossular solid solution: Alm47-60Pyp8-17Sps4-7Grs24-39 (Fig. 32, right). Clinopyroxene in the gneiss is not zoned and is a diopside-hedenbergite solid solution with a minor jadeite component (Fig. 32, bottom).

Retrogressed eclogite in the FMZ preserves plagioclase that is slightly more albitic than the plagioclase in the mylonitic gneiss: An56-73An26-43Or1-2 (Fig. 32, left). Garnet in retrogressed eclogite is unzoned and is primarily an almandine-pyrope-grossular solid solution: Alm47-49Pyp18-19Sps4-5Grs28-30 (Fig. 32, right). Clinopyroxene in the retrogressed eclogite is not zoned and is a diopside hedenbergite solid solution with a minor jadeite component (Fig. 32, bottom).

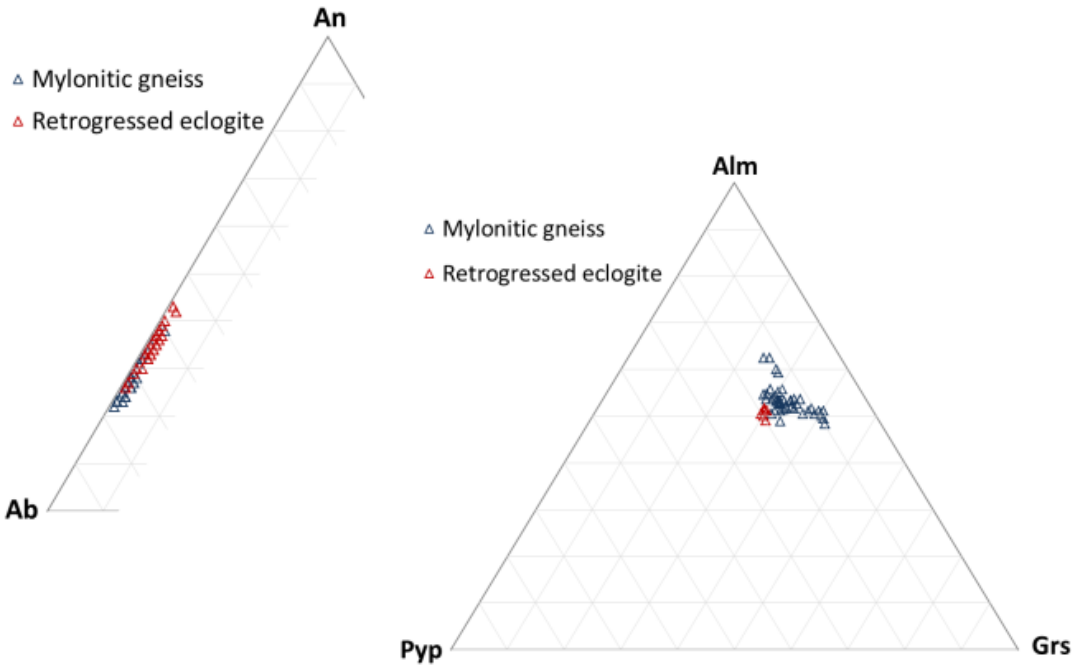

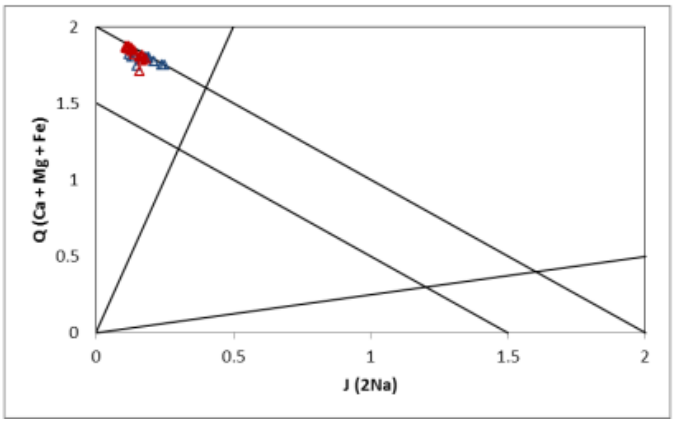

Figure 32. EMPA results for rock types in the FMZ. Left: Ternary Pl diagram with compositions plotted by rock type. Right: Grt ternary diagram with compositions plotted by rock type. Bottom: Cpx quad diagram.

4.5.4. Thermobarometry

Garnet-clinopyroxene thermobarometry was conducted on one grain pair from retrogressed eclogite in the FMZ (Table 8). Coesite on the nearby island of Harøya (Butler et al., 2012) suggests that UHP conditions were reached locally. Using this pressure (2.8 GPa), crystallization temperature of the retrogressed eclogite is estimated at 850 º C. If a lower pressure is assumed (P = 2.0 GPa), the resulting temperature is near 800 ºC (Fig. 33).

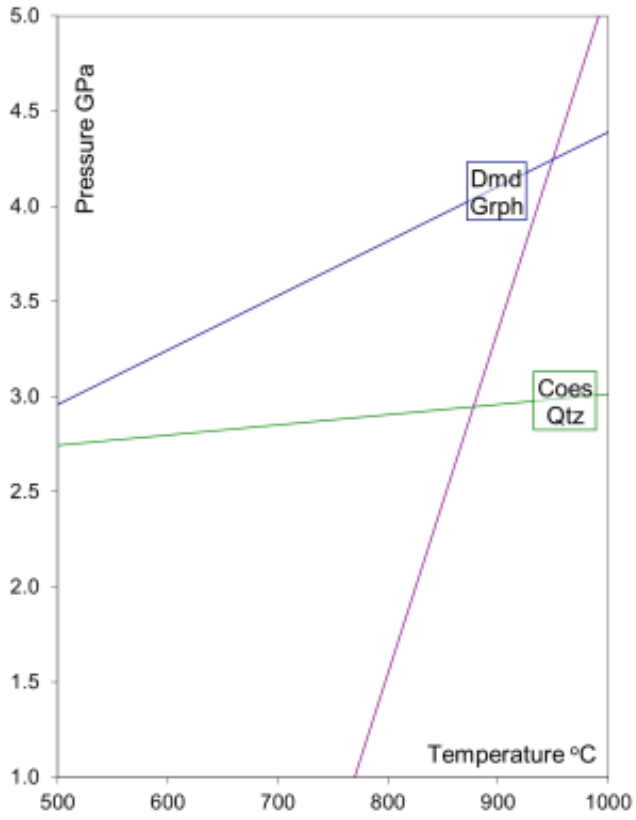

Figure 33. Grt-Cpx thermobarometry results for the SMZ. Two Grt-Cpx pairs are plotted in P-T space. Coe-Qz and Gr-Dia transition are indicated. The range of likely equilibration pressure is indicated (gray box).

4.6. Svartberget Mylonite Zone

4.6.1. Field description

The Svartberget mylonite zone (SvMZ) is located in the northernmost UHP domain (Figs. 20 and 34). The region is characterized by tonalitic to dioritic biotite gneiss ± sillimanite ± garnet that is interlayered with amphibolite (Vrijmoed et al., 2000, 2006); the SvMZ is hosted in the biotite-gneiss ± sillimanite ± garnet. The southern end of the SvMZ is at the contact of a large Fe-Ti type peridotite body with garnet websterite veins that has been the focus of prior study (Vrijmoed et al., 2006) (Fig. 35a).

Within the SvMZ are four discrete, anastomosing mylonite zones which are characterized by vertical foliation and a horizontal to sub-horizontal, E-plunging lineation (Figs. 34, 35 b, c, and d). Metabasaltic pods and layers occur throughout the shear zone. They range in size from 25 cm long to > 3 m (Figs. 35e, f) and in composition from eclogite to amphibolite. Pods within the discrete shear zones are more elongate (long axis foliation-parallel) than those found outside of the discrete mylonite zones.

The Svartberget region is melt rich, the inferred melt percent reachess > 25% locally. Melt commonly occurs as foliation-parallel leucosomes (Fig. 35g), but also occurs on the margins of mafic pods, within mafic pods (Fig. 35f), and as cross-cutting pegmatites.

4.6.2. Petrography

Gneiss within and directly adjacent to the SvMZ is compositionally similar. It preserves the assemblage quartz + plagioclase+ K-feldspar + biotite ± sillimanite ± garnet ± white mica. Accessory minerals include zircon, epidote, allanite, apatite, ilmenite, and rutile. It is common for garnet-bearing gneiss to be sillimanite-poor or sillimanite-absent and for garnet-absent gneiss to be sillimanite-rich. Though the assemblage is similar, important microstructural variations are observed between the non-mylonitic and mylonitic gneiss of the SvMZ. The non-mylonitic gneiss is coarse-grained. Quartz, plagioclase, and garnets are large (up to 5 mm), inequant, and commonly preserve evidence of internal deformation (undulatory extinction and twinning) (Figs. 36a, b). Quartz and plagioclase grain boundaries are lobate and display evidence of bulging recrystallization (Fig. 36b); phase boundaries are irregular.

The mylonitic gneiss has a variable grain size, but is overall finer-grained than the non-mylonitic gneiss. Sillimanite is abundant; it occurs dominantly as elongate, foliation-parallel, fibrolitic clusters which create an anastomosing network throughout the gneiss (Figs. 36c, d). Quartz, plagioclase, and biotite grain sizes are significantly smaller adjacent to, and within, the sillimanite clusters (Fig. 36f). Sillimanite can also occur as needles that are included in quartz grains in the gneiss. Within the quartz grain the sillimanite is randomly oriented (Fig. 36e). Quartz can be up to 4 mm, but is commonly < 500 μm. Quartz grains commonly preserve evidence of internal deformation including subgrains, deformation bands, and undulatory extinction. Clusters of quartz grains and discontinuous quartz ribbons are common (Fig. 36e). Plagioclase ranges in grain size, but is commonly < 500 μm. Twinning is common. Grain boundaries are irregular and

controlled by adjacent phases (Figs. 36g, h). Garnets in gneiss are extensively retrogressed. They are subhedral with embayed edges and range in size from 1 to 5 mm. Biotite is abundant in the gneiss of the SvMZ, and grains can be up to 7 mm long. Biotite, along with sillimanite, defines the foliation.

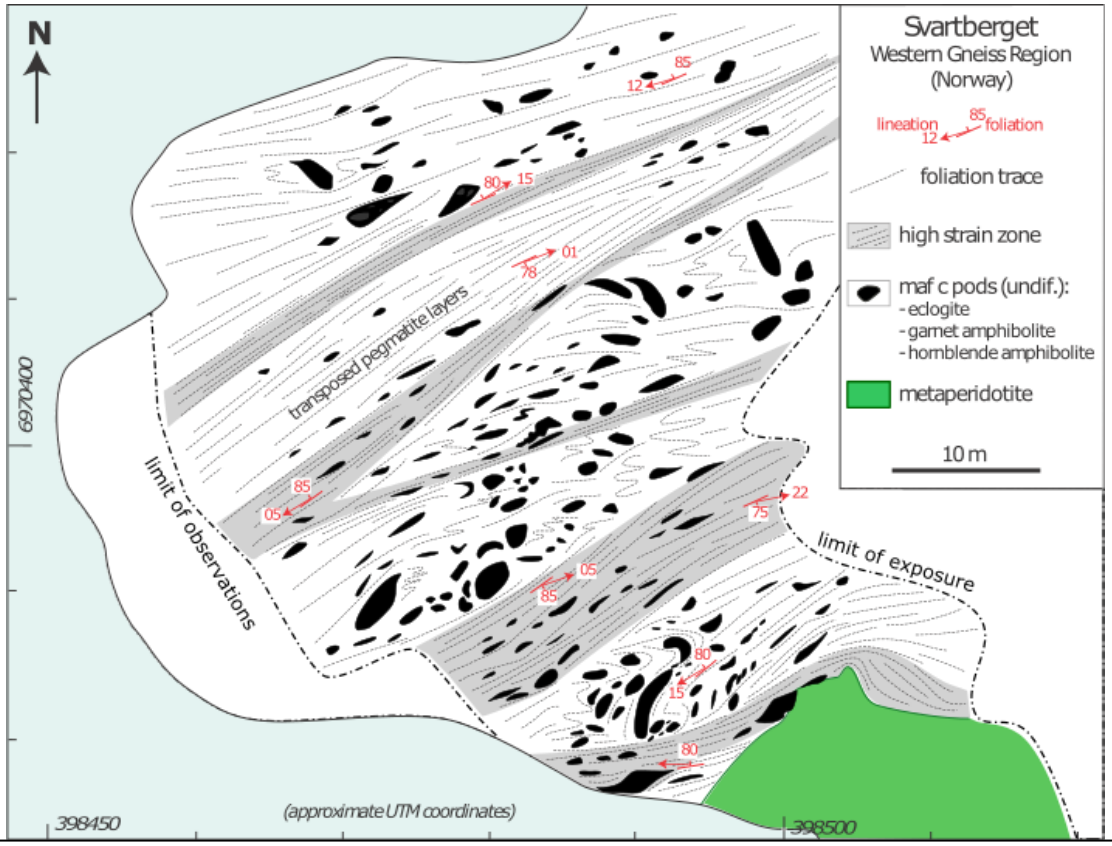

Figure 34. Map of the SvMZ with anastomosing high strain zones (highlighted in gray), mafic pods (black) and peridotite body (green). Strike and dip of gneiss shown throughout.

Metabasaltic material in the SvMZ ranges from amphibolite to eclogite. Amphibolite ± garnet is the most abundant metabasalt in the SvMZ. Garnets are retrogressed with irregular, embayed grain boundaries and are surrounded by plagioclase coronas. The remainder of the amphibolite is composed of a coarse hornblende + plagioclase symplectite. Eclogite is preserved at the core of larger metabasaltic pods in

the SvMZ. Eclogite is coarse-grained (up to 8 mm). Garnets are retrogressed and irregularly shaped. Clinopyroxene is present but shows evidence of replacement by hornblende.

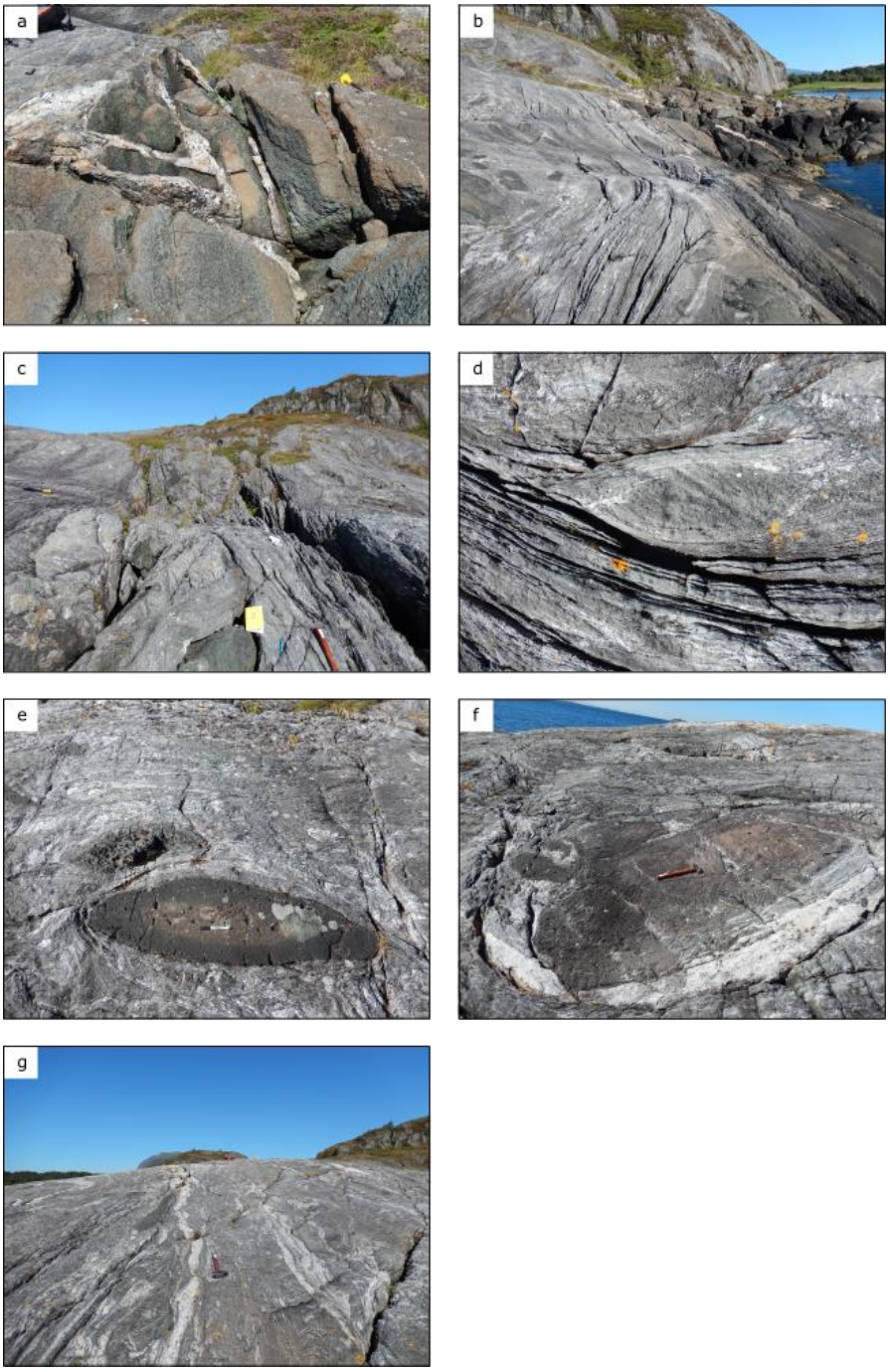

Figure 35. Field photos of the SvMZ. (a) Metaperidotite with cross-cutting websterite veins .(b) Highly strained gneiss (foreground) is adjacent to metaperidotite (background). (c) Anastomosing shear zones erode preferentially, mafic pod visible in foreground. (d) Contact between mylonitic gneiss in an anastomosing shear zone and surrounding gneiss. (e)Retrogressed mafic pod: eclogite core, amphibolite rims. Gneiss foliation deflects around the pod. (f) Large mafic pod with abundant melt on the edges and cross-cutting the pod. (g) Melt rich region of the SvMZ, melt is deformed with the gneiss.

4.6.3. Mineral composition

Plagioclase in gneiss in the SvMZ preserves a consistent composition: Ab63-69An30-36Or1-2 (Fig. 37, left). Larger grains show evidence of minor reverse zoning with a maximum intragranular core to rim difference of An5. Garnets in the gneiss preserve a range of compositions: Alm51-55Pyp11-17Sps23-34Grs4-6. No evidence of zoning is preserved.

In eclogite, there are two distinct plagioclase compositions which correspond to two distinct habits (Fig. 37, right). Plagioclase that forms a corona around garnet is relatively An-poor: Ab48-63An51-36Or1. Plagioclase in the symplectite, which replaces clinopyroxene with hornblende, is relatively An-rich: Ab76-85An14-23Or1-2. Garnets in the eclogite have a consistent composition of Alm52-55Pyp22-24Grs1-2Sps22-24. No evidence of zoning is preserved (Fig. 37, right). Clinopyroxene in the retrogressed eclogite is not zoned and preserves a similar composition to that of clinopyroxene in the gneiss – dominantly a diopside-hedenbergite solid solution with a minor jadeite component (Fig. 37, bottom).

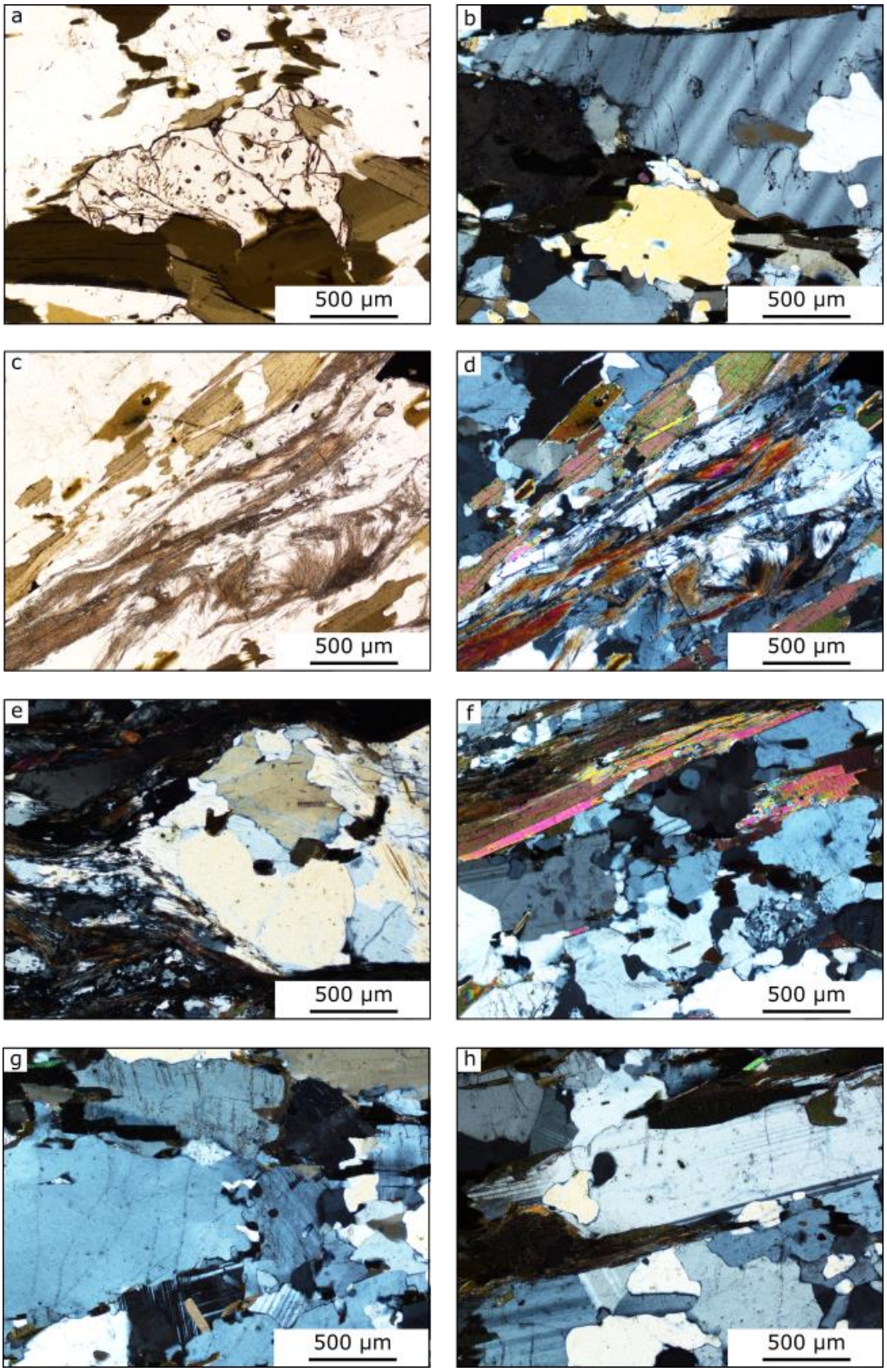
a
500 µm
b
500 µm
c
500 µm
d
500 µm
e
500 µm
f
500 µm
g
500 µm
h
500 µm

Figure 36. Photomicrographs (cross-polarized: b, d-h; plane-polarized: a, c) of SvMZ gneiss (a) Grt in non-mylonitic gneiss with embayed edges, subhedral shape. (b) Non-mylonitic gneiss with coarse grains, Qz displays deformation bands. Lobate Pl and Qz grain boundaries visible. (c) Sil bundles in gneiss. Sil occurs as both foliation parallel and randomly oriented inclusions in Qz. (d) Cross-polarized light image of (c). Grains in between foliation-parallel Sil are fine-grained and elongate. (e) Qz cluster with randomly oriented Sil inclusions. Subgrains and undulatory extinction visible. (f) Gneiss Pl has irregular grain boundaries. Foliation parallel Wm and Sil are visible. (g) Pl-rich region, small grains nucleating on Pl grain boundaries. Lobate boundaries are ubiquitous. (h)Elongate, twinned Pl grain adjacent to Sil clusters. Qz and Pl grains are homogeneously distributed in gneiss.

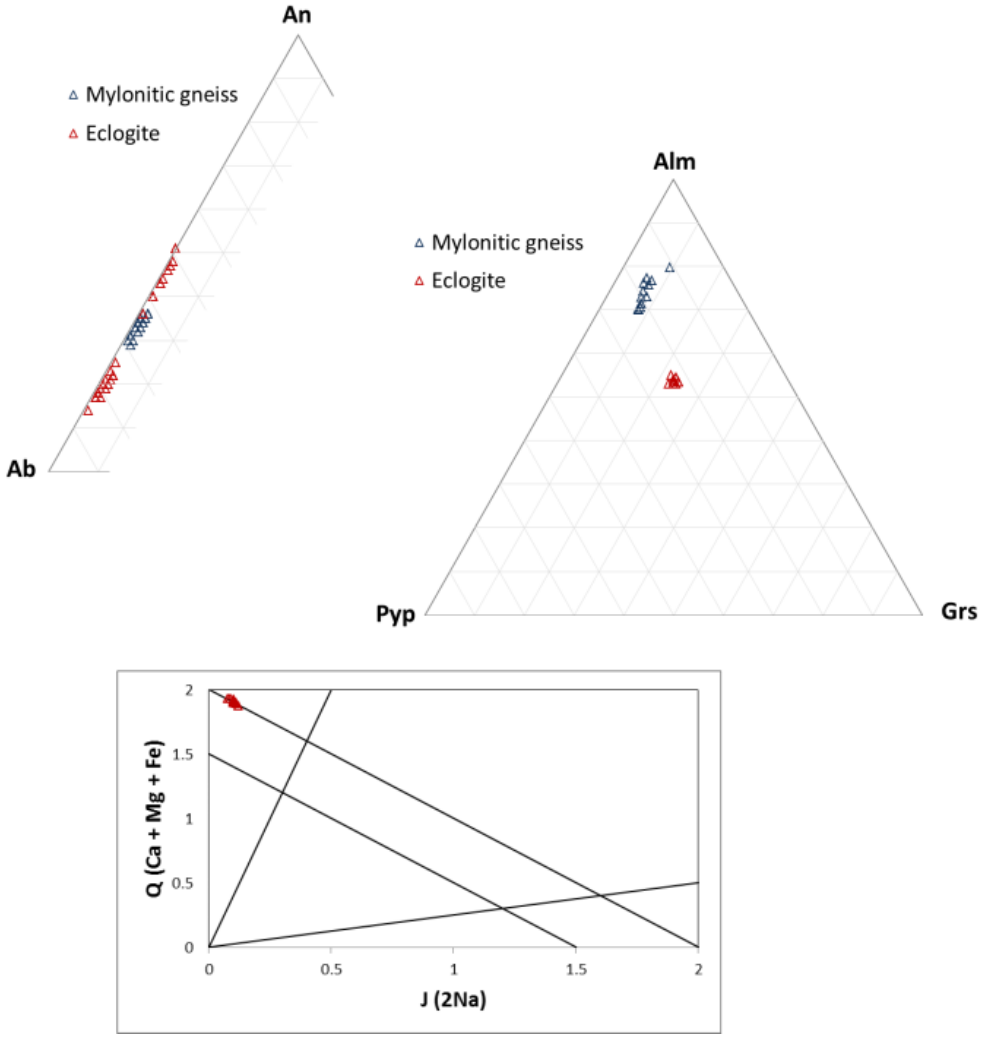

Figure 37. EMPA results for rock types in the SvMZ. Left: Ternary Pl diagram with compositions plotted by rock type. Right: Grt ternary diagram with compositions plotted by rock type. Bottom: Cpx quad diagram.

4.6.4. Thermobarometry

Garnet-clinopyroxene thermobarometry was conducted on a retrogressed eclogite sample from the SvMZ. Clinopyroxene is present only as relicts within the hornblende that replaced it. The garnet and clinopyroxene pair used in the analysis are closely associated, but are not in contact. This pressure-temperature estimate, therefore, assumes that the pyroxene composition has not changed during retrogression, an assumption that may or may not be valid. The resulting temperature estimate is the highest of the three; thermobarometry suggests temperatures > 900 º C at a pressure of 2.0 GPa (Fig. 38).

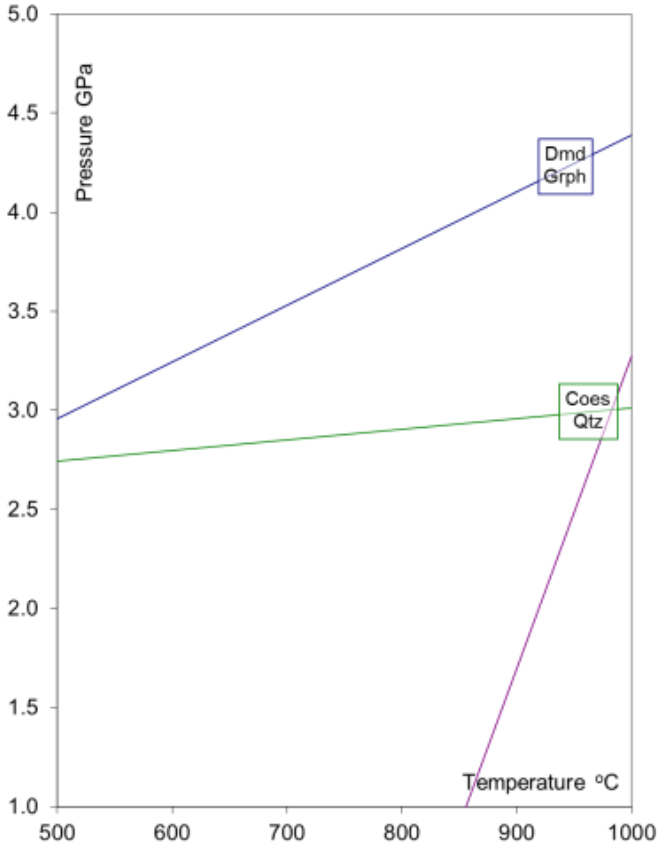

Figure 38. Grt-Cpx thermobarometry results for the SMZ. One Grt-Cpx "pair" is plotted in P-T space. Coe-Qz and Gr-Dia transition are indicated.

4.7. Discussion

Timing of the Caledonian UHP metamorphism and the preceding HP metamorphism has been well defined through the dating of HP and UHP eclogites in the three UHP domains of the WGR. Some evidence of the subsequent exhumation is preserved in mafic rocks; however, much of the exhumation record is preserved in the gneisses which retrogressed more readily during decompression. In this way, careful consideration of the gneiss and associated mafic material in shear zones in the WGR can provide new information to our understanding of exhumation of this UHP terrane.

4.7.1. The Salt Mylonite Zone

The SMZ is located in the best-studied region of the WGR, the southern UHP domain. The careful study of abundant eclogites in the southern UHP domain has resulted in a well-defined UHP boundary with a continuous P-T gradient from the UHP domain into the HP domain (Wain, 1997; Wain et al., 2000; Cuthbert et al., 2000). This suggests that there is no tectonic boundary juxtaposing the HP and UHP material; instead the gradient supports the interpretation that the WGR was exhumed as a largely coherent body. Timing of the Caledonian UHP metamorphism and the preceding HP metamorphism in the southern domain has been constrained through the dating of HP and UHP eclogites. HP metamorphism prior to the Caledonian UHP event occurred ~420 Ma (Kylander-Clark et al., 2007) and was followed by UHP metamorphism from ~410 to ~400 Ma (e.g. Carswell et al., 2003; 2003b; Root et al., 2004; Young et al., 2007). The subsequent exhumation from UHP to HP conditions is recorded in gneiss and local melt

and suggests exhumation to amphibolite facies by 390 Ma (Kylander-Clark et al., 2008; Gordon et al., 2013).

The SMZ provides an opportunity to observe the exhumation path from peak P-T conditions, in the form of coesite eclogite, through amphibolite facies, in mylonitized gneiss, and the relationship between the two in one location. The primary eclogite body in the SMZ is an exceptional example of UHP eclogite. This eclogite preserves unequivocal evidence for UHP metamorphism in the form of coesite inclusions (Carswell et al., 2003) and polycrystalline quartz inclusions (Wain et al., 2000; Renedo et al, 2015). This eclogite body has been dated at ~408 Ma (Carswell et al., 2003). The foliation and lineation of elongate omphacite is consistent with the surrounding gneiss, and omphacite fabrics are constrictional (Renedo et al., 2015). Thermobarometry of the eclogite suggests equilibration at P >2.8 GPa and T from 650-700 ºC. These results are consistent with P-T estimates of local eclogite bodies (Carswell et al., 2003; Wain et al., 2000).

Amphibolite (± garnet) is also present throughout the SMZ. Amphibolite is uncommonly explicitly associated with eclogite, however textural and compositional evidence of amphibolite as the product of retrogression is observed in the SMZ. At the northern end of the SMZ a rare opportunity exists to observe the petrologic transition from UHP eclogite to amphibolite, to mafic gneiss. Direct observation of this *in situ* transition confirms that mafic material is progressively retrogressed from eclogite to lower pressure assemblages during exhumation. Additionally, amphibole is commonly observed overprinting clinopyroxene and there exists considerable overlap between garnet compositions in amphibolite and some eclogite bodies (Fig. 26, right).

The eclogite and amphibolite are contained within mylonitized quartzofeldspathic gneiss that makes up the SMZ. The gneiss is relatively lithologically homogeneous and preserves a uniform amphibolite-facies assemblage. Despite the lower-pressure assemblage there is structural and petrologic evidence that the gneiss experienced UHP conditions with the eclogite and subsequently retrogressed to amphibolite facies conditions. Structurally, the foliation and lineation of gneiss and eclogite are consistent and the gneiss foliation deflects around the edges of mafic pods. Petrologically, the rare occurrence of extensively retrogressed garnets in the gneiss suggests a previous higher-pressure assemblage. Additionally, titanium concentrations in quartz in the gneiss range from concentrations of quartz in eclogite to significantly higher (consistent with lower P) (Renedo et al., 2015) which suggests that the gneiss experienced similar conditions to the UHP eclogite.

4.7.2. The Finnøya Mylonite Zone

The FMZ is located at the northern end of the Nordøyane, a well-studied chain of islands that make up the westernmost extent of the northern UHP domain. The islands are lithologically heterogeneous. The dominant rock type in the area is migmatitic granitoid gneiss, the gneiss is highly variable and can include garnet porphyroclasts, K-feldspar augen, and amphibole porphyroclasts. Minor amounts of mafic material, including metamorphosed gabbro, are also found throughout the area. This lithologically complex region has been mapped as the contact between the WGR and the nappes that overly the WGR (e.g. Terry et al., 2000a).

UHP metamorphism on the islands is evidenced by microdiamond in gneiss (Dobrzhinetskaya et al., 1993; Dobrzhinetskaya et al., 1995), and coesite in eclogite (Butler et al., 2013). The microdiamond-bearing gneiss suggests peak P-T conditions in excess of 3.5 GPa and 700 ºC (Dobrzhinetskaya et al., 1995). The coesite-eclogite, contained in migmatitic orthogneiss, records peak P-T conditions of ~3 GPa and 760 ºC (Butler et al., 2013) and an UHP eclogite from Fjortøft records peak P-T conditions ~3.4-3.9 GPa and 820 ºC (Terry et al., 2000b). The timing of UHP metamorphism in the Nordøyane, from monazite ages, is between 415 to 408 Ma (Terry et al., 2000b). Despite the gneiss rarely preserving evidence of UHP metamorphism in the Nordøyane, there is structural evidence that the gneiss experienced eclogite-facies metamorphism: gneiss is intimately interlayered with eclogite (Terry et al., 2004; Butler et al., 2013). The geometry of folds in eclogite-facies gneiss suggests that they were formed in a constrictional strain field (Terry et al., 2004).

Petrologic evidence of the exhumation path in the Nordøyane is preserved in the heavily retrogressed mafic material, the gneiss, and the melt. The coesite-bearing eclogite (Butler et al., 2013) also preserves a post-UHP amphibolite facies retrogression. Amphibolite replaces pyroxene and garnets are retrogressed; conditions of the retrogression are ~1 GPa and 813 ºC (Butler et al., 2013). Gneiss records evidence of the exhumation structurally in amphibolite-facies shear zones in gneiss; the orientations of shear zones range from sub-horizontal in the earlier stages to near vertical in later stages. This progression of orientations is consistent with transtensional exhumation at

amphibolite-facies conditions (Terry et al., 2003). Monazite ages throughout the Nordøyane suggest that HP conditions were reached by 395 Ma (Terry et al., 2000b).

The FMZ is a complex shear zone in the gneiss of the WGR where interactions between eclogite, lithologically-variable gneiss, and multiple generations of melt can be observed in one place. The most mylonitized gneiss in the FMZ is the pyroxene gneiss; it preserves the same assemblage as the retrogressed eclogite with differing modal abundances. Both rock types show evidence of extensive retrogression whereby pyroxene is replaced by amphibole and garnets are embayed and surrounded by plagioclase coronas. Thermobarometry of a retrogressed eclogite sample suggests crystallization T > 800 ºC, which is consistent with existing P-T estimates in the region (e.g. Terry et al., 2000; Holmberg, 2015). The clinopyroxene and garnet compositions in the mylonitic gneiss and the retrogressed eclogite are similar (Fig. 32). This compositional similarity suggests, importantly, that the mylonitic, pyroxene gneiss may have been derived from the eclogite.

The multiple generations of melt in the FMZ provide important time constraints on the evolution of the FMZ. Early melt in the FMZ is in the form of layer-parallel leucosomes. These layer-parallel leucosomes preserve evidence of deformation in the field (Fig. 29e) and in thin section (Fig. 30h). The zircons have a weighted mean average age of 401 Ma and crystallized during plagioclase-absent conditions (Gordon et al., 2013). Later generations of melt are found in boudin necks (Fig. 29c) and a pegmatite dike that crosscuts the foliation (Fig. 29f). Zircons from these melts have weighted mean average ages of 393 Ma and 396 Ma, respectively. Zircon rims grew over changing

conditions from plagioclase absent to plagioclase present (Gordon et al., 2013). These results suggest that melt was present in the FMZ at UHP conditions and melt crystallization continued during decompression of the FMZ.

4.7.3. The Svartberget Mylonite Zone

The SvMZ is located in the northern UHP domain directly adjacent to the well-documented, diamond-bearing Svartberget metaperidotite (Vrijmoed et al., 2006; Vrijmoed et al., 2008). The metaperidotite body crystallized at 3.4 GPa and 800 ºC and the later websterite veins crystallized at 5.5 GPa and 800 ºC (Vrijmoed et al., 2006) indicating that UHP conditions were locally reached and exceeded. Abundant eclogite are found throughout the Svartberget region, however clear evidence of UHP metamorphism is difficult to identify due to extensive retrogression. The Svartberget area is composed of two dominant rocks types: (1) gneiss with sillimanite/white mica and (2) migmatitic gneiss. The two rock types are interlayered and were folded during the late stages of exhumation (Vrijmoed et al., 2006).

The SvMZ provides an opportunity to study the complexity of the gneiss and its structures at a scale that has not been previously conducted in this part of the northern UHP domain. The close association between the gneiss and the UHP metaperidotite begs investigation into whether the adjacent area, including the gneiss, also experienced UHP conditions. Structurally, the SvMZ region is made up of highly strained gneiss with four distinct, discrete mylonite zones in the otherwise highly-deformed gneiss. The presence of these four, distinct mylonite zones show that strain is partitioned, at least locally in the

Svartberget region. The gneiss is pelitic in origin: it is biotite, garnet, and sillimanite-rich and the garnets are spessartine-rich. Microstructurally, the gneiss preserves features that are consistent with mylonitization during sillimanite-stable conditions: sillimanite included in quartz porphyroclasts (pre-kinematic) has a random orientation while sillimanite in the matrix of the gneiss is syn-kinematic with foliation-parallel, elongate clusters of fibrolitic sillimanite (Fig. 36c, d).

Metabasaltic material is preserved throughout the SvMZ. The majority is amphibolite; however some pods have escaped complete retrogression and preserve eclogite cores. The eclogite thermobarometry presented here was conducted on mineral pairs that were not in direct contact owing to extensive retrogression. The results suggest crystallization temperatures > 900 ºC at amphibolite-facies pressures. This estimate is high compared to previous work; it is likely that the mineral pair does not reflect equilibrium. Mafic pods in the discrete mylonite zones are elongate such that the long axis of the pod is foliation parallel; gneiss foliation wraps the pod edges. Pods outside of the shear zones show little preference for elongation with respect to the foliation.

Melt in the SvMZ occurs in two primary structural positions: (1) as layer-parallel leucosomes commonly localized in the discrete high-strain zones, and (2) on the margins of eclogite pods (Figs. 35f, g). Melt in the SvMZ formed from both mafic and felsic sources (Ganzhorn et al., 2014) and originated at peak P (> 2 GPa) and T < 800º C (Labrousse et al., 2011; Ganzhorn et al., 2014) and continued during decompression. This melt history suggests that melting and strain localization may have developed as positive feedback mechanisms that promoted exhumation.

5. Conclusions

Continental crust forms the bulk of UHP terranes, and yet it is rarely studied owing to the lack of traditionally-useful assemblages for thermobarometry and the complexity of the multiphase systems. Here, the metamorphic and structural characteristics of metamorphosed continental crust in three shear zones in the WGR were documented in addition to the closely associated (U)HP metabasaltic material. The metamorphosed continental crust and associated metabasalt record the decompression path from peak to amphibolite-facies conditions through textural and compositional changes.

The Salt Mylonite Zone is comprised of quartzofeldspathic gneiss and was exhumed from (U)HP with a coesite-eclogite body as evidenced by a consistent foliation and lineation. The omphacite fabric in eclogite is consistent with transtensional deformation at UHP conditions. The gneiss preserves evidence of exhumation through plagioclase reverse zoning which formed during grain growth during decompression. Additionally, an investigation into the effects of phase distribution in quartzofeldspathic gneiss (phase-separated v. phase-mixed mylonite) shows that habit affects strain partitioning, and in turn the mechanisms by which plagioclase and quartz deform.

The Finnøya Mylonite Zone is lithologically diverse and exemplifies the complexity of the WGR. One of the mylonites, a clinopyroxene gneiss, is compositionally similar to the associated eclogite suggesting that part of the mylonite zone is derived from eclogite. Zircons from syn-kinematic melt are Caledonian in age

suggesting that this melt and the mylonitization occurred during UHP conditions (Gordon et al., 2013).

The Svartberget Mylonite Zone is comprised of sillimanite-biotite gneiss and is adjacent to a well-studied UHP metaperidotite body (Vrijmoed et al., 2006; 2008). Four discrete shear zones occur in the region and show that strain is partitioned, at least locally. Sillimanite preserves pre- and syn-kinematic textures suggesting that shearing occurred during sillimanite-stable conditions. The mylonitic gneiss hosts amphibolite and retrogressed eclogite bodies that are deformed parallel to foliation. Syn-kinematic, Caledonian melt was derived from felsic and mafic material in the Svartberget region (Ganzhorn et al., 2014).

Gneiss in the WGR was subducted to HP conditions and UHP conditions, at least locally, as documented in these shear zones. Additionally, constrictional and extensional fabrics in minerals are widely documented throughout the WGR at amphibolite-facies (e.g. Krabbendam and Dewey, 1998; Terry and Robinson, 2004) and at near UHP conditions (Renedo et al., 2015). The shear zones represent a class of transtensional shear zones that are self-exhuming and therefore record structural an metamorphic increments of exhumation from mantle to crustal depths. A broad implication of this work is the agreement at a microstructural level with syn-extensional exhumation (Butler et al., 2015) at high pressures. The macrostructural, microstructural, and compositional information the shear zones preserve are necessary for understanding the exhumation path of UHP terranes and, by extension, the exhumation mechanisms.

References

Ábalos, B., 1997. Omphacite fabric variation in the Cabo Ortegal eclogite (NW Spain): relationships with strain symmetry during high-pressure deformation. Journal of Structural Geology 19, 621-637.

Andersen, T.B., Berry, H.N., Lux, D.R., Andresen, A., 1998. The tectonic significance of pre-Scandian $^{40}Ar/^{39}Ar$ phengite cooling ages in the Caledonides of western Norway. Journal of the Geological Society 155, 297–309.

Andersen, T.B., Jamtveit, B., Dewey, J.F., Swensson, E., 1991. Subduction and eduction of continental crust: major mechanism during continent-continent collision and orogenic extensional collapse, a model based on the south Caledonides. Terra Nova 3, 303-310.

Barth, N.C., Hacker, B.R., Seward, G.G.E., Walsh, E.O., Young, D., Johnston, S., 2010. Strain within the ultrahigh-pressure Western Gneiss region of Norway recorded by quartz CPOs. Geological Society, London, Special Publications 335, 663-685.

Bascou, J., Barruol, G., Vauchez, A., Mainprice, D., Egydio-Silva, M., 2001. EBSD-measured lattice-preferred orientations and seismic properties of eclogites. Tectonophysics 342, 61–80.

Bascou, J., Tommasi, A., Mainprice, D., 2002. Plastic deformation and development of clinopyroxene lattice preferred orientations in eclogites. Journal of Structural Geology 24, 1357–1368.

Behr, W.M., Platt, J.P., 2011. A naturally constrained stress profile through the middle crust in an extensional terrane. Earth and Planetary Science Letters 303, 181-192.

Blumenfeld, P., Mainprice, D., Bouchez, J.L., 1986. C-slip in quartz from subsolidus deformed granite. Tectonophysics 127, 97-115.

Bons, P.D., den Brok, B., 2000. Crystallographic preferred orientation development by dissolution-precipitation creep. Journal of Structural Geology 22.

Boundy, T.M., Fountain, D.M., Austrheim, H., 1992. Structural development and petrofabrics of eclogite facies shear zones, Bergen Arcs, western Norway: implications for deep crustal deformational processes. Journal of Metamorphic Geology 10, 127-146.

Braathen, A., Nordgulen, Ø., Osmundsen, P.-T., Andersen, T.B., Solli, A., Roberts, D., 2000. Devonian, orogen-parallel, opposed extension in the Central Norwegian Caledonides. Geology 28, 615-618.

Brown, W.L., Macaudière, J., Ohnenstetter, M., 1980. Ductile shear zones in a meta-anorthosite from Harris, Scotland: textural and compositional changes in plagioclase. Journal of Structural Geology 2.

Brueckner, H. K., & Van Roermund, H. L. M., 2004. Dunk tectonics: A multiple subduction/ eduction model for the evolution of the Scandinavian Caledonides. Tectonics, 23.

Bruegmann, R., Dresen, G., 2008. Rheology of the lower crust and upper mantle: Evidence from rock mechanics, geodesy, and field observations. Annual Review of Earth and Planteary Science 36, 531-567.

Butler, J., Beaumont, C., Jamieson, R.A., 2015. Paradigm lost: Buoyancy thwarted by the strength of the Western Gneiss Region (ultra)high-pressure terrane, Norway. Lithosphere.

Butler, J.P., Jamieson, R.A., Steenkamp, H.M., Robinson, P., 2012. Discovery of coesite-eclogite from the Nordøyane UHP domain, Western Gneiss Region, Norway: Field relations, metamorphic history, and tectonic significance. Journal of Metamorphic Geology 31, 147-163.

Carswell, D.A., Brueckner, H.K., Cuthbert, S.J., Mehta, K., O'Brien, P.J., 2003a. The timing of stabilisation and the exhumation rate for ultra-high pressure rocks in the Western Gneiss Region of Norway. Journal of Metamorphic Geology 21, 601–612.

Carswell, D., Tucker, R., O'Brien, P., Krogh, T., 2003b. Coesite micro-inclusions and the U/Pb age of zircons from the Hareidland Eclogite in the Western Gneiss Region of Norway. Lithos 67, 181–190.

Carter, N.L., Tsenn, M.C., 1987. Flow properties of continental lithosphere. Tectonophysics 136.

Chemenda, A. I., Mattauer, M., Malavieille, J., & Bokun, A. N., 1995. A mechanism for syn-collisional rock exhumation and associated normal faulting: Results from physical modelling. Earth and Planetary Science Letters, 132.

Chopin, C., 1984. Coesite and pure pyrope in high-grade blueschists of the western Alps: a first record and some consequences. Contributions to Mineralogy and Petrology, 86.

Culshaw, N.G., Fyson, W.K., 1984. Quartz ribbons in high grade granite gneiss: modifications of dynamically formed quartz c-axis preferred orientation by oriented grain growth. Journal of Structural Geology 6, 6.

Cuthbert, S.J., Carswell, D.A., Krogh-Ravna, E.J., Wain, A., 2000. Eclogites and eclogites in the Western Gneiss Region, Norwegian Caledonides. Lithos 52, 165-195.

Czaplińska, D., Piazolo, S., Zibra, I., 2015. The influence of phase and grain size distribution on the dynamics of strain localization in polymineralic rocks. Journal of Structural Geology 72.

DesOrmeau, J.W., Gordon, S.M., Kylander-Clark, A.R.C., Hacker, B.R., Bowring, S.A., Schoene, B., Samperton, K.M., 2015. Insights into (U)HP metamorphism of the Western Gneiss Region, Norway: A high-spatial resolution and high-precision zircon study. Chemical Geology, 414.

Dimanov, A., Dresen, G., Xiao, X., Wirth, R., 1999. Grain boundary diffusion creep of synthetic anorthite aggregates: The effect of water. Journal of Geophysical Research **104**, B5.

Dobrzhinetskaya, L.F., Eide, E.A., Larsen, R.B., Sturt, B.A., Trønnes, R.G., Smith, D.C., Taylor, W.R., Psukhova, T.V., 1995. Microdiamond in high-grade metamorphic rocks of the Western Gneiss region, Norway. Geology 23, 597–600.

Fliervoet, T.F., White, S.H., Drury, M.R., 1997. Evidence for dominant grain boundary sliding deformation in greenschist and amphibolite-grade polymineralic mylonites

from Redbank deformed zone, Central Australia. Journal of Structural Geology, 12.
Fossen, H., 2010. Extensional tectonics in the North Atlantic Caledonides: a regional view. Geological Society, London, Special Publications 335, 767–793.
Fossen, H., Teyssier, C., Whitney, D.L, 2013. Transtensional Folding. Journal of Structural Geology 56, 89-102.
Gabrielsen, R.H., Ramberg, I.B., 1979. Fracture patterns in Norway from Landsat imagery: Results and potential use, Proceedings, Norwegian Sea Symposium, 1-28.
Ganguly, J., Cheng, W., Tiron, M., 1996. Thermodynamics of aluminosilicate garnet solid solution: new experimental data, an optimized model, and thermometric applications. Contributions to Mineralogy and Petrology, 126.
Garbutt, J.M., Teyssier, C., 1991. Prism <c> slip in the quartzites of the Oakhurst Mylonite Belt, California. Journal of Structural Geology 13, 657-666.
Gee, D. G., 1975. A tectonic model for the central part of the Scandinavian Caledonides. American Journal of Science, 275-A.
Gerya, T.V., Perchuk, L.L., Burg, J.-P., 2008. Transient hot channels: Perpetrating and regurgitating ultrahigh-pressure, high-temperature crust-mantle associations in collision belts. Lithos, 103.
Ghent, E.D., Stout, M.Z., 1984. TiO2 activity in metamorphosed politic and basic rocks: principles and applications to metamorphism in southeastern Canadian Cordillera. Contributions to Mineralogy and Petrology 86, 248-255.
Gilotti, J.A., 2013. The Realm of Ultrahigh-Pressure Metamorphism. Elements, 9.
Godard, G., van Roermund, H.L.M., 1995. Deformation-induced clinopyroxene fabrics from eclogites. Journal of Structural Geology 17, 1425-1443.
Griffin, W.L., Bruekner, H.K., 1985. REE, Rb-Sr and Sm-Nd studies of Norwegian eclogites. Chemical Geology 52, 249–271.
Guillope, M., Poirier, J.P., 1979. Dynamic recrystallization during creep of single-crystalline halite: An experimental study. Journal of Geophysical Research, 84, B10.
Hacker, B.R., 2007. Ascent of the ultrahigh-pressure Western Gneiss Region, Norway. *In:* Cloos, M., Carlson, W.D., Gilbert, M.C., Liou, J.G., Sorensen, S.S. (Eds.), Convergent Margin Terranes and Associated Regions: A Tribute to W.G. Ernst, 171–184.
Hacker, B.R., Andersen, T.B., Johnston, S., Kylander-Clark, A.R.C., Peterman, E.M., Walsh, E.O., Young, D., 2010. High-temperature deformation during continental-margin subduction and exhumation: The ultrahigh-pressure Western Gneiss Region of Norway. Tectonophysics 480, 149–171.
Hacker, B. R., & Gans, P. B., 2005. Continental collisions and the creation of ultrahigh-pressure terranes: Petrology and thermochronology of nappes in the central Scandinavian Caledonides. Geological Society of America Bulletin, 117.

Hacker, B. R., Wallis, S. R., Ratschbacher, L., Grove, M., & Gehrels, G., 2006. High-temperature geochronology constraints on the tectonic history and architecture of the ultrahigh-pressure Dabie-Sulu Orogen. Tectonics, 25.

Halfpenny, A., Prior, D.J., Wheeler, J., 2012. Electron backscatter diffraction analysis to determine the mechanisms that operated during dynamic recrystallization of quartz-rich rocks. Journal of Structural Geology, 36.

Handy, M.R., 1990. The solid-state flow of polymineralic rocks. Journal of Geophysical Research, 95.

Helmstaedt, H., Anderson, O.L., Gavasci, A.T., 1972. Petrofabric studies of eclogite, spinel-websterite, and spinel-lherzolite xenoliths from kimberlite-bearing breccia pipes in southeastern Utah and northeastern Arizona. Journal of Geophysical Research 77, 4350-4364.

Henry, C., Michard, A. & Chopin, C., 1993. Geometry and structural evolution of ultra-high pressure and high pressure rocks from the Dora Maira massif, Western Alps. Journal of Structural Geology, 15.

Hippertt., J., Rocha, A., Lana, C., Egydio-Silva, M., Takeshita, T., 2001. Quartz plastic segregation and ribbon development in high-grade striped gneisses. Journal of Structural Geology, 23.

Hirth, G., Tullis, J., 1992. Dislocation creep regimes in quartz aggregates. Journal of Structural Geology 14, 145-159.

Holland, T.J.B., 1990. Activities of components in omphacitic solid solutions: An application of Landau theory to mixtures. Contributions to Mineralogy and Petrology, 105.

Holness, M.B., Watt, G.R., 2001. Quartz recrystallization and fluid flow during contact metamorphism: a cathodoluminescence study. Geofluids, 1.

Huang, R., Audétat, A., 2012. The titanium-in-quartz (Ti-in-quartz) thermobarometer: A critical examination and re-calibration. Geochimica et Cosmochimica Acta 84, 75–89.

Imon, R., Okudaira, T., Kanagawa, K., 2004. Development of shape- and lattice-preferred orientations of amphibole grains during initial cataclastic deformation and subsequent deformation by dissolution-precipitation creep in amphibolites from the Ryoke metamorphic belt, SW Japan, Journal of Structural Geology, 26.

Jessell, M.W., Kostenko, O., Jamtveit, B., 2003. The preservation potential of microstructures during static grain growth. Journal of Metamorphic Geology, 21.

Ji, S., Mainprice, D., 1990. Recrystallization and fabric development in plagioclase. The Journal of Geology, 98.

Jiang, Z., Prior, D., Wheeler, J., 2000. Albite crystallographic preferred orientation and grain misorientation distribution in a low-grade mylonite: implications for granular flow. Journal of Structural Geology, 22.

Johnston, S., Hacker, B.R., Ducea, M.N., 2007. Exhumation of ultrahigh-pressure rocks beneath the Hornelen segment of the Nordfjord-Sogn Detachment Zone, western Norway. Geological Society of America Bulletin 119, 1232–1248.

Kirby, S.H., 1983. Rheology of the lithosphere. Tectonophysics, 21.

Krabbendam, M., Dewey, J.F., 1998. Exhumation of UHP rocks by transtension in the Western Gneiss Region, Scandinavian Caledonides. Geological Society, London, Special Publications 135, 159–181.

Krabbendam, M. & Wain, A., 1997. Late-orogenic structures, differential retrogression and structural position of HP and UHP rocks in the Nordfjord-Stadlandet area, Western Gneiss Region. Norges Geologiske Undersøkelse Bulletin, 432.

Kruse, R., Stünitz, H., 1999. Deformation mechanisms and phase distribution in mafic high-temperature mylonites from the Jotun Nappe, southern Norway. Tectonophysics, 303.

Kylander-Clark, A.R.C., Hacker, B. R., & Mattinson, J. M., 2008. Slow exhumation of UHP terranes: Titanite and rutile ages of the Western Gneiss Region, Norway. Earth and Planetary Science Letters, 272.

Kylander-Clark, A. R. C., Hacker, B. R., Johnson, C. M., Beard, B. L., Mahlen, N. J., 2009. Slow subduction of a thick ultrahigh-pressure terrane. Tectonics, 28.

Kylander-Clark, Andrew R.C., Hacker, B. R., Mattinson, C. G., 2012. Size and exhumation rate of ultrahigh-pressure terranes linked to orogenic stage. Earth and Planetary Science Letters, 321-322.

Labrousse, L., Jolivet, L., Agard, P., Hébert, R., & Andersen, T. B., 2002. Crustal-scale boudinage and migmatization of gneiss during their exhumation in the UHP Province of Western Norway. Terra Nova, 14.

Labrousse, L., Jolivet, L., Andersen, T.B., Agard, P., Hébert, R., Maluski, H., Schärer, U., 2004. Pressure-temperature-time deformation history of the exhumation of ultra-high pressure rocks in the Western Gneiss Region, Norway. *In:* Whitney, D.L., Teyssier, C., Siddoway, C.S. (Eds.), Gneiss domes in orogeny: Geological Society of America Special Paper 380, 155–183.

Law, R.D., 2014. Deformation thermometry based on quartz c-axis fabrics and recrystallization microstructures: A review. Journal of Structural Geology, 66.

Lister, G.S., Snoke, A.W.,1984. S-C Mylonites. Journal of Structural Geology, 6.

Lloyd, G.E., Farmer, A.B., Mainprice, D., 1997. Misorientation analysis and the formation and orientation of subgrain and grain boundaries. Tectonophysics, 279.

Mainprice, D., Bouchez, J.-L., Bluemenfeld, P., Tubià, J. M., 1986. Dominant *c* slip in naturally deformed quartz: Implications for dramatic plastic softening at high temperature. Geology 14, 819-822.

Marshall, D.B., McLaren, A.C., 1977. Deformation mechanisms in experimentally deformed plagioclase feldspars. Physics and Chemistry of Minerals, 1.

Mattinson , C.G., Wooden, J.L., Liou, J.G., Bird, D.K., Wu, C.L., 2006. Age and duration of eclogite-facies metamorphism, North Qaidam HP/UHP terrane, Western China. American Journal of Science, 9.

Mauler, A., Bystricky, M., Kunze, K., Mackwell, S., 2000. Microstructures and lattice preferred orientations in experimentally deformed clinopyroxene aggregates. Journal of Structural Geology 22, 1633-1648.

McClay, K.R.,1977. Pressure solution and Coble creep in rocks and minerals: a review. Journal of the Geological Society, 134.

Mehl, L., Hirth, G., 2008. Plagioclase preferred orientation in layered mylonites: Evaluation of flow laws for the lower crust. Journal of Geophysical Research, 113.

Menegon, L., Pennachioni, G., Spiess, R., 2008. Dissolution-precipitation creep of K-feldspar in mid-crustal granite mylonites. Journal of Structural Geology, 30.

Miyazaki, T., Sueyoshi, K., Hiraga, T., 2013. Olivine crystals align during diffusion creep of Earth's upper mantle. Nature, 502.

Molli, G., 1994 Microstructural features of high temperature shear zones in gabbros of the Northern Apennine Ophiolites. Journal of Structural Geology, 16.

Monteleone, B. D., Baldwin, S. L., Webb, L. E., Fitzgerald, P. G., Grove, M., & Schmitt, A.K., 2007. Late Miocene-Pliocene eclogite facies metamorphism, D'Entrecasteaux Islands, SE Papua New Guinea. Journal of Metamorphic Geology, 25.

Müller, A., Wiedenbeck, M., van den Kerkhof, A.M., Kronz, A., Simon, K., 2003. Trace elements in quartz – a combined electron microprobe, secondary ion mass spectrometry, laser-ablation ICP-MS, and cathodoluminescence study. European Journal of Mineralogy 15, 747-763.

Neumann, B., 2000. Texture development of recrystallized quartz polycrystals unravelled by orientation and misorientation characteristics. Journal of Structural Geology, 22.

Nachlas, W.O., Whitney, D.L., Teyssier, C., Bagley, B., Mulch, A., 2014. Titanium concentration in quartz as a record of multiple deformation mechanisms in an extensional shear zone. Geochemistry, Geophysics, Geosystems 15, 1374-1397.

Norton, M.G., 1986. Late Caledonide extension in Western Norway - a response to extreme crustal thickening. Tectonics 5, 195-204.

Norton, M.G., 1987. The Nordfjord-Sogn detachment. Western Norway. Norsk Geologisk Tidsskrift 67, 93-106.

Olsen, T.S., Kohlstedt, D.L., 1984. Analysis of dislocations in some naturally-deformed plagioclase feldspars. Physics and Chemistry of Minerals, 11.

Olsen, T.S., Kohlstedt, D.L., 1985. Natural deformation and recrystallization of some intermediate plagioclase feldspars. Tectonophysics, 111.

Ord A., Hobbs, B.E., 1989. The strength of the continental crust, detachment zones and the development of plastic instabilities. *Tectonophysics*, 158.

Passchier, C.W., Simpson, C., 1986. Porphyroclast systems as kinematic indicators. Journal of Structural Geology 8, 831-843.

Passchier, C.W., Trouw, 2005. Microtectonics. Springer, New York.

Paterson, M.S., Weiss, L.E., 1961 Symmetry concepts in the structural analysis of deformed rocks. Bulletin of Geological Society of America, 72.

Pearce, M.A., Wheeler, J., 2014. Microstructural and Metamorphic Constraints on the Thermal Evolution of the Southern Region of the Lewisian Gneiss Complex, NW Scotland. Journal of Petrology, 55.

Pearce, M.A., Wheeler, J., 2010. Modelling grain-recycling zoning during metamorphism. Journal of Metamorphic Geology, 28.

Piazolo S., Bons, P.D., Jessell, M.W., Evans, L., Passchier, C.W., 2002. Dominance of microstructural processes and their effect on microstructural development: insights from numerical modelling of dynamic recrystallization. Geological Society, London, Special Publication, 200.

Prior, D.J., Wheeler, J., 1999. Feldspar fabrics in a greenschist facies albite-rich mylonite from backscatter diffraction. Tectonophysics, 303.

Prior, D.J., Hirth, G., 2007. Microstructural recognition of grain boundary sliding and its rheological implications. DRT conference abstracts, 5.

Raj, R., Ashby, M.F., 1971. On grain boundary sliding and diffusion creep. Metallurgical and Material Transactions, 2.

Rambaldi, E.R., 1973. Variation in the Composition of Plagioclase and Epidote in some Metamorphic Rocks near Bancroft, Ontario. Canadian Journal of Earth Science, 10.

Renedo, R.N., Nachlas, W.O., Whitney, D.L., Teyssier, C., Piazolo, S., Gordon, S.M., Fossen, H., 2015. Fabric development during exhumation from ultrahigh-pressure in an eclogite-bearing shear zone, Western Gneiss Region, Norway. Journal of Structural Geology, 71.

Root, D.B., Hacker, B.R., Gans, P.B., Ducea, M.N., Eide, E.A., Mosenfelder, J.L., 2005. Discrete ultrahigh-pressure domains in the Western Gneiss Region, Norway: implications for formation and exhumation. Journal of Metamorphic Geology 23, 45–61.

Root, D.B., Hacker, B.R., Mattinson, J.M., Wooden, J.L., 2004. Zircon geochronology and ca. 400 Ma exhumation of Norwegian ultrahigh-pressure rocks: an ion microprobe and chemical abrasion study. Earth and Planetary Science Letters 228, 325–341.

Rubatto, D., & Hermann, J., 2001. Exhumation as fast as subduction ? Geology, 29.

Rybacki, E., Dresen, G., 2000. Dislocation and diffusion creep of synthetic anorthite aggregates. Journal of Geophysical Research, 105.

Smith, D.C., 1984. Coesite in clinopyroxene in the Caledonides and its implications for geodynamics. Nature 310, 641–644.

Smith, D.C., Godard, G., 2013. A Raman spectroscopic study of diamond and disordered sp^3-carbon in the coesite-bearing Straumen Eclogite Pod, Norway. Journal of Metamorphic Geology 31, 19–33.

Smyth, J.R., 1977. Quartz pseudomorphs after coesite. American Mineralogist 65, 1185-1191.

Sodre Borges, F., White, S.H., 1980. Microstructural and chemical studies of sheared anorthosites, Roneval, South Harris. Journal of Structural Geology, 2.

Stipp, M., Stünitz, H., Heilbronner, R., Schmid, S., 2002. The eastern Tonale fault zone: a 'natural laboratory' for crystal plastic deformation of quartz over a temperature range from 250 to 700 °C. Journal of Structural Geology 24, 1861-1884.

Stunitz, H., 1993. Transition from fracturing to viscous flow in a naturally deformed metagabbro. In: Boland, J.N., & Fitzgerald, J.D. (eds) Defects and Processes in

the Solid State: Geoscience Applications, the McLaren Volume, Elsevier, 121-150.

Suo, S., Zhong, Z., You, Z., Zhang, Z., 2001. Post-Collisional Ductile Extensional Tectonic Framework in the UHP and HP Metamorphic Belts in the Dabie-Sulu Region, China. Acta Geologica Sinica, 75.

Svahnberg, H., Piazolo, S., 2013. Interaction of chemical and physical processes during deformation at fluid-present conditions: a case study from an anorthosite-leucogabbro deformed at amphibolite facies conditions. Contributions to Mineralogy and Petrology, 165.

Svahnberg, H., Piazolo, S., 2010. The initiation of strain localization in plagioclase-rich rocks: Insights from detailed microstructural analysis. Journal of Structural Geology, 32.

Terry, M.P., Robinson, P., 2003. Evolution of amphibolite-facies structural features and boundary conditions for deformation during exhumation of high- and ultrahigh-pressure rocks, Nordøyane, Western Gneiss Region, Norway. Tectonics, 22.

Terry, M.P., Robinson, P.R., Krogh Ravna, E.J., 2000. Kyanite eclogite thermobarometry and evidence for thrusting of UHP over HP metamorphic rocks, Nordøyane, Western Gneiss Region, Norway. American Mineralogist 85, 1637–1650.

Thomas, J.B., Spear, F.S., Webb, L.E., 2012. Experimental study of titanium-in-coesite solubility. Abstract V33C-2885 presented at 2012 Fall Meeting, American Geophysical Union, San Francisco, California, 3-7 Dec.

Thomas, J.B., Watson, E.B., Spear, F.S., Shemella, P.T., Nayak, S.K., Lanzirotti, A., 2010. TitaniQ under pressure: the effect of pressure and temperature on the solubility of Ti in quartz. Contributions to Mineralogy and Petrology 160, 743-759.

Torsvik, T. H., Smethurst, M. A., Meert, J. G., Van der Voo, R., McKerrow, W. S., Brasier, M. D., Sturt, B. A., 1996. Continental break-up and collision in the Neoproterozoic and Palaeozoic — A tale of Baltica and Laurentia. Earth-Science Reviews, 40.

Trimby, P.W., Prior, D.J., Wheeler, J., 1998. Grain boundary hierarchy development in a quartz mylonite, Journal of Structural Geology, 20.

Tucker, R. D., Robinson, P., Solli, A., Gee, D. G., Thorsnes, T., Krogh, T. E., Nordgulen, Ø., 2004. Thrusting and extension in the Scandian hinterland, Norway: New U-Pb ages and tectonostratigraphic evidence. American Journal of Science, 304.

Tullis, J., 1977. Preferred orientation of quartz produced by slip during plane strain. Tectonophysics 39, 87-102.

Tullis, J., Yund, R.A., 1991. Diffusion creep in feldspar aggregates: experimental evidence, Journal of Structural Geology, 12.

Tullis, J., Yund, R.A., 1985. Dynamic recrystallization of feldspar: A mechanism for ductile shear zone formation. Geology, 13.

Tullis, J., Yund, R.A., 1980. Hydrolytical weakening of experimentally deformed Westerly granite and Hale albite rock. Journal of Structural Geology, 24.

Vrijmoed, J.C., van Roermund, H.L.M., Davies, G.R., 2006. Evidence for diamond-grade ultra-high pressure metamorphism and fluid interaction in the Svartberget Fe–Ti garnet peridotite–websterite body, Western Gneiss Region, Norway. Mineralogy and Petrology 88, 381–405.

Vrijmoed, J.C., Smith, D.C., Van Roermund, H.L.M., 2008. Raman confirmation of microdiamond in the Svartberget Fe-Ti type garnet peridotite, Western Gneiss Region, Western Norway. Terra Nova 20, 295-301.

Wain, A., 1997. New evidence for coesite in eclogite and gneisses: Defining an ultrahigh-pressure province in the Western Gneiss region of Norway. Geology 25, 927–930.

Wain, A., Waters, D., Jephcoat, A. Olijyink, H., 2000. The high-pressure to ultrahigh-pressure eclogite transition in the Western Gneiss Region, Norway. European Journal of Mineralogy 12, 667-687.

Wark, D.A., Watson, E.B., 2006. TitaniQ: a titanium-in-quartz geothermometer. Contributions to Mineralogy and Petrology 152, 743-754.

Wheeler, J., Prior, D.J., Jiang, Z., Spiess, R., Trimby, P.W., 2001. The petrological significance of misorientations between grains. Contributions to Mineralogy and Petrology, 141.

Wheeler, J., 1992. Importance of pressure solution and coble creep in the deformation of polymineralic rocks. Journal of Geophysical Research, 97.

Wheeler, J., 2009. The preservation of seismic anisotropy in the Earth's mantle during diffusion creep. Geophysical Journal International, 178.

Whitney, D.L., Evans, B.W., 2010. Abbreviations for names of rock-forming minerals. American Mineralogist 95, 185–187.

Young, D.J., Hacker, B.R., Andersen, T.B., Gans, P.B., 2011. Structure and $^{40}Ar/^{39}Ar$ thermochronology of an ultrahigh-pressure transition in western Norway. Journal of the Geological Society 168, 887–898.

Young, David J., Hacker, B. R., Andersen, T. B., & Corfu, F., 2007. Prograde amphibolite facies to ultrahigh-pressure transition along Nordfjord, western Norway: Implications for exhumation tectonics. Tectonics, 26.

Zhang, J., Green, H.W., 2007. On the Deformation of UHP eclogite: From Laboratory to Nature. International Geology Review 29, 487-508.

Zhang, J., Green, H.W., Bozhilov, K.N., 2006. Rheology of omphacite at high temperature and pressure and significance of its lattice preferred orientations. Earth and Planetary Science Letters 246, 432–443.

Zhang, J.F., Shi, F., Xu, H.J., Wang, L., Feng, S.Y., Liu, W.L., Wang, Y.F., Green, H.W., 2013. Petrofabric and strength of SiO_2 near the quartz-coesite phase boundary. Journal of Metamorphic Geology 31, 83–92.

Zheng, Y.-F., 2012. Metamorphic chemical geodynamics in continental subduction zones. Chemical Geology 328, 5–48.

Appendix 1. Raw SIMS data for measurement of Ti concentration of quartz in eclogite and quartzofeldspathic gneiss.

Quartzofeldspathic gneiss (samples NW10-40G)

Point	48Ti/30Si measured		40Ca/30Si measured		48Ti/30Si corrected		Ti concentration (ppm)		Site
	mean	std. dev.	mean	std. dev.	mean	std. dev.	mean	std. dev.	
50	8.5×10^{-4}	3.2×10^{-5}	2.8×10^{-3}	3.3×10^{-4}	8.4×10^{-4}	3.2×10^{-3}	10.8	0.4	Qz ribbon
51	8.3×10^{-4}	1.6×10^{-5}	3.8×10^{-4}	4.0×10^{-3}	8.3×10^{-4}	1.6×10^{-3}	10.7	0.2	Qz ribbon
52	7.3×10^{-4}	1.6×10^{-5}	4.2×10^{-4}	5.7×10^{-5}	7.3×10^{-4}	1.6×10^{-5}	9.4	0.2	Qz ribbon
53	4.7×10^{-4}	1.3×10^{-5}	3.5×10^{-4}	5.2×10^{-5}	4.7×10^{-4}	1.2×10^{-5}	6.0	0.2	Qz ribbon
54	4.9×10^{-4}	1.1×10^{-5}	1.1×10^{-2}	2.3×10^{-4}	4.7×10^{-4}	1.1×10^{-5}	6.0	0.1	Qz ribbon
55	8.6×10^{-4}	3.7×10^{-5}	4.3×10^{-4}	6.1×10^{-5}	8.6×10^{-4}	3.7×10^{-5}	11.0	0.5	Qz ribbon
56	8.2×10^{-4}	3.4×10^{-5}	7.2×10^{-4}	8.5×10^{-5}	8.2×10^{-4}	3.4×10^{-5}	10.5	0.4	Qz ribbon
57	4.5×10^{-3}	1.2×10^{-4}	2.4×10^{0}	7.0×10^{-2}	1.6×10^{-4}	-8.6×10^{-6}	2.0	-0.1	Qz ribbon
58	4.1×10^{-3}	1.5×10^{-4}	2.1×10^{0}	6.8×10^{-2}	1.5×10^{-4}	1.7×10^{-3}	2.0	0.2	Qz ribbon
59	7.9×10^{-4}	1.7×10^{-5}	5.3×10^{-4}	6.0×10^{-5}	7.8×10^{-4}	1.7×10^{-5}	10.1	0.2	Qz ribbon
60	7.5×10^{-4}	1.2×10^{-5}	6.9×10^{-4}	1.2×10^{-4}	7.5×10^{-4}	1.2×10^{-5}	9.6	0.2	Qz ribbon
61	7.9×10^{-4}	4.1×10^{-5}	8.2×10^{-4}	1.4×10^{-4}	7.9×10^{-4}	4.1×10^{-5}	10.2	0.5	Qz ribbon
62	5.9×10^{-4}	8.4×10^{-6}	3.2×10^{-4}	3.4×10^{-5}	5.9×10^{-4}	8.3×10^{-6}	7.5	0.1	Qz ribbon
63	7.8×10^{-4}	9.6×10^{-6}	5.2×10^{-4}	3.6×10^{-5}	7.8×10^{-4}	9.6×10^{-6}	10.0	0.1	Qz ribbon
64	7.9×10^{-4}	1.6×10^{-5}	4.7×10^{-4}	5.3×10^{-5}	7.9×10^{-4}	1.6×10^{-5}	10.2	0.2	Qz ribbon
65	1.3×10^{-3}	7.1×10^{-5}	4.5×10^{-4}	3.6×10^{-4}	1.3×10^{-3}	7.0×10^{-3}	16.7	0.9	Qz ribbon

Eclogite (sample NW11-21B)	86	4.1×10^{-4}	1.2×10^{-5}	3.8×10^{-4}	4.4×10^{-5}	4.1×10^{-4}	1.1×10^{-5}	5.2	0.1	vein
	87	4.6×10^{-4}	2.1×10^{-5}	5.5×10^{-4}	8.0×10^{-5}	4.6×10^{-4}	2.0×10^{-5}	5.9	0.3	vein
	88	4.9×10^{-4}	2.5×10^{-5}	6.8×10^{-4}	9.5×10^{-5}	4.9×10^{-4}	2.5×10^{-5}	6.3	0.3	vein
	89	4.4×10^{-4}	3.5×10^{-5}	1.2×10^{-5}	1.6×10^{-4}	4.4×10^{-4}	3.5×10^{-5}	5.6	0.4	vein
	90	4.7×10^{-4}	1.1×10^{-5}	3.9×10^{-4}	4.5×10^{-5}	4.7×10^{-4}	1.1×10^{-5}	6.1	0.1	vein
	91	4.8×10^{-4}	2.7×10^{-5}	4.9×10^{-4}	6.1×10^{-5}	4.8×10^{-4}	2.7×10^{-5}	6.1	0.3	vein
	92	5.0×10^{-4}	1.6×10^{-5}	4.3×10^{-4}	5.4×10^{-5}	5.0×10^{-4}	1.6×10^{-5}	6.4	0.2	vein
	93	5.4×10^{-4}	1.2×10^{-5}	4.0×10^{-4}	6.1×10^{-5}	5.4×10^{-4}	1.2×10^{-5}	6.9	0.2	vein
	94	5.3×10^{-4}	1.5×10^{-5}	3.7×10^{-4}	7.0×10^{-5}	5.3×10^{-4}	1.5×10^{-5}	6.8	0.2	vein
	95	5.4×10^{-4}	1.1×10^{-5}	1.6×10^{-4}	1.8×10^{-5}	5.4×10^{-4}	1.0×10^{-5}	6.9	0.1	vein
	96	5.3×10^{-4}	1.9×10^{-5}	2.1×10^{-4}	3.5×10^{-5}	5.3×10^{-4}	1.9×10^{-5}	6.8	0.2	vein
	97	4.9×10^{-4}	1.1×10^{-5}	3.0×10^{-4}	4.5×10^{-5}	4.9×10^{-4}	1.0×10^{-5}	6.9	0.1	Inclusion
	98	5.9×10^{-2}	3.2×10^{-4}	2.9×10^{1}	6.4×10^{-2}	5.5×10^{-5}	2.0×10^{-4}	70.6	2.6	Inclusion
	99	4.0×10^{-4}	9.1×10^{-6}	4.3×10^{-4}	6.0×10^{-5}	4.0×10^{-4}	9.0×10^{-6}	5.1	0.1	Inclusion
	100	5.8×10^{-2}	7.5×10^{-4}	2.8×10^{1}	9.6×10^{-2}	7.1×10^{-3}	5.7×10^{-4}	91.0	7.3	Inclusion
	101	5.0×10^{-4}	1.8×10^{-5}	6.7×10^{-4}	9.1×10^{-5}	5.0×10^{-4}	1.8×10^{-5}	6.4	0.2	Inclusion
	102	4.2×10^{-4}	1.9×10^{-5}	1.4×10^{-3}	1.5×10^{-4}	4.2×10^{-4}	1.9×10^{-5}	5.4	0.2	Inclusion
	103	5.4×10^{-4}	1.8×10^{-5}	7.8×10^{-4}	1.2×10^{-4}	5.3×10^{-4}	1.8×10^{-5}	6.8	0.2	Inclusion

Appendix 2. Mineral assemblages by sample. Mineral abbreviations after Whitney and Evans, 2010.

Sample		Rock type	Major minerals	Minor minerals	EMPA
Salt Mylonite Zone					
NW10-40					
	A	felsic gneiss	Qz Pl Ksp Bt Wm	Zrn Ep Aln Ilm	Fsp quant
	B	mafic gneiss	Qz Pl Hbl Bt	Zrn Ep Ttn Ap	
	C	mylonitic felsic gneiss	Qz Pl Ksp Hbl Bt	Zrn Ep Ttn Ap	Fsp quant
	D	amphibolite	Qz Pl Hbl Bt	Zrn Ilm	Fsp quant Grt quant
	E	garnet amphibolite	Qz Pl Grt Hbl Bt	Zrn Ilm	Fsp quant Grt quant
	F	mylonitic felsic gneiss	Qz Pl Ksp Bt	Zrn Ep Ilm	
	G	mylonitic felsic gneiss	Qz Pl Ksp Grt Hbl Bt	Zrn Ep Ttn Aln Ilm	Fsp quant
	H	pegmatite	Qz Pl Ksp Bt	Zrn	Fsp quant
	I	garnet amphibolite	Qz Pl Grt Hbl Bt	Zrn Ttn Ilm	Fsp quant Grt quant

	J	mylonitic felsic gneiss	Qz Pl Ksp Grt Hbl Bt	Zrn Ep Aln Ilm	Fsp quant Grt quant
	K	garnet amphibolite	Pl Grt Hbl Bt	Zrn Ep Ilm Ap	
	L	retrogressed eclogite	Qz Pl Grt Hbl	Zrn Rt	
	M	eclogite	Qz Pl Grt **Pyx** Hbl Bt	Zrn Rt	Grt quant Pyx quant
	N	pegmatite	Qz Pl Ksp Bt Wm	Zrn Ep	
	P	mafic gneiss	Qz Pl Grt Hbl Bt	Zrn Ep Aln Ilm	
	Q	pegmatite	Qz Pl Ksp Bt	Zrn Ilm	
	R	leucosome	Qz Pl Ksp Bt	Zrn Wm	
Finnoya Mylonite Zone					
NW10-53					
	A	retrogressed eclogite	Qz Pl Grt Pyx Hbl Bt	Zrn Ap Aln	Fsp quant Pyx quant Grt quant
	B	leucosome	Qz Pl Ksp Hbl Bt	Zrn Scap Aln	

	C	retrogressed eclogite	Qz Pl Grt Pyx Hbl Bt	Zrn Ap Aln	
NW10-54					
	A	gneiss	Qz Pl Ksp Grt Hbl Bt	Zrn Aln Ap Scp	
	B	gneiss	Qz Pl Ksp Grt Hbl Bt	Zrn Aln Ap Scp	
	C	gneiss	Qz Pl Ksp Grt **Pyx** Hbl Bt	Zrn Aln Ap Scp	Fsp quant Pyx quant Grt quant
	D	gneiss + leucosome	Qz Pl Ksp Grt Hbl Bt	Zrn Aln Ap Scp	
	E	gneiss	Qz Pl Ksp Grt **Pyx** Hbl Bt	Zrn Aln Ap Scp	
	F	gneiss	Qz Pl Ksp Grt Hbl Bt	Zrn Aln Ap Ilm Ttn	
	G	gneiss + leucosome	Qz Pl Ksp Grt Hbl Bt	Zrn Aln Ap Ilm Ttn	

	H	gneiss	Qz Pl Ksp Grt Hbl Bt	Zrn Ap Ilm	Fsp quant Grt quant
	I	gneiss	Qz Pl Ksp Grt **Pyx** Hbl Bt	Zrn Aln Ap Ilm Ttn	
	J	gneiss + leucosome	Qz Pl Ksp Grt Hbl Bt	Zrn Aln Ap Ilm Ttn Scp	
	K	gneiss	Qz Pl Ksp Grt **Pyx** Hbl Bt	Zrn Aln Ap Ilm Ttn Scp	
	L	gneiss + leucosome	Qz Pl Ksp Grt **Pyx** Hbl Bt	Zrn Aln Ap Ilm	Grt quant
	M	gneiss	Qz Pl Ksp Grt **Pyx** Hbl Bt	Zrn Aln Ap Ilm Scp	Fsp quant Pyx quant Grt quant
	N	gneiss	Qz Pl Ksp Grt **Pyx** Hbl Bt	Zrn Aln Ap Ilm Scp	
	P	gneiss	Qz Pl Ksp Grt **Pyx**	Zrn Aln Ap Ilm Scp	

			Hbl Bt		
	Q	gneiss + leucosome	Qz Pl Ksp Grt Hbl Bt	Zrn Aln Ap Ilm Scp	Grt quant
Svartberget Mylonite Zone					
NW11-10					
	A	mylonitic gneiss	Qz Pl Ksp Sil Grt Bt Wm	Zrn Ilm	Fsp quant Grt quant
	B	gneiss	Qz Pl Ksp Sil Grt Bt Wm	Zrn Ilm	Fsp quant Grt quant
	C	gneiss	Qz Pl Ksp Grt Bt	Zrn Aln Ilm	
	D	retrogressed eclogite	Qz Pl Grt Hbl	Zrn Ilm Rt	
	E	mylonitic gneiss	Qz Pl Ksp Bt Wm	Zrn Ilm	
	F	mylonitic gneiss	Qz Pl Ksp Sil Bt Wm	Zrn Ilm	Fsp quant
	G	gneiss	Qz Pl Ksp	Zrn Ap Ilm	

			Bt		
	H	gneiss	Qz Pl Ksp Sil Bt Wm	Zrn Ilm	
	J	mylonitic gneiss	Qz Pl Ksp Sil Bt Wm	Zrn Ilm	
	K	mylonitic gneiss	Qz Pl Ksp Sil Bt Wm	Zrn Ilm	
	L	gneiss	Qz Pl Ksp Bt	Zrn Ep Ilm	
	M	gneiss	Qz Pl Ksp Sil Bt Wm	Zrn Ilm	
	N	eclogite	Qz Pl Grt **Pyx** Hbl	Zrn Ilm Rt	Fsp quant Grt quant Pyx quant
	P	mylonitic gneiss	Qz Pl Ksp Bt Wm	Zrn Ilm Ap	
	Q	eclogite	Qz Pl Grt **Pyx** Hbl Bt	Zrn Ilm Rt Ttn	
	R	gneiss	Qz Pl Ksp Sil Bt Wm	Zrn Ilm Ap	

	S	gneiss	Qz Pl Ksp Sil Bt Wm	Zrn Ilm Ap	
	T	gneiss	Qz Pl Ksp Grt Bt Wm	Zrn Ilm	
	U	gneiss	Qz Pl Ksp Sil Grt Bt Wm	Zrn Ilm	
NW11-21	A	mafic gneiss	Qz Pl Grt Hbl Bt	Zrn Aln Ep Ilm	
	B	retrogressed eclogite	Qz Pl Grt Pyx Hbld	Zrn Rt	Grt quant Pyx quant
	C	eclogite	Qz Grt Pyx	Zrn Rt	
MW11-30					
	A	amphibolite	Qz Pl Hbl Bt	Zrn Ep Rt Ttn Ilm	
	B	gneiss	Qz Pl Ksp Bt	Zrn Aln Ap Ttn	
	D	eclogite	Qz Grt Pyx Bt	Zrn Rt	
	E	felsic gneiss	Qz Pl Ksp Bt Hbl	Zrn Ep Ttn Ap Aln Ilm	

	F	mylonitic felsic gneiss	Qz Pl Ksp Bt Wm	Zrn Ep Ap Ilm	
	G	mylonitic felsic gneiss	Qz Pl Ksp Bt Wm	Zrn Ap Aln Ilm	
	J	mylonitic felsic gneiss	Qz Pl Ksp Grt Bt Hbl	Zrn Ep Ap Aln Ilm	
	K	gneiss	Qz Pl Ksp Bt	Zrn Ep Aln Ap	
	L	amphibolite	Qz Pl Hbl Bt	Zrn Ep Rt Ttn Ilm	
	M	eclogite	Qz Grt Hbl Bt Ky	Zrn Rt Ap Ilm	
	N	mylonitic gneiss	Qz Pl Ksp Bt	Zrn Ep Aln Ap Ttn Ilm	
NW11-31					
	A	eclogite	Qz Pl Grt Pyx Hbl	Zrn Rt Ilm	Grt quant Pyx quant
	B	amphibolite	Qz Pl Grt Hbl Bt	Zrn Ilm Ap	Grt quant
	C	amphibolite	Qz Pl Hbl Bt	Zrn Ilm Ttn Ap	

	D	gneiss	Qz Pl Ksp Bt	Zrn Ep Aln Ap Ttn	
	E	gneiss	Qz Pl Ksp Hbl Bt	Zrn Ep Ap Ttn Ilm	
NW11-32					
	A	amphibolite	Qz Pl Grt Hbl Bt	Zrn Ilm	
	B	amphibolite	Qz Pl Hbl Bt	Zrn Ilm Ttn Ap Ep	
	C	gneiss	Qz Pl Ksp Hbl Bt	Zrn Ep Ap Ttn Ilm	
	D	gneiss	Qz Pl Ksp Bt	Zrn Ep Aln Ilm	
	E	gneiss	Qz Pl Ksp Hbl Bt	Zrn Ep Aln Ttn	

Appendix 3: Microprobe analyses by shear zone

Salt Mylonite Zone																								
Plagioclase	Normalized Atoms											Weight Percent												
Sample	Si	Ti	Al	Fe	Mn	Mg	Ca	Na	K	Total	SiO2	TiO2	Al2O3	FeO	MnO	MgO	CaO	Na2O	K2O	Total
Line 1 40AB_Line1	2.66	0.00	1.35	0.00	0.00	0.00	0.31	0.67	0.00	5.00	60.27	0.00	25.98	0.09	0.00	0.00	6.51	7.79	0.07	100.71
Line 2 40AB_Line1	2.65	0.00	1.36	0.00	0.00	0.00	0.31	0.69	0.01	5.02	60.14	0.00	26.09	0.10	0.00	0.00	6.49	8.05	0.21	101.09
Line 3 40AB_Line1	2.68	0.00	1.32	0.01	0.00	0.00	0.29	0.70	0.02	5.01	60.92	0.00	25.51	0.14	0.00	0.00	6.05	8.18	0.28	101.08
Line 4 40AB_Line1	2.77	0.00	1.26	0.00	0.00	0.00	0.17	0.76	0.01	4.98	61.71	0.00	23.81	0.11	0.00	0.00	3.61	8.75	0.13	98.13
Line 5 40AB_Line1	2.70	0.00	1.31	0.00	0.00	0.00	0.27	0.71	0.01	5.01	60.87	0.00	25.16	0.10	0.00	0.00	5.66	8.27	0.25	100.31
Line 6 40AB_Line1	2.75	0.00	1.27	0.00	0.00	0.00	0.23	0.73	0.02	4.99	62.49	0.00	24.54	0.09	0.00	0.00	4.79	8.56	0.30	100.76
Line 7 40AB_Line1	2.72	0.00	1.30	0.00	0.00	0.00	0.25	0.72	0.01	5.00	61.32	0.00	24.85	0.12	0.00	0.00	5.27	8.43	0.24	100.24
Line 8 40AB_Line1	2.69	0.00	1.32	0.00	0.00	0.00	0.27	0.72	0.01	5.01	60.65	0.00	25.13	0.09	0.00	0.00	5.61	8.35	0.20	100.04
Line 9 40AB_Line1	2.68	0.00	1.33	0.00	0.00	0.00	0.29	0.70	0.01	5.01	60.36	0.00	25.50	0.09	0.00	0.00	6.02	8.12	0.17	100.26
Line 10 40AB_Line1	2.68	0.00	1.33	0.00	0.00	0.00	0.28	0.69	0.01	5.00	61.47	0.00	25.94	0.08	0.00	0.00	6.03	8.10	0.13	101.75
Line 1 40AB_Line3	2.67	0.00	1.34	0.01	0.00	0.00	0.30	0.67	0.01	5.00	60.12	0.00	25.63	0.15	0.00	0.00	6.39	7.83	0.18	100.30
Line 2 40AB_Line3	2.68	0.00	1.33	0.00	0.00	0.00	0.29	0.68	0.01	5.00	60.55	0.00	25.54	0.13	0.00	0.00	6.01	7.94	0.25	100.42
Line 3 40AB_Line3	2.68	0.00	1.33	0.01	0.00	0.00	0.29	0.69	0.01	5.01	60.55	0.00	25.52	0.15	0.00	0.00	6.10	8.05	0.23	100.60
Line 4 40AB_Line3	2.69	0.00	1.32	0.00	0.00	0.00	0.27	0.71	0.01	5.01	61.11	0.00	25.34	0.12	0.00	0.00	5.80	8.35	0.24	100.95
Line 5 40AB_Line3	2.69	0.00	1.32	0.00	0.00	0.00	0.28	0.71	0.01	5.01	60.75	0.00	25.29	0.10	0.00	0.00	5.85	8.27	0.21	100.47
Line 6 40AB_Line3	2.69	0.00	1.31	0.00	0.00	0.00	0.28	0.70	0.01	5.01	61.03	0.00	25.27	0.11	0.00	0.00	5.93	8.19	0.24	100.77
Line 7 40AB_Line3	2.70	0.00	1.31	0.00	0.00	0.00	0.26	0.71	0.01	5.01	61.40	0.00	25.24	0.08	0.00	0.00	5.62	8.36	0.24	100.94
Line 8 40AB_Line3	2.69	0.00	1.32	0.00	0.00	0.00	0.28	0.69	0.01	5.00	60.71	0.00	25.35	0.08	0.00	0.00	5.94	7.99	0.26	100.34
Line 9 40AB_Line3	2.66	0.00	1.36	0.01	0.00	0.00	0.31	0.66	0.01	5.00	59.89	0.00	25.97	0.14	0.00	0.00	6.49	7.71	0.23	100.42
Line 10 40AB_Line3	2.68	0.00	1.33	0.00	0.00	0.00	0.28	0.70	0.01	5.00	61.52	0.00	25.86	0.10	0.00	0.00	5.97	8.26	0.11	101.82
Line 1 40AB_Line2	2.67	0.00	1.34	0.01	0.00	0.00	0.31	0.66	0.01	5.00	59.13	0.00	25.25	0.21	0.00	0.00	6.52	7.57	0.16	98.82
Line 2 40AB_Line2	2.70	0.00	1.31	0.01	0.00	0.00	0.26	0.71	0.01	5.01	61.40	0.00	25.15	0.20	0.00	0.00	5.58	8.36	0.24	100.92
Line 3 40AB_Line2	2.71	0.00	1.31	0.00	0.00	0.00	0.27	0.70	0.01	4.99	61.36	0.00	25.10	0.13	0.00	0.00	5.67	8.15	0.19	100.59
Line 4 40AB_Line2	2.73	0.00	1.28	0.00	0.00	0.00	0.25	0.73	0.01	5.00	61.85	0.00	24.74	0.05	0.00	0.00	5.31	8.57	0.14	100.67
Line 5 40AB_Line2	2.78	0.00	1.23	0.00	0.00	0.00	0.20	0.77	0.01	4.99	63.02	0.00	23.67	0.09	0.00	0.00	4.17	9.04	0.17	100.15
Line 6 40AB_Line2	2.81	0.00	1.20	0.00	0.00	0.00	0.16	0.81	0.01	5.00	63.64	0.00	23.09	0.12	0.00	0.00	3.46	9.46	0.22	100.00
Line 7 40AB_Line2	2.77	0.00	1.24	0.00	0.00	0.00	0.19	0.78	0.01	5.00	62.65	0.00	23.76	0.10	0.00	0.00	4.09	9.07	0.25	99.93
Line 8 40AB_Line2	2.69	0.00	1.34	0.01	0.00	0.00	0.24	0.69	0.02	4.99	59.42	0.00	25.18	0.15	0.00	0.00	5.05	7.83	0.37	98.00
Line 9 40AB_Line2	2.71	0.00	1.31	0.00	0.00	0.00	0.26	0.70	0.01	5.00	61.04	0.00	25.05	0.10	0.00	0.00	5.57	8.18	0.19	100.13
Line 10 40AB_Line2	2.80	0.00	1.21	0.00	0.00	0.00	0.17	0.80	0.01	4.99	63.72	0.00	23.40	0.03	0.00	0.00	3.60	9.38	0.10	100.23
Line 1 40AB_Line4	2.67	0.00	1.34	0.00	0.00	0.00	0.30	0.68	0.01	5.00	60.21	0.00	25.73	0.05	0.00	0.00	6.35	7.91	0.17	100.41
Line 2 40AB_Line4	2.70	0.00	1.31	0.00	0.00	0.00	0.27	0.70	0.01	5.00	61.66	0.00	25.31	0.09	0.00	0.00	5.73	8.28	0.26	101.34
Line 3 40AB_Line4	2.69	0.00	1.33	0.00	0.00	0.00	0.28	0.68	0.01	5.00	60.54	0.00	25.39	0.11	0.00	0.00	5.92	7.92	0.25	100.12
Line 4 40AB_Line4	2.68	0.00	1.33	0.00	0.00	0.00	0.29	0.68	0.02	5.00	60.44	0.00	25.49	0.08	0.00	0.00	6.17	7.86	0.28	100.32
Line 5 40AB_Line4	2.67	0.00	1.34	0.00	0.00	0.00	0.30	0.67	0.02	5.00	60.10	0.00	25.55	0.06	0.00	0.00	6.25	7.81	0.27	100.05
Line 6 40AB_Line4	2.67	0.00	1.34	0.00	0.00	0.00	0.30	0.66	0.02	4.99	60.59	0.00	25.83	0.12	0.00	0.00	6.26	7.76	0.27	100.83
Line 7 40AB_Line4	2.66	0.00	1.35	0.00	0.00	0.00	0.31	0.66	0.02	5.00	60.27	0.00	25.89	0.07	0.00	0.00	6.45	7.72	0.29	100.70

Salt Mylonite Zone

Plagioclase	Normalized Atoms											Weight Percent									
Sample	Si	Ti	Al	Fe	Mn	Mg	Ca	Na	K	Total		SiO2	TiO2	Al2O3	FeO	MnO	MgO	CaO	Na2O	K2O	Total
Line 8 40AB_Line4	2.66	0.00	1.35	0.00	0.00	0.00	0.31	0.68	0.02	5.02		60.19	0.00	25.83	0.10	0.00	0.00	6.53	7.98	0.27	100.90
Line 9 40AB_Line4	2.67	0.00	1.35	0.00	0.00	0.00	0.31	0.65	0.02	4.99		60.27	0.00	25.88	0.09	0.00	0.00	6.52	7.61	0.28	100.65
Line 10 40AB_Line4	2.67	0.00	1.34	0.00	0.00	0.00	0.31	0.65	0.01	4.99		60.03	0.00	25.64	0.11	0.00	0.00	6.48	7.55	0.26	100.08
Line 11 40AB_Line4	2.67	0.00	1.34	0.00	0.00	0.00	0.31	0.67	0.01	5.00		60.31	0.00	25.72	0.12	0.00	0.00	6.45	7.81	0.24	100.65
Line 12 40AB_Line4	2.66	0.00	1.35	0.01	0.00	0.00	0.31	0.66	0.01	5.00		60.38	0.00	25.86	0.17	0.00	0.00	6.57	7.76	0.17	100.90
Line 13 40AB_Line4	2.65	0.00	1.36	0.01	0.00	0.00	0.31	0.67	0.01	5.01		60.24	0.00	26.17	0.20	0.00	0.00	6.65	7.82	0.17	101.25
Line 14 40AB_Line4	2.70	0.00	1.27	0.04	0.00	0.00	0.33	0.63	0.01	4.98		38.91	0.00	15.55	0.66	0.00	0.00	4.43	4.72	0.07	64.33
Line 1 40CB_Line1	2.73	0.00	1.28	0.01	0.00	0.00	0.25	0.66	0.07	5.00		51.02	0.00	20.26	0.18	0.00	0.00	4.38	6.39	0.99	83.23
Line 2 40CB_Line1	2.68	0.00	1.34	0.00	0.00	0.00	0.29	0.69	0.02	5.01		58.95	0.00	24.97	0.12	0.00	0.00	5.92	7.87	0.27	98.11
Line 3 40CB_Line1	2.68	0.00	1.33	0.00	0.00	0.00	0.28	0.71	0.01	5.02		59.39	0.00	25.05	0.10	0.00	0.00	5.79	8.14	0.26	98.74
Line 4 40CB_Line1	2.69	0.00	1.32	0.00	0.00	0.00	0.28	0.70	0.02	5.01		59.26	0.00	24.61	0.08	0.00	0.00	5.67	8.00	0.30	97.92
Line 5 40CB_Line1	2.69	0.00	1.31	0.00	0.00	0.00	0.26	0.73	0.02	5.03		58.83	0.00	24.33	0.11	0.00	0.00	5.36	8.28	0.31	97.22
Line 6 40CB_Line1	2.70	0.00	1.31	0.00	0.00	0.00	0.26	0.72	0.02	5.01		59.21	0.00	24.27	0.09	0.00	0.00	5.33	8.13	0.38	97.41
Line 7 40CB_Line1	2.66	0.00	1.31	0.03	0.00	0.00	0.34	0.67	0.02	5.04		55.92	0.00	23.40	0.85	0.00	0.00	6.77	7.33	0.33	94.59
Line 8 40CB_Line1	2.69	0.00	1.31	0.00	0.00	0.00	0.26	0.74	0.02	5.03		59.07	0.00	24.48	0.11	0.00	0.00	5.28	8.36	0.38	97.68
Line 9 40CB_Line1	2.70	0.00	1.30	0.00	0.00	0.00	0.24	0.77	0.02	5.04		62.08	0.00	25.41	0.02	0.00	0.00	5.19	9.17	0.37	102.23
Line 10 40CB_Line1	2.69	0.00	1.32	0.00	0.00	0.00	0.26	0.73	0.02	5.02		59.41	0.00	24.71	0.08	0.00	0.00	5.39	8.27	0.34	98.21
Line 11 40CB_Line1	2.70	0.00	1.32	0.00	0.00	0.00	0.26	0.72	0.02	5.01		60.94	0.00	25.35	0.06	0.00	0.00	5.39	8.37	0.35	100.46
Line 12 40CB_Line1	2.69	0.00	1.32	0.00	0.00	0.00	0.27	0.73	0.02	5.03		59.22	0.00	24.71	0.10	0.00	0.00	5.51	8.36	0.31	98.20
Line 13 40CB_Line1	2.69	0.00	1.32	0.00	0.00	0.00	0.28	0.70	0.02	5.01		59.37	0.00	24.62	0.09	0.00	0.00	5.68	7.98	0.32	98.04
Line 14 40CB_Line1	2.67	0.00	1.34	0.00	0.00	0.00	0.29	0.69	0.01	5.01		58.97	0.00	25.14	0.10	0.00	0.00	6.04	7.83	0.26	98.33
Line 15 40CB_Line1	2.69	0.00	1.33	0.00	0.00	0.00	0.27	0.68	0.02	4.99		57.79	0.00	24.16	0.10	0.00	0.00	5.38	7.52	0.38	95.33
Line 1 40CB_Line2	2.66	0.00	1.35	0.00	0.00	0.00	0.30	0.71	0.01	5.03		59.60	0.00	25.59	0.11	0.00	0.00	6.22	8.22	0.13	99.88
Line 2 40CB_Line2	2.67	0.00	1.34	0.00	0.00	0.00	0.29	0.68	0.02	5.01		59.63	0.00	25.43	0.10	0.00	0.00	6.07	7.85	0.28	99.35
Line 3 40CB_Line2	2.70	0.00	1.31	0.00	0.00	0.00	0.27	0.69	0.02	5.00		60.33	0.00	24.86	0.11	0.00	0.00	5.63	7.98	0.30	99.20
Line 4 40CB_Line2	2.71	0.00	1.30	0.00	0.00	0.00	0.26	0.72	0.02	5.01		60.58	0.00	24.62	0.07	0.00	0.00	5.36	8.28	0.37	99.28
Line 5 40CB_Line2	2.71	0.00	1.30	0.00	0.00	0.00	0.25	0.71	0.02	5.00		60.38	0.00	24.54	0.11	0.00	0.00	5.27	8.09	0.35	98.75
Line 6 40CB_Line2	2.72	0.00	1.30	0.00	0.00	0.00	0.25	0.72	0.02	5.00		60.75	0.00	24.57	0.06	0.00	0.00	5.19	8.26	0.40	99.24
Line 7 40CB_Line2	2.71	0.00	1.31	0.00	0.00	0.00	0.25	0.72	0.02	5.01		60.15	0.00	24.70	0.07	0.00	0.00	5.19	8.24	0.35	98.70
Line 8 40CB_Line2	2.71	0.00	1.30	0.00	0.00	0.00	0.25	0.74	0.02	5.02		60.15	0.00	24.38	0.08	0.00	0.00	5.13	8.47	0.32	98.53
Line 9 40CB_Line2	2.71	0.00	1.30	0.00	0.00	0.00	0.25	0.73	0.01	5.01		60.68	0.00	24.66	0.11	0.00	0.00	5.30	8.38	0.25	99.38
Line 10 40CB_Line2	2.69	0.00	1.32	0.00	0.00	0.00	0.27	0.72	0.01	5.01		59.44	0.00	24.67	0.09	0.00	0.00	5.54	8.16	0.19	98.08
Line 1 40CB_Line3	2.68	0.00	1.33	0.00	0.00	0.00	0.28	0.70	0.01	5.00		59.53	0.00	25.07	0.06	0.00	0.00	5.86	7.97	0.17	98.65
Line 2 40CB_Line3	2.70	0.00	1.31	0.00	0.00	0.00	0.26	0.72	0.01	5.01		63.24	0.00	25.98	0.09	0.00	0.00	5.57	8.73	0.20	103.81
Line 3 40CB_Line3	2.72	0.00	1.29	0.00	0.00	0.00	0.25	0.73	0.01	5.01		60.85	0.00	24.61	0.05	0.00	0.00	5.26	8.44	0.20	99.41
Line 4 40CB_Line3	2.74	0.00	1.27	0.00	0.00	0.00	0.22	0.75	0.01	5.00		61.61	0.00	24.16	0.08	0.00	0.00	4.70	8.73	0.19	99.47
Line 5 40CB_Line3	2.70	0.00	1.30	0.01	0.00	0.00	0.26	0.73	0.01	5.02		60.24	0.00	24.66	0.14	0.00	0.00	5.51	8.41	0.16	99.13

Salt Mylonite Zone

Plagioclase	Normalized Atoms											Weight Percent									
Sample	Si	Ti	Al	Fe	Mn	Mg	Ca	Na	K	Total		SiO2	TiO2	Al2O3	FeO	MnO	MgO	CaO	Na2O	K2O	Total
Line 6 40CB_Line3	2.71	0.00	1.30	0.00	0.00	0.00	0.26	0.72	0.01	5.01		60.83	0.00	24.84	0.11	0.00	0.00	5.41	8.39	0.19	99.77
Line 7 40CB_Line3	2.67	0.00	1.34	0.00	0.00	0.00	0.30	0.71	0.01	5.02		59.42	0.00	25.26	0.07	0.00	0.00	6.15	8.13	0.21	99.23
Line 1 40CB_Line4	2.69	0.00	1.32	0.01	0.00	0.00	0.27	0.71	0.01	5.01		60.43	0.00	25.15	0.16	0.00	0.00	5.72	8.19	0.24	99.90
Line 2 40CB_Line4	2.71	0.00	1.32	0.00	0.00	0.00	0.26	0.70	0.02	4.99		61.46	0.00	25.37	0.06	0.00	0.00	5.43	8.19	0.29	100.80
Line 3 40CB_Line4	2.73	0.00	1.29	0.00	0.00	0.00	0.25	0.69	0.02	4.98		63.70	0.00	25.47	0.07	0.00	0.00	5.39	8.26	0.32	103.21
Line 4 40CB_Line4	2.71	0.00	1.30	0.00	0.00	0.00	0.26	0.73	0.01	5.02		61.17	0.00	24.80	0.06	0.00	0.00	5.46	8.54	0.24	100.26
Line 5 40CB_Line4	2.72	0.00	1.29	0.00	0.00	0.00	0.25	0.72	0.02	5.00		61.21	0.00	24.73	0.07	0.00	0.00	5.32	8.33	0.31	99.95
Line 6 40CB_Line4	2.73	0.00	1.29	0.00	0.00	0.00	0.24	0.72	0.02	5.00		61.35	0.00	24.64	0.08	0.00	0.00	5.04	8.31	0.33	99.76
Line 7 40CB_Line4	2.71	0.00	1.31	0.00	0.00	0.00	0.27	0.70	0.02	5.00		59.59	0.00	24.45	0.06	0.00	0.00	5.47	7.95	0.30	97.82
Line 8 40CB_Line4	2.65	0.00	1.36	0.00	0.00	0.00	0.32	0.66	0.01	5.00		59.28	0.00	25.83	0.07	0.00	0.00	6.72	7.58	0.16	99.63
Line 1 40GB_Line1	2.61	0.00	1.40	0.01	0.00	0.00	0.36	0.63	0.01	5.01		58.23	0.00	26.52	0.18	0.00	0.00	7.50	7.23	0.23	99.90
Line 2 40GB_Line1	2.61	0.00	1.40	0.01	0.00	0.00	0.35	0.62	0.01	5.00		58.34	0.00	26.46	0.16	0.00	0.00	7.39	7.12	0.23	99.70
Line 3 40GB_Line1	2.66	0.00	1.35	0.00	0.00	0.00	0.31	0.67	0.02	5.01		59.54	0.00	25.66	0.10	0.00	0.00	6.38	7.77	0.28	99.74
Line 4 40GB_Line1	2.65	0.00	1.36	0.00	0.00	0.00	0.32	0.66	0.01	5.01		59.46	0.00	25.97	0.06	0.00	0.00	6.71	7.61	0.25	100.08
Line 5 40GB_Line1	2.72	0.00	1.29	0.00	0.00	0.00	0.25	0.72	0.02	5.00		61.49	0.00	24.66	0.11	0.00	0.00	5.30	8.36	0.33	100.24
Line 6 40GB_Line1	2.77	0.00	1.24	0.00	0.00	0.00	0.20	0.77	0.02	5.00		62.69	0.00	23.94	0.09	0.00	0.00	4.34	8.95	0.36	100.37
Line 7 40GB_Line1	2.68	0.00	1.33	0.00	0.00	0.00	0.29	0.68	0.02	5.00		60.82	0.00	25.63	0.08	0.00	0.00	6.07	7.98	0.32	100.91
Line 8 40GB_Line1	2.67	0.00	1.34	0.00	0.00	0.00	0.30	0.67	0.01	5.00		60.88	0.00	25.99	0.10	0.00	0.00	6.28	7.88	0.27	101.40
Line 9 40GB_Line1	2.58	0.00	1.39	0.00	0.00	0.00	0.44	0.45	0.19	5.05		35.76	0.00	16.39	-0.01	0.00	0.00	5.68	3.22	2.06	63.11
Line 1 40GB_Line2	2.73	0.00	1.28	0.00	0.00	0.00	0.24	0.74	0.02	5.01		61.82	0.00	24.55	0.13	0.00	0.00	5.02	8.64	0.29	100.45
Line 2 40GB_Line2	2.77	0.00	1.24	0.00	0.00	0.00	0.21	0.75	0.02	4.99		62.81	0.00	23.77	0.09	0.00	0.00	4.35	8.77	0.39	100.17
Line 3 40GB_Line2	2.82	0.00	1.20	0.00	0.00	0.00	0.16	0.78	0.02	4.99		63.90	0.00	23.10	0.09	0.00	0.00	3.46	9.19	0.40	100.14
Line 4 40GB_Line2	2.76	0.00	1.25	0.00	0.00	0.00	0.21	0.76	0.02	5.01		62.66	0.00	23.96	0.09	0.00	0.00	4.47	8.90	0.37	100.45
Line 5 40GB_Line2	2.71	0.00	1.30	0.00	0.00	0.00	0.27	0.71	0.02	5.01		61.54	0.00	25.14	0.05	0.00	0.00	5.73	8.32	0.31	101.09
Line 6 40GB_Line2	2.63	0.00	1.38	0.00	0.00	0.00	0.34	0.63	0.01	5.00		59.52	0.00	26.42	0.11	0.00	0.00	7.09	7.40	0.26	100.80
Line 7 40GB_Line2	2.65	0.00	1.37	0.00	0.00	0.00	0.33	0.63	0.01	4.99		59.87	0.00	26.28	0.09	0.00	0.00	6.93	7.37	0.24	100.80
Line 8 40GB_Line2	2.63	0.00	1.38	0.00	0.00	0.00	0.34	0.61	0.04	5.01		57.47	0.00	25.69	0.12	0.00	0.00	6.99	6.89	0.65	97.82
Line 1 40GB_Line3	2.61	0.00	1.39	0.00	0.00	0.00	0.36	0.64	0.01	5.02		59.05	0.00	26.76	0.06	0.00	0.00	7.63	7.41	0.19	101.10
Line 2 40GB_Line3	2.59	0.00	1.42	0.00	0.00	0.00	0.38	0.60	0.01	5.00		58.48	0.00	27.09	0.07	0.00	0.00	7.89	7.00	0.21	100.75
Line 3 40GB_Line3	2.64	0.00	1.37	0.00	0.00	0.00	0.34	0.65	0.01	5.01		59.20	0.00	26.06	0.09	0.00	0.00	7.03	7.49	0.25	100.11
Line 4 40GB_Line3	2.69	0.00	1.32	0.00	0.00	0.00	0.28	0.69	0.02	5.00		60.86	0.00	25.23	0.04	0.00	0.00	6.00	8.03	0.30	100.46
Line 5 40GB_Line3	2.77	0.00	1.24	0.00	0.00	0.00	0.21	0.75	0.02	5.00		62.83	0.00	23.87	0.07	0.00	0.00	4.46	8.82	0.35	100.39
Line 6 40GB_Line3	2.70	0.00	1.31	0.00	0.00	0.00	0.27	0.70	0.02	5.01		61.68	0.00	25.40	0.09	0.00	0.00	5.83	8.29	0.30	101.58
Line 7 40GB_Line3	2.63	0.00	1.38	0.00	0.00	0.00	0.34	0.63	0.01	5.00		59.88	0.00	26.65	0.08	0.00	0.00	7.28	7.42	0.26	101.56
Line 8 40GB_Line3	2.61	0.00	1.40	0.00	0.00	0.00	0.36	0.62	0.01	5.00		59.33	0.00	26.93	0.08	0.00	0.00	7.63	7.21	0.17	101.34
Line 1 40GB_Line4	2.62	0.00	1.39	0.00	0.00	0.00	0.35	0.62	0.01	5.00		59.38	0.00	26.81	0.10	0.00	0.00	7.45	7.30	0.24	101.28
Line 2 40GB_Line4	2.72	0.00	1.30	0.00	0.00	0.00	0.25	0.72	0.02	5.01		61.64	0.00	24.96	0.06	0.00	0.00	5.31	8.48	0.32	100.77

Salt Mylonite Zone

Plagioclase	Normalized Atoms											Weight Percent									
Sample	Si	Ti	Al	Fe	Mn	Mg	Ca	Na	K	Total		SiO2	TiO2	Al2O3	FeO	MnO	MgO	CaO	Na2O	K2O	Total
Line 3 40GB_Line4	2.74	0.00	1.27	0.00	0.00	0.00	0.23	0.74	0.02	5.00		62.30	0.00	24.45	0.07	0.00	0.00	4.91	8.69	0.28	100.70
Line 4 40GB_Line4	2.63	0.00	1.38	0.00	0.00	0.00	0.34	0.64	0.01	5.01		59.49	0.00	26.55	0.08	0.00	0.00	7.18	7.53	0.23	101.05
Line 5 40GB_Line4	2.65	0.00	1.36	0.00	0.00	0.00	0.32	0.67	0.01	5.01		59.73	0.00	25.98	0.08	0.00	0.00	6.69	7.74	0.26	100.49
Line 6 40GB_Line4	2.67	0.00	1.34	0.00	0.00	0.00	0.31	0.67	0.01	5.00		60.40	0.00	25.84	0.08	0.00	0.00	6.49	7.82	0.26	100.88
Line 7 40GB_Line4	2.65	0.00	1.35	0.00	0.00	0.00	0.32	0.68	0.01	5.01		60.50	0.00	26.23	0.07	0.00	0.00	6.76	7.95	0.22	101.73
Line 8 40GB_Line4	2.61	0.00	1.39	0.00	0.00	0.00	0.36	0.64	0.01	5.02		58.96	0.00	26.73	0.07	0.00	0.00	7.59	7.41	0.25	101.01
Line 9 40GB_Line4	2.70	0.00	1.30	0.00	0.00	0.00	0.26	0.45	0.34	5.05		56.34	0.00	22.97	0.09	0.00	0.00	4.98	4.90	5.55	94.83
Line 1 40GB_Line5	2.59	0.00	1.43	0.00	0.00	0.00	0.38	0.59	0.01	5.00		58.45	0.00	27.34	0.06	0.00	0.00	8.05	6.86	0.18	100.93
Line 2 40GB_Line5	2.61	0.00	1.40	0.00	0.00	0.00	0.36	0.62	0.01	5.00		59.47	0.00	27.05	0.04	0.00	0.00	7.73	7.23	0.15	101.67
Line 3 40GB_Line5	2.71	0.00	1.30	0.00	0.00	0.00	0.27	0.70	0.02	5.00		61.38	0.00	25.05	0.08	0.00	0.00	5.68	8.23	0.29	100.70
Line 4 40GB_Line5	2.78	0.00	1.24	0.00	0.00	0.00	0.20	0.76	0.02	5.00		62.79	0.00	23.75	0.06	0.00	0.00	4.27	8.87	0.34	100.08
Line 5 40GB_Line5	2.74	0.00	1.27	0.00	0.00	0.00	0.24	0.74	0.02	5.00		62.22	0.00	24.48	0.08	0.00	0.00	5.02	8.65	0.32	100.77
Line 6 40GB_Line5	2.68	0.00	1.33	0.00	0.00	0.00	0.29	0.68	0.02	5.00		60.35	0.00	25.33	0.09	0.00	0.00	6.01	7.90	0.30	99.99
Line 7 40GB_Line5	2.62	0.00	1.39	0.00	0.00	0.00	0.35	0.63	0.01	5.00		59.54	0.00	26.71	0.05	0.00	0.00	7.43	7.36	0.23	101.31
Line 8 40GB_Line5	2.64	0.00	1.37	0.00	0.00	0.00	0.33	0.60	0.04	4.99		58.72	0.00	25.88	0.09	0.00	0.00	6.90	6.89	0.73	99.22

Salt Mylonite Zone

Garnet	Normalized Atoms											Weight Percent									
Sample	Si	Ti	Al	Fe	Mn	Mg	Ca	Na	K	Total		SiO2	TiO2	Al2O3	FeO	MnO	MgO	CaO	Na2O	K2O	Total
21BA4(NW11)	2.95	0.00	2.06	1.06	0.02	1.40	0.54	0.00	0.00	8.02		40.09	0.02	23.76	17.19	0.38	12.74	6.90	0.00	0.00	101.08
21BA4(NW11)	2.95	0.00	2.06	1.08	0.02	1.40	0.51	0.00	0.00	8.02		40.32	0.00	23.89	17.67	0.35	12.83	6.56	0.00	0.00	101.62
21BA4(NW11)	2.94	0.00	2.07	1.07	0.02	1.38	0.54	0.00	0.00	8.02		40.26	0.01	24.05	17.48	0.38	12.65	6.93	0.00	0.00	101.77
21BA4(NW11)	2.53	0.00	2.33	1.23	0.02	1.58	0.60	0.00	0.00	8.30		30.64	0.04	23.94	17.79	0.35	12.79	6.77	0.00	0.00	92.33
21BA4(NW11)	2.95	0.00	2.05	1.08	0.02	1.38	0.54	0.00	0.00	8.03		40.61	0.00	23.91	17.82	0.32	12.76	6.97	0.00	0.00	102.39
21BA4(NW11)	2.94	0.00	2.05	1.09	0.02	1.41	0.51	0.00	0.00	8.03		40.46	0.02	23.92	17.91	0.39	13.02	6.51	0.00	0.00	102.22
21BA4(NW11)	2.95	0.00	2.04	1.10	0.02	1.42	0.50	0.00	0.00	8.03		40.34	0.00	23.60	17.89	0.40	12.97	6.42	0.00	0.00	101.62
21BAgrt1	2.93	0.00	2.04	1.10	0.03	1.41	0.53	0.00	0.00	8.04		39.75	0.00	23.43	17.87	0.49	12.85	6.71	0.00	0.00	101.11
21BAgrt1	2.94	0.00	2.03	1.08	0.03	1.37	0.59	0.00	0.00	8.04		39.87	0.00	23.38	17.55	0.44	12.48	7.48	0.00	0.00	101.20
21BAgrt1	2.93	0.00	2.03	1.10	0.03	1.39	0.55	0.00	0.00	8.04		39.82	0.00	23.43	17.85	0.50	12.63	6.99	0.00	0.00	101.21
21BAgrt1	2.93	0.00	2.04	1.21	0.03	1.30	0.53	0.00	0.00	8.04		39.62	0.00	23.35	19.53	0.51	11.78	6.63	0.00	0.00	101.42
21BAgrt2	2.93	0.00	2.04	1.14	0.03	1.38	0.51	0.00	0.00	8.04		39.98	0.00	23.65	18.64	0.49	12.62	6.51	0.00	0.00	101.90
21BAgrt2	2.94	0.00	2.04	1.09	0.03	1.37	0.56	0.00	0.00	8.03		40.42	0.00	23.85	17.91	0.45	12.66	7.23	0.00	0.00	102.52
21BAgrt2	2.94	0.00	2.04	1.10	0.03	1.38	0.55	0.00	0.00	8.04		39.93	0.00	23.56	17.94	0.49	12.60	6.94	0.00	0.00	101.47
21BAgrt2	2.94	0.00	2.04	1.08	0.03	1.40	0.55	0.00	0.00	8.03		40.28	0.00	23.67	17.63	0.47	12.83	6.97	0.00	0.00	101.84
21BAgrt2	2.93	0.00	2.05	1.09	0.03	1.42	0.51	0.00	0.00	8.04		39.33	0.00	23.37	17.52	0.48	12.81	6.41	0.00	0.00	99.92
21BAtest1	2.97	0.00	2.05	1.08	0.03	1.34	0.54	0.00	0.00	8.01		39.93	0.00	23.43	17.33	0.46	12.11	6.79	0.00	0.00	100.04
21BAtest2	2.98	0.00	2.05	1.08	0.03	1.36	0.49	0.00	0.00	8.00		40.32	0.00	23.51	17.55	0.56	12.37	6.25	0.00	0.00	100.56
21BAtest3	3.01	0.00	2.05	1.10	0.03	1.25	0.54	0.00	0.00	7.97		40.19	0.04	23.21	17.50	0.48	11.17	6.68	0.00	0.00	99.27
21BAtest3	3.00	0.00	2.05	1.09	0.03	1.24	0.56	0.00	0.00	7.97		40.13	0.00	23.33	17.40	0.44	11.15	7.04	0.00	0.00	99.49
21BAtest4	3.01	0.00	2.09	1.08	0.03	1.15	0.58	0.00	0.00	7.94		39.87	0.02	23.43	17.09	0.49	10.17	7.20	0.00	0.00	98.27
21BAtest5	2.99	0.00	2.06	1.06	0.03	1.25	0.58	0.00	0.00	7.98		40.43	0.04	23.59	17.17	0.49	11.37	7.28	0.00	0.00	100.38
21BAtest6	3.00	0.00	2.04	1.08	0.03	1.27	0.55	0.00	0.00	7.98		40.50	0.08	23.39	17.50	0.50	11.48	6.98	0.00	0.00	100.43
21BAtest7	2.97	0.00	2.05	1.07	0.03	1.34	0.54	0.00	0.00	8.01		40.03	0.00	23.51	17.19	0.51	12.17	6.83	0.00	0.00	100.23
21BAtest8	2.99	0.00	2.02	1.08	0.03	1.32	0.56	0.00	0.00	8.00		40.60	0.02	23.34	17.49	0.48	11.99	7.08	0.00	0.00	101.01
21BAtest9	2.99	0.00	2.02	1.07	0.03	1.32	0.57	0.00	0.00	8.00		40.19	0.01	23.10	17.14	0.45	11.95	7.14	0.00	0.00	99.99
21BAtest10	2.99	0.00	2.02	1.06	0.03	1.33	0.55	0.00	0.00	7.99		40.66	0.02	23.28	17.25	0.52	12.11	6.99	0.00	0.00	100.83
21Bgrt1.1	3.00	0.00	2.03	1.06	0.03	1.33	0.54	0.00	0.00	7.98		41.12	0.00	23.65	17.30	0.49	12.19	6.91	0.00	0.00	101.66
21Bgrt1.2	2.98	0.00	2.04	1.07	0.03	1.35	0.54	0.00	0.00	8.00		40.42	0.03	23.43	17.39	0.43	12.31	6.80	0.00	0.00	100.82
21Bgrt1.3	2.99	0.00	2.03	1.06	0.03	1.33	0.54	0.00	0.00	7.98		40.92	0.08	23.57	17.29	0.44	12.20	6.84	0.00	0.00	101.33
21Bgrt1.4	3.00	0.00	2.03	1.07	0.03	1.33	0.54	0.00	0.00	7.99		40.73	0.00	23.41	17.34	0.46	12.16	6.82	0.00	0.00	100.92
21Bgrt2.1	2.99	0.00	2.02	1.08	0.03	1.34	0.55	0.00	0.00	8.00		40.37	0.07	23.11	17.43	0.45	12.12	6.95	0.00	0.00	100.49
21Bgrt2.2	2.99	0.00	2.02	1.08	0.03	1.37	0.51	0.00	0.00	8.00		40.31	0.02	23.12	17.47	0.51	12.39	6.48	0.00	0.00	100.30
21Bgrt2.3	2.97	0.00	2.00	1.08	0.03	1.41	0.54	0.00	0.00	8.03		39.35	0.02	22.51	17.17	0.53	12.59	6.66	0.00	0.00	98.83
21Bgrt2.4	2.99	0.00	2.01	1.07	0.03	1.36	0.53	0.00	0.00	8.00		40.52	0.01	23.08	17.38	0.52	12.38	6.73	0.00	0.00	100.62
21Bgrt3.1	2.98	0.00	2.00	1.10	0.03	1.36	0.54	0.00	0.00	8.02		40.17	0.03	22.84	17.69	0.53	12.25	6.81	0.00	0.00	100.32
21Bgrt3.2	2.97	0.00	2.00	1.09	0.03	1.38	0.56	0.00	0.00	8.03		39.84	0.04	22.67	17.45	0.50	12.36	6.94	0.00	0.00	99.80

Salt Mylonite Zone

Garnet	Normalized Atoms											Weight Percent									
21Bgrt3.3	2.99	0.00	1.99	1.08	0.03	1.37	0.55	0.00	0.00	8.02		39.98	0.01	22.62	17.34	0.53	12.28	6.87	0.00	0.00	99.64
21Bgrt3.4	2.99	0.00	2.01	1.08	0.03	1.35	0.54	0.00	0.00	8.00		40.29	0.03	22.93	17.42	0.47	12.16	6.78	0.00	0.00	100.08
21Btest1	3.02	0.00	2.02	1.07	0.03	1.31	0.52	0.00	0.00	7.97		41.12	0.05	23.29	17.43	0.53	11.96	6.66	0.00	0.00	101.05
21Btest2	3.01	0.00	2.02	1.08	0.03	1.30	0.53	0.00	0.00	7.98		41.12	0.01	23.44	17.61	0.47	11.94	6.78	0.00	0.00	101.37
21B_Garnet1_c1	3.03	0.00	1.94	1.08	0.03	1.37	0.54	0.00	0.00	7.99		41.43	0.04	22.49	17.61	0.43	12.56	6.84	0.00	0.00	101.39
21B_Garnet1_c2	3.03	0.00	1.95	1.07	0.03	1.37	0.54	0.00	0.00	7.99		41.28	0.03	22.61	17.43	0.47	12.52	6.86	0.00	0.00	101.20
21B_Garnet1_c3	3.04	0.00	1.94	1.07	0.03	1.36	0.54	0.00	0.00	7.98		41.28	0.02	22.41	17.44	0.49	12.43	6.79	0.00	0.00	100.85
21B_Garnet1_c4	3.03	0.00	1.95	1.07	0.03	1.37	0.53	0.00	0.00	7.99		41.24	0.03	22.61	17.52	0.47	12.56	6.73	0.00	0.00	101.15
21B_Garnet2_c1	3.03	0.00	1.94	1.08	0.03	1.37	0.54	0.00	0.00	7.98		41.27	0.02	22.38	17.57	0.47	12.48	6.89	0.00	0.00	101.08
21B_Garnet2_c2	3.03	0.00	1.95	1.08	0.03	1.38	0.53	0.00	0.00	7.99		41.06	0.01	22.45	17.46	0.48	12.56	6.70	0.00	0.00	100.72
21B_Garnet2_c3	3.03	0.00	1.94	1.08	0.03	1.38	0.52	0.00	0.00	7.98		41.35	-0.01	22.49	17.59	0.52	12.67	6.56	0.00	0.00	101.17
21B_Garnet2_c4	3.03	0.00	1.94	1.08	0.03	1.38	0.52	0.00	0.00	7.98		41.12	0.04	22.32	17.50	0.53	12.57	6.61	0.00	0.00	100.69
21B_Garnet3_c1	3.02	0.00	1.94	1.09	0.03	1.37	0.55	0.00	0.00	8.00		40.90	0.01	22.29	17.61	0.44	12.44	6.96	0.00	0.00	100.64
21B_Garnet3_c2	3.04	0.00	1.93	1.08	0.03	1.36	0.54	0.00	0.00	7.98		41.27	0.02	22.19	17.59	0.48	12.39	6.84	0.00	0.00	100.77
21B_Garnet3_c3	3.03	0.00	1.93	1.10	0.03	1.36	0.53	0.00	0.00	7.99		41.34	0.01	22.36	17.99	0.45	12.45	6.72	0.00	0.00	101.33
21B_Garnet3_c4	3.03	0.00	1.94	1.07	0.03	1.39	0.53	0.00	0.00	7.99		41.29	0.02	22.43	17.44	0.53	12.70	6.75	0.00	0.00	101.17
31Agrt1.1	2.98	0.00	2.04	1.31	0.03	0.72	0.91	0.00	0.00	7.99		39.71	0.05	23.07	20.87	0.41	6.41	11.37	0.00	0.00	101.89
31Agrt1.2	2.99	0.00	2.03	1.32	0.03	0.73	0.89	0.00	0.00	7.99		39.96	0.05	23.08	21.07	0.47	6.56	11.14	0.00	0.00	102.33
31Agrt1.3	2.98	0.00	2.03	1.34	0.03	0.74	0.88	0.00	0.00	8.00		39.80	0.04	23.01	21.32	0.45	6.61	10.98	0.00	0.00	102.20
31Agrt1.4	2.99	0.00	2.00	1.37	0.02	0.75	0.89	0.00	0.00	8.02		39.12	0.02	22.19	21.43	0.37	6.63	10.85	0.00	0.00	100.60
31Agrt2.1	3.00	0.00	2.02	1.34	0.03	0.72	0.87	0.00	0.00	7.98		40.17	0.03	22.89	21.35	0.45	6.48	10.90	0.00	0.00	102.28
31Agrt2.2	2.99	0.00	2.03	1.33	0.03	0.72	0.90	0.00	0.00	7.99		39.96	0.06	22.96	21.18	0.40	6.41	11.21	0.00	0.00	102.17
31Agrt2.3	2.98	0.00	2.02	1.37	0.03	0.73	0.87	0.00	0.00	8.00		39.56	0.04	22.69	21.66	0.43	6.52	10.76	0.00	0.00	101.67
31Agrt2.4	2.99	0.01	2.01	1.36	0.03	0.74	0.87	0.00	0.00	8.00		39.78	0.09	22.66	21.71	0.46	6.62	10.76	0.00	0.00	102.07
31Agrt1.1	2.93	0.00	2.07	1.30	0.04	0.75	0.94	0.00	0.00	8.03		38.56	0.06	23.02	20.39	0.57	6.61	11.53	0.00	0.00	100.76
31Agrt1.2	2.93	0.00	2.08	1.34	0.03	0.81	0.83	0.00	0.00	8.03		38.51	0.02	23.19	21.12	0.41	7.15	10.22	0.00	0.00	100.62
31Agrt2.1	2.94	0.00	2.07	1.35	0.03	0.80	0.84	0.00	0.00	8.02		38.62	0.06	23.14	21.27	0.40	7.02	10.26	0.00	0.00	100.78
31Agrt2.2	2.94	0.00	2.07	1.32	0.03	0.79	0.87	0.00	0.00	8.02		38.61	0.07	23.09	20.68	0.40	7.00	10.69	0.00	0.00	100.54
31Agrt2.3	2.93	0.00	2.07	1.31	0.03	0.83	0.86	0.00	0.00	8.03		38.56	0.05	23.08	20.58	0.40	7.28	10.60	0.00	0.00	100.55
31Agrt3.1	2.93	0.00	2.07	1.31	0.03	0.82	0.85	0.00	0.00	8.03		38.45	0.03	23.08	20.60	0.42	7.23	10.46	0.00	0.00	100.28
31Agrt3.2	2.93	0.00	2.07	1.31	0.03	0.77	0.91	0.00	0.00	8.03		38.41	0.01	23.04	20.44	0.39	6.81	11.17	0.00	0.00	100.27
31Agrt3.3	2.93	0.00	2.08	1.31	0.03	0.79	0.90	0.00	0.00	8.03		38.28	0.03	23.04	20.51	0.40	6.91	10.96	0.00	0.00	100.12

Salt Mylonite Zone

Pyroxene	Normalized Atoms											Weight Percent									
Sample	Si	Ti	Al	Fe	Mn	Mg	Ca	Na	K	Total		SiO2	TiO2	Al2O3	FeO	MnO	MgO	CaO	Na2O	K2O	Total
21BAcpx1.1	1.95	0.00	0.43	0.08	0.00	0.59	0.61	0.35	0.00	4.01		54.66	0.07	10.25	2.71	0.05	11.05	16.01	5.10	0.02	100.05
21BAcpx1.2	1.95	0.00	0.43	0.08	0.00	0.58	0.60	0.35	0.00	4.00		54.94	0.07	10.33	2.64	0.03	11.04	15.83	5.13	0.02	100.17
21BAcpx1.3	1.94	0.00	0.43	0.08	0.00	0.58	0.61	0.36	0.00	4.01		54.59	0.07	10.32	2.63	0.03	11.01	15.97	5.27	0.02	100.06
21BAcpx1.4	1.96	0.00	0.42	0.08	0.00	0.58	0.59	0.37	0.00	4.00		55.28	0.07	10.08	2.59	0.05	10.89	15.40	5.34	0.01	99.91
21BAcpx2.1	1.94	0.00	0.44	0.08	0.00	0.59	0.61	0.35	0.00	4.01		54.70	0.10	10.49	2.80	0.02	11.12	15.93	5.08	0.02	100.35
21BAcpx2.2	1.94	0.00	0.43	0.08	0.00	0.60	0.61	0.36	0.00	4.02		54.07	0.09	10.18	2.72	0.05	11.29	16.01	5.12	0.01	99.60
21BAcpx2.3	1.95	0.00	0.43	0.08	0.00	0.59	0.60	0.36	0.00	4.01		54.32	0.06	10.18	2.72	0.05	11.09	15.71	5.12	0.02	99.37
21BAcpx2.4	1.93	0.00	0.43	0.09	0.00	0.59	0.63	0.33	0.00	4.01		54.41	0.13	10.35	2.89	0.04	11.15	16.45	4.85	0.01	100.41
21BAcpx3.1	1.94	0.00	0.43	0.08	0.00	0.59	0.61	0.35	0.00	4.02		54.13	0.07	10.26	2.74	0.03	11.09	15.99	5.08	0.01	99.52
21BAcpx3.2	1.93	0.00	0.44	0.08	0.00	0.59	0.61	0.35	0.00	4.02		53.94	0.09	10.42	2.67	0.05	11.06	16.00	5.10	0.02	99.46
21BAcpx3.3	1.93	0.00	0.44	0.08	0.00	0.60	0.61	0.34	0.00	4.01		53.64	0.08	10.45	2.71	0.05	11.11	15.95	4.89	0.02	99.06
31Acpx1.1	1.93	0.00	0.60	0.12	0.00	0.39	0.46	0.52	0.00	4.03		54.69	0.12	14.31	4.04	0.04	7.40	12.11	7.60	0.02	100.33
31Acpx1.2	1.95	0.00	0.62	0.10	0.00	0.38	0.42	0.55	0.00	4.01		55.41	0.04	15.03	3.32	0.02	7.19	11.06	8.03	0.03	100.11
31Acpx1.3	1.94	0.00	0.63	0.09	0.00	0.38	0.43	0.55	0.00	4.02		54.93	0.05	15.04	3.02	0.02	7.21	11.24	8.07	0.02	99.57
31Acpx1.4	1.94	0.00	0.63	0.09	0.00	0.39	0.43	0.54	0.00	4.02		54.56	0.04	15.02	3.05	0.02	7.28	11.37	7.89	0.03	99.21
31Acpx2.1	1.96	0.00	0.61	0.09	0.00	0.38	0.41	0.55	0.00	4.01		56.42	0.04	14.86	3.19	0.00	7.27	10.96	8.15	0.02	100.90
31Acpx2.2	1.96	0.00	0.61	0.09	0.00	0.38	0.41	0.54	0.00	4.00		56.26	0.05	14.95	3.16	0.02	7.26	11.04	8.05	0.02	100.78
31Acpx2.3	1.96	0.00	0.61	0.09	0.00	0.38	0.42	0.54	0.00	4.00		56.15	0.04	14.91	3.17	0.03	7.21	11.18	7.91	0.02	100.60
31Acpx2.4	1.95	0.00	0.62	0.09	0.00	0.38	0.42	0.55	0.00	4.01		55.72	0.07	14.93	3.23	0.01	7.24	11.29	8.09	0.02	100.59
31Acpx3.1	1.95	0.00	0.61	0.10	0.00	0.38	0.43	0.52	0.00	4.00		55.62	0.07	14.62	3.55	0.02	7.30	11.43	7.69	0.01	100.31
31Acpx3.2	1.94	0.00	0.60	0.10	0.00	0.39	0.45	0.53	0.00	4.02		54.70	0.08	14.43	3.50	0.02	7.43	11.72	7.77	0.02	99.65
31Acpx3.3	1.95	0.00	0.62	0.10	0.00	0.38	0.42	0.54	0.00	4.01		55.11	0.07	14.87	3.32	0.04	7.27	11.14	7.92	0.02	99.72
31Acpx3.4	1.93	0.00	0.61	0.12	0.00	0.38	0.46	0.53	0.00	4.03		54.26	0.10	14.57	4.04	0.02	7.26	12.08	7.64	0.02	100.00

Finnoya Mylonite Zone

Plagioclase	Normalized Atoms											Weight Percent									
Sample	Si	Ti	Al	Fe	Mn	Mg	Ca	Na	K	Total		SiO2	TiO2	Al2O3	FeO	MnO	MgO	CaO	Na2O	K2O	Total
NW10-53Agrtcpxleft-fsp	1.97	0.00	1.36	0.97	0.10	0.34	0.62	0.00	0.00	5.35		38.62	0.04	22.60	22.88	2.23	4.45	11.32	0.00	0.00	102.14
NW10-53Agrtcpxleft-fsp	2.66	0.00	1.34	0.01	0.00	0.00	0.33	0.64	0.01	5.00		59.67	0.00	25.63	0.20	0.00	0.00	7.01	7.38	0.26	100.15
NW10-53Agrtcpxleft-fsp	2.63	0.00	1.37	0.00	0.00	0.00	0.37	0.61	0.02	4.99		59.20	0.00	26.27	0.09	0.00	0.00	7.69	7.04	0.27	100.56
NW10-53Agrtcpxleft-fsp	2.74	0.00	1.27	0.00	0.00	0.00	0.25	0.52	0.20	4.98		62.21	0.01	24.33	0.08	0.00	0.01	5.27	6.04	3.64	101.58
NW10-53Agrtcpxleft-fsp	2.63	0.00	1.38	0.01	0.00	0.00	0.36	0.60	0.01	4.99		59.26	0.01	26.46	0.16	0.01	0.00	7.61	7.00	0.26	100.78
NW10-53Agrtcpxleft-fsp	2.59	0.00	1.42	0.01	0.00	0.00	0.40	0.55	0.02	4.98		58.43	0.00	27.31	0.15	0.00	0.00	8.52	6.40	0.27	101.09
NW10-53Agrtcpxleft-fsp	2.63	0.00	1.38	0.01	0.00	0.00	0.35	0.61	0.01	4.99		59.68	0.01	26.50	0.14	0.00	0.00	7.33	7.13	0.24	101.03
NW10-53Agrtcpxleft-fsp	2.65	0.00	1.35	0.01	0.00	0.00	0.35	0.61	0.02	4.99		59.97	0.00	26.02	0.20	0.02	0.00	7.40	7.11	0.28	100.99
NW10-53Agrtcpxleft-fsp	2.68	0.00	1.33	0.00	0.00	0.00	0.32	0.65	0.02	4.99		60.74	0.00	25.57	0.11	0.00	0.01	6.69	7.57	0.27	100.96
NW10-53Agrtcpxleft-fsp	2.65	0.00	1.35	0.01	0.00	0.00	0.34	0.62	0.02	4.99		60.01	0.00	25.89	0.16	0.00	0.00	7.18	7.25	0.30	100.79
NW10-53Agrtcpxleft-fsp	2.64	0.00	1.36	0.01	0.00	0.00	0.35	0.62	0.02	4.99		59.87	0.00	26.18	0.15	0.00	0.00	7.33	7.25	0.27	101.05
NW10-53Agrtcpxleft-fsp	2.68	0.00	1.32	0.01	0.00	0.00	0.31	0.65	0.02	4.99		60.86	0.04	25.44	0.17	0.05	0.00	6.61	7.57	0.33	101.07
NW10-53Agrtcpxleft-fsp	2.70	0.00	1.31	0.00	0.00	0.00	0.29	0.68	0.01	4.99		61.21	0.01	25.14	0.11	0.00	0.00	6.13	7.95	0.26	100.82
NW10-53Agrtcpxctr_fsp	1.97	0.00	1.35	0.98	0.08	0.38	0.58	0.00	0.00	5.35		38.71	0.01	22.47	23.02	1.84	5.01	10.68	0.04	0.00	101.78
NW10-53Agrtcpxctr_fsp	1.97	0.00	1.34	0.99	0.09	0.37	0.58	0.00	0.00	5.35		38.64	0.07	22.35	23.10	2.18	4.91	10.53	0.04	0.00	101.82
NW10-53Agrtcpxctr_fsp	1.98	0.00	1.34	0.99	0.09	0.37	0.57	0.00	0.00	5.35		38.73	0.06	22.27	23.10	2.11	4.85	10.43	0.04	0.01	101.62
NW10-53Agrtcpxctr_fsp	1.97	0.00	1.36	0.98	0.10	0.36	0.57	0.00	0.00	5.35		38.69	0.02	22.64	22.96	2.26	4.75	10.52	0.05	0.01	101.89
NW10-53Agrtcpxctr_fsp	1.98	0.00	1.35	0.98	0.09	0.37	0.58	0.00	0.00	5.35		38.76	0.08	22.43	22.92	2.01	4.87	10.58	0.03	0.01	101.70
NW10-53Agrtcpxctr_fsp	1.97	0.00	1.35	0.98	0.09	0.38	0.58	0.00	0.00	5.35		38.68	0.06	22.59	23.04	2.03	5.05	10.56	0.03	0.00	102.04
NW10-53Agrtcpxctr_fsp	1.98	0.00	1.34	0.97	0.09	0.37	0.58	0.01	0.00	5.35		38.85	0.08	22.27	22.71	2.15	4.89	10.53	0.06	0.02	101.56
NW10-53Agrtcpxctr_fsp	1.98	0.00	1.34	0.98	0.09	0.38	0.58	0.01	0.00	5.35		38.90	0.07	22.42	22.95	2.02	4.97	10.57	0.05	0.00	101.97
NW10-53Agrtcpxctr_fsp	1.98	0.00	1.34	0.99	0.09	0.37	0.57	0.00	0.00	5.35		38.99	0.07	22.48	23.21	2.04	4.91	10.50	0.05	0.03	102.28
NW10-53Agrtcpxctr_fsp	1.97	0.00	1.34	0.98	0.10	0.36	0.58	0.00	0.00	5.35		38.75	0.12	22.40	23.09	2.28	4.79	10.63	0.04	0.01	102.11
NW10-53Agrtcpxctr_fsp	1.98	0.00	1.34	0.98	0.10	0.37	0.58	0.00	0.00	5.35		38.53	0.08	22.19	22.73	2.38	4.83	10.50	0.04	0.00	101.28
NW10-53Agrtcpxctr-fsp	2.60	0.00	1.40	0.01	0.00	0.00	0.40	0.57	0.01	4.99		58.46	0.01	26.66	0.20	0.02	0.00	8.35	6.64	0.21	100.56
NW10-53Agrtcpxctr-fsp	2.62	0.00	1.38	0.01	0.00	0.00	0.39	0.58	0.01	4.99		58.70	0.01	26.19	0.25	0.03	0.00	8.07	6.69	0.23	100.16
NW10-53Agrtcpxctr-fsp	2.69	0.00	1.30	0.01	0.00	0.00	0.33	0.64	0.02	4.98		60.28	0.00	24.76	0.14	0.01	0.00	6.81	7.40	0.29	99.69
NW10-53Agrtcpxctr-fsp	2.63	0.00	1.37	0.01	0.00	0.00	0.37	0.59	0.01	4.99		59.10	0.00	26.15	0.21	0.01	0.01	7.83	6.82	0.23	100.36
NW10-53Agrtcpxctr-fsp	2.58	0.00	1.43	0.00	0.00	0.00	0.42	0.54	0.01	4.99		57.78	0.01	27.23	0.13	0.00	0.00	8.84	6.27	0.20	100.47
NW10-53Agrtcpxctr-fsp	2.62	0.00	1.39	0.01	0.00	0.00	0.38	0.58	0.01	4.98		58.99	0.00	26.49	0.14	0.01	0.01	8.07	6.73	0.20	100.62
NW10-53Agrtcpxctr-fsp	2.66	0.00	1.34	0.01	0.00	0.00	0.33	0.63	0.01	4.99		59.99	0.00	25.70	0.14	0.00	0.00	6.91	7.32	0.25	100.31
NW10-53Agrtcpxctr-fsp	2.68	0.00	1.32	0.00	0.00	0.00	0.33	0.64	0.01	4.98		60.41	0.00	25.26	0.05	0.03	0.00	6.84	7.41	0.22	100.23
NW10-53Agrtcpxctr-fsp	2.69	0.00	1.31	0.00	0.00	0.00	0.32	0.64	0.02	4.98		60.41	0.00	24.99	0.11	0.00	0.00	6.68	7.38	0.36	99.94
NW10-53Agrtcpxctr-fsp	2.71	0.00	1.29	0.00	0.00	0.00	0.30	0.66	0.02	4.98		61.09	0.00	24.63	0.10	0.02	0.00	6.26	7.68	0.36	100.15
NW10-53A_plag	2.23	0.00	1.68	0.01	0.00	0.00	0.44	1.14	0.02	5.52		25.54	0.00	16.35	0.13	0.00	0.00	4.70	6.77	0.17	53.66
NW10-53A_plagkspar	2.75	0.00	1.26	0.01	0.00	0.00	0.25	0.70	0.01	4.98		62.24	0.01	24.15	0.15	0.01	0.00	5.33	8.17	0.22	100.28
NW10-53A_plagkspar	2.72	0.00	1.28	0.00	0.00	0.00	0.30	0.67	0.01	4.98		61.34	0.00	24.52	0.08	0.04	0.01	6.23	7.84	0.19	100.25

Finnoya Mylonite Zone

Plagioclase	Normalized Atoms											Weight Percent									
Sample	Si	Ti	Al	Fe	Mn	Mg	Ca	Na	K	Total		SiO2	TiO2	Al2O3	FeO	MnO	MgO	CaO	Na2O	K2O	Total
NW10-53Agrtcpxleft-fsp	2.66	0.00	1.34	0.01	0.00	0.00	0.33	0.64	0.01	5.00		59.67	0.00	25.63	0.20	0.00	0.00	7.01	7.38	0.26	100.15
NW10-53Agrtcpxleft-fsp	2.63	0.00	1.37	0.00	0.00	0.00	0.37	0.61	0.02	4.99		59.20	0.00	26.27	0.09	0.00	0.00	7.69	7.04	0.27	100.56
NW10-53Agrtcpxleft-fsp	2.74	0.00	1.27	0.00	0.00	0.00	0.25	0.52	0.20	4.98		62.21	0.01	24.33	0.08	0.00	0.01	5.27	6.04	3.64	101.58
NW10-53Agrtcpxleft-fsp	2.63	0.00	1.38	0.01	0.00	0.00	0.36	0.60	0.01	4.99		59.26	0.01	26.46	0.16	0.01	0.00	7.61	7.00	0.26	100.78
NW10-53Agrtcpxleft-fsp	2.59	0.00	1.42	0.01	0.00	0.00	0.40	0.55	0.02	4.98		58.43	0.00	27.31	0.15	0.00	0.00	8.52	6.40	0.27	101.09
NW10-53Agrtcpxleft-fsp	2.63	0.00	1.38	0.01	0.00	0.00	0.35	0.61	0.01	4.99		59.68	0.01	26.50	0.14	0.00	0.00	7.33	7.13	0.24	101.03
NW10-53Agrtcpxleft-fsp	2.65	0.00	1.35	0.01	0.00	0.00	0.35	0.61	0.02	4.99		59.97	0.00	26.02	0.20	0.02	0.00	7.40	7.11	0.28	100.99
NW10-53Agrtcpxleft-fsp	2.68	0.00	1.33	0.00	0.00	0.00	0.32	0.65	0.02	4.99		60.74	0.00	25.57	0.11	0.00	0.01	6.69	7.57	0.27	100.96
NW10-53Agrtcpxleft-fsp	2.65	0.00	1.35	0.01	0.00	0.00	0.34	0.62	0.02	4.99		60.01	0.00	25.89	0.16	0.00	0.00	7.18	7.25	0.30	100.79
NW10-53Agrtcpxleft-fsp	2.64	0.00	1.36	0.01	0.00	0.00	0.35	0.62	0.02	4.99		59.87	0.00	26.18	0.15	0.00	0.00	7.33	7.25	0.27	101.05
NW10-53Agrtcpxleft-fsp	2.68	0.00	1.32	0.01	0.00	0.00	0.31	0.65	0.02	4.99		60.86	0.04	25.44	0.17	0.05	0.00	6.61	7.57	0.33	101.07
NW10-53Agrtcpxleft-fsp	2.70	0.00	1.31	0.00	0.00	0.00	0.29	0.68	0.01	4.99		61.21	0.01	25.14	0.11	0.00	0.00	6.13	7.95	0.26	100.82
NW10-53Agrtcpxctr_fsp	1.97	0.00	1.35	0.98	0.08	0.38	0.58	0.00	0.00	5.35		38.71	0.01	22.47	23.02	1.84	5.01	10.68	0.04	0.00	101.78
NW10-53Agrtcpxctr_fsp	1.97	0.00	1.34	0.99	0.09	0.37	0.58	0.00	0.00	5.35		38.64	0.07	22.35	23.10	2.18	4.91	10.53	0.04	0.00	101.82
NW10-53Agrtcpxctr_fsp	1.98	0.00	1.34	0.99	0.09	0.37	0.57	0.00	0.00	5.35		38.73	0.06	22.27	23.10	2.11	4.85	10.43	0.04	0.01	101.62
NW10-53Agrtcpxctr_fsp	1.97	0.00	1.36	0.98	0.10	0.36	0.57	0.00	0.00	5.35		38.69	0.02	22.64	22.96	2.26	4.75	10.52	0.05	0.01	101.89
NW10-53Agrtcpxctr_fsp	1.98	0.00	1.35	0.98	0.09	0.37	0.58	0.00	0.00	5.35		38.76	0.08	22.43	22.92	2.01	4.87	10.58	0.03	0.01	101.70
NW10-53Agrtcpxctr_fsp	1.97	0.00	1.35	0.98	0.09	0.38	0.58	0.00	0.00	5.35		38.68	0.06	22.59	23.04	2.03	5.05	10.56	0.03	0.00	102.04
NW10-53Agrtcpxctr_fsp	1.98	0.00	1.34	0.97	0.09	0.37	0.58	0.01	0.00	5.35		38.85	0.08	22.27	22.71	2.15	4.89	10.53	0.06	0.02	101.56
NW10-53Agrtcpxctr_fsp	1.98	0.00	1.34	0.98	0.09	0.38	0.58	0.01	0.00	5.35		38.90	0.07	22.42	22.95	2.02	4.97	10.57	0.05	0.00	101.97
NW10-53Agrtcpxctr_fsp	1.98	0.00	1.34	0.99	0.09	0.37	0.57	0.00	0.00	5.35		38.99	0.07	22.48	23.21	2.04	4.91	10.50	0.05	0.03	102.28
NW10-53Agrtcpxctr_fsp	1.97	0.00	1.34	0.98	0.10	0.36	0.58	0.00	0.00	5.35		38.75	0.12	22.40	23.09	2.28	4.79	10.63	0.04	0.01	102.11
NW10-53Agrtcpxctr_fsp	1.98	0.00	1.34	0.98	0.10	0.37	0.58	0.00	0.00	5.35		38.53	0.08	22.19	22.73	2.38	4.83	10.50	0.04	0.00	101.28
NW10-53Agrtcpxctr-fsp	2.60	0.00	1.40	0.01	0.00	0.00	0.40	0.57	0.01	4.99		58.46	0.01	26.66	0.20	0.02	0.00	8.35	6.64	0.21	100.56
NW10-53Agrtcpxctr-fsp	2.62	0.00	1.38	0.01	0.00	0.00	0.39	0.58	0.01	4.99		58.70	0.01	26.19	0.25	0.03	0.00	8.07	6.69	0.23	100.16
NW10-53Agrtcpxctr-fsp	2.69	0.00	1.30	0.01	0.00	0.00	0.33	0.64	0.02	4.98		60.28	0.00	24.76	0.14	0.01	0.00	6.81	7.40	0.29	99.69
NW10-53Agrtcpxctr-fsp	2.63	0.00	1.37	0.01	0.00	0.00	0.37	0.59	0.01	4.99		59.10	0.00	26.15	0.21	0.01	0.01	7.83	6.82	0.23	100.36
NW10-53Agrtcpxctr-fsp	2.58	0.00	1.43	0.00	0.00	0.00	0.42	0.54	0.01	4.99		57.78	0.01	27.23	0.13	0.00	0.00	8.84	6.27	0.20	100.47
NW10-53Agrtcpxctr-fsp	2.62	0.00	1.39	0.01	0.00	0.00	0.38	0.58	0.01	4.98		58.99	0.00	26.49	0.14	0.01	0.01	8.07	6.73	0.20	100.62
NW10-53Agrtcpxctr-fsp	2.66	0.00	1.34	0.01	0.00	0.00	0.33	0.63	0.01	4.99		59.99	0.00	25.70	0.14	0.00	0.00	6.91	7.32	0.25	100.31
NW10-53Agrtcpxctr-fsp	2.68	0.00	1.32	0.00	0.00	0.00	0.33	0.64	0.01	4.98		60.41	0.00	25.26	0.05	0.03	0.00	6.84	7.41	0.22	100.23
NW10-53Agrtcpxctr-fsp	2.69	0.00	1.31	0.00	0.00	0.00	0.32	0.64	0.02	4.98		60.41	0.00	24.99	0.11	0.00	0.00	6.68	7.38	0.36	99.94
NW10-53Agrtcpxctr-fsp	2.71	0.00	1.29	0.00	0.00	0.00	0.30	0.66	0.02	4.98		61.09	0.00	24.63	0.10	0.02	0.00	6.26	7.68	0.36	100.15
NW10-53A_plag	2.23	0.00	1.68	0.01	0.00	0.00	0.44	1.14	0.02	5.52		25.54	0.00	16.35	0.13	0.00	0.00	4.70	6.77	0.17	53.66
NW10-53A_plagkspar	2.75	0.00	1.26	0.01	0.00	0.00	0.25	0.70	0.01	4.98		62.24	0.01	24.15	0.15	0.01	0.00	5.33	8.17	0.22	100.28
NW10-53A_plagkspar	2.72	0.00	1.28	0.00	0.00	0.00	0.30	0.67	0.01	4.98		61.34	0.00	24.52	0.08	0.04	0.01	6.23	7.84	0.19	100.25
NW10-53A_plagkspar	2.72	0.00	1.28	0.00	0.00	0.00	0.29	0.68	0.01	4.99		61.43	0.00	24.62	0.07	0.03	0.00	6.12	7.96	0.15	100.38

Finnoya Mylonite Zone

Plagioclase	Normalized Atoms											Weight Percent									
Sample	Si	Ti	Al	Fe	Mn	Mg	Ca	Na	K	Total		SiO2	TiO2	Al2O3	FeO	MnO	MgO	CaO	Na2O	K2O	Total
NW10-53A_plagkspar	2.75	0.00	1.25	0.00	0.00	0.00	0.26	0.71	0.01	4.99		62.03	0.01	23.91	0.07	0.00	0.01	5.53	8.25	0.26	100.07
NW10-53A_plagkspar	2.74	0.00	1.26	0.01	0.00	0.00	0.25	0.71	0.01	4.99		62.16	0.00	24.23	0.14	0.00	0.00	5.38	8.26	0.24	100.41
NW1054Cgrt_fsp	2.70	0.00	1.30	0.01	0.00	0.00	0.31	0.65	0.01	4.98		60.23	0.00	24.68	0.25	0.00	0.00	6.39	7.51	0.24	99.30
NW1054Cgrt_fsp	2.68	0.00	1.31	0.01	0.00	0.00	0.34	0.63	0.01	4.98		59.98	0.00	24.94	0.13	0.01	0.00	7.04	7.25	0.20	99.56
NW1054Cgrt_fsp	2.69	0.00	1.31	0.00	0.00	0.00	0.33	0.64	0.01	4.98		60.33	0.00	24.86	0.10	0.03	0.00	6.83	7.38	0.21	99.74
NW1054Cgrt_fsp	2.63	0.00	1.36	0.01	0.00	0.00	0.38	0.58	0.01	4.98		58.91	0.02	25.83	0.21	0.02	0.00	7.97	6.72	0.17	99.85
NW1054Cgrt_fsp	2.66	0.00	1.34	0.01	0.00	0.00	0.36	0.63	0.01	5.00		59.17	0.00	25.26	0.16	0.00	0.01	7.48	7.21	0.23	99.50
NW1054Cgrt_fsp	2.74	0.00	1.26	0.00	0.00	0.00	0.27	0.70	0.01	4.99		61.75	0.02	24.09	0.09	0.02	0.01	5.75	8.11	0.23	100.07
NW1054Cgrt_fsp	2.75	0.00	1.25	0.00	0.00	0.00	0.27	0.70	0.01	4.99		61.65	0.00	23.82	0.13	0.00	0.00	5.63	8.15	0.24	99.63
NW1054Cgrt_fsp	2.75	0.00	1.25	0.00	0.00	0.00	0.26	0.70	0.01	4.98		61.82	0.02	23.97	0.13	0.02	0.00	5.57	8.09	0.24	99.85
NW1054Cgrt_fsp	2.70	0.00	1.30	0.00	0.00	0.00	0.32	0.64	0.01	4.98		60.59	0.01	24.87	0.09	0.00	0.00	6.79	7.39	0.25	99.99
NW1054Cgrt_fsp	2.69	0.00	1.32	0.01	0.00	0.00	0.31	0.64	0.02	4.98		60.72	0.00	25.23	0.15	0.00	0.00	6.60	7.43	0.27	100.42
NW1054Cgrt_fsp	2.63	0.00	1.36	0.01	0.00	0.00	0.38	0.60	0.01	5.00		58.92	0.00	25.82	0.20	0.03	0.00	7.99	6.96	0.18	100.12
NW1054Cgrt_fsp	2.66	0.00	1.34	0.00	0.00	0.00	0.35	0.62	0.01	4.99		59.38	0.01	25.41	0.11	0.04	0.00	7.33	7.18	0.16	99.61
NW1054Cgrt_fsp	2.73	0.00	1.28	0.01	0.00	0.00	0.28	0.68	0.01	4.98		60.57	0.00	24.03	0.14	0.00	0.00	5.83	7.79	0.25	98.62
NW1054Cgrt_fsp	2.23	0.04	0.72	0.83	0.02	0.75	0.65	0.15	0.10	5.49		41.82	1.04	11.44	18.68	0.53	9.37	11.35	1.42	1.47	97.14
NW1054Cgrt_fsp	2.74	0.00	1.26	0.00	0.00	0.00	0.28	0.68	0.01	4.98		61.88	0.03	24.10	0.13	0.00	0.02	5.86	7.98	0.24	100.23
NW1054Cgrt_fsp	2.21	0.04	0.74	0.85	0.03	0.74	0.65	0.16	0.11	5.52		41.43	1.00	11.77	19.02	0.63	9.34	11.31	1.50	1.67	97.68
NW1054Cgrt_fsp	2.22	0.05	0.72	0.83	0.03	0.75	0.66	0.15	0.11	5.50		41.40	1.17	11.45	18.46	0.64	9.36	11.42	1.45	1.60	96.92
NW1054Cgrt_fsp	2.21	0.06	0.73	0.83	0.03	0.74	0.66	0.15	0.11	5.51		41.39	1.37	11.59	18.51	0.57	9.30	11.57	1.49	1.65	97.44
NW1054Cleft_plag	2.72	0.00	1.28	0.00	0.00	0.00	0.30	0.68	0.01	4.99		61.36	0.00	24.46	0.09	0.02	0.00	6.21	7.88	0.20	100.22
NW1054Cleft_plag	2.76	0.00	1.25	0.00	0.00	0.00	0.26	0.69	0.02	4.97		62.21	0.01	23.85	0.08	0.02	0.00	5.53	7.99	0.31	100.00
NW1054Cleft_plag	2.76	0.00	1.24	0.00	0.00	0.00	0.26	0.70	0.01	4.98		62.37	0.01	23.80	0.10	0.02	0.00	5.50	8.14	0.26	100.21
NW1054Cleft_plag	2.73	0.00	1.27	0.00	0.00	0.00	0.28	0.68	0.01	4.98		61.76	0.02	24.40	0.09	0.01	0.00	5.90	7.90	0.24	100.31
NW1054Cleft_plag	2.75	0.00	1.30	0.00	0.00	0.00	0.27	0.56	0.01	4.88		64.27	0.00	25.71	0.10	0.00	0.00	5.85	6.70	0.18	102.82
NW1054Cleft_plag	2.73	0.00	1.26	0.00	0.00	0.00	0.29	0.70	0.01	4.99		60.99	0.01	23.92	0.08	0.00	0.00	6.08	8.06	0.19	99.32
NW1054Cleft_plag	2.72	0.00	1.28	0.00	0.00	0.00	0.29	0.68	0.01	4.98		61.21	0.01	24.32	0.10	0.00	0.00	6.08	7.88	0.17	99.77
NW1054Cleft_plag	2.75	0.00	1.25	0.00	0.00	0.00	0.26	0.70	0.01	4.98		62.12	0.00	23.92	0.07	0.00	0.00	5.44	8.20	0.22	99.96
NW1054Cleft_plag	2.74	0.00	1.27	0.00	0.00	0.00	0.26	0.70	0.02	4.98		62.31	0.00	24.40	0.10	0.00	0.00	5.45	8.19	0.28	100.72
NW1054Cleft_plag	2.77	0.00	1.23	0.00	0.00	0.00	0.25	0.72	0.02	4.99		61.96	0.00	23.33	0.09	0.01	0.00	5.26	8.30	0.28	99.23
NW1054Cleft_plag	2.76	0.00	1.24	0.00	0.00	0.00	0.26	0.71	0.01	4.99		62.05	0.00	23.62	0.10	0.04	0.00	5.44	8.29	0.23	99.78
NW1054Cleft_plag	2.76	0.00	1.24	0.00	0.00	0.00	0.25	0.72	0.01	4.99		62.19	0.01	23.80	0.07	0.00	0.00	5.28	8.41	0.25	100.02
NW1054Ctop_fsp	2.74	0.00	1.26	0.00	0.00	0.00	0.27	0.69	0.01	4.98		61.81	0.00	24.05	0.10	0.00	0.00	5.77	8.04	0.15	99.92
NW1054Ctop_fsp	2.75	0.00	1.25	0.00	0.00	0.00	0.28	0.70	0.01	4.98		61.77	0.02	23.74	0.02	0.00	0.01	5.82	8.11	0.17	99.65
NW1054Ctop_fsp	2.74	0.00	1.26	0.00	0.00	0.00	0.28	0.70	0.01	4.99		61.53	0.01	24.02	0.02	0.00	0.00	5.77	8.10	0.18	99.63
NW1054Ctop_fsp	2.74	0.00	1.26	0.00	0.00	0.00	0.30	0.67	0.01	4.97		62.18	0.02	24.27	0.02	0.01	0.00	6.34	7.81	0.10	100.76
NW1054Ctop_fsp	2.74	0.00	1.25	0.00	0.00	0.00	0.27	0.70	0.01	4.98		61.71	0.02	23.86	0.12	0.03	0.00	5.77	8.08	0.23	99.81

Finnoya Mylonite Zone

Plagioclase	Normalized Atoms											Weight Percent									
Sample	Si	Ti	Al	Fe	Mn	Mg	Ca	Na	K	Total		SiO2	TiO2	Al2O3	FeO	MnO	MgO	CaO	Na2O	K2O	Total
NW1054Ctop_fsp	2.73	0.00	1.27	0.00	0.00	0.00	0.30	0.68	0.01	4.98		61.21	0.00	24.21	0.04	0.00	0.00	6.22	7.84	0.10	99.62
NW1054Ctop_fsp	2.77	0.00	1.23	0.00	0.00	0.00	0.26	0.70	0.01	4.98		62.32	0.00	23.52	0.07	0.00	0.00	5.44	8.15	0.25	99.75
NW1054Ctop_fsp	2.74	0.00	1.26	0.00	0.00	0.00	0.28	0.68	0.01	4.98		61.43	0.02	23.90	0.05	0.00	0.00	5.92	7.87	0.21	99.41
NW1054Ctop_fsp	2.72	0.00	1.27	0.00	0.00	0.00	0.30	0.68	0.01	4.99		61.28	0.01	24.18	0.09	0.00	0.00	6.39	7.93	0.16	100.04
NW1054Ctop_fsp	2.75	0.00	1.25	0.00	0.00	0.00	0.27	0.70	0.01	4.98		61.56	0.00	23.78	0.06	0.00	0.00	5.68	8.14	0.16	99.37
NW1054Ctop_melt	2.73	0.00	1.27	0.00	0.00	0.00	0.28	0.69	0.01	4.98		61.58	0.00	24.22	0.09	0.00	0.00	5.91	7.98	0.20	99.98
NW1054Ctop_melt	2.74	0.00	1.26	0.00	0.00	0.00	0.28	0.69	0.01	4.98		61.73	0.00	24.12	0.05	0.02	0.01	5.89	7.99	0.21	100.02
NW1054Ctop_melt	2.73	0.00	1.27	0.00	0.00	0.00	0.27	0.69	0.01	4.98		61.75	0.02	24.36	0.05	0.01	0.00	5.67	8.04	0.21	100.11
NW1054Ctop_melt	2.75	0.00	1.25	0.00	0.00	0.00	0.26	0.71	0.01	4.98		62.24	0.00	23.90	0.04	0.00	0.00	5.43	8.31	0.19	100.11
NW1054Ctop_melt	2.74	0.00	1.26	0.00	0.00	0.00	0.26	0.70	0.01	4.98		62.00	0.00	24.26	0.07	0.00	0.00	5.58	8.13	0.24	100.28
NW1054Ctop_melt	2.75	0.00	1.26	0.00	0.00	0.00	0.25	0.71	0.02	4.99		62.17	0.00	24.18	0.07	0.00	0.00	5.37	8.32	0.27	100.38
NW1054Ctop_melt	2.72	0.00	1.29	0.00	0.00	0.00	0.29	0.67	0.01	4.98		61.40	0.00	24.64	0.05	0.01	0.00	6.17	7.79	0.13	100.19
NW1054Ctop_melt	2.73	0.00	1.28	0.00	0.00	0.00	0.28	0.68	0.01	4.98		61.57	0.01	24.43	0.07	0.00	0.00	5.90	7.90	0.16	100.03
NW1054Ctop_melt	2.71	0.00	1.30	0.00	0.00	0.00	0.29	0.66	0.01	4.97		61.46	0.01	24.95	0.05	0.00	0.01	6.18	7.75	0.12	100.53
NW1054Ctop_melt	2.71	0.00	1.29	0.00	0.00	0.00	0.30	0.67	0.01	4.98		61.17	0.00	24.72	0.10	0.01	0.00	6.32	7.79	0.17	100.28
NW1054Ctop_melt	2.72	0.00	1.29	0.01	0.00	0.00	0.29	0.67	0.01	4.98		61.37	0.00	24.65	0.16	0.00	0.00	6.12	7.83	0.22	100.36
NW1054Ctop_melt	2.74	0.00	1.26	0.00	0.00	0.00	0.27	0.70	0.01	4.98		61.82	0.02	24.13	0.09	0.01	0.00	5.67	8.13	0.18	100.04
NW1054Ctop_melt	2.74	0.00	1.26	0.00	0.00	0.00	0.27	0.69	0.01	4.98		62.03	0.00	24.24	0.04	0.00	0.00	5.74	8.04	0.18	100.28
NW1054Ctop_melt_ksp	2.99	0.00	1.01	0.00	0.00	0.00	0.00	0.08	0.90	4.99		64.89	0.01	18.60	0.03	0.00	0.00	0.05	0.86	15.33	99.78
NW1054HxGrt_pl	2.65	0.00	1.36	0.00	0.00	0.00	0.37	0.59	0.02	4.98		59.19	0.00	25.73	0.12	0.00	0.00	7.73	6.77	0.27	99.81
NW1054HxGrt_pl	2.70	0.00	1.30	0.01	0.00	0.00	0.32	0.64	0.01	4.98		60.43	0.00	24.68	0.15	0.02	0.00	6.79	7.34	0.24	99.66
NW1054HxGrt_pl	2.70	0.00	1.29	0.01	0.00	0.00	0.32	0.65	0.01	4.98		60.66	0.01	24.65	0.14	0.00	0.00	6.81	7.51	0.25	100.03
NW1054HxGrt_pl	2.32	0.00	1.63	0.01	0.00	0.00	0.36	1.07	0.03	5.41		30.97	0.00	18.41	0.12	0.00	0.00	4.53	7.33	0.32	61.69
NW1054HxGrt_pl	2.31	0.00	1.64	0.01	0.00	0.00	0.35	1.08	0.03	5.43		30.72	0.01	18.49	0.11	0.00	0.00	4.37	7.40	0.36	61.47
NW1054HxGrt_pl	2.76	0.00	1.23	0.00	0.00	0.00	0.26	0.70	0.02	4.98		61.89	0.01	23.37	0.09	0.02	0.00	5.53	8.10	0.31	99.32
NW1054HxGrt_pl	2.70	0.00	1.29	0.00	0.00	0.00	0.32	0.65	0.01	4.98		60.48	0.01	24.52	0.11	0.00	0.01	6.73	7.52	0.23	99.60
NW1054HxGrt_pl	2.78	0.00	1.22	0.00	0.00	0.00	0.25	0.70	0.02	4.97		62.70	0.01	23.36	0.11	0.00	0.00	5.32	8.12	0.27	99.89
NW1054HxGrt_pl	2.65	0.00	1.34	0.01	0.00	0.00	0.37	0.60	0.01	4.98		59.35	0.00	25.48	0.21	0.02	0.00	7.66	6.91	0.23	99.86
NW1054HxGrt_pl	2.78	0.00	1.23	0.00	0.00	0.00	0.25	0.69	0.02	4.96		62.65	0.00	23.47	0.09	0.00	0.01	5.29	7.99	0.37	99.87
NW1054HxBtpoor_ksp	2.79	0.00	1.21	0.00	0.00	0.00	0.24	0.72	0.01	4.97		62.98	0.01	23.23	0.05	0.03	0.00	5.06	8.41	0.15	99.91
NW1054HxBtpoor_ksp	2.77	0.00	1.22	0.00	0.00	0.00	0.25	0.72	0.01	4.97		62.90	0.01	23.53	0.08	0.01	0.00	5.29	8.37	0.12	100.30
NW1054HxBtpoor_ksp	2.79	0.00	1.21	0.00	0.00	0.00	0.23	0.73	0.01	4.97		63.40	0.00	23.25	0.13	0.00	0.00	4.78	8.51	0.20	100.28
NW1054HxBtpoor_ksp	2.79	0.00	1.21	0.00	0.00	0.00	0.24	0.72	0.01	4.97		62.99	0.00	23.28	0.05	0.00	0.00	5.06	8.41	0.19	99.98
NW1054HxBtpoor_ksp	2.78	0.00	1.22	0.00	0.00	0.00	0.24	0.72	0.01	4.98		62.79	0.00	23.47	0.07	0.00	0.00	5.17	8.41	0.18	100.07
NW1054HxBtpoor_ksp	2.80	0.00	1.20	0.00	0.00	0.00	0.22	0.73	0.01	4.97		63.53	0.02	23.10	0.10	0.01	0.00	4.65	8.58	0.22	100.22
NW1054HxBtpoor_ksp	2.79	0.00	1.22	0.00	0.00	0.00	0.23	0.73	0.01	4.98		63.05	0.03	23.37	0.09	0.00	0.00	4.79	8.53	0.22	100.08

Finnoya Mylonite Zone

Plagioclase	Normalized Atoms											Weight Percent									
Sample	Si	Ti	Al	Fe	Mn	Mg	Ca	Na	K	Total		SiO2	TiO2	Al2O3	FeO	MnO	MgO	CaO	Na2O	K2O	Total
NW1054HxBtpoor_ksp	2.81	0.00	1.19	0.00	0.00	0.00	0.22	0.74	0.01	4.97		63.59	0.01	22.97	0.08	0.01	0.00	4.60	8.65	0.21	100.12
NW1054HxBtpoor_ksp	2.81	0.00	1.19	0.00	0.00	0.00	0.22	0.74	0.01	4.97		63.65	0.00	22.93	0.12	0.00	0.00	4.66	8.60	0.25	100.22
NW1054HxBtrich_pl	2.78	0.00	1.23	0.00	0.00	0.00	0.23	0.72	0.02	4.98		62.88	0.01	23.59	0.12	0.02	0.00	4.87	8.37	0.31	100.18
NW1054HxBtrich_pl	2.79	0.00	1.21	0.00	0.00	0.00	0.23	0.71	0.02	4.97		63.04	0.00	23.28	0.13	0.01	0.01	4.85	8.31	0.28	99.89
NW1054HxBtrich_pl	2.80	0.00	1.20	0.00	0.00	0.00	0.22	0.72	0.02	4.97		63.53	0.00	23.17	0.12	0.01	0.00	4.68	8.45	0.27	100.23
NW1054HxBtrich_pl	2.77	0.00	1.24	0.00	0.00	0.00	0.24	0.70	0.01	4.97		62.76	0.00	23.95	0.11	0.01	0.00	5.14	8.18	0.25	100.41
NW1054HxBtrich_pl	2.77	0.00	1.24	0.01	0.00	0.00	0.24	0.72	0.02	4.98		62.71	0.01	23.78	0.15	0.00	0.00	5.02	8.41	0.30	100.37
NW1054HxBtrich_pl	2.73	0.00	1.28	0.00	0.00	0.00	0.27	0.68	0.02	4.98		61.63	0.01	24.64	0.07	0.03	0.00	5.69	7.93	0.27	100.26
NW1054HxBtrich_pl	2.73	0.00	1.30	0.00	0.00	0.00	0.23	0.71	0.02	4.98		63.30	0.00	25.48	0.10	0.01	0.00	4.98	8.46	0.28	102.60
NW1054HxBtrich_pl	2.77	0.00	1.24	0.01	0.00	0.00	0.24	0.72	0.01	4.98		62.79	0.00	23.78	0.14	0.00	0.00	5.06	8.42	0.21	100.41
NW1054HxBtrich_pl	2.73	0.00	1.28	0.00	0.00	0.00	0.28	0.67	0.01	4.97		61.61	0.01	24.57	0.05	0.01	0.01	5.86	7.86	0.17	100.15
NW1054HxBtrich_pl	2.77	0.00	1.24	0.00	0.00	0.00	0.25	0.71	0.01	4.97		62.32	0.02	23.62	0.09	0.01	0.00	5.26	8.19	0.22	99.73
NW1054HxBtrich_pl	2.29	0.00	1.65	0.01	0.00	0.00	0.37	1.10	0.02	5.45		29.34	0.00	17.97	0.11	0.00	0.00	4.46	7.25	0.25	59.39
NW1054HxBtrich_pl	2.77	0.00	1.24	0.00	0.00	0.00	0.25	0.71	0.01	4.97		62.74	0.01	23.74	0.13	0.02	0.00	5.19	8.25	0.19	100.27
NW1054HxBtrich_pl	2.71	0.00	1.30	0.00	0.00	0.00	0.27	0.67	0.01	4.98		61.56	0.01	25.09	0.11	0.00	0.00	5.82	7.88	0.24	100.73
NW1054HxBtrich_pl	2.76	0.00	1.25	0.00	0.00	0.00	0.25	0.70	0.01	4.97		62.79	0.00	24.20	0.08	0.02	0.01	5.22	8.17	0.26	100.75
NW1054HxBtrich_pl	2.78	0.00	1.23	0.01	0.00	0.00	0.23	0.72	0.02	4.97		63.41	0.01	23.71	0.15	0.00	0.00	4.86	8.42	0.30	100.87

Finnoya Mylonite Zone

Garnet	Normalized Atoms											Weight Percent									
Sample	Si	Ti	Al	Fe	Mn	Mg	Ca	Na	K	Total		SiO2	TiO2	Al2O3	FeO	MnO	MgO	CaO	Na2O	K2O	Total
NW10-53Agrtcpxleft-grt	2.99	0.00	1.95	1.46	0.12	0.59	0.92	0.00	0.00	8.03		38.44	0.05	21.26	22.52	1.82	5.05	11.07	0.01	0.00	100.22
NW10-53Agrtcpxleft-grt	3.00	0.00	1.95	1.49	0.14	0.58	0.87	0.00	0.00	8.03		38.80	0.03	21.36	23.09	2.09	5.07	10.48	0.03	0.01	100.97
NW10-53Agrtcpxleft-grt	3.00	0.00	1.94	1.48	0.13	0.57	0.90	0.00	0.00	8.03		38.78	0.05	21.21	22.80	2.03	4.94	10.89	0.00	0.02	100.72
NW10-53Agrtcpxleft-grt	3.01	0.00	1.94	1.50	0.14	0.57	0.88	0.00	0.00	8.02		38.92	0.02	21.29	23.15	2.11	4.92	10.61	0.01	0.00	101.03
NW10-53Agrtcpxleft-grt	3.01	0.00	1.94	1.48	0.13	0.58	0.88	0.00	0.00	8.02		39.04	0.06	21.31	22.88	2.00	5.00	10.60	0.03	0.01	100.93
NW10-53Agrtcpxleft-grt	3.02	0.00	1.93	1.47	0.13	0.57	0.88	0.01	0.00	8.02		39.18	0.07	21.29	22.90	2.00	4.98	10.69	0.05	0.00	101.17
NW10-53Agrtcpxleft-grt	3.00	0.00	1.95	1.48	0.13	0.58	0.88	0.01	0.00	8.03		38.91	0.05	21.43	22.88	1.96	5.06	10.65	0.05	0.00	101.01
NW10-53Agrtcpxleft-grt	2.44	0.00	2.04	1.98	0.18	0.67	1.23	0.01	0.00	8.54		20.91	0.05	14.88	20.31	1.80	3.85	9.82	0.04	0.00	71.65
NW10-53Agrtcpxctr_fsp	2.96	0.00	2.03	1.47	0.12	0.57	0.87	0.01	0.00	8.03		38.71	0.01	22.47	23.02	1.84	5.01	10.68	0.04	0.00	101.78
NW10-53Agrtcpxctr_fsp	2.96	0.00	2.02	1.48	0.14	0.56	0.86	0.01	0.00	8.03		38.64	0.07	22.35	23.10	2.18	4.91	10.53	0.04	0.00	101.82
NW10-53Agrtcpxctr_fsp	2.97	0.00	2.01	1.48	0.14	0.55	0.86	0.01	0.00	8.02		38.73	0.06	22.27	23.10	2.11	4.85	10.43	0.04	0.01	101.62
NW10-53Agrtcpxctr_fsp	2.96	0.00	2.04	1.47	0.15	0.54	0.86	0.01	0.00	8.02		38.69	0.02	22.64	22.96	2.26	4.75	10.52	0.05	0.01	101.89
NW10-53Agrtcpxctr_fsp	2.97	0.00	2.02	1.47	0.13	0.56	0.87	0.01	0.00	8.02		38.76	0.08	22.43	22.92	2.01	4.87	10.58	0.03	0.01	101.70
NW10-53Agrtcpxctr_fsp	2.95	0.00	2.03	1.47	0.13	0.57	0.86	0.00	0.00	8.03		38.68	0.06	22.59	23.04	2.03	5.05	10.56	0.03	0.00	102.04
NW10-53Agrtcpxctr_fsp	2.98	0.00	2.01	1.46	0.14	0.56	0.86	0.01	0.00	8.02		38.85	0.08	22.27	22.71	2.15	4.89	10.53	0.06	0.02	101.56
NW10-53Agrtcpxctr_fsp	2.97	0.00	2.02	1.46	0.13	0.57	0.86	0.01	0.00	8.02		38.90	0.07	22.42	22.95	2.02	4.97	10.57	0.05	0.00	101.97
NW10-53Agrtcpxctr_fsp	2.97	0.00	2.02	1.48	0.13	0.56	0.86	0.01	0.00	8.02		38.99	0.07	22.48	23.21	2.04	4.91	10.50	0.05	0.03	102.28
NW10-53Agrtcpxctr_fsp	2.96	0.01	2.02	1.48	0.15	0.55	0.87	0.01	0.00	8.03		38.75	0.12	22.40	23.09	2.28	4.79	10.63	0.04	0.01	102.11
NW10-53Agrtcpxctr_fsp	2.97	0.00	2.01	1.46	0.16	0.55	0.87	0.01	0.00	8.03		38.53	0.08	22.19	22.73	2.38	4.83	10.50	0.04	0.00	101.28
NW1054Cgrt_grt	3.03	0.00	1.91	1.52	0.19	0.43	0.94	0.00	0.00	8.02		38.53	0.05	20.58	23.11	2.80	3.69	11.16	0.02	0.02	99.96
NW1054Cgrt_grt	3.02	0.00	1.90	1.53	0.16	0.41	1.01	0.01	0.00	8.03		38.59	0.02	20.60	23.37	2.43	3.52	12.00	0.05	0.00	100.59
NW1054Cgrt_grt	3.02	0.00	1.91	1.52	0.18	0.41	0.99	0.00	0.00	8.03		38.29	0.02	20.53	23.12	2.73	3.45	11.73	0.00	0.00	99.88
NW1054Cgrt_grt	3.03	0.00	1.90	1.55	0.16	0.37	1.01	0.00	0.00	8.02		38.52	0.05	20.47	23.62	2.38	3.14	12.03	0.01	0.00	100.21
NW1054Cgrt_grt	3.02	0.00	1.90	1.58	0.16	0.35	1.02	0.00	0.00	8.03		38.34	0.06	20.48	23.93	2.42	2.96	12.05	0.02	0.00	100.26
NW1054Cgrt_grt	3.37	0.00	2.32	0.14	0.00	0.02	0.91	1.36	0.02	8.15		24.55	0.04	14.36	1.25	0.04	0.08	6.20	5.11	0.10	51.73
NW1054Cgrt_grt	3.03	0.00	1.91	1.56	0.15	0.36	0.99	0.00	0.00	8.01		38.61	0.03	20.67	23.85	2.22	3.11	11.83	0.00	0.01	100.31
NW1054Cgrt_grt	3.02	0.00	1.91	1.46	0.32	0.36	0.93	0.01	0.00	8.02		38.19	0.04	20.49	22.08	4.84	3.05	10.94	0.03	0.01	99.67
NW1054Cgrt_grt	3.03	0.00	1.90	1.56	0.18	0.46	0.90	0.00	0.00	8.02		38.45	0.03	20.49	23.73	2.68	3.90	10.62	0.00	0.02	99.92
NW1054Cgrt_grt	3.02	0.00	1.92	1.52	0.14	0.41	1.00	0.01	0.00	8.02		38.53	0.05	20.78	23.27	2.15	3.53	11.93	0.04	0.00	100.28
NW1054Cgrt_grt	3.02	0.00	1.91	1.56	0.13	0.40	1.00	0.00	0.00	8.02		38.63	0.02	20.69	23.84	1.89	3.46	11.92	0.02	0.00	100.47
NW1054Cgrt_grt	3.02	0.00	1.93	1.57	0.10	0.44	0.95	0.00	0.00	8.02		38.48	0.02	20.91	24.00	1.56	3.78	11.30	0.01	0.01	100.06
NW1054Cgrt_grt	3.02	0.00	1.93	1.47	0.21	0.42	0.96	0.00	0.00	8.02		38.57	0.05	20.89	22.46	3.18	3.58	11.44	0.03	0.00	100.19
NW1054HxGrt_grt	3.03	0.00	1.89	1.50	0.16	0.37	1.07	0.00	0.00	8.02		38.90	0.06	20.59	22.95	2.44	3.17	12.83	0.00	0.00	100.93
NW1054HxGrt_grt	3.02	0.00	1.88	1.52	0.15	0.34	1.11	0.00	0.00	8.04		38.49	0.02	20.34	23.20	2.30	2.91	13.25	0.03	0.00	100.55
NW1054HxGrt_grt	3.03	0.00	1.87	1.51	0.16	0.31	1.13	0.00	0.00	8.03		38.65	0.06	20.20	23.04	2.46	2.67	13.42	0.03	0.00	100.53
NW1054HxGrt_grt	3.04	0.00	1.87	1.51	0.16	0.31	1.14	0.00	0.00	8.03		38.70	0.06	20.19	22.98	2.35	2.66	13.52	0.01	0.00	100.47
NW1054HxGrt_grt	3.04	0.00	1.89	1.47	0.17	0.29	1.16	0.00	0.00	8.02		38.85	0.05	20.49	22.48	2.63	2.47	13.81	0.01	0.01	100.81

Finnoya Mylonite Zone

Garnet	Normalized Atoms											Weight Percent									
Sample	Si	Ti	Al	Fe	Mn	Mg	Ca	Na	K	Total		SiO2	TiO2	Al2O3	FeO	MnO	MgO	CaO	Na2O	K2O	Total
NW1054HxGrt_grt	3.01	0.00	1.90	1.46	0.19	0.27	1.19	0.00	0.00	8.03		38.45	0.06	20.57	22.35	2.86	2.31	14.18	0.02	0.00	100.79
NW1054HxGrt_grt	3.04	0.00	1.87	1.45	0.18	0.27	1.20	0.01	0.00	8.03		38.83	0.05	20.34	22.18	2.72	2.31	14.33	0.05	0.01	100.83
NW1054HxGrt_grt	3.02	0.00	1.90	1.48	0.18	0.27	1.17	0.00	0.00	8.03		38.52	0.03	20.56	22.54	2.78	2.33	13.98	0.01	0.00	100.74
NW1054HxGrt_grt	3.03	0.00	1.89	1.46	0.18	0.27	1.19	0.01	0.00	8.03		38.66	0.07	20.52	22.29	2.67	2.32	14.13	0.06	0.02	100.74
NW1054HxGrt_grt	3.03	0.00	1.89	1.49	0.16	0.31	1.14	0.00	0.00	8.03		38.71	0.06	20.52	22.74	2.44	2.67	13.62	0.03	0.00	100.79
NW1054HxGrt_grt	3.03	0.00	1.90	1.54	0.09	0.46	1.00	0.00	0.00	8.02		38.77	0.06	20.65	23.58	1.29	3.93	11.95	0.03	0.01	100.28
NW1054HxGrt_grt	3.03	0.01	1.90	1.59	0.08	0.46	0.96	0.00	0.00	8.02		39.17	0.09	20.82	24.62	1.25	3.97	11.54	0.01	0.01	101.48
NW1054HxGrt_grt	3.03	0.00	1.89	1.35	0.28	0.27	1.18	0.01	0.00	8.02		38.75	0.06	20.47	20.66	4.25	2.30	14.08	0.05	0.00	100.61
NW1054HxGrt_grt	3.03	0.00	1.89	1.46	0.23	0.25	1.16	0.01	0.00	8.03		38.70	0.04	20.51	22.25	3.46	2.16	13.85	0.06	0.01	101.05
NW1054HxGrt_grt	3.03	0.00	1.89	1.45	0.23	0.25	1.15	0.00	0.00	8.02		38.59	0.02	20.42	22.08	3.45	2.17	13.65	0.02	0.02	100.41
NW1054M_grtright_grt	2.32	0.00	2.02	2.10	0.17	0.93	1.10	0.01	0.01	8.68		16.39	0.03	12.09	17.75	1.44	4.42	7.25	0.05	0.05	59.47
NW1054M_grtright_grt	3.01	0.00	1.92	1.56	0.04	0.54	0.95	0.00	0.00	8.03		38.81	0.06	21.05	24.08	0.61	4.71	11.51	0.01	0.02	100.86
NW1054M_grtright_grt	3.01	0.00	1.92	1.62	0.07	0.52	0.87	0.00	0.00	8.03		38.66	0.06	20.88	24.80	1.05	4.51	10.47	0.03	0.01	100.46
NW1054M_grtright_grt	2.38	0.00	2.06	2.24	0.21	0.60	1.08	0.01	0.00	8.59		19.85	0.03	14.60	22.36	2.12	3.36	8.44	0.04	0.02	70.82
NW1054M_grtright_grt	2.99	0.00	1.96	1.60	0.14	0.48	0.84	0.00	0.00	8.03		38.20	0.01	21.27	24.47	2.11	4.15	9.96	0.03	0.01	100.21
NW1054M_grtright_grt	3.00	0.00	1.94	1.58	0.12	0.47	0.90	0.00	0.00	8.02		38.65	0.02	21.19	24.35	1.84	4.07	10.79	0.00	0.00	100.91
NW1054M_grtright_grt	2.99	0.00	1.94	1.50	0.05	0.53	1.02	0.00	0.00	8.04		38.68	0.06	21.37	23.26	0.82	4.58	12.29	0.03	0.01	101.11
NW1054M_grtright_grt	3.01	0.00	1.93	1.55	0.04	0.52	0.97	0.00	0.00	8.02		38.89	0.08	21.10	23.90	0.67	4.49	11.68	0.00	0.01	100.83
NW1054M_grtright_grt	3.00	0.00	1.96	1.61	0.15	0.47	0.83	0.00	0.00	8.02		38.32	0.04	21.26	24.62	2.29	4.04	9.93	0.01	0.00	100.51
NW1054M_grtright_grt	3.00	0.00	1.95	1.58	0.13	0.46	0.89	0.00	0.00	8.03		38.48	0.02	21.21	24.24	2.03	3.98	10.71	0.03	0.00	100.71
NW1054M_grtmiddle	3.00	0.00	1.95	1.83	0.13	0.40	0.71	0.01	0.00	8.03		38.06	0.07	20.95	27.80	1.90	3.37	8.46	0.04	0.00	100.64
NW1054M_grtmiddle	3.01	0.00	1.94	1.63	0.16	0.39	0.87	0.00	0.00	8.02		38.27	0.00	20.98	24.85	2.43	3.35	10.37	0.02	0.01	100.28
NW1054M_grtmiddle	2.99	0.00	1.95	1.77	0.14	0.38	0.80	0.00	0.00	8.03		38.07	0.05	21.04	26.87	2.03	3.24	9.46	0.03	0.03	100.82
NW1054M_grtmiddle	2.27	0.00	2.01	2.74	0.18	0.47	1.06	0.00	0.00	8.72		16.91	0.03	12.70	24.37	1.56	2.34	7.36	0.01	0.00	65.29
NW1054M_grtmiddle	2.99	0.00	1.95	1.85	0.13	0.36	0.74	0.00	0.00	8.03		37.82	0.07	20.87	28.02	1.89	3.09	8.77	0.02	0.00	100.55
NW1054M_grtmiddle	3.00	0.00	1.95	1.74	0.13	0.37	0.82	0.00	0.00	8.02		38.15	0.02	21.07	26.51	2.01	3.13	9.77	0.01	0.00	100.68
NW1054M_grtmiddle	3.00	0.00	1.97	1.61	0.13	0.42	0.89	0.00	0.00	8.02		38.60	0.01	21.45	24.72	1.96	3.64	10.64	0.03	0.01	101.04
NW1054M_grtmiddle	2.99	0.00	1.96	1.54	0.07	0.50	0.97	0.00	0.00	8.03		38.61	0.05	21.41	23.72	1.06	4.30	11.68	0.01	0.00	100.83
Line 1 54Cgrt1line	2.95	0.00	2.00	1.48	0.29	0.42	0.91	0.00	0.00	8.05		37.23	0.05	21.41	22.30	4.35	3.55	10.69	0.00	0.00	99.58
Line 2 54Cgrt1line	2.94	0.00	2.01	1.56	0.13	0.47	0.93	0.00	0.00	8.05		37.43	0.06	21.66	23.67	2.02	4.01	11.06	0.00	0.00	99.91
Line 3 54Cgrt1line	2.96	0.00	2.01	1.56	0.14	0.45	0.90	0.00	0.00	8.03		38.03	0.05	21.89	24.00	2.13	3.87	10.81	0.00	0.00	100.79
Line 4 54Cgrt1line	2.94	0.00	2.01	1.57	0.13	0.45	0.94	0.00	0.00	8.05		37.32	0.08	21.57	23.87	1.98	3.85	11.08	0.00	0.00	99.75
Line 5 54Cgrt1line	3.00	0.00	2.04	1.54	0.11	0.49	0.79	0.00	0.00	7.97		38.62	0.06	22.28	23.67	1.69	4.19	9.53	0.00	0.00	100.04
Line 6 54Cgrt1line	3.00	0.00	1.94	1.52	0.10	0.78	0.69	0.00	0.00	8.03		38.06	0.07	20.83	23.00	1.47	6.64	8.21	0.00	0.00	98.28
Line 7 54Cgrt1line	2.93	0.00	2.01	1.61	0.13	0.47	0.93	0.00	0.00	8.07		36.90	0.05	21.48	24.23	1.90	3.93	10.91	0.00	0.00	99.40
Line 8 54Cgrt1line	2.94	0.00	1.99	1.62	0.12	0.48	0.91	0.00	0.00	8.06		37.09	0.07	21.29	24.49	1.80	4.07	10.67	0.00	0.00	99.49
Line 9 54Cgrt1line	2.94	0.01	2.00	1.62	0.11	0.49	0.89	0.00	0.00	8.05		37.24	0.09	21.56	24.55	1.59	4.15	10.54	0.00	0.00	99.72

Finnoya Mylonite Zone

Garnet	Normalized Atoms											Weight Percent									
Sample	Si	Ti	Al	Fe	Mn	Mg	Ca	Na	K	Total		SiO2	TiO2	Al2O3	FeO	MnO	MgO	CaO	Na2O	K2O	Total
Line 10 54Cgrt1line	2.96	0.01	1.99	1.60	0.10	0.49	0.89	0.00	0.00	8.04		37.45	0.11	21.44	24.29	1.49	4.14	10.57	0.00	0.00	99.49
Line 1 54Lgrt1left	2.94	0.00	2.01	1.47	0.15	0.53	0.93	0.00	0.00	8.05		37.62	0.08	21.83	22.50	2.23	4.55	11.15	0.00	0.00	99.96
Line 2 54Lgrt1left	2.92	0.00	2.01	1.53	0.12	0.56	0.92	0.00	0.00	8.07		37.05	0.07	21.65	23.11	1.73	4.80	10.86	0.00	0.00	99.27
Line 3 54Lgrt1left	2.93	0.00	2.01	1.53	0.13	0.56	0.89	0.00	0.00	8.06		37.10	0.02	21.60	23.12	2.00	4.76	10.54	0.00	0.00	99.14
Line 4 54Lgrt1left	2.93	0.00	2.04	1.49	0.11	0.58	0.90	0.00	0.00	8.05		37.03	0.04	21.85	22.51	1.71	4.93	10.62	0.00	0.00	98.70
Line 5 54Lgrt1left	2.94	0.00	2.01	1.51	0.14	0.53	0.92	0.00	0.00	8.05		37.13	0.05	21.59	22.75	2.14	4.48	10.88	0.00	0.00	99.02
Line 1 54Lgrt1right	2.93	0.00	2.03	1.50	0.31	0.45	0.83	0.00	0.00	8.05		36.20	0.01	21.26	22.12	4.59	3.70	9.62	0.00	0.00	97.50
Line 3 54Lgrt1right	2.93	0.00	2.04	1.50	0.10	0.58	0.92	0.00	0.00	8.05		36.95	0.01	21.77	22.59	1.42	4.87	10.77	0.00	0.00	98.37
Line 4 54Lgrt1right	2.92	0.00	2.03	1.52	0.10	0.58	0.90	0.00	0.00	8.06		36.69	0.06	21.68	22.79	1.56	4.92	10.59	0.00	0.00	98.28
Line 5 54Lgrt1right	2.90	0.00	2.03	1.53	0.12	0.59	0.92	0.00	0.00	8.09		35.58	0.02	21.17	22.53	1.70	4.84	10.58	0.00	0.00	96.42
Line 6 54Lgrt1right	2.92	0.00	2.01	1.51	0.11	0.58	0.92	0.00	0.00	8.07		36.60	0.03	21.38	22.66	1.63	4.91	10.79	0.00	0.00	97.99
Line 7 54Lgrt1right	2.93	0.00	2.04	1.48	0.25	0.47	0.89	0.00	0.00	8.06		36.44	0.00	21.51	22.11	3.63	3.96	10.31	0.00	0.00	97.96
Line 1 54Lgrt2	2.93	0.00	2.01	1.48	0.19	0.57	0.88	0.00	0.00	8.06		36.40	0.05	21.21	21.97	2.72	4.71	10.25	0.00	0.00	97.31
Line 2 54Lgrt2	2.93	0.00	2.01	1.50	0.14	0.63	0.85	0.00	0.00	8.06		36.41	0.05	21.23	22.33	1.99	5.25	9.81	0.00	0.00	97.07
Line 3 54Lgrt2	2.94	0.00	2.00	1.50	0.14	0.62	0.85	0.00	0.00	8.06		36.61	0.07	21.16	22.36	2.12	5.19	9.85	0.00	0.00	97.33
Line 4 54Lgrt2	2.92	0.00	2.01	1.49	0.13	0.63	0.88	0.00	0.00	8.07		36.33	0.04	21.24	22.11	1.90	5.24	10.17	0.00	0.00	97.03
Line 5 54Lgrt2	3.06	0.00	1.97	1.45	0.25	0.47	0.75	0.00	0.00	7.96		37.40	0.04	20.46	21.20	3.63	3.88	8.59	0.00	0.00	95.20
Line 1 54Q1grt1aline	2.95	0.00	2.02	1.49	0.06	0.65	0.86	0.00	0.00	8.04		37.69	0.01	21.88	22.79	0.88	5.61	10.26	0.00	0.00	99.11
Line 2 54Q1grt1aline	2.95	0.00	2.03	1.52	0.04	0.76	0.73	0.00	0.00	8.04		38.01	0.04	22.21	23.52	0.69	6.61	8.76	0.00	0.00	99.83
Line 3 54Q1grt1aline	2.94	0.00	2.04	1.48	0.05	0.71	0.82	0.00	0.00	8.04		37.83	0.04	22.25	22.79	0.69	6.16	9.82	0.00	0.00	99.58
Line 4 54Q1grt1aline	2.94	0.00	2.05	1.50	0.05	0.72	0.78	0.00	0.00	8.04		37.71	0.01	22.34	23.05	0.69	6.22	9.38	0.00	0.00	99.41
Line 5 54Q1grt1aline	2.94	0.00	2.05	1.57	0.05	0.79	0.65	0.00	0.00	8.04		38.04	0.01	22.50	24.25	0.70	6.85	7.85	0.00	0.00	100.19
Line 6 54Q1grt1aline	2.93	0.00	2.05	1.60	0.04	0.82	0.60	0.00	0.00	8.05		37.63	0.02	22.38	24.67	0.67	7.06	7.21	0.00	0.00	99.64
Line 7 54Q1grt1aline	2.93	0.00	2.03	1.52	0.05	0.73	0.78	0.00	0.00	8.05		37.70	0.04	22.18	23.30	0.82	6.30	9.32	0.00	0.00	99.66
Line 1 54Q1grt1bline	2.94	0.00	2.03	1.72	0.04	0.79	0.51	0.00	0.00	8.04		37.65	0.04	22.13	26.45	0.66	6.81	6.14	0.00	0.00	99.88
Line 2 54Q1grt1bline	2.94	0.00	2.03	1.62	0.04	0.87	0.54	0.00	0.00	8.04		37.90	0.02	22.15	24.91	0.55	7.54	6.44	0.00	0.00	99.52
Line 4 54Q1grt1bline	2.92	0.00	2.02	1.63	0.04	0.86	0.60	0.00	0.00	8.07		36.95	0.01	21.78	24.75	0.56	7.34	7.07	0.00	0.00	98.45
Line 5 54Q1grt1bline	2.94	0.00	2.01	1.62	0.04	0.83	0.62	0.00	0.00	8.06		37.32	0.02	21.62	24.60	0.60	7.09	7.40	0.00	0.00	98.65
Line 6 54Q1grt1bline	2.95	0.00	2.03	1.56	0.04	0.79	0.65	0.00	0.00	8.04		37.61	0.02	22.04	23.88	0.66	6.80	7.76	0.00	0.00	98.78
Line 7 54Q1grt1bline	2.94	0.00	2.04	1.52	0.17	0.53	0.85	0.00	0.00	8.05		36.68	0.02	21.60	22.69	2.52	4.44	9.95	0.00	0.00	97.89
54Q1grt2pt1	2.94	0.00	2.02	1.57	0.04	0.80	0.68	0.00	0.00	8.05		37.34	0.01	21.80	23.91	0.66	6.86	8.06	0.00	0.00	98.64
54Q1grt2pt2	2.94	0.00	2.02	1.54	0.06	0.68	0.79	0.00	0.00	8.05		37.19	0.02	21.69	23.28	0.94	5.81	9.33	0.00	0.00	98.26
54Q1grt2pt3	2.94	0.00	2.02	1.51	0.06	0.67	0.85	0.00	0.00	8.05		37.06	0.00	21.67	22.84	0.86	5.69	10.06	0.00	0.00	98.18
54Q1grt2pt4	2.92	0.00	2.03	1.56	0.05	0.77	0.75	0.00	0.00	8.07		36.68	0.00	21.60	23.37	0.69	6.45	8.81	0.00	0.00	97.60
54Q1grt2pt5	2.93	0.00	2.03	1.49	0.05	0.72	0.84	0.00	0.00	8.06		37.03	-0.01	21.77	22.50	0.71	6.11	9.89	0.00	0.00	97.99
54Q1grt2pt6	2.92	0.00	2.02	1.51	0.05	0.69	0.87	0.00	0.00	8.07		36.68	0.01	21.52	22.64	0.81	5.79	10.16	0.00	0.00	97.61

Finnoya Mylonite Zone

Pyroxene	Normalized Atoms											Weight Percent									
Sample	Si	Ti	Al	Fe	Mn	Mg	Ca	Na	K	Total		SiO2	TiO2	Al2O3	FeO	MnO	MgO	CaO	Na2O	K2O	Total
NW10-53Agrtcpxleft-cpx	1.62	0.02	0.63	0.56	0.01	0.62	0.49	0.11	0.09	4.15		40.48	0.73	13.36	16.78	0.25	10.40	11.54	1.43	1.72	96.71
NW10-53Agrtcpxleft-cpx	1.67	0.02	0.56	0.52	0.01	0.66	0.50	0.10	0.07	4.12		42.60	0.54	12.04	15.91	0.23	11.29	11.95	1.35	1.42	97.33
NW10-53Agrtcpxleft-cpx	1.89	0.01	0.23	0.33	0.01	0.61	0.85	0.09	0.00	4.03		50.35	0.18	5.29	10.52	0.38	10.86	21.21	1.25	0.06	100.10
NW10-53Agrtcpxleft-cpx	1.89	0.01	0.25	0.31	0.01	0.59	0.88	0.09	0.00	4.02		50.44	0.19	5.61	9.94	0.33	10.64	21.82	1.18	0.00	100.17
NW10-53Agrtcpxleft-cpx	1.64	0.01	0.60	0.56	0.01	0.63	0.50	0.10	0.08	4.14		41.31	0.34	12.90	16.87	0.22	10.57	11.80	1.33	1.61	96.96
NW10-53Agrtcpxleft-cpx	1.63	0.01	0.62	0.57	0.01	0.60	0.51	0.10	0.08	4.14		40.93	0.38	13.10	17.13	0.22	10.16	11.85	1.34	1.63	96.75
NW10-53Agrtcpxleft-cpx	1.67	0.01	0.56	0.56	0.01	0.64	0.51	0.10	0.07	4.12		42.29	0.40	11.94	16.84	0.25	10.77	11.91	1.30	1.44	97.13
NW10-53Agrtcpxleft-cpx	1.68	0.01	0.55	0.56	0.01	0.64	0.51	0.10	0.07	4.12		42.41	0.42	11.70	16.82	0.21	10.76	11.96	1.28	1.39	96.95
NW10-53Agrtcpxleft-cpx	1.68	0.02	0.53	0.56	0.01	0.64	0.51	0.10	0.07	4.12		42.49	0.51	11.34	16.83	0.21	10.90	12.02	1.27	1.43	97.00
NW10-53Agrtcpxleft-cpx	1.84	0.01	0.30	0.36	0.01	0.61	0.83	0.08	0.01	4.05		48.26	0.23	6.69	11.31	0.30	10.63	20.30	1.07	0.23	99.02
NW10-53Agrtcpxleft-cpx	1.89	0.00	0.23	0.31	0.01	0.61	0.89	0.09	0.00	4.04		50.69	0.17	5.29	10.11	0.36	11.04	22.27	1.21	0.01	101.15
NW10-53Agrtcpxleft-cpx	1.92	0.00	0.16	0.31	0.01	0.65	0.91	0.06	0.00	4.03		51.22	0.16	3.61	9.91	0.26	11.62	22.79	0.86	0.00	100.43
NW10-53Agrtcpxleft-cpx	1.88	0.01	0.26	0.33	0.01	0.60	0.87	0.08	0.00	4.03		49.78	0.19	5.78	10.44	0.30	10.59	21.56	1.15	0.03	99.82
NW10-53Agrtcpxleft-cpx	1.90	0.00	0.21	0.32	0.01	0.63	0.91	0.06	0.00	4.03		50.25	0.15	4.63	9.98	0.30	11.12	22.49	0.83	0.01	99.76
NW10-53Agrtcpxleft-cpx	1.63	0.01	0.62	0.57	0.01	0.61	0.50	0.11	0.08	4.14		40.93	0.43	13.24	16.95	0.23	10.24	11.75	1.39	1.64	96.80
NW10-53Agrtcpxleft-cpx	1.69	0.01	0.53	0.53	0.01	0.71	0.48	0.09	0.06	4.11		42.73	0.38	11.47	15.96	0.19	11.97	11.28	1.15	1.26	96.40
NW10-53Agrtcpxleft-cpx	1.89	0.01	0.23	0.32	0.01	0.62	0.89	0.07	0.00	4.03		50.08	0.20	5.19	10.08	0.26	11.07	21.93	0.96	0.05	99.81
NW10-53Agrtcpxleft-cpx	1.93	0.00	0.15	0.30	0.01	0.67	0.90	0.06	0.00	4.02		51.45	0.10	3.34	9.44	0.31	12.02	22.33	0.77	0.05	99.80
NW10-53Agrtcpxctr-cpx	1.62	0.01	0.63	0.56	0.01	0.63	0.51	0.10	0.08	4.14		40.80	0.35	13.43	16.78	0.18	10.55	11.89	1.35	1.59	96.92
NW10-53Agrtcpxctr-cpx	1.65	0.01	0.59	0.54	0.01	0.64	0.50	0.10	0.08	4.13		41.66	0.37	12.69	16.35	0.19	10.77	11.84	1.34	1.52	96.74
NW10-53Agrtcpxctr-cpx	1.91	0.00	0.19	0.32	0.01	0.64	0.88	0.07	0.00	4.02		51.10	0.15	4.37	10.12	0.32	11.42	22.09	0.93	0.00	100.49
NW10-53Agrtcpxctr-cpx	1.90	0.00	0.21	0.31	0.01	0.63	0.90	0.07	0.00	4.03		50.57	0.14	4.71	9.99	0.34	11.19	22.28	0.93	0.02	100.16
NW10-53Agrtcpxctr-cpx	1.90	0.00	0.20	0.31	0.01	0.63	0.91	0.07	0.00	4.03		50.52	0.17	4.52	9.84	0.33	11.23	22.50	0.90	0.02	100.03
NW10-53Agrtcpxctr-cpx	1.91	0.00	0.18	0.31	0.01	0.64	0.91	0.06	0.00	4.03		50.88	0.18	4.09	9.85	0.28	11.42	22.71	0.88	0.00	100.27
NW10-53Agrtcpxctr-cpx	1.89	0.00	0.21	0.31	0.01	0.64	0.91	0.06	0.00	4.03		50.14	0.17	4.71	9.83	0.24	11.38	22.57	0.79	0.01	99.85
NW10-53Agrtcpxctr-cpx	1.79	0.01	0.41	0.44	0.01	0.65	0.62	0.08	0.04	4.05		46.88	0.43	9.22	13.88	0.21	11.36	15.23	1.11	0.76	99.07
NW10-53Agrtcpxctr-cpx	1.68	0.01	0.55	0.55	0.01	0.65	0.50	0.10	0.07	4.13		42.51	0.34	11.78	16.64	0.23	11.07	11.83	1.37	1.48	97.25
NW10-53Agrtcpxctr-cpx	1.90	0.00	0.19	0.32	0.01	0.67	0.88	0.05	0.00	4.03		50.57	0.16	4.34	10.07	0.23	11.96	21.91	0.74	0.09	100.07
NW10-53Agrtcpxctr-cpx	1.53	0.09	0.70	0.57	0.00	0.87	0.00	0.01	0.51	4.29		37.24	2.95	14.37	16.44	0.09	14.25	0.02	0.08	9.78	95.23
NW10-53Agrtcpxctr-cpx	1.65	0.01	0.59	0.56	0.01	0.63	0.49	0.11	0.09	4.14		41.58	0.34	12.64	16.81	0.23	10.58	11.62	1.45	1.71	96.96
NW1054M_pyxleft_pyx	1.88	0.01	0.25	0.28	0.01	0.63	0.91	0.06	0.00	4.02		50.10	0.26	5.60	9.01	0.19	11.32	22.54	0.81	0.01	99.84
NW1054M_pyxleft_pyx	1.87	0.01	0.30	0.33	0.01	0.66	0.75	0.07	0.01	4.01		49.88	0.25	6.82	10.39	0.18	11.85	18.71	1.00	0.27	99.35
NW1054M_pyxleft_pyx	1.46	0.01	0.32	0.42	0.01	0.78	1.31	0.14	0.00	4.44		22.82	0.16	4.21	7.77	0.17	8.13	19.02	1.09	0.00	63.37
NW1054M_pyxleft_pyx	1.79	0.01	0.48	0.42	0.00	0.65	0.57	0.07	0.03	4.02		46.85	0.35	10.65	13.14	0.13	11.47	13.89	1.00	0.57	98.05
NW1054M_pyxleft_pyx	1.85	0.01	0.30	0.29	0.01	0.59	0.91	0.07	0.00	4.03		49.25	0.28	6.84	9.32	0.16	10.63	22.59	0.90	0.01	99.98
NW1054M_pyxleft_pyx	1.84	0.01	0.31	0.29	0.00	0.61	0.90	0.07	0.00	4.03		48.66	0.23	6.88	9.20	0.14	10.75	22.07	1.02	0.00	98.94
NW1054M_pyxleft_pyx	1.88	0.01	0.26	0.28	0.00	0.63	0.89	0.07	0.00	4.02		50.00	0.18	5.95	8.91	0.11	11.23	22.17	0.99	0.01	99.54
NW1054M_pyxleft_pyx	1.87	0.01	0.28	0.28	0.00	0.60	0.89	0.08	0.00	4.02		49.81	0.25	6.42	8.99	0.12	10.80	22.07	1.09	0.00	99.55

Svartberget Mylonite Zone

Plagioclase	Normalized Atoms											Weight Percent									
Sample	Si	Ti	Al	Fe	Mn	Mg	Ca	Na	K	Total		SiO2	TiO2	Al2O3	FeO	MnO	MgO	CaO	Na2O	K2O	Total
NW11-10AAgrt1_pl	1.51	0.00	1.45	1.44	0.96	0.27	0.14	0.00	0.00	5.77		16.28	0.01	13.33	18.61	12.22	1.97	1.40	0.01	0.00	63.83
NW11-10AAgrt1_pl	2.68	0.00	1.34	0.00	0.00	0.00	0.29	0.67	0.01	4.99		60.17	0.00	25.53	0.05	0.02	0.00	6.14	7.72	0.26	99.89
NW11-10AAgrt1_pl	2.65	0.00	1.35	0.00	0.00	0.00	0.33	0.65	0.01	5.00		59.46	0.02	25.75	0.02	0.00	0.00	6.86	7.50	0.24	99.85
NW11-10AAgrt1_pl	2.66	0.00	1.35	0.00	0.00	0.00	0.32	0.64	0.01	4.99		59.76	0.00	25.70	0.01	0.02	0.00	6.80	7.43	0.21	99.93
NW11-10AAgrt1_pl	2.68	0.00	1.34	0.00	0.00	0.00	0.30	0.65	0.01	4.99		60.24	0.00	25.53	0.12	0.03	0.00	6.34	7.60	0.20	100.07
NW11-10AAgrt1_pl	2.68	0.00	1.34	0.00	0.00	0.00	0.29	0.66	0.01	4.99		59.81	0.00	25.28	0.09	0.03	0.00	6.02	7.59	0.23	99.04
NW11-10AAgrt1_pl	2.69	0.00	1.33	0.00	0.00	0.00	0.29	0.67	0.01	4.99		60.45	0.01	25.37	0.08	0.01	0.00	6.14	7.75	0.16	99.97
NW11-10N_symp1_pl	2.81	0.00	1.19	0.01	0.00	0.00	0.19	0.76	0.02	4.98		64.21	0.02	22.98	0.20	0.02	0.00	4.10	8.93	0.29	100.74
NW11-10N_symp1_pl	2.82	0.00	1.19	0.01	0.00	0.00	0.19	0.76	0.02	4.98		64.05	0.01	22.87	0.31	0.00	0.00	4.09	8.86	0.28	100.47
NW11-10N_symp1_pl	2.79	0.00	1.22	0.01	0.00	0.00	0.20	0.75	0.01	4.99		63.98	0.00	23.78	0.34	0.01	0.00	4.29	8.90	0.24	101.55
NW11-10N_symp1_pl	2.77	0.00	1.24	0.01	0.00	0.00	0.21	0.74	0.02	4.99		63.74	0.01	24.22	0.36	0.00	0.00	4.45	8.75	0.29	101.82
NW11-10N_symp1_pl	2.78	0.00	1.22	0.01	0.00	0.00	0.21	0.74	0.02	4.98		63.55	0.00	23.72	0.25	0.00	0.00	4.56	8.72	0.28	101.08
NW11-10N_symp1_pl	2.80	0.00	1.21	0.01	0.00	0.00	0.18	0.77	0.02	4.99		64.19	0.01	23.43	0.24	0.00	0.00	3.90	9.09	0.32	101.17
NW11-10N_symp1_pl	2.83	0.00	1.18	0.01	0.00	0.00	0.16	0.79	0.02	4.98		65.02	0.01	23.01	0.20	0.00	0.00	3.52	9.31	0.32	101.39
NW11-10N_symp1_pl	2.82	0.00	1.19	0.01	0.00	0.00	0.16	0.80	0.01	4.99		64.97	0.01	23.22	0.17	0.00	0.00	3.47	9.51	0.26	101.61
NW11-10N_symp1_pl	2.80	0.00	1.21	0.01	0.00	0.00	0.20	0.74	0.02	4.97		64.07	0.00	23.53	0.24	0.02	0.00	4.19	8.72	0.28	101.05
NW11-10N_symp1_pl	2.79	0.00	1.22	0.01	0.00	0.00	0.21	0.74	0.02	4.98		63.46	0.00	23.51	0.23	0.01	0.00	4.54	8.71	0.28	100.72
NW11-10N_grt1_pl	2.53	0.00	1.48	0.01	0.00	0.00	0.47	0.50	0.01	4.99		56.61	0.01	28.08	0.27	0.00	0.00	9.87	5.77	0.09	100.69
NW11-10N_grt1_pl	2.57	0.00	1.43	0.01	0.00	0.00	0.42	0.56	0.01	5.00		57.98	0.00	27.43	0.23	0.00	0.00	8.84	6.51	0.12	101.10
NW11-10N_grt1_pl	2.83	0.00	1.18	0.01	0.00	0.00	0.17	0.79	0.01	4.98		64.85	0.00	22.95	0.17	0.02	0.02	3.61	9.30	0.20	101.12
NW11-10N_grt1_pl	2.76	0.00	1.25	0.00	0.00	0.00	0.24	0.73	0.01	4.99		62.64	0.00	24.01	0.13	0.00	0.00	5.15	8.50	0.18	100.61
NW11-10N_grt1_pl	2.53	0.00	1.47	0.01	0.00	0.00	0.45	0.53	0.00	5.00		57.02	0.00	28.05	0.29	0.00	0.01	9.42	6.13	0.09	101.00
NW11-10N_grt1_pl	2.59	0.00	1.41	0.01	0.00	0.00	0.40	0.58	0.01	4.99		58.43	0.00	26.98	0.18	0.00	0.00	8.37	6.70	0.14	100.80
NW11-10N_grt1_pl	2.60	0.00	1.41	0.01	0.00	0.00	0.39	0.58	0.01	4.99		58.51	0.00	26.87	0.25	0.00	0.03	8.23	6.75	0.15	100.79
NW11-10N_grt1_pl	2.55	0.00	1.45	0.01	0.00	0.00	0.43	0.54	0.01	4.99		57.31	0.00	27.66	0.20	0.00	0.00	8.99	6.30	0.10	100.56
NW11-10N_grt1_pl	2.60	0.00	1.41	0.01	0.00	0.00	0.39	0.58	0.01	5.00		58.51	0.02	26.86	0.20	0.03	0.00	8.21	6.79	0.13	100.76
NW11-10N_grt2_pl	2.57	0.00	1.44	0.00	0.00	0.00	0.41	0.55	0.01	4.99		58.10	0.00	27.49	0.13	0.00	0.00	8.72	6.44	0.09	100.97
NW11-10N_grt2_pl	2.04	0.00	1.88	0.01	0.00	0.00	0.64	0.87	0.01	5.45		25.56	0.00	20.02	0.22	0.00	0.00	7.45	5.61	0.05	58.90
NW11-10N_grt2_pl	2.54	0.00	1.45	0.03	0.00	0.03	0.44	0.49	0.01	4.98		55.66	0.00	26.99	0.66	0.03	0.37	8.96	5.58	0.12	98.37
NW11-10N_grt2_pl	2.60	0.00	1.41	0.01	0.00	0.00	0.39	0.58	0.01	4.99		58.08	0.02	26.75	0.20	0.00	0.00	8.24	6.68	0.09	100.07
NW11-10N_grt2_pl	1.51	0.00	1.48	1.54	0.03	0.53	0.65	0.00	0.00	5.75		18.11	0.03	15.04	22.00	0.38	4.29	7.24	0.02	0.01	67.12
NW11-10N_grt2_pl	2.77	0.00	1.24	0.01	0.00	0.00	0.22	0.72	0.01	4.97		63.37	0.01	23.99	0.16	0.00	0.01	4.73	8.49	0.18	100.94
NW11-10N_grt2_pl	2.48	0.00	1.52	0.02	0.00	0.00	0.50	0.47	0.00	5.00		55.56	0.02	28.94	0.42	0.00	0.01	10.49	5.47	0.08	100.98
NW11-10N_grt2_pl	2.78	0.00	1.05	0.11	0.00	0.30	0.09	0.70	0.02	5.05		60.87	0.00	19.55	2.99	0.01	4.40	1.76	7.90	0.26	97.75
NW11-10N_grt2_pl	2.59	0.00	1.42	0.01	0.00	0.00	0.39	0.58	0.01	4.99		58.58	0.00	27.23	0.27	0.00	0.00	8.28	6.78	0.09	101.22
NW11-10N_grt2_pl	2.64	0.00	1.37	0.01	0.00	0.00	0.35	0.61	0.01	4.98		59.79	0.00	26.34	0.19	0.00	0.00	7.38	7.15	0.10	100.96
NW11-10N_grt2_pl	2.49	0.00	1.52	0.01	0.00	0.00	0.50	0.48	0.00	4.99		55.83	0.01	28.88	0.21	0.00	0.00	10.40	5.53	0.06	100.91

Svartberget Mylonite Zone

Plagioclase	Normalized Atoms											Weight Percent									
Sample	Si	Ti	Al	Fe	Mn	Mg	Ca	Na	K	Total		SiO2	TiO2	Al2O3	FeO	MnO	MgO	CaO	Na2O	K2O	Total
NW11-10N_symp2_pl	2.81	0.00	1.20	0.01	0.00	0.00	0.18	0.77	0.01	4.98		64.59	0.00	23.36	0.20	0.02	0.00	3.80	9.15	0.17	101.29
NW11-10N_symp2_pl	2.82	0.00	1.19	0.01	0.00	0.00	0.16	0.79	0.01	4.98		64.78	0.03	23.21	0.17	0.04	0.00	3.49	9.36	0.20	101.29
NW11-10N_symp2_pl	2.83	0.00	1.18	0.01	0.00	0.00	0.16	0.79	0.01	4.98		64.88	0.02	23.07	0.17	0.04	0.00	3.42	9.35	0.20	101.14
NW11-10N_symp2_pl	2.86	0.00	1.15	0.01	0.00	0.00	0.14	0.82	0.01	4.98		65.80	0.00	22.50	0.16	0.00	0.00	2.98	9.68	0.17	101.30
NW11-10N_symp2_pl	2.81	0.00	1.20	0.01	0.00	0.00	0.18	0.76	0.01	4.97		64.73	0.01	23.51	0.18	0.00	0.00	3.84	9.02	0.21	101.51
NW11-10N_symp2_pl	2.80	0.00	1.21	0.01	0.00	0.00	0.17	0.77	0.01	4.98		64.57	0.00	23.67	0.16	0.00	0.00	3.76	9.19	0.19	101.53
NW11-10N_symp2_pl	2.79	0.00	1.22	0.01	0.00	0.00	0.19	0.75	0.01	4.98		63.84	0.01	23.72	0.26	0.00	0.00	4.15	8.90	0.18	101.06
NW11-10FAmatrix_pl	2.69	0.00	1.32	0.01	0.00	0.00	0.30	0.66	0.01	4.98		60.50	0.02	25.23	0.19	0.04	0.00	6.25	7.63	0.20	100.06
NW11-10FAmatrix_pl	2.50	0.00	1.43	0.01	0.00	0.00	0.00	0.17	1.51	5.62		26.10	0.06	12.62	0.09	0.00	0.00	0.01	0.92	12.32	52.13
NW11-10FAmatrix_pl	2.67	0.00	1.34	0.00	0.00	0.00	0.32	0.63	0.01	4.98		60.18	0.00	25.63	0.08	0.04	0.00	6.71	7.38	0.20	100.22
NW11-10FAmatrix_pl	2.68	0.00	1.34	0.00	0.00	0.00	0.30	0.65	0.01	4.98		60.94	0.00	25.84	0.10	0.00	0.00	6.39	7.66	0.20	101.12
NW11-10BAgrt1_pl	2.61	0.00	1.41	0.01	0.00	0.00	0.34	0.62	0.01	5.00		58.55	0.01	26.89	0.14	0.00	0.00	7.11	7.19	0.23	100.12
NW11-10BAgrt1_pl	2.63	0.00	1.39	0.00	0.00	0.00	0.33	0.62	0.02	4.99		59.21	0.01	26.63	0.05	0.00	0.00	7.01	7.16	0.27	100.35
NW11-10BAgrt1_pl	2.62	0.00	1.39	0.00	0.00	0.00	0.34	0.62	0.01	4.99		59.09	0.00	26.63	0.09	0.01	0.00	7.18	7.18	0.23	100.41
NW11-10BAgrt1_pl	2.62	0.00	1.40	0.00	0.00	0.00	0.35	0.61	0.01	4.99		59.54	0.00	26.94	0.08	0.02	0.00	7.35	7.11	0.20	101.25
NW11-10BAgrt1_pl	2.63	0.00	1.39	0.00	0.00	0.00	0.33	0.64	0.02	5.00		59.85	0.00	26.78	0.06	0.01	0.00	7.02	7.46	0.27	101.45
NW11-10BAgrt1_pl	2.63	0.00	1.38	0.00	0.00	0.00	0.33	0.64	0.01	5.00		59.48	0.00	26.51	0.09	0.00	0.00	7.03	7.45	0.23	100.80
NW11-10BAgrt1_pl	2.65	0.00	1.37	0.00	0.00	0.00	0.34	0.63	0.01	4.99		59.92	0.00	26.31	0.05	0.01	0.00	7.08	7.34	0.17	100.90
NW11-10BAgrt1_pl	2.63	0.00	1.39	0.00	0.00	0.00	0.34	0.62	0.02	5.00		59.62	0.00	26.69	0.05	0.01	0.00	7.20	7.30	0.27	101.14
NW11-10BAgrt1_pl	2.64	0.00	1.38	0.00	0.00	0.00	0.33	0.62	0.02	4.99		59.74	0.01	26.48	0.05	0.01	0.00	6.88	7.28	0.31	100.77
NW11-10BAgrt1_pl	1.45	0.09	1.53	1.17	0.03	0.96	0.00	0.01	0.94	6.17		16.57	1.35	14.82	15.96	0.37	7.36	0.02	0.08	8.41	64.93
NW11-10BAgrt1_pl	2.63	0.00	1.39	0.00	0.00	0.00	0.35	0.60	0.02	4.99		59.23	0.00	26.50	0.02	0.03	0.01	7.39	7.02	0.30	100.49
NW11-10BAgrt1_pl	2.63	0.00	1.38	0.00	0.00	0.00	0.33	0.63	0.01	5.00		59.62	0.00	26.57	0.03	0.00	0.00	7.04	7.37	0.20	100.82
NW11-10BAgrt1_pl	2.63	0.00	1.39	0.00	0.00	0.00	0.34	0.61	0.02	4.99		59.56	0.00	26.61	0.08	0.00	0.00	7.25	7.08	0.27	100.86
NW11-10BApl1_pl	2.63	0.00	1.39	0.00	0.00	0.00	0.34	0.62	0.02	5.00		59.18	0.00	26.53	0.04	0.03	0.01	7.09	7.23	0.28	100.38
NW11-10BApl1_pl	2.14	0.00	1.82	0.00	0.00	0.00	0.51	0.93	0.02	5.43		26.98	0.02	19.54	0.06	0.03	0.00	5.99	6.07	0.17	58.86
NW11-10BApl1_pl	2.63	0.00	1.39	0.00	0.00	0.00	0.33	0.63	0.02	5.00		59.50	0.00	26.65	0.06	0.03	0.00	6.88	7.40	0.34	100.87
NW11-10BApl1_pl	2.68	0.00	1.34	0.00	0.00	0.00	0.29	0.66	0.02	4.99		60.77	0.02	25.74	0.03	0.02	0.00	6.16	7.77	0.36	100.87
NW11-10BApl1_pl	2.67	0.00	1.34	0.00	0.00	0.00	0.30	0.65	0.01	4.99		60.41	0.00	25.77	0.01	0.00	0.01	6.40	7.57	0.24	100.41
NW11-10BApl1_pl	2.67	0.00	1.35	0.00	0.00	0.00	0.29	0.67	0.02	5.00		60.61	0.00	26.01	0.05	0.02	0.00	6.06	7.78	0.40	100.92
NW11-10BApl1_pl	2.65	0.00	1.37	0.00	0.00	0.00	0.31	0.64	0.02	4.99		60.06	0.00	26.25	0.05	0.03	0.00	6.48	7.49	0.33	100.69
NW11-10BApl1_pl	2.63	0.00	1.39	0.00	0.00	0.00	0.33	0.62	0.02	5.00		59.20	0.00	26.65	0.06	0.05	0.00	6.97	7.22	0.32	100.47
NW11-10BApl1_pl	2.62	0.00	1.40	0.00	0.00	0.00	0.33	0.62	0.02	4.99		59.28	0.00	26.88	0.04	0.00	0.00	7.02	7.20	0.29	100.70
NW11-10BApl1_pl	2.62	0.00	1.39	0.00	0.00	0.00	0.35	0.61	0.02	4.99		59.20	0.00	26.67	0.07	0.01	0.00	7.35	7.09	0.27	100.66

Svartberget Mylonite Zone

Garnet	Normalized Atoms											Weight Percent									
Sample	Si	Ti	Al	Fe	Mn	Mg	Ca	Na	K	Total		SiO2	TiO2	Al2O3	FeO	MnO	MgO	CaO	Na2O	K2O	Total
NW11-10AAgrt1_grt	2.85	0.00	1.95	1.77	1.07	0.37	0.16	0.01	0.01	8.18		26.64	0.00	15.48	19.77	11.82	2.31	1.39	0.04	0.04	77.49
NW11-10AAgrt1_grt	2.97	0.00	1.99	1.63	0.74	0.51	0.18	0.00	0.00	8.03		37.22	0.02	21.13	24.44	10.93	4.26	2.16	0.00	0.00	100.16
NW11-10AAgrt1_grt	2.99	0.00	1.98	1.65	0.69	0.52	0.18	0.00	0.00	8.02		37.36	0.01	20.94	24.58	10.11	4.37	2.15	0.01	0.00	99.52
NW11-10AAgrt1_grt	2.98	0.00	2.00	1.54	0.99	0.37	0.13	0.00	0.00	8.02		36.67	0.00	20.82	22.67	14.42	3.03	1.46	0.03	0.00	99.09
NW11-10AAgrt1_grt	3.00	0.00	1.96	1.62	0.75	0.49	0.19	0.00	0.00	8.02		37.56	0.03	20.84	24.26	11.12	4.13	2.26	0.02	0.00	100.21
NW11-10AAgrt1_grt	3.00	0.00	1.98	1.60	0.78	0.47	0.18	0.00	0.00	8.01		37.27	0.00	20.94	23.76	11.43	3.93	2.13	0.01	0.00	99.47
NW11-10AAgrt1_grt	3.03	0.00	1.95	1.52	0.90	0.43	0.15	0.00	0.00	7.99		37.79	0.02	20.68	22.72	13.24	3.57	1.79	0.01	0.01	99.82
NW11-10AAgrt1_grt	3.01	0.00	1.98	1.53	1.01	0.33	0.13	0.00	0.00	8.00		37.44	0.02	20.87	22.79	14.86	2.74	1.48	0.00	0.01	100.21
NW11-10N_grt1_grt	3.02	0.00	1.95	1.58	0.05	0.69	0.71	0.00	0.00	8.00		39.29	0.03	21.54	24.56	0.83	5.98	8.58	0.01	0.00	100.82
NW11-10N_grt1_grt	3.01	0.00	1.96	1.63	0.02	0.69	0.70	0.00	0.00	8.01		39.17	0.07	21.62	25.32	0.27	5.99	8.54	0.01	0.01	101.00
NW11-10N_grt1_grt	3.01	0.01	1.95	1.62	0.02	0.69	0.72	0.00	0.00	8.01		39.09	0.15	21.49	25.10	0.27	6.00	8.74	0.02	0.01	100.86
NW11-10N_grt1_grt	3.01	0.00	1.94	1.68	0.02	0.69	0.66	0.00	0.00	8.01		39.12	0.07	21.38	26.11	0.34	5.99	8.03	0.00	0.00	101.04
NW11-10N_grt1_grt	3.01	0.00	1.96	1.60	0.02	0.69	0.72	0.00	0.00	8.01		39.50	0.06	21.76	25.15	0.30	6.10	8.75	0.01	0.00	101.64
NW11-10N_grt1_grt	3.00	0.01	1.97	1.62	0.02	0.69	0.70	0.00	0.00	8.00		39.09	0.12	21.80	25.19	0.29	6.00	8.48	0.00	0.01	100.97
NW11-10N_grt1_grt	3.03	0.00	1.95	1.59	0.02	0.68	0.71	0.00	0.00	7.99		40.03	0.05	21.88	25.15	0.25	6.03	8.72	0.02	0.02	102.16
NW11-10N_grt1_grt	3.02	0.00	1.93	1.64	0.02	0.69	0.72	0.00	0.00	8.02		39.35	0.04	21.29	25.58	0.26	6.01	8.71	0.02	0.00	101.25
NW11-10N_grt1_grt	3.01	0.00	1.94	1.62	0.02	0.70	0.71	0.00	0.00	8.01		39.15	0.04	21.43	25.23	0.32	6.06	8.61	0.01	0.00	100.85
NW11-10N_grt2_grt	3.01	0.00	1.96	1.60	0.03	0.70	0.68	0.00	0.00	8.00		39.45	0.01	21.82	25.11	0.52	6.14	8.36	0.01	0.00	101.43
NW11-10N_grt2_grt	3.01	0.00	1.97	1.62	0.02	0.68	0.70	0.01	0.00	8.01		39.02	0.05	21.64	25.16	0.38	5.88	8.45	0.04	0.00	100.63
NW11-10N_grt2_grt	3.00	0.01	1.96	1.62	0.02	0.67	0.72	0.00	0.00	8.01		39.21	0.11	21.77	25.35	0.35	5.91	8.74	0.02	0.01	101.47
NW11-10N_grt2_grt	3.02	0.00	1.96	1.61	0.02	0.70	0.69	0.00	0.00	8.01		39.53	0.05	21.76	25.31	0.32	6.12	8.50	0.03	0.01	101.64
NW11-10N_grt2_grt	3.02	0.00	1.94	1.65	0.02	0.67	0.71	0.00	0.00	8.01		39.16	0.05	21.32	25.58	0.36	5.79	8.64	0.00	0.00	100.92
NW11-10N_grt2_grt	3.02	0.01	1.96	1.61	0.02	0.66	0.72	0.00	0.00	8.00		39.29	0.09	21.66	25.08	0.36	5.77	8.75	0.02	0.00	101.01
NW11-10N_grt2_grt	3.01	0.01	1.95	1.63	0.02	0.69	0.70	0.00	0.00	8.01		39.18	0.09	21.60	25.39	0.38	5.99	8.47	0.02	0.01	101.13
NW11-10N_grt2_grt	3.02	0.00	1.96	1.57	0.06	0.71	0.68	0.00	0.00	8.00		39.33	0.03	21.74	24.53	0.89	6.22	8.23	0.00	0.00	100.96
NW11-10BAgrt1_grt	3.00	0.00	1.99	1.60	0.92	0.32	0.16	0.00	0.00	8.00		37.04	0.00	20.85	23.53	13.46	2.67	1.84	0.02	0.01	99.41
NW11-10BAgrt1_grt	6.00	0.00	0.00	0.00	0.00	0.00	0.00	0.00	0.00	6.00		44.74	0.00	0.00	0.01	0.02	0.00	0.00	0.00	0.00	44.78
NW11-10BAgrt1_grt	2.97	0.00	2.03	1.53	1.09	0.21	0.18	0.00	0.00	8.02		35.95	0.03	20.89	22.10	15.60	1.71	2.03	0.00	0.03	98.35
NW11-10BAgrt1_grt	3.00	0.00	1.99	1.66	0.78	0.43	0.15	0.00	0.00	8.01		37.35	0.00	21.05	24.75	11.41	3.56	1.76	0.02	0.00	99.90
NW11-10BAgrt1_grt	3.01	0.00	1.97	1.67	0.69	0.48	0.19	0.00	0.00	8.00		37.86	0.02	20.96	25.14	10.17	4.00	2.21	0.00	0.00	100.37
NW11-10BAgrt1_grt	3.02	0.00	1.97	1.66	0.70	0.47	0.18	0.00	0.00	8.00		37.96	0.00	21.05	24.95	10.42	3.99	2.06	0.00	0.00	100.44
NW11-10BAgrt1_grt	3.00	0.00	1.99	1.63	0.78	0.43	0.17	0.00	0.00	8.01		37.46	0.00	21.14	24.34	11.51	3.61	2.03	0.02	0.00	100.10
NW11-10BAgrt1_grt	3.01	0.00	1.98	1.58	0.91	0.37	0.14	0.00	0.00	8.00		37.35	0.00	20.86	23.48	13.33	3.05	1.67	0.02	0.00	99.76

Svartberget Mylonite Zone

Pyroxene	Normalized Atoms											Weight Percent									
Sample	Si	Ti	Al	Fe	Mn	Mg	Ca	Na	K	Total		SiO2	TiO2	Al2O3	FeO	MnO	MgO	CaO	Na2O	K2O	Total
NW11-10N_symp1_pyx	1.80	0.05	0.36	0.49	0.00	0.73	0.47	0.10	0.02	4.02		46.82	1.79	7.88	15.29	0.11	12.64	11.46	1.31	0.34	97.63
NW11-10N_symp1_pyx	1.79	0.05	0.37	0.50	0.00	0.71	0.47	0.11	0.02	4.03		46.20	1.87	8.18	15.51	0.08	12.36	11.29	1.42	0.36	97.27
NW11-10N_symp1_pyx	1.97	0.01	0.07	0.30	0.01	0.73	0.88	0.05	0.00	4.02		52.56	0.18	1.52	9.70	0.17	13.08	21.93	0.69	0.01	99.85
NW11-10N_symp1_pyx	1.98	0.00	0.07	0.30	0.00	0.73	0.87	0.05	0.00	4.01		52.96	0.18	1.64	9.62	0.12	13.14	21.77	0.74	0.00	100.16
NW11-10N_symp1_pyx	1.98	0.00	0.06	0.30	0.01	0.73	0.89	0.05	0.00	4.01		52.99	0.16	1.43	9.61	0.16	13.10	22.18	0.70	0.00	100.34
NW11-10N_symp1_pyx	1.98	0.00	0.05	0.29	0.00	0.74	0.90	0.04	0.00	4.01		52.95	0.12	1.18	9.34	0.16	13.27	22.39	0.59	0.01	100.00
NW11-10N_symp1_pyx	1.98	0.00	0.05	0.29	0.00	0.74	0.90	0.04	0.00	4.01		53.28	0.15	1.18	9.44	0.15	13.30	22.49	0.56	0.01	100.57
NW11-10N_symp1_pyx	1.97	0.01	0.08	0.30	0.00	0.72	0.88	0.05	0.00	4.01		52.67	0.21	1.72	9.61	0.11	12.97	21.86	0.70	0.00	99.86
NW11-10N_symp2_pyx	1.95	0.01	0.11	0.30	0.00	0.70	0.87	0.06	0.00	4.01		52.34	0.31	2.62	9.61	0.15	12.66	21.77	0.84	0.00	100.30
NW11-10N_symp2_pyx	1.97	0.00	0.07	0.29	0.01	0.74	0.88	0.05	0.00	4.01		52.94	0.18	1.66	9.30	0.17	13.24	22.00	0.69	0.00	100.18
NW11-10N_symp2_pyx	1.96	0.01	0.10	0.29	0.01	0.72	0.87	0.06	0.00	4.01		52.58	0.27	2.31	9.32	0.18	13.02	21.95	0.76	0.00	100.39
NW11-10N_symp2_pyx	2.01	0.00	0.78	0.06	0.00	0.15	0.37	0.45	0.01	3.83		59.77	0.01	19.77	2.18	0.01	2.99	10.41	6.89	0.13	102.18
NW11-10N_symp2_pyx	1.81	0.04	0.35	0.49	0.00	0.73	0.51	0.10	0.01	4.03		43.77	1.36	7.14	14.23	0.09	11.79	11.44	1.20	0.21	91.23
NW11-10N_symp2_pyx	1.74	0.06	0.45	0.49	0.00	0.70	0.48	0.13	0.02	4.05		44.98	1.90	9.82	15.15	0.12	12.18	11.49	1.70	0.32	97.65
NW11-10N_symp2_pyx	1.79	0.05	0.39	0.48	0.00	0.72	0.48	0.11	0.01	4.03		46.22	1.75	8.55	14.87	0.11	12.56	11.50	1.48	0.26	97.29
NW11-10N_symp2_pyx	1.78	0.05	0.39	0.49	0.00	0.73	0.47	0.10	0.01	4.03		46.32	1.69	8.55	15.20	0.14	12.66	11.38	1.38	0.28	97.59
NW11-10N_symp2_pyx	1.97	0.00	0.07	0.29	0.01	0.73	0.89	0.05	0.00	4.01		52.69	0.17	1.68	9.32	0.20	13.10	22.11	0.68	0.00	99.95